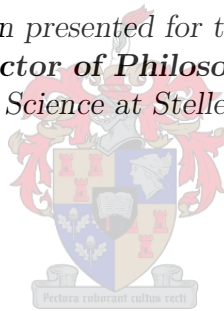


# Structural Dynamics in DCNQI Salts and Transition Metal Dichalcogenides Studied by Electron Diffraction Simulation

by

Olufemi Opeyemi Olaoye

*Dissertation presented for the degree of*  
**Doctor of Philosophy**  
*in the Faculty of Science at Stellenbosch University*



Department of Physics,  
University of Stellenbosch,  
Private Bag X1, Matieland 7602, South Africa.

Supervisor:

Prof. Heinrich PH Schwoerer

December 2015

# Declaration

By submitting this thesis electronically, I declare that the entirety of the work contained therein is my own, original work, that I am the sole author thereof (save to the extent explicitly otherwise stated), that reproduction and publication thereof by Stellenbosch University will not infringe any third party rights and that I have not previously in its entirety or in part submitted it for obtaining any qualification.

December, 2015.

Copyright © 2015 Stellenbosch University  
All rights reserved.

# Contents

Declaration	i
Contents	ii
Abstract	iv
Opsomming	v
Acknowledgements	vi
Dedications	vii
<b>1 Introduction</b>	<b>1</b>
<b>2 Electron diffraction and charge density waves</b>	<b>4</b>
2.1 Introduction . . . . .	4
2.2 Electron diffraction . . . . .	4
2.2.1 Interpreting electron diffraction patterns . . . . .	4
2.2.2 Electron density and electrostatic potential in crystal lattices . . . . .	8
2.3 Simulation's models: 'Weak' versus 'strong' phase object approximation . . . . .	11
2.4 Electronic structure of and charge density wave formation in crystalline solids . .	12
<b>3 Transition metal dichalcogenides</b>	<b>17</b>
3.1 Introducing transition metal dichalcogenides . . . . .	17
3.2 A retrospect of charge density wave dynamics in $4H_b$ -TaSe <sub>2</sub> single crystals . . . . .	19
3.3 Commensurate charge density wave formation in $1T$ -TiSe <sub>2</sub> single crystals . . . . .	30
3.4 Closing inferences . . . . .	35
<b>4 General perspectives on the radical anion organic salts of Cu-DCNQI</b>	<b>37</b>
4.1 Introduction to organic molecular crystals . . . . .	37
4.2 Organic molecular crystals of dicyanoquinonediimine (DCNQI) salts . . . . .	39
4.3 Phase transitions and charge density wave formation in Cu[2,5R <sub>1</sub> ,R <sub>2</sub> -DCNQI] <sub>2</sub> salts	43
<b>5 Structural transition studies of Cu-DCNQI salts via diffraction analysis</b>	<b>48</b>
5.1 Introduction . . . . .	48
5.2 Analysis of room temperature electron diffraction patterns in undeuterated and deuterated Cu-DCNQI salts . . . . .	48
5.3 Why do Cu-DCNQI salts with halogen or mixed radicals have <i>high</i> transition temperatures? . . . . .	58
5.4 Structural lability, molecular motion and fluctuating Bragg reflections in Cu-DCNQI salts . . . . .	62

5.5	Electron diffraction simulation and analysis of charge ordering and CDW formation in Cu-DCNQI salts . . . . .	67
5.6	Evidence of CDW formation in Cu(MeBr-DCNQI) <sub>2</sub> through X-ray and electron diffraction experiments . . . . .	78
5.6.1	X-ray diffraction experiment on Cu-DCNQI structures . . . . .	78
5.6.2	Electron diffraction experiment on Cu-DCNQI in our laboratory . . . . .	80
5.7	Closing inferences . . . . .	83
<b>6</b>	<b>Summary and conclusion</b>	<b>84</b>
	<b>Appendices</b>	<b>87</b>
<b>A</b>	<b>Decoupled superlattice domain analysis in <math>4H_b</math>-TaSe<sub>2</sub> single crystals</b>	<b>88</b>
<b>B</b>	<b>Matlab codes</b>	<b>89</b>
<b>C</b>	<b>Procedure for electron diffraction simulation</b>	<b>92</b>
<b>D</b>	<b>CIF codes used in electron diffraction simulation</b>	<b>93</b>
	<b>List of References</b>	<b>125</b>

# Abstract

An in-depth understanding of the working principles of and phenomena governing strongly correlated condensed matter materials has paved way for technological advancement in electronics in the recent decades. The discovery and characterisation of many functional materials ranging from superconductors to insulators are hinged on the progressive understanding of the driving mechanisms behind macroscopic properties like superconductivity and magneto-resistance. Stemming from the nature of structural transitions in highly correlated solids and the corresponding abrupt changes in their conductivity or resistivity, various degrees of order parameters have been investigated using different experimental techniques such as angle resolved photoelectron spectroscopy, optical reflectivity measurements, X-ray crystallography and pump-probe spectroscopy, among others. One major technique that could be used to gain further understanding of these correlated systems is electron diffraction analysis.

In this dissertation, we demonstrate a qualitative working relationship between electron diffraction simulation and the corresponding X-ray and electron diffraction experiments. These structural analysis techniques are used to investigate metal-insulator structural transitions in strong electron-lattice correlated charge density wave compounds of the radical anion organic molecular crystals of Cu-DCNQI and two members of transition metal dichalcogenides, namely,  $4H_b$ -TaSe<sub>2</sub> and  $1T$ -TiSe<sub>2</sub> single crystals. This study contributes to the observation and dynamics of charge density waves on the atomic spatial and temporal resolutions. A systematic analysis of electron diffraction patterns obtainable from femtosecond electron diffraction experiments opens up new perspectives on the interpretation of structural evolution in solids.

# Opsomming

'n In-diepte begrip van die werkingsbeginsels en verskynsels van sterk gekorreleerde gekondenseerde materie het die pad oopgemaak vir tegnologiese deurbreke in elektronika in die afgelope dekades. Die ontdekking en karakterisering van vele funksionele materiale, vanaf supergeleiers tot isolators, is afhanklik van 'n voortdurende dryf om die meganismes agter hierdie makroskopiese eienskappe van materiaal te verstaan. Vanuit die natuur van strukturele transisies in hoogs gekorreleerde vastestowwe en die ooreenstemmende skielike verandering in hulle geleidings vermoë en weerstand, kan verskeie vryheidsgrade en orde parameters ondersoek word deur gebruik te maak van verskillende eksperimentele tegnieke soos hoek opgeloste foto-elektron spektroskopie, optiese weerkaatsings metings, X-straal kristallografie en aktiveer interrogeer spektroskopie onder andere. Een van die hoof tegnieke wat gebruik kan word om hierdie hoogs gekorreleerde sisteme te ondersoek is elektron diffraksie analise.

In hierdie skripsie demonstreer ons 'n kwalitatiewe verhouding tussen 'n elektron diffraksie simulasie en die ooreenstemmende X-straal en elektron diffraksie eksperimente. Hierdie struktuur ontledings tegnieke word gebruik om metaal-tot-insulator struktuur oorgange in sterk elektronrooster gekorreleerde ladings digtheid golf stowwe van radikale anioon organiese molekulere kristalle van Cu-DCNQI en twee lede van die oorgang metale  $4H_b$ -TaSe<sub>2</sub> en  $1T$ -TiSe<sub>2</sub> se kristalle te ondersoek. Hierdie studie dra by tot die waarneming en dinamika van ladings digtheid golwe op ruimtelike en tydelike atoomskaal resolusies. 'n Sistematiese analise van elektron diffraksie patrone verkrygbaar van femtosekonde elektron diffraksie eksperimente stel ons in staat daartoe om nuwe interpretasies van die strukturele veranderinge in vastestowwe te maak.

# Acknowledgements

To God be the glory, great things He has done. I bless His holy name for the successful completion of this study.

My first and foremost gratitude goes to my supervisor, Professor Heinrich Schwoerer, whose dexterity has helped shape my career. Thank you for your open door, your regular concern, your belief in me and your strong passion that made me gain the skills and accrue the priceless knowledge in both molecular spectroscopy and structural dynamics of solids. I will forever be grateful for these.

My profound gratitude goes to DAAD, who sponsored my study through the African Institute for Mathematical Sciences. Without this funding, I might not have been able to pursue a doctoral degree at Stellenbosch University. I am also grateful for the additional funding provided through South African Research Chair Initiative of Department of Science and Technology and the National Research Foundation. I am grateful to Xingzhong Li, who developed the electron diffraction software used in this study, for the priceless clues he provided during the analysis. I appreciate the Centre for High Performance Computing (CHPC), Cape Town, for making available Gaussian software used in density functional calculations presented in this study. I am grateful to Florian Hüewe of University of Würzburg, Germany, for the fruitful discussions we had on DCNQi salts. I appreciate Professor Len Barbour and Dr. Vincent Smit of Chemistry Department, Stellenbosch University for helping me with X-ray diffraction measurements done in this study and the fruitful discussion we had. I appreciate Angelina Wilson for proof reading the dissertation; Dirk Spangenberg and Ruan Viljoen for translating the abstract into Afrikaans.

Special thanks go to Nicolas Erasmus and Kerstin Haupt, who had thoroughly furnished the experimental set up in the UED projects, especially the LabView programs that I also used for analysing my results. I am grateful to my immediate colleagues; Aminat Suleiman, Andrea Rohwer, Nancy Payne and Bart Smit for the insightful discussions we had together during this study. I appreciate all the technical staff of Physics Department, Stellenbosch University for the technical help rendered during the course of my study.

My sincere gratitude goes to my parent, Mr. and Mrs Timothy Kolawole Olaoye, for the education legacy they bestowed upon me and for training me up in the way of the Lord. Thank you dad and mum. I thank all my siblings for their supports and prayers throughout my study. I also want to mention my mentors in the Lord: Pastor Blessing Oyekanmi, Pastor Funlola Olojede and Deacon John Babafemi, for their counsels and prayers throughout my study. A shout of thanks to all friends and loved ones and all the workers of the Redeemed Christian Church of God (Desire of Nations).

Adejumoke is a land of wonder and a meadow of loveliness, whose support and love are beyond estimation. Thank you.

**"O the depth of the riches both of the wisdom and knowledge of God! How unsearchable are his judgements, and his ways past finding out!" Romans 11:33 (KJV).**

# Dedications

*Printed palms, destiny designer,  
Unequaled, unsearchable, love so great,  
My dwelling place, unfathomable,  
Pure, unrefined flow of wisdom,  
Undistorted time changer, awesome God!*

# Chapter 1

## Introduction

Gaining useful understanding from different stages of structural evolution in solids plays an important role in interpreting their properties. Solids, like other forms of matter, respond to influences posed by external environmental factors such as temperature and pressure. Perturbations on a microscopic scale to some solids' structural arrangements lead to responses that could translate into a drastic change in their macroscopic properties. These perturbations often result in in-equilibrium and/or out-of-equilibrium states, which could characterise phase transitions of metallic (conducting) to insulating solids or vice versa.

One distinctive property found in certain solids is superconductivity, a phenomenon whereby the electric resistance in a metal reaches a negligibly small value when it is cooled below a *critical* or a *transition temperature* [1, 2]. Whereas the degrees of superconductivity in metals could be affected by the presence of a strong magnetic field, a colossal magneto-resistance was found in manganese oxide perovskites surrounded by a strong magnetic field [3], with their electric resistance decreasing or increasing by orders of magnitude. The discoveries of superconductivity and magneto-resistance in different solids raised many questions and resulted in many applications, paving way for technological advancement in electronics. In retrospect these two exotic properties are usually characterised by phase transitions between a metallic and an insulating state. In other words, solids are classified according to the degree of conductivity or resistivity found in them. The degree of electric conductivity and/or resistivity in crystalline solids primarily depends on temperature, phonons and surface or interstitial defects [1].

The existence of superconductivity and magneto-resistance in certain solids puts them at the frontiers of research. Exploring the properties associated with superconducting and magneto-resistant solids in relation to their morphologies (the common being 1-D, 2-D and 3-D solids) posed a new challenge, and one may validly ask: "What are the microscopic explanations backing these two phenomena?" It was thus an instinctive breakthrough in Solid State Physics in the 20th century when Bardeen, Cooper and Schrieffer (BCS theory) [4] gave a microscopic explanation governing superconducting solids. Almost in parallel, Rudolf Peierls in 1950 developed a microscopic theory that explains phase transition in 1-D solids, judging from a periodic lattice distortion and the accompanied electron density modulation. The spatial *modulation* of electron density (or electrostatic potential)<sup>1</sup> in certain crystalline solids results in the screening of an electric potential of the ion cores of the solids and sets up a Coulomb repulsion in the process, a phenomenon referred to as *charge density wave* (CDW) formation in crystal lattices [5]. Charge density wave formation has been shown to invoke insulating domains in erstwhile conducting solids [6, 7].

---

<sup>1</sup>X-ray probes interact with electrons only, thereby setting up a perturbation of the electron density distribution in a crystal. On the other hand, electron probes interact with electron and the nucleus, thereby setting up a perturbation of the electrostatic potential in a crystal [18].

One class of materials in which charge density wave signatures were found are the layered inorganic single crystals of transition metal dichalcogenides (TMDs). These diatomic layered compounds are particularly famous for their rich structural dynamics, colossal magnetoresistance and subtle phase transitions. While new discoveries and methods put forward to understand the processes involved in the metal-insulator phase transitions in TMDs are gaining ground, Aumüller *et al.* [14] in 1987 discovered a novel radical anion organic crystal, namely, Copper II dimethyl-dicyanoquinonediimine (hereafter called DCNQI salts). Interestingly, DCNQI salts show high anisotropy electric conductivities, with up to eight orders of magnitude depending on the radicals and the cations used [14, 64, 74, 75]. Charge density wave formations in TMDs and DCNQI salts have been famed to be one of the microscopic explanations underlying the abrupt changes in their macroscopic properties.

Phase transitions in solids arise from the interplay between temperature, pressure and volume. A plethora of experimental techniques that could be used to probe structural dynamics in solids include angle resolved photo-electron spectroscopy [5], optical reflectivity measurements [70], X-ray crystallography [18] and electron diffraction [7, 10]. Of these, two closely related experimental techniques are X-ray and electron diffraction analysis. In particular, the structural arrangements of the constituent atoms in TMD and DCNQI crystals investigated in this study were determined via X-ray diffraction structural refinements [64, 65, 35]. Here, based on these structural refinements, electron diffraction analysis is primarily used to investigate phase transitions in TMD and DCNQI crystals.

The successes [7, 8, 9, 10, 12, 13] of the newly built diffractometer for ultrafast electron diffraction experiments have fanned to flame more passion to pursue an excellent research through this formidable experimental technique. There are many technicalities associated with running electron diffraction experiments and analysing diffraction patterns obtained. Typically, a team work of a few students is required, where students are allocated to different tasks that will culminate into unified results and successes of concurrent UED projects. This ranges from sample preparations to analysis of diffraction patterns obtained from experiments. An important go-between of this team work is the simulation of ideal electron diffraction patterns for crystals of interest, with the purpose of analysing, comparing, qualifying and quantifying both the experimental and simulated data. In addition, having a foreknowledge of some of the sample parameters and the details of their ideal diffraction patterns through theoretical simulations cannot be overemphasised, as it promises to give more insight to the understanding of dynamics in the crystal under investigation.

This dissertation sets out to describe and analyse the simulation of the ideal diffraction patterns and charge density wave formations in selected TMDs and DCNQI salts, together with the available experimental data. The software we used for all simulations in this thesis is called "Simulation and Analysis of Electron Diffraction" (SAED), which was developed by Xingzhong Li [15]. The principle employed in the software is based on *selected area electron diffraction* and *kinematic diffraction theory*.

A sense of systematic studies of structural transitions in crystalline solids through electron diffraction simulation, electron and X-ray diffraction experiments is launched in this dissertation by making provisions to gain profound insights at different stages of temperature-dependent structural evolution. This dissertation bridges the gap in the context of qualifying and quantifying structural dynamics in solids, and of a better understanding in the interpretation of obtainable Bragg reflections in ultrafast electron diffraction (UED) experiments. A qualitative working relationship between X-ray crystallography, UED experiments and electron diffraction simulation is envisaged to provide better insights into structural evolution in crystalline solids.

In Chapter 2, a brief introduction to basic background of electron diffraction theory, electron density and charge density wave formations in crystals of interest will first be treated. Nature

often inclines us to explain complexity by using simplicity; therefore, simulation of diffraction patterns, with an embedded charge density wave signature, in simple cubic lattices composed of tantalum atoms are analysed to give a background insight. Then, in Chapter 3 the simulation of diffraction patterns of the metallic and the charge density wave (insulating) phase in two selected members of transition metal dichalcogenides crystals, namely,  $4H_b$ -TaSe<sub>2</sub>, and  $1T$ -TiSe<sub>2</sub> are introduced and analysed. It should be noted that experimental measurements and analysis on  $4H_b$ -TaSe<sub>2</sub> single crystals have been done by previous students in the group [7, 9, 10]. However, the simulation analysis presented here opens up new perspectives of the structural transition in  $4H_b$ -TaSe<sub>2</sub> single crystals, and adds to the existing knowledge and techniques.

Chapter 4 introduces the readers to the general perspectives on DCNQUI salts. In Chapter 5, using the knowledge and skills gained in simulating diffraction patterns obtainable from cubic lattices and TMD crystals, a similar but somewhat subtle procedure will be carried out on the DCNQUI salts. The highlights are structural evolution and analysis through theoretical simulations, infra-red active frequency calculations, mixed valency and charge orderings in DCNQUI salts' insulating phases, as well as the first observation and characterisation of charge density wave signatures through X-ray and electron diffraction experiments; with a view towards unravelling the ultrafast structural dynamics in DCNQUI salts while undergoing photoinduced metal-insulator phase transitions. Finally, some general critical interpretations and inferences from the selected crystals' diffraction patterns will be made, together with recommendations and future outlooks.

## Chapter 2

# Electron diffraction and charge density waves

### 2.1 Introduction

This chapter concentrates on the foundation needed to understand and interpret electron diffraction patterns obtainable from simulation and experiments of both high and low temperature phases of the crystals investigated in this dissertation. The images obtained from electron diffraction experiment or simulation present the Fourier space of the structural arrangement of the crystal under investigation. Solids generally are categorised into amorphous and crystalline solids. For example, diffuse or ring diffraction patterns obtainable from amorphous solids (e.g. glass or aluminium foil) show the randomness of the lattice positions in their real space: obtainable information from these kinds of diffraction patterns are therefore restricted to the regions along the rings. Conversely, crystalline solids possess periodic arrangement of the constituent atoms or molecules. The diffraction patterns obtainable from crystalline solids therefore show distinct minima and maxima, which characterise the lattice positions in the real space [16, 17]. Imposing an external factor on a crystalline solid distorts its structural arrangement and this translates to one or all of contraction or expansion; strengthening or melting of Bragg planes in the reciprocal space. Thus, the structural evolution/dynamics in solids could be followed by analysing different electron diffraction patterns obtained from probing the solids under varied external factors (such as temperature and pressure).

The influence of these external factors on charge density wave compounds is often associated with the appearance of extra spots in addition to the normal diffracted spots, which are also periodic. The processes involved in charge density wave formation in crystal lattices, as well as basic background into electron diffraction techniques, form the focus of the rest of this chapter.

### 2.2 Electron diffraction

#### 2.2.1 Interpreting electron diffraction patterns

Electron diffraction is a proven technique used in unravelling structural dynamics in solids [6, 7, 10, 12]. The signature of diffraction patterns obtainable from any crystal depends primarily on the crystal family, its space group and the zone axis of interest. A diffraction image obtainable from simulation or experiment reveals the reciprocal space or more intuitively, the energy-momentum space. These images are characterised by the amount of energy (e.g. the energy of an electron probe or the fluence of a laser pump) deposited in the crystal and the response of the crystal structure to the perturbation of its periodic potential.

In crystalline <sup>1</sup> solids the arrangement of constituent molecules or atoms follows a trend, or arises from a building block known as a unit cell. The unit cell of a crystal can take on one of the seven crystal families, as outlined in Table 2.1 [2, 18].

Table 2.1: Bravais lattice types, space groups and crystal families [2, 18]

Crystal families	Bravais lattice types	No. of space groups	Cell Parameters
Cubic	P, I, F	36	$a = b = c; \quad \alpha = \beta = \gamma = 90^\circ$
Hexagonal	P	27	$a = b \neq c; \quad \alpha = \beta = 90^\circ, \gamma = 120^\circ$
Trigonal	P, R	25	$a = b = c; \quad \alpha = \beta = \gamma < 120^\circ, \neq 90^\circ$
Tetragonal	P, I	68	$a = b \neq c; \quad \alpha = \beta = \gamma = 90^\circ$
Orthorhombic	P, C, A, B, I, F	59	$a \neq b \neq c; \quad \alpha = \beta = \gamma = 90^\circ$
Monoclinic	P, C, A, B	13	$a \neq b \neq c; \quad \alpha = \gamma = 90^\circ \neq \beta$
Triclinic	P	2	$a \neq b \neq c; \quad \alpha \neq \beta \neq \gamma$

Conventionally, three translation real space vectors ( $\mathbf{a}$ ,  $\mathbf{b}$  and  $\mathbf{c}$ ) describe a primitive unit cell, related to one another by a lattice position vector [2, 19]:

$$\mathbf{r}_j = x_j\mathbf{a} + y_j\mathbf{b} + z_j\mathbf{c}, \quad (2.1)$$

where  $0 \leq x_j, y_j, z_j < 1$  are the fractional coordinates of the atomic positions. Similarly, the reciprocal lattice vector is the linear superposition of the three translation reciprocal space vectors,

$$\mathbf{G}(hkl) = h\mathbf{a}^* + k\mathbf{b}^* + l\mathbf{c}^*, \quad (2.2)$$

$$\mathbf{a}^* = \frac{\mathbf{b} \times \mathbf{c}}{\mathbf{a} \cdot (\mathbf{b} \times \mathbf{c})}, \quad \mathbf{b}^* = \frac{\mathbf{c} \times \mathbf{a}}{\mathbf{a} \cdot (\mathbf{b} \times \mathbf{c})}, \quad \mathbf{c}^* = \frac{\mathbf{a} \times \mathbf{b}}{\mathbf{a} \cdot (\mathbf{b} \times \mathbf{c})},$$

where  $(hkl)$  are the Miller indices describing the Bragg reflections in the reciprocal space. The reciprocal lattice vector  $\mathbf{G}(hkl)$  is always perpendicular to the zone axis along the direction of the electron beam. The zone axes, designated by  $[uvw]$ , of the unit cells of a particular crystal structure determine the allowed Bragg reflections obtainable from probing the crystal, justifying the indexing of the obtainable diffraction pattern according to the Laue zone axis formula [18, 23]:

$$u \cdot h + v \cdot k + w \cdot l = m, \quad (2.3)$$

where  $m = 0, 1, 2, \dots$  is an integer describing the Laue zone number [22]. Assigning the orders of Laue zone axes requires a caution. The nomenclature of this assignment is determined by the number of rings outside the zeroth order Laue zone (ZOLZ), so that the closest ring to the undiffracted spot, excluding ZOLZ, is referred to as the first order Laue zone (FOLZ) [18, 23] <sup>2</sup>.

In Equation 2.3,  $m = 0$  is referred to as the zeroth order Laue zone (ZOLZ) for a standard coherent electron diffraction pattern. For example, in a standard diffraction pattern (where

<sup>1</sup>All the solids treated in this dissertation are crystalline. As such, we shall focus on the underlying theory of periodic structures of crystalline solids.

<sup>2</sup>Ref. [23] particularly pointed it out that there are cases when there is no reflection corresponding to  $m = 1$ . In this situation, if, apart from ZOLZ, the next sets of Bragg reflections fall on  $m = 2$ , then it becomes the first order Laue zone (FOLZ).

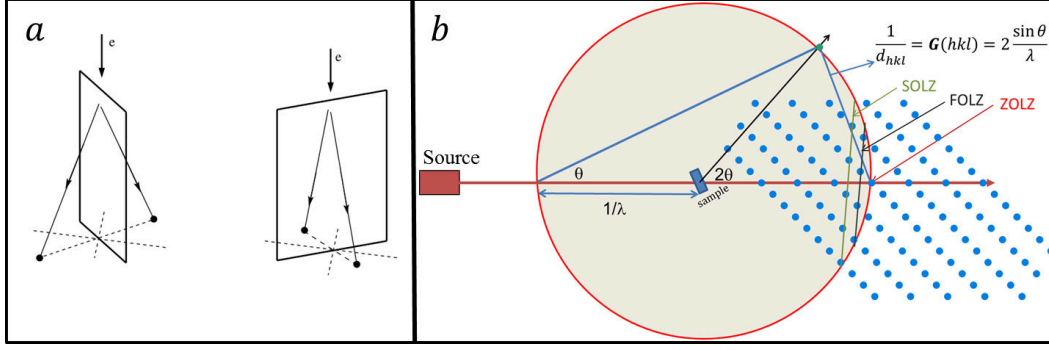


Figure 2.1: Conditions for a Bragg plane to diffract electrons are illustrated. In panel (a), the direction of the electron beam and the orientation of planes are drawn. This shows that the electron beam is always nearly parallel to the plane of diffraction, leaving only a small Bragg angle  $\theta$  shown in (b). In panel (b), the coherence property of the Ewald sphere is determined by  $\lambda$ , whose integral multiple determines the distance  $d_{hkl}$  between the planes of diffraction. Orders of Laue zone and their representative diffraction spots are also indicated.

$m = 0$ ), [001] Laue zone axis requires the indexing of the Bragg reflections to be of the form  $(hk0)$  in order to satisfy Equation 2.3. Higher order Laue zones (HOLZ), such as shown in Figure 2.1, describe nearly coherent diffraction spots that could be included to compensate for forbidden spots that appear as a result of imperfection of experimental beam parameter [18, 27, 28, 30]. On the other hand, the need to include the HOLZ in the diffraction pattern may also be due to long periodicity and high resolution of the electron beam [18]. The Ewald's sphere, together with Laue zones, describes the allowed and the forbidden Bragg planes in a given diffraction pattern. The coherence property of the Ewald sphere links to the Bragg condition for an allowed reflection (see Figure 2.1) [2, 18, 19]:

$$n\lambda = 2d\sin\theta, \quad (2.4)$$

where  $\theta$  is the scattering angle,  $n$  is an integer and  $\lambda$  is the wavelength corresponding to the energy of the electron probe used.

The intensity distribution profile for a particular diffraction pattern arises from the structure factor of a crystal, with the magnitude of diffracted intensity defined as [18, 20, 21]:

$$I(hkl) \sim |F(hkl)|^2,$$

given that

$$F(\mathbf{G}) = \sum_{i=1}^N f_i(\mathbf{G}) \exp[2\pi i(\mathbf{G} \cdot \mathbf{r}_i)] = \sum_{i=1}^N f_i(hkl) \exp[2\pi i(hx_i + ky_i + lz_i)], \quad (2.5)$$

where  $N$  is the number of atoms in a unit cell or an asymmetry unit of a crystal,  $f_i(hkl)$  are the atomic form factors and the term in the exponential represents the phase  $\phi(hkl)$  of the structure factor. The atomic form factor for the individual atoms in a crystal depends on their atomic numbers, scattering angles, thermal vibrations and positions in the crystal [18]. It is parametrized as:

$$f(\sin\theta/\lambda) = \sum_{i=1}^4 a_i \exp(-b_i \sin^2\theta/\lambda^2) + c, \quad (2.6)$$

where  $a_i, b_i$  and  $c$  are nine (9) parametrization constants listed in [21]. The atomic form factor of an atom in a crystal represents its scattering power. The heavier an atom is, the higher

its contribution to diffraction spots in a given diffraction pattern. Atoms that are orders of magnitude smaller, when compared to other atoms in a crystal, are of little or no effect when analysing the contributions of the atoms to the formation of periodic Bragg reflections.

For a suitable homogeneous (or an achiral) crystal, Friedel's law is one of the unique properties of intensity distribution profile of a diffraction pattern. Friedel's law can be described by the relations [2, 18]:

$$|F(hkl)| = |F(-h - k - l)| \quad \text{and} \quad \phi(hkl) = -\phi(-h - k - l).$$

These relations show that for every Bragg plane in a diffraction pattern, there is a pair; the only exception is the (000) plane. However, these two relations are often treated as approximate because of the difficulty to obtain homogeneous samples during sample preparations. Moreover, the distribution of planes and/or interstitial sites (defect sites) in crystals could also result in the inequality of the Friedel's relations. It should be noted that Friedel's laws are valid for both amorphous and crystalline solids [18].

X-ray diffraction structural refinement has been a useful tool employed to solve the structure of a crystal. Based on Bragg reflections obtained by probing the crystal with X-rays, the symmetry of the crystal is determined. The information obtained from this refinement is often written into a file generally known as crystallographic information file (CIF). The standard code approved for exchanging CIF for better interpretation of refined crystal structures is given in [24, 25]. However, there are different modifications to the writing of these files, depending on the software that is being used for data analysis. Furthermore, a software used to simulate electron diffraction patterns may also require certain modifications for the files to be readable, as is the case in this study. Crystallographic information files generally contain crystals' properties such as the constituent atoms, the space group, the atomic positions of the asymmetry unit of the crystal, the crystals' volume, the atomic form factors of the constituent atoms, etc.

The space group of a crystal could belong to one of the 230 space groups listed in [26]. The space group describes the symmetry of a crystal. Each space group starts with one of the 14 Bravais lattice types in crystals, as listed in Table 2.1. In this dissertation, primitive (P) and body-centered (I) unit cells are discussed. Two examples of transition metal dichalcogenides treated in Chapter 3 belong to the primitive lattice type, where all the Bragg reflections are allowed. Associated with the body-centered unit cells of DCNQI salts treated in Chapter 4 is a glide plane<sup>3</sup>, which introduces systematic absences or forbidden reflections.

For a proper understanding and interpretation of diffraction patterns obtained from complex crystals, such as treated in Chapters 3 and 5, we first of all study basic properties of ideal diffraction patterns obtainable from primitive and body-centered lattices of simple crystals. Shown in Figure 2.2 are the real and reciprocal space of cubic lattices that are composed of tantalum atoms. Tantalum atoms naturally crystallize into body-centered cubic (BCC) lattices with side  $a = 3.30 \text{ \AA}$ , as determined by X-ray diffraction analysis [2, 31]. There are distinct systematic absences in the simulated diffraction patterns of the BCC lattice of tantalum atoms (Figure 2.2(c & d)), as against its simple cubic counterpart (Figure 2.2(e)). An example of indexing of Bragg reflections in primitive and body-centered cells is shown in Figure 2.3. The primitive translation vectors of a BCC lattice of side  $a$  are given as [2]:

$$\mathbf{a} = \frac{1}{2}a(\hat{x} + \hat{y} - \hat{z}); \quad \mathbf{b} = \frac{1}{2}a(-\hat{x} + \hat{y} + \hat{z}); \quad \mathbf{c} = \frac{1}{2}a(\hat{x} - \hat{y} + \hat{z}), \quad (2.7)$$

where  $\hat{x}$ ,  $\hat{y}$  and  $\hat{z}$  are orthogonal unit vectors parallel to  $\mathbf{a}$ ,  $\mathbf{b}$  and  $\mathbf{c}$ . Applying Equation 2.2 to Equation 2.7, we have:

---

<sup>3</sup>A glide plane combines mirror reflection symmetry with translation symmetry [18].

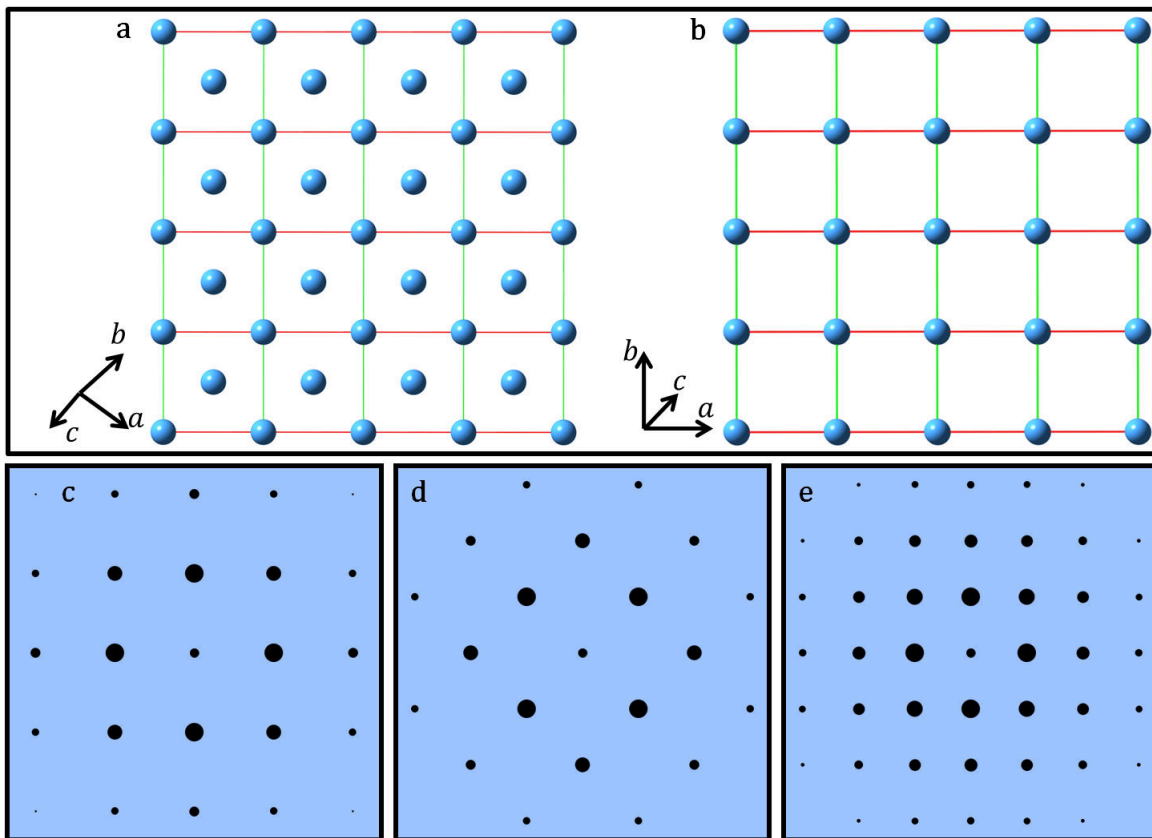


Figure 2.2: Simulation of obtainable diffraction patterns from (a) a body-centered and (b) a simple cubic crystals composed of tantalum atoms. Panel (a) is the real space lattice for patterns shown in (c) with space group  $Im\bar{3}m$  and (d) with space group  $Pm\bar{3}m$ . Panel (e) shows the diffraction patterns obtained from real space lattice shown in (b), also with a space group  $Pm\bar{3}m$ . Patterns displayed in (d) and (e) are thus of  $P$ -type lattice, while (c) is of  $I$ -type lattice. Tantalum atoms naturally crystallize into BCC lattices [2], with lattice parameters:  $a = b = c = 3.30 \text{ \AA}$  and  $\alpha = \beta = \gamma = 90^\circ$ . Figure 2.3 shows the indexing of these reciprocal space electron diffraction patterns.

$$\mathbf{a}^* = \frac{1}{a}(\hat{x} + \hat{y}); \quad \mathbf{b}^* = \frac{1}{a}(\hat{y} + \hat{z}); \quad \mathbf{c}^* = \frac{1}{a}(\hat{x} + \hat{z}). \quad (2.8)$$

Equation 2.8 describes the primitive translation reciprocal vectors for a face centred cubic (FCC) lattice [2, 16, 17, 18, 19]. Hence, a body-centered cubic lattice always gives rise to a face centred diffraction pattern and vice-versa. The forbidden reflections associated with an FCC or a BCC lattice arise when the phase of the structure factor in Equation 2.5 becomes zero. A BCC lattice requires  $h + k + l = 2n$  while an FCC lattice requires all  $h, k, l$  to be even or odd integers. A simple cubic lattice has no restriction.

### 2.2.2 Electron density and electrostatic potential in crystal lattices

Another quantity that is associated with diffraction analysis is the electron density (or the electrostatic potential). The distribution of electron density in a crystal depends on the type of bonds between neighbouring atoms and the type of orbitals formed. These bonds or orbitals influence the net charge created near the Fermi surface of the crystals. Put differently, the hybridisation of the orbitals of the atoms or molecules present in a crystal determines the distribution of electron density in the crystal. Electron beams are generally scattered by the electrostatic potential

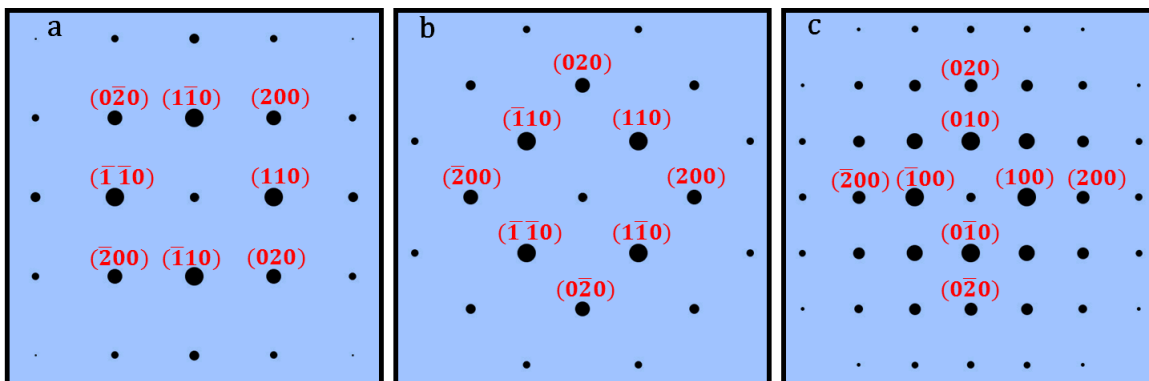


Figure 2.3: Panels (a), (b) and (c) respectively show the indexing of selected Bragg reflections of the simulated diffraction patterns obtained from cubic lattice shown in Figure 2.2 (c, d & e). The reciprocal space of the simple cubic shown in (c) has a simple cubic diffraction patterns, hence there are no forbidden reflections. The  $hkl$  reflections in this case take on any integer. The body-centered cubic lattices shown in (a) & (b) give rise to face centred diffraction patterns, so that the allowed Bragg reflections have  $h + k + l = 2n$ . The difference between the indexing of the Bragg peaks in (a) & (b) is due to the lattice types, which are  $I$  and  $P$  for panels (a) & (b) respectively.

(electrostatic potential could be projected as contour lines on the electron density distribution in a crystal) created by the net potential differences (or hybridised orbital) at different regions of a crystal [18].

An example of a mapped electrostatic potential of an asymmetry unit of organic molecular conductor (DCNQI salts) treated in Chapter 4 is shown in Figure 2.4. The distribution of electron density and electrostatic potential contours of constant densities are overlapped. A quick inference that can be made from Figure 2.4 is that the cloud of electrons around the whole asymmetry unit arises from the hybridised orbitals of the constituent atoms. Each atomic position has a surrounding electron cloud, whose strength depends on the number of electrons in the atom. Moreover, the delocalised  $\pi$ -orbital of the benzene ring is clearly shown, together with the  $d$ - $p$ - $\pi$ -hybridised orbitals of the whole asymmetry unit. In general, electrons get scattered by these clouds of electrons in such a way that the resulting Fourier transform gives rise to intensity peaks of different sizes. The electron density is highest around the copper atoms. This means that the copper atoms should have the highest contribution to the diffracted intensities obtainable from Cu-DCNQI salts.

Indeed, for a diatomic (or a polyatomic) crystal, the Bragg reflections observed in an obtainable diffraction pattern cannot be attributed to the scattering by a single type of atom in the crystal, especially when the constituent atoms have comparable atomic form factors. This is to say that electron probes sense a continuous distribution of electrostatic potential (arising from contributions from all atoms in a crystal), which when Fourier transformed leads to the generation of a periodic diffraction pattern.

Mathematically, the inverse Fourier transform of the structure factor leads to a relation for electrostatic potential, given by [18]:

$$\varphi(xyz) = \mathcal{F}^{-1}[F(hkl)] = \frac{\lambda}{\sigma\Omega} \sum_{hkl} F(hkl) \exp[-2\pi i(hx + ky + lz)] \quad (2.9)$$

where  $\lambda$  is the electron wavelength,  $\Omega$  is the volume of a unit cell and  $\sigma$  is the interaction constant, defined as [18]:

$$\sigma = \frac{2\pi me\lambda}{h^2} = \frac{\pi}{\lambda U}, \quad (2.10)$$

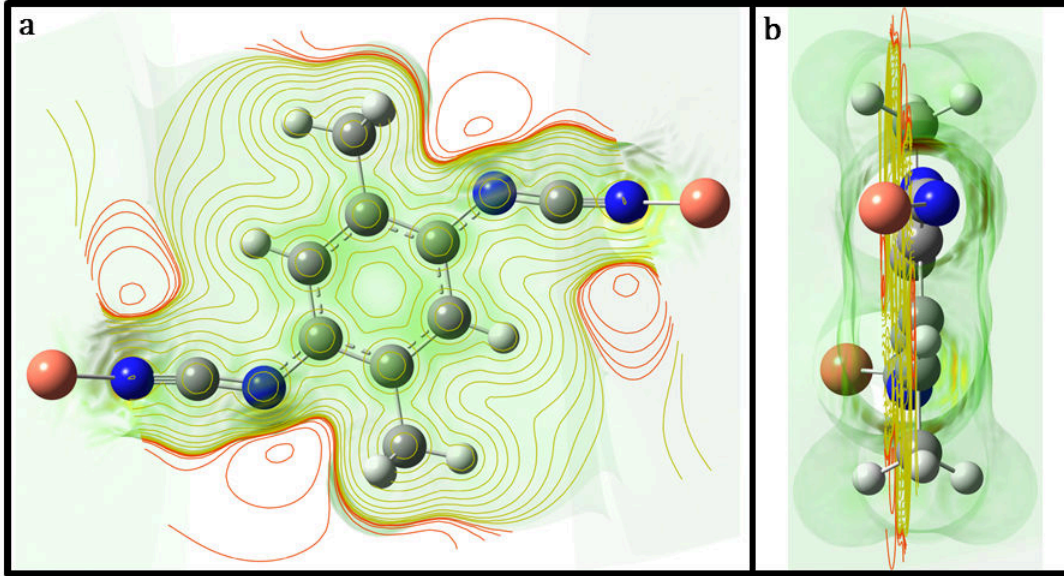


Figure 2.4: Plotted are the (a) front view and (b) side view of a mapped electrostatic potential (ESP) calculated for the asymmetry unit of  $\text{Cu}[2,5\text{-DMe-DCNQI}]_2$ , through density functional (DFT)(B3LYP functional + CEP-31G basis set). The mapped ESP was derived from the total density of the molecular orbital of the unit. The contour lines describe regions of constant densities or equipotential, with an isovalue of  $4 \times 10^{-3} \text{ e}/\text{\AA}^3$ . The region of deep shading connotes high electron density. The delocalised  $\pi$ -electrons is revealed, together with the overall hybridised  $d$ - $p$ - $\pi$  orbitals, which are contributed by  $p$ -orbital of the cyano group (N-C-N), Cu- $d$ -orbital and  $\pi$  orbital of the benzene ring. (Key:- Cu: Orange; Nitrogen: Blue; Carbon: Grey; Hydrogen: White.)

such that  $m$  and  $e$  are respectively the electron relativistic mass and charge,  $h$  is the Planck's constant and  $U$  the accelerating voltage. The interaction of an electron beam of wavelength  $\lambda$  with a crystal of thickness  $t$  has a projected (or a mapped) potential of the form [18]:

$$\varphi_{\text{projected}}(xyz) = \frac{\lambda t}{\sigma \Omega} \sum_{hkl} F(hkl) \exp[-2\pi i(hx + ky + lz)]. \quad (2.11)$$

Peculiar to our electron diffraction experimental set-up, the typical range  $t = 30 - 100 \text{ nm}$  and  $U = 30 \text{ kV}$  for sample thickness and electron energy, respectively, are used [7, 10]. This electron energy corresponds to  $\lambda = 7 \text{ pm}$  (picometer) in vacuum and at the sample surface. For this electron wavelength, the interaction constant  $\sigma \approx 1.5 \times 10^{-3} \text{ V}^{-1} \text{ \AA}^{-1}$ . Due to the interaction of electron beam with the electrostatic potential in a crystal, the propagation of this energy (inherently  $\lambda$ ) through the crystal is ideally different since it possesses a different medium of propagation than the vacuum. Therefore, the wavelength of an electron beam going through a crystal depends on the density of electron cloud in a particular region, and is given as [18]:

$$\frac{1}{\lambda_{\text{crystal}}} = \frac{1}{\lambda_{\text{vacuum}}} \left[ 1 + \frac{\varphi(xyz)}{2U} \right], \quad (2.12)$$

for  $\varphi(xyz) \ll U$ . A very thin crystal is customarily used in electron diffraction, in which case the crystal is considered as homogeneously irradiated [10]. Thus, the terms in the square bracket of Equation 2.12 is close to 1, ultimately making the crystal to undergo elastic scattering (Note that  $\varphi(xyz) \ll U$  for a thin crystal). The thinner the crystal, the stronger the elastic scattering. Increasing the crystal thickness will require an increase in the electron energy, which is not always

desirable in electron diffraction experiments. The homogeneity of a relatively thick crystal is not certain, or is difficult to attain. Moreover, if a crystal is thin enough, the influence of non-linear effects and multiple scatterings on its diffraction patterns could be ignored. This leads us to an important consideration in electron diffraction simulation: Do we use a *kinematic* or a *dynamic* scattering model? This question is often addressed with *phase object approximation*.

### 2.3 Simulation's models: 'Weak' versus 'strong' phase object approximation

In the previous section we described how an electron diffraction pattern image could be interpreted, and established that electron probes passing through a crystal get scattered by the ESP field of the crystal. The next step is to consider the right model to use when simulating obtainable electron diffraction patterns of a crystal. Two methods associated with electron diffraction simulations are the kinematic and the dynamic scattering models.

Kinematic scattering model takes the magnitude of a diffracted intensity in an electron diffraction pattern as the square of the structure factor amplitude. It satisfies Bragg's and Ewald's conditions described in the previous section. Kinematic diffraction model supports single scattering, working with the ideal that if the crystal to be used is thin and homogeneous, there will be less multiple scattering or secondary interactions [18, 19].

Dynamical scattering model on the other hand takes into consideration the possibilities of secondary interactions, corrects for double reflections, extinction lengths, absorption, long periodicity, and so on [19]. For example, there could be multiple interactions between the undiffracted beam and the scattered beams. This is especially the case when the crystal is too thick or is not homogeneous. A very thin crystal could also undergo multiple scattering if there are interstitial sites or if the crystal is not properly aligned to the direction of electron beams [18, 19].

The validity of any of these two methods depends on the constituent atoms or molecules, that is, the scatterers of electron probes in a given crystal lattice, the accelerating voltage and how thin or thick the crystal is. Often, electron diffraction models make use of kinematic scattering whenever possible. Dynamic scattering model is not trivial to resolve due to many (achievable and not achievable) constant factors to be included. At the end, the approximations made may worsen the quality of the diffraction patterns obtained, and this may be far deviated from corresponding experimental diffraction patterns.

The propagating waves of an electron beam passing through a given crystal have an amplitude and a phase. If the electric field of the waves only experiences a phase shift, but its amplitude remains approximately unchanged after passing through a crystal, the crystal is said to be a phase object. This is often expressed mathematically as follows [18]:

$$\left| \frac{t\lambda}{\Omega} F(\mathbf{G}) \right|^2 \ll 1, \quad (2.13)$$

where  $t$  is the crystal thickness,  $\Omega$  is the crystal's volume and  $\lambda$  is the electron wavelength. This equation expresses the *weak phase object approximation* (WPOA) [18]. Whenever a crystal prepared for an electron diffraction experiment or simulation satisfies Equation 2.13, kinematic scattering model is employed. In the kinematic model the phase of the wave propagating through a crystal at its exit surface is proportional to the phase of the structure factor of the crystal; this is not so for strong phase objects, for which dynamical scattering must be employed. The justification for this is that the crystal's potential field is very strong or not smooth, thereby leading to not only a phase shift but also an amplitude shift in the exiting electron waves. The thickness of the crystals investigated in this study ranges between 25–35 nm. Samples' thickness

in this range has been shown to provide a nearly homogeneous excitation profile [10]. Therefore, kinematic scattering model is employed throughout this study.

Of course, obtaining a sample of this range during sample preparation is not trivial. A generally accepted sample thickness for a successful transmission of electron beams is ideally  $< 100$  nm [10, 18]. For a sample's thickness  $> 100$  nm, the energy of electron probes used is usually  $> 30$  kV in order to eliminate the possibility of double reflections, improve image resolution quality and for electrons to pass through the sample [6, 18]. Increasing the electron energy introduces different experimental conditions. For example, it could potentially lead to break down in the space charge and worsen the spatial-temporal resolution [6, 8, 10]. Therefore, choosing between sample thickness and electron energy requires a trade off, depending on the overall experimental conditions.

## 2.4 Electronic structure of and charge density wave formation in crystalline solids

**Electronic structure of crystalline solids:** This is often described by the allowed and forbidden bands formed through the overlaps of atomic and/or molecular orbitals. Put differently, the interaction of electron clouds between neighbouring atoms or molecules in a given crystal gives rise to the electronic density of states, demonstrating a continuous spectrum of free electron states in the crystal. The unit cell in the  $k$ -space of a crystal characterises the crystal structure's properties, and represents the region from which Brillouin zones can be constructed. Integration over the first Brillouin zone in the  $k$ -space is often used to obtain densities of states in a crystal [1]. The area from which the shape of the Fermi surface could be derived and over which a Brillouin zone will span depends on the periodicity and symmetry of the crystal under investigation. The signature of electron density distribution, or simply the electron density of states near a crystal's Fermi surface is generally used to classify the crystal into one of metal, semi-metal, semiconductor and insulator [1, 60]. The shape and the position of Fermi surface across the electronic bands of a crystal serve as a guide to distinguish between the filled and empty bands, and are often used to describe the properties of the crystal [1, 5, 60, 65].

The solution to electronic band structure of crystals, arising from Bloch waves and multi-slice methods, results in an energy parabola, with well-defined discrete energy levels defined by  $E(\mathbf{k}) = \hbar^2 \mathbf{k}^2 / 2m$ , where  $k$  is the wave vector of the free electron energy states [1, 18]. Due to the periodicity and symmetry requirements for and electron correlation associated with a crystal's potential field, the energy parabola is periodic so that  $E(\mathbf{k}) = E(\mathbf{k} + \mathbf{G}) = \hbar^2 |\mathbf{k} + \mathbf{G}|^2 / 2m$ . This results in intersection of energy parabolas, with the degeneracy of energy values spanning throughout the  $k$ -space. Since the energy parabola is periodic the  $k$ -space can be reduced to the first Brillouin zone, with  $k = -\frac{\pi}{a}$  and  $+\frac{\pi}{a}$ , as shown in Figure 2.5. Atomic or molecular vibrations, as well as perturbation to a crystal's potential field could lead to the lowering of the crystal energy, with band gap opening at the point of intersection of energy parabolas [1]. In the process, the degeneracies of energy values are lifted. The behaviour and/or properties of crystals' electronic structures are generally founded on the Drude-Sommerfeld's nearly free electron approximation theory, which incorporate electron correlations by introducing weak modulation of a crystal's potential field. Electron correlations have been found to induce one or both of electron-electron and electron-phonon interactions in crystals [1, 2, 6, 7, 10].

**Charge density waves:** The diffraction patterns obtained from a crystal lattice, such as shown in Figure 2.2 and 2.3, usually show the periodic arrays of Bragg reflections. These Bragg reflections, which represent the Fourier component of the crystal's structure factor, correspond to a uniform distribution of electron density or electrostatic potential (see Figure 2.4) in the

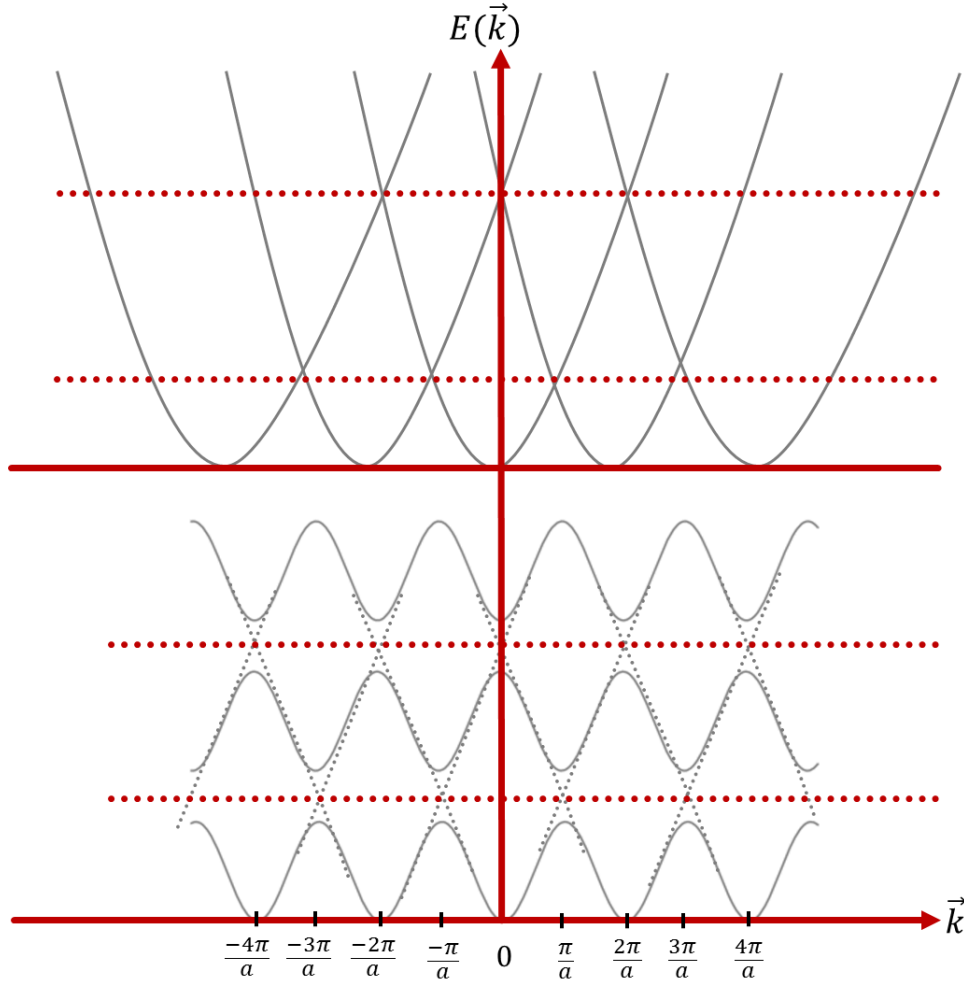


Figure 2.5: *Top panel*: Degeneracy of the periodic energy parabola based on repeated zone energy band scheme. The degenerate states, which occur at points of intersection, are lifted when the equilibrium states of the atomic ion cores in a crystal experience perturbation. As a result, band gaps are formed as shown in the *bottom panel*. Formation of charge density wave, in addition to Drude-Sommerfeld's weak perturbation, increases the opening of the band gaps.

unperturbed regime of the real space. A small but sufficient perturbation to this electron density distribution could result in the formation of energy band gap, opening across the erstwhile continuous spectrum of free electron states in the crystal [1, 5]. A cosinusoidal modulation of electron density given by [5],  $\rho(\mathbf{r}) = \rho_0(\mathbf{r})[1 + A\cos(\mathbf{q}_0\mathbf{r} + \phi)]$  gives rise to a periodic lattice distortion (PLD) of the form:  $u_n = u_0\sin(n|\mathbf{q}_0|a + \phi)$ , where  $\rho_0$  is the unperturbed density;  $A$ ,  $\mathbf{q}_0$  and  $\phi$  are respectively the amplitude, the wave vector and the phase of the electron density modulation. The combination of electron density modulation and periodic lattice distortion is referred to as charge density wave. When the ion cores of the constituent atoms in a crystal in positions  $n$  are slightly moved (or modulated) out of their equilibrium positions, there is a redistribution of electron density with the crystal's free (conduction) electrons screening a new potential thereby moving to a new ordered state. However, this new-ordered state does not necessarily mean charge density wave state.

Elastic energy is required to either compress or stretch the bonds between the atoms of a crystal. When the energy cost to overcome the elastic distortion of these bonds leads to energy

gain for the whole crystal system, then the preferred ordered state is the charge density wave state. In other words, the potential field's screening by the conduction electrons usually leads to a further lowering of the crystal's energy, in addition to the band gap opening at the edge of the first Brillouin zone. Different theories that have been used to explain the origin of charge density wave in solid materials include Peierls instability, giant Kohn anomaly, Fermi surface nesting and Jahn-Teller distortion [5]. The formation of charge density wave in crystal lattices often requires reduced dimensionality in high dimensional solids, just as Peierls phase transition theory is based on 1-D metals. The formation and treatment of charge density waves in higher crystal's morphologies (2-D or 3-D) constitute an on-going debate in Solid State Physics.

**Modulating electron density leading to charge density wave formation in crystal lattices:** Here, we consider a cubic lattice composed of tantalum atoms whose diffraction patterns are presented in Figures 2.2 and 2.3. These diffraction patterns correspond to the unperturbed regime of electron density distribution in the cubic crystal lattices. Modulating this uniform electron density distribution gives rise to the appearance of extra diffraction spots, in addition to the main Bragg spots obtained from the unmodulated crystal. As stated in Section 2.2, a crystal lattice is described in three dimensions by primitive translation vectors ( $\mathbf{a}$ ,  $\mathbf{b}$  and  $\mathbf{c}$ ). However, the diffraction pattern images are usually shown in two dimensions, constituting one of  $a - b$ ,  $a - c$  or  $b - c$  planes. Generally, the modulation of the ion core of an atom from its equilibrium position could be linear (along one axis in 1-D), or diagonal (along a plane in 2-D) or diagonal (along a surface in 3-D). Thus, the extra spots' positions in the  $k$ -space depend on the direction of modulation.

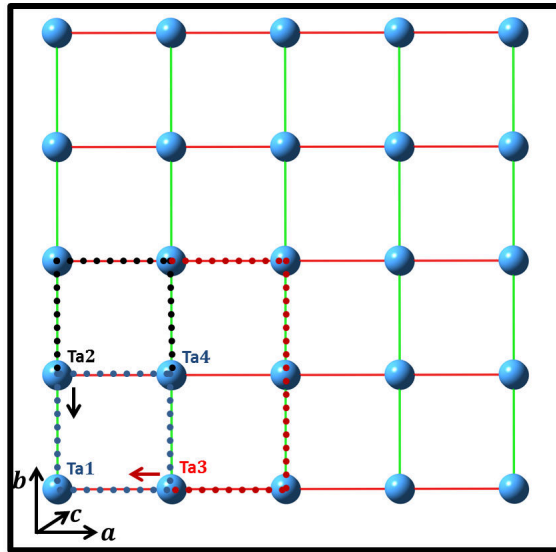


Figure 2.6: Modulating the real space of a simple cubic lattice composed of tantalum atoms. The unmodulated lattice requires only Ta1 in simulation, since all tantalum atoms are equivalent (see Figure 2.7 (a)). Modulating Ta2 and its crystallographic equivalent leads to doubling of the unit cell along the black dotted lines, with lattice dimension  $a \times 2b \times c$ . This results in CDW formation shown in Figure 2.7 (b). Modulating both Ta2 and Ta3 simultaneously leads to doubling of the unit cell along both the black and the red dotted lines, with lattice dimension  $2a \times 2b \times c$ . Charge density waves formed in these cases are shown in Figure 2.7 (c).

The simulation of diffraction patterns (see Figure 2.2 a) of the cubic lattice shown in Fig-

ure 2.6 requires only Ta1, with an imposition of  $Pm\bar{3}m$  (crystallographic number: 221) space group and a Laue zone axis [001]. A one dimensional modulation (Ta2 and its crystallographic equivalents across the cubic lattice) along the  $b$ -axis leads to a reduced symmetry from a space group  $Pm\bar{3}m$  (number: 221)  $\rightarrow Pm2m$  (number: 25). The unit cell is doubled and it corresponds to  $a \times 2b \times c$  as indicated by the black dotted lines in Figure 2.6. As expected, the extra spots appear along the  $b$ -axis (see Figure 2.7b). The second case is to modulate along both  $a$  and  $b$  axes. This incorporates Ta3 and its crystallographic equivalence and the superstructure corresponds to a new periodicity  $2a \times 2b \times c$ , with a reduced symmetry  $P11m$  (number: 6). The diffraction pattern for this case is shown in Figure 2.7c. A similar diffraction pattern for [001] zone axis could also be obtained by modulating either of Ta2 or Ta3 (and its equivalence) diagonally along  $a, b$ , and  $c$ , so that the unit cell doubling's dimension corresponds to a periodicity given by  $2a \times 2b \times 2c$ .

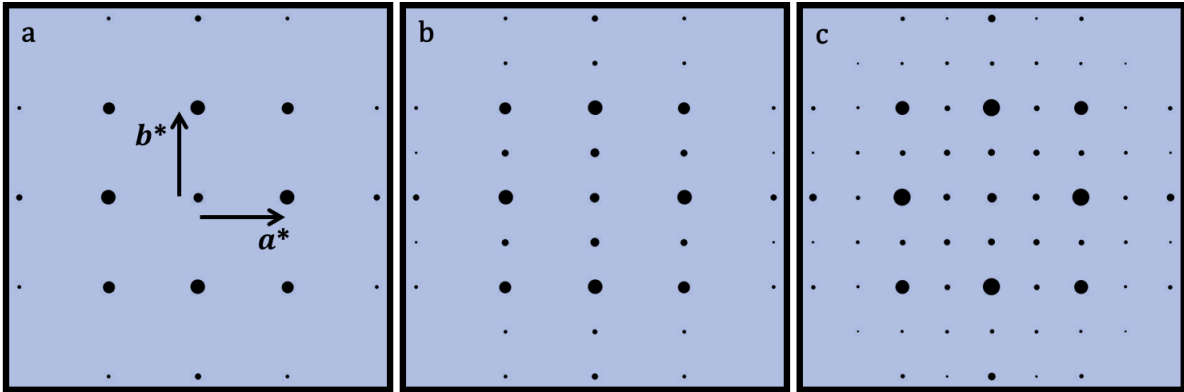


Figure 2.7: Panels (b) and (c) show electron diffraction patterns obtained from modulation explained in Figure 2.6, in contrast to the unmodulated lattice reciprocal space shown in (a). The atomic positions are modulated by 1%. The Bragg intensities are equally scaled.

An example of how to index a diffraction pattern with CDW spots is shown in Figure 2.8. A direct inference from the diffraction patterns obtained from a modulated crystal lattice is the reduction of the area defined by the first Brillouin zone boundary, for example, from  $k = -\frac{\pi}{a}$  and  $+\frac{\pi}{a} \rightarrow k = -\frac{\pi}{2a}$  and  $+\frac{\pi}{2a}$ . This is depicted in Figure 2.8. In essence, the formation of charge density wave in crystal lattices usually lead to the reduction of the first Brillouin zone in the  $k$ -space. This points to the formation of insulating domain walls in the crystal undergoing phase transition with an accompanied charge density waves. It is also evident that the shape of the first Brillouin zone depends on the dimension and the direction of crystal modulation.

The simple idea of obtaining and analysing electron diffraction patterns from both the modulated and the unmodulated mono-atomic crystals gives a valuable insight when interpreting obtainable diffraction patterns from complex crystals. The modulation of the atomic positions in the cubic lattices points to the existence of reference (unmodulated or undistorted) atoms or unit cells in every crystal undergoing phase transition. It also tells us that the transport or formation of charge density wave signatures in crystalline solids leads to the depletion or reduction of the electronic density of states, which translate to different distributions of host lattice Bragg reflections. The expected positions of the charge density wave signatures are also known apriori.

The structural and/or electronic transition in low dimensional crystalline solids could lead to one of commensurate, nearly commensurate and incommensurate superstructure lattices, whose distinct properties define the orientations of charge density wave signatures with respect to the host lattice Bragg reflections. The formation of each of these superstructure lattices is associated

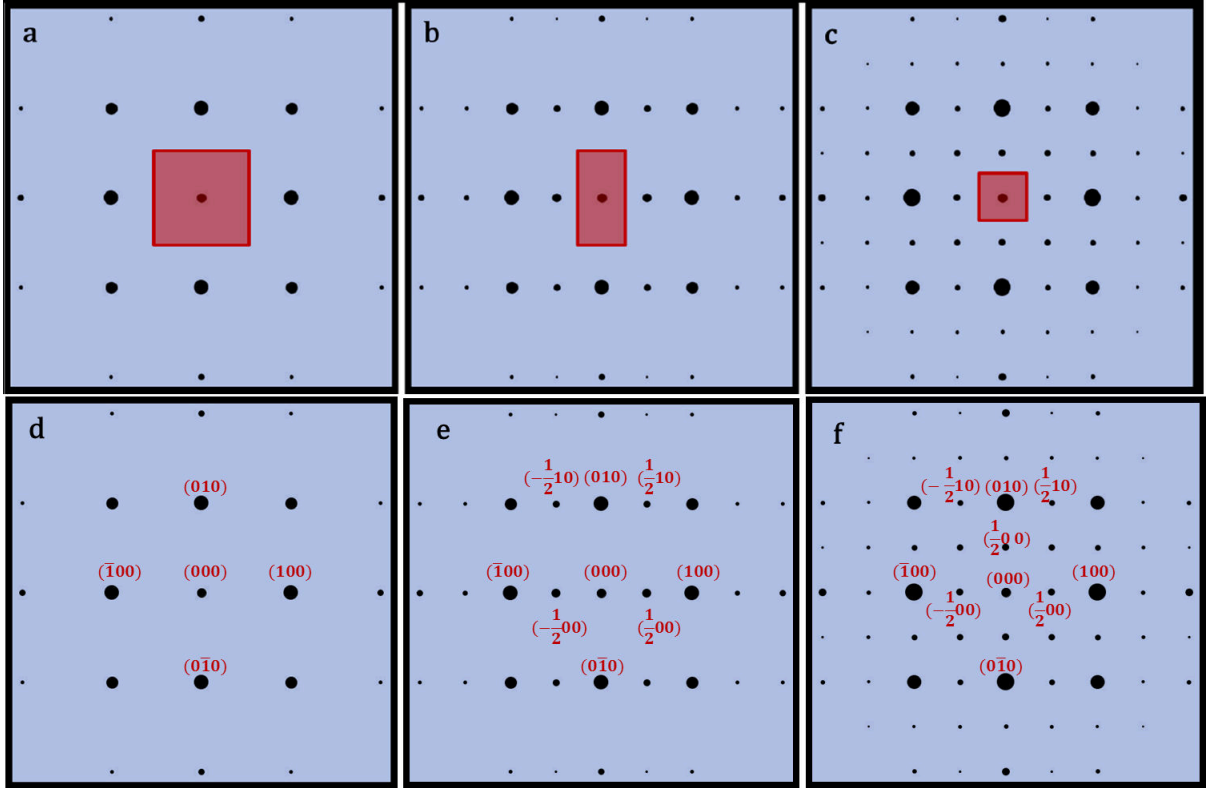


Figure 2.8: Diffraction patterns presented in Figure 2.7 are shown to illustrate the reduction of first Brillouin zones (regions designated with red backgrounds), which arises as a result of charge density wave formation. The indexing of the selected Bragg reflections are also indicated, along with the CDW spots. Panels (a) & (d), (b) & (e) and (c) & (f) are equivalent.

with a broken crystal symmetry and is due to thermodynamic fluctuations and Peierls instability in 1D and 2D metals. A charge density wave signature is commensurate if the CDW vector is a rational multiple of the host reciprocal lattice vector (i.e.,  $\mathbf{q}_{\text{CDW}} = (m/n) \times \mathbf{a}^*$ , where  $m$  and  $n$  are integers and  $\mathbf{a}^*$  is the reciprocal lattice vector), otherwise it is either incommensurate or nearly commensurate. Thus, the commensurability of the charge density wave signatures determines the positions they occupy in the reciprocal space, which sometimes could be at an inclined angle with respect to the host lattice Bragg reflections. In essence the positions erstwhile marked with a zero electron density now possess a periodic distribution of electronic charges.

Classical models describe the transport of charge density waves in terms of a threshold energy required to overcome the crystal potential field, which forms a barrier often referred to as the *pinning energy*. On the other hand, quantum mechanical models reckon that CDW transport is through *tunnelling*. The two models hold true [32] in analogy to electronic transition driven by electron-electron and electron-phonon couplings in charge density wave compounds, which form a center of interest for the rest of this dissertation, as we investigate structural evolution in transition metal dichalcogenides and DCNQI salts through electron diffraction simulation and experiment.

## Chapter 3

# Transition metal dichalcogenides

### 3.1 Introducing transition metal dichalcogenides

Transition metal dichalcogenides (TMDs) are quasi-two-dimensional inorganic crystals, which are famous for rich phase transitions relating to orders of magnitude change in their electric resistivity (See Figure 3.1). The inorganic crystals of TMDs usually comprise a three-atom thick slab with the configuration, chalcogen-metal-chalcogen (e.g. Se-Ta-Se), where the chalcogen atoms are group XVI elements (e.g. selenium (Se) and sulphur (S)) and the metal atoms are the transition  $d$  elements (e.g. titanium (Ti) and tantalum (Ta)). TMDs are layered charge density wave compounds and are fundamentally described according to the polytype to which each crystal group belongs. The polytypes are conventionally designated by the number of layers ( $1T$  has one layer,  $2H$  has two layers,  $4H$  has four layers per unit cell) and the type of coordination (trigonal-prismatic coordination ( $H$  layer) and the octahedral coordination, represented by  $T$  layer).

All TMDs crystallise into hexagonal lattice ( $a = b \neq c$ ;  $\alpha = \beta = 90^\circ$ ;  $\gamma = 120^\circ$ ), where  $c$  is the crystallographic unique axis pointing in the direction of the hexagonal stacking layers. The layers are held together by a weak van der Waals force of interaction, in contrast to a strong interaction force that is mediated by the covalent bonds between the constituent atoms of a TMD crystal. Thus, the modulation of electron density in TMDs is characterised by a weak potential screening (attributed to elastic coupling between two layers) along the unique crystallographic  $c$  axis, and a strong potential screening arising from elongation or shortening of the covalent bonds along the hexagonal  $b \angle a$  plane. This strong potential screening leads to a lowering of the crystal system's energy, paving way for the crystal to lock into a favourable charge density wave energy ground state.

Generally, charge density wave (CDW) formation in TMDs is primarily driven by strongly correlated transition metal  $d$ -electrons and mediated by two-dimensional Peierls instability. The interaction and/or correlation (in form of orbital mixing) between the  $p$ -bands of the chalcogen atoms and the  $d$ -bands of the transition metals drives both the metallic and the CDW phases of TMD crystals. The phase transitions between the metallic and the CDW phases in TMDs have been studied and analysed through angle resolved photo-electron spectroscopy (ARPES) [5, 33], neutron scattering [40], reflectivity measurements [50, 51], resistivity measurements [40] and ultrafast electron diffraction experiments [7, 10, 12, 34]. The observable Bragg reflections' intensity distributions in both phases are influenced by the degree of correlation between the constituent atoms along the hexagonal basal plane and the coupling between the layers along the crystallographic unique axis. Indeed, the research interest in CDW compounds has considerably increased with the discovery of TMD crystals [5].

The CDW phases of two transition metal dichalcogenide crystals, namely  $1T$ -TaS<sub>2</sub> [10] and

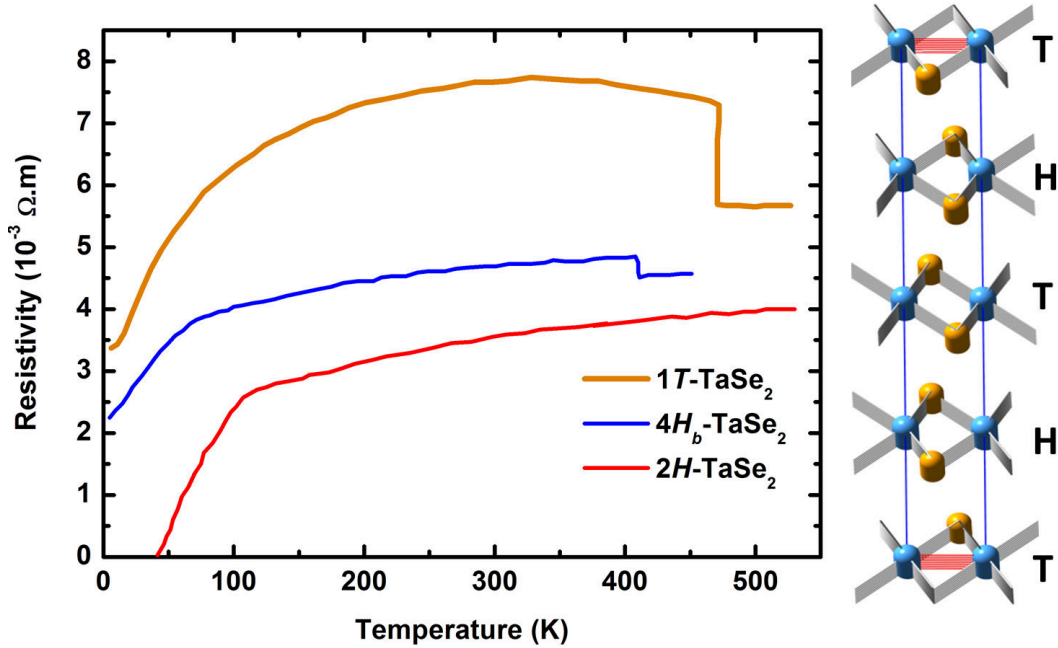


Figure 3.1: Temperature-dependent resistivity measurements [40] in three transition metal dichalcogenide (TMD) layered crystals, showing different phase transition orders from a metallic to a charge density wave state.  $4H_b\text{-TaSe}_2$  has four layers along  $c$ -axis, with alternating octahedral (T) and trigonal prismatic (H) coordinations, per unit cell.  $1T\text{-TaSe}_2$  has one octahedral coordinating layer per unit cell and  $2H\text{-TaSe}_2$  has two trigonal prismatic coordinating layers per unit cell. Both  $4H_b\text{-TaSe}_2$  and  $1T\text{-TaSe}_2$  undergo first order phase transition at around 410 K and 470 K respectively, while  $2H\text{-TaSe}_2$  undergoes a second-order ("knee") phase transition at around 122 K. (Key:- Ta: Blue; Se: Orange.)

$4H_b\text{-TaSe}_2$  [7, 12] had been characterised and studied through ultrafast electron diffraction experiment in our research group, and  $1T\text{-TiSe}_2$  is now at the initial stage of characterisation. The clustering of the constituent atoms and the dimension of superstructures' unit cells ( $\sqrt{13}a \times \sqrt{13}a \times c$ ) in  $1T\text{-TaSe}_2$  and  $4H_b\text{-TaSe}_2$  due to the modulation of electron density are essentially similar. There are different charge density wave phases associated with different transition temperatures, each inherent to one of commensurate, nearly commensurate and incommensurate states in the two TMD crystal groups, as were reported by Refs. [5, 7, 10, 12, 34, 35, 36, 39, 37]. The modulation of electron density and the mode of atomic clustering in  $1T\text{-TiSe}_2$  involve a different approach: A commensurate CDW phase obtainable from the crystal's low temperature structure reveals that the superstructure's unit cell dimension is given by  $2a \times 2a \times 2c$  [5, 38]. The parameters for some TMD compounds are shown in Table 3.1. For the sake of variety, we shall analyse charge density formation in  $1T\text{-TiSe}_2$  and  $4H_b\text{-TaSe}_2$  single crystals through electron diffraction simulation in this chapter, and compare and contrast the simulated diffraction results with those obtained in the electron diffraction experiment. The insights gained through the electron diffraction simulation and analysis will then be used to analyse the femtosecond dynamics of decoupled superlattice domains in  $4H_b\text{-TaSe}_2$  single crystals, with a view to adding to the existing knowledge of the crystal's spatial-temporal evolution during phase transition.

Table 3.1: Cell parameters, commensurate ( $T_C$ ) and incommensurate ( $T_{IC}$ ) phase transition temperatures and the superstructure dimensions in transition metal dichalcogenides.  $T$  represents the octahedral coordinated layer while  $H$  represents trigonal prismatic coordinated layer. Data taken from Refs. [5, 38].

TMDs	$T_C$ (K)	$T_{IC}$ (K)	Cell parameters ( $\text{\AA}$ )	Superstructure dimension
$4H_b$ -TaSe <sub>2</sub>	( $T$ ) 410 ( $H$ ) -	600 $\approx 75$	$a = b = 3.455$ ; $c = 25.18$	$\sqrt{13}a \times \sqrt{13}a \times c$ $3a \times 3a \times c$
$1T$ -TaSe <sub>2</sub>	473	$> 600$	$a = b = 3.477$ ; $c = 6.263$	$\sqrt{13}a \times \sqrt{13}a \times c$
$2H$ -TaSe <sub>2</sub>	$\approx 90$	$\approx 122$	$a = b = 3.434$ ; $c = 12.692$	$3a \times 3a \times c$
$4H_b$ -TaS <sub>2</sub>	( $T$ ) 315 ( $H$ ) -	$\leq 600$ 22	$a = b = 3.332$ ; $c = 23.62$	$\sqrt{13}a \times \sqrt{13}a \times c$ $3a \times 3a \times c$
$1T$ -TaS <sub>2</sub>	150	$> 600$	$a = b = 3.346$ ; $c = 5.859$	$\sqrt{13}a \times \sqrt{13}a \times c$
$2H$ -TaS <sub>2</sub>	-	$\approx 75$	$a = b = 3.315$ ; $c = 12.104$	$3a \times 3a \times c$
$1T$ -TiSe <sub>2</sub>	202	-	$a = b = 3.54$ ; $c = 6.004$	$2a \times 2a \times 2c$
$1T$ -TiS <sub>2</sub>	-	-	$a = b = 3.405$ ; $c = 5.699$	No CDW

### 3.2 A retrospect of charge density wave dynamics in $4H_b$ -TaSe<sub>2</sub> single crystals

A study on time-resolved femtosecond electron diffraction measurements on  $4H_b$ -TaSe<sub>2</sub> single crystals had been carried out in our ultrafast laboratory by my senior colleagues [7, 10, 12], shortly before I joined the group. The experiment is based on a pump-probe technique: The pump is a laser pulse centred at 775 nm, with a 1 kHz repetition rate and a 150 fs pulse duration. The pump pulse is usually used to drive the crystal sample under investigation to a different phase through the deposition of energy into the sample. In this way, properties like Debye-Waller effects, spatial-temporal evolution of charge density wave signatures and/or characterisation of Bragg intensity signals could be studied. A sub-picosecond ( $\sim 0.5$  ps) temporal resolution relating to atomic or molecular motion in crystals is achievable in the current ultrafast electron diffraction (UED) experiment set-up. The time constants characterising the electronic degrees of freedom, in relation to electron-electron and/or electron-phonon couplings, usually form a foundation for the nature of suppression and recovery of charge density wave signatures and Bragg intensities' fluctuations in crystals [7, 10, 34]. These time constants are retrieved as the relaxation times and/or the time required for a sample to be switched from one phase to another, after it has been photo-induced in UED experiments.

The pump pulse initiates structural dynamics in the crystal by transferring optical excitation density to the crystal's atomic constituents so that they are excited or perturbed: the resulting evolution of the crystal's periodicities is then investigated by the probe beam. The probe beams are short electron pulses, which are photoelectrically generated by irradiating a gold-coated cathode with 258 nm laser pulses. The electron probes thus generated are accelerated by a 30 kV energy through the anode and collimated onto the sample by a magnetic lens. The measurement is usually run in a vacuum chamber, which is characterised by  $\approx 10^{-6}$  mbar pressure. The need for low pressure vacuum chamber is to enhance electron beam propagation, as highlighted in Refs. [7, 10].

Here, we want to investigate structural transitions in  $4H_b$ -TaSe<sub>2</sub> by characterising and analysing the formation and transport of charge density wave signatures through electron diffrac-

tion simulation.  $4H_b$ -TaSe<sub>2</sub> is a quasi-two-dimensional transition metal dichalcogenide, which comprises four alternating layers of octahedral and trigonal prismatic coordinations per unit cell. The crystal structure along the [001] ( $b \perp a$  plane) and [110] zone axes (showing the different coordinations) are shown in Figure 3.2 (a) and (b). Generally, each tantalum atom is coordinated by six selenium atoms along the [001] axis. The unit cell comprises two tantalum atoms and two selenium atoms (one for each layers:  $H$  and  $T$ ) that are crystallographically independent. These four atoms make up the asymmetry unit needed in the simulation of the metallic phase of  $4H_b$ -TaSe<sub>2</sub>. There are 18 atoms altogether per unit cell of  $4H_b$ -TaSe<sub>2</sub> crystals, when all the four layers are considered. The space group for the average structure in the metallic phase ( $> 600$  K) is  $P6_3/mmc$  [35]. The hexagonal unit cell parameters are given as:  $a = b = 3.455$  Å;  $c = 25.15$  Å [12, 35].

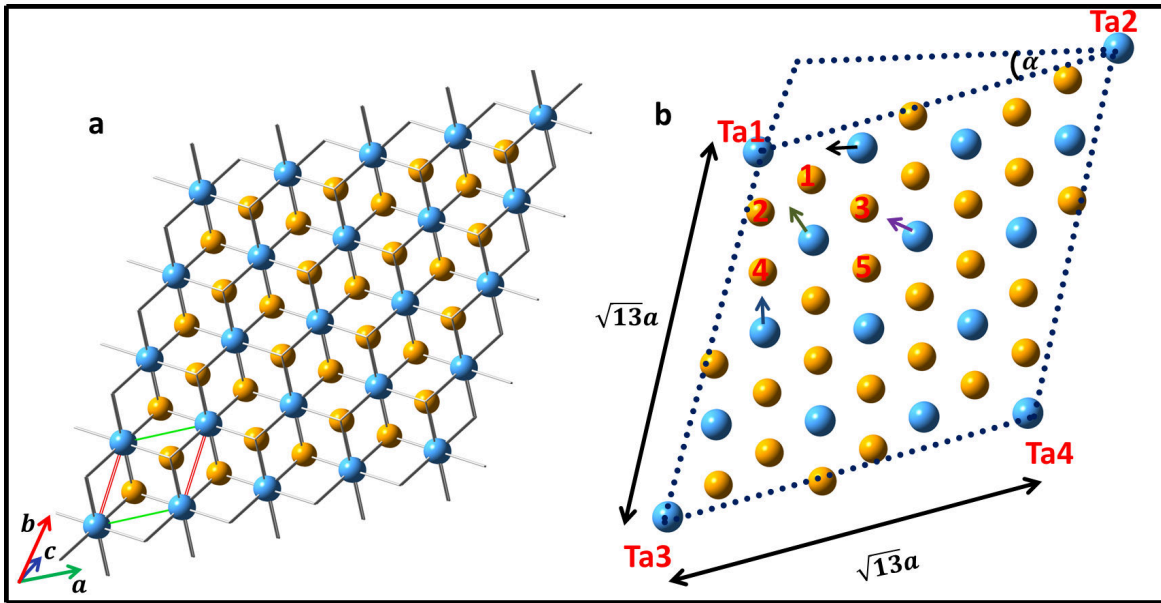


Figure 3.2: Panel (a) shows the crystal structure of  $4H_b$ -TaSe<sub>2</sub> projected along the  $b \perp a$  octahedral plane ([001] zone axis). In (b) the dimension of the superstructure is shown, together with the angle of rotation  $\alpha = 13.9^\circ$ , which is associated with the commensurate charge density wave phase. Ta1–Ta4 are crystallographically equivalent, each of which serves as the unmodulated reference point. X-ray diffraction analysis revealed that there are altogether 5 tantalum atoms and 5 selenium atoms in the octahedral layer; 3 tantalum atoms and 5 selenium atoms in the trigonal prismatic layer (not shown), all of which are independent [35]. The tantalum with color arrows and the referenced Ta1, together with the selenium atoms (labels 1 – 5), form the asymmetry unit of  $4H_b$ -TaSe<sub>2</sub> superstructure in the octahedral ( $T$ ) layer.

$4H_b$ -TaSe<sub>2</sub> crystals exhibit different phases at different temperatures. The average structure for the metallic state exists above 600 K. Below 600 K the structure undergoes a phase transition from the metallic phase into an incommensurate CDW phase, with the signature of the CDW being only present in the octahedral ( $T$ ) layer [35, 38, 40]. At 410 K the structure locks into a commensurate CDW phase, still only in the  $T$  layer. The commensurate CDW signatures in the octahedral ( $T$ ) layer persist down to 75 K, where the structure reveals a development of incommensurate CDW in the trigonal prismatic ( $H$ ) layer, in co-existence with the commensurate CDW in the  $T$  layer. Indeed,  $4H_b$ -TaSe<sub>2</sub> crystals are considered to be the parent compounds of both the  $2H$ -TaSe<sub>2</sub> and the  $1T$ -TaSe<sub>2</sub> crystals: the signatures of the incommensurate CDW found in the  $H$  layer of  $4H_b$ -TaSe<sub>2</sub> around 75 K was reported to be similar to those found in

$2H$ -TaSe<sub>2</sub> around 122 K [38, 40]. Likewise, the signature of the commensurate CDW found in the  $T$  layer of the  $1T$ -TaSe<sub>2</sub> around 473 K was similar to those found in the  $T$  layer of  $4H_b$ -TaSe<sub>2</sub> at 410 K [40]. Moreover, the resistivity measurements shown in Figure 3.1 revealed that the phase transitions' orders found in the mono-layered polytypes ( $2H$ -TaSe<sub>2</sub> and  $1T$ -TaSe<sub>2</sub>) were combined in  $4H_b$ -TaSe<sub>2</sub> [40]. The CDW-carrying octahedral ( $H$ ) layers sandwiched between non-CDW-carrying trigonal prismatic ( $T$ ) layers point to the existence of alternating metallic and insulating layers in  $4H_b$ -TaSe<sub>2</sub> single crystals [42].

The structural transition in  $4H_b$ -TaSe<sub>2</sub> compound is accompanied by electronic transition, which is manifested by the formation of charge density waves. The modulation of electron density associated with shortening or elongating the covalent bonds and the  $p$ - $d$  hybridisation between tantalum and selenium atoms allows for the in-plane periodic lattice distortion, which could lead to either commensurate or incommensurate charge density wave formation. The band structures obtained from electronic band structure calculations in the isostructures of  $1T$ -TaSe<sub>2</sub> and  $1T$ -TaS<sub>2</sub> are attributed to the clustering modes and the in-plane lattice distortion in these crystals [40, 41].

Fundamentally, the band structures obtained from the undistorted, normal metallic states of these TMDs are due to the splitting of the Ta  $5d$  band to three sub-bands, of which the  $5d_{z^2}$  is raised above the Fermi energy level [5, 34, 41]. The ordering of the octahedrally-coordinated tantalum atoms' shifts, coupled with the contributions from the disordered selenium atoms at low temperatures, are expected to give rise to 13 bands. Of these 13 bands, six are filled bonding bands, six are empty antibonding bands and one is a partially filled bonding band [39]. Generally, a combination of a degree of disorderliness due to Anderson localisation (strongly correlated charge localisation due to impurities and lattice defects), Peierls instability and mutual Coulombic repulsion between the ions (due to Mott localisation) of the constituent atoms (transition metals and the chalcogen atoms) were reported to be the origin of and/or driving force behind charge density wave formation in TMD crystals [34, 39, 41].

$4H_b$ -TaSe<sub>2</sub> single crystals are usually grown using the iodine-vapour transport technique [35, 40]. X-ray diffraction studies [35, 37] on  $4H_b$ -TaSe<sub>2</sub> single crystals revealed that the contributions from the in-plane tantalum and selenium atoms in the trigonal prismatic layer could not be ignored: a tenth of periodic lattice distortion amplitude found in the octahedral layer was found in the trigonal prismatic layer. Thus, a total of 18 independent atoms representing the asymmetry unit of the superstructure of  $4H_b$ -TaSe<sub>2</sub> and comprising 8 tantalum and 10 selenium atoms were refined in Ref. [35]. In the commensurate CDW phase, the superstructure's atomic arrangement reveals a broken symmetry in the lattice, where the crystal's space group goes from a higher symmetry ( $P6_3/mmc$ ) to a lower symmetry ( $P6_3/m$ ). The atomic coordinates of the refined structure at room temperature are used in the simulated diffracted patterns presented here. Shown in Figure 3.3 (a) and (c) are the simulated diffraction patterns for the high temperature (above 600 K) metallic phase and the room temperature commensurate CDW phase. The corresponding commensurate CDW phase experimental electron diffraction pattern shown in Figure 3.3 (b) was obtained at room temperature ( $\sim 300$  K). Pumped with an optical excitation density of  $\sim 2.5$  mJ (corresponding to about  $\sim 110$  K sample's temperature increase) [7], the sample is believed to be driven into an incommensurate CDW (IC-CDW) phase (see Table 3.1). However, the current UED experimental set-up is not sensitive enough to resolve the IC-CDW signatures.

Notably, the observable intensity distributions of the experimental diffraction patterns clearly validate the corresponding simulated diffraction patterns. This proves the credibility of the X-ray diffraction refinement done by Lüdecke *et al.* [35]. Conceptually, the asymmetry unit of  $4H_b$ -TaSe<sub>2</sub> crystal is composed of four sheets (or layers): one layer each of the octahedral and trigonal coordinated tantalum and selenium atoms. Atomic perturbations from each of the layers are

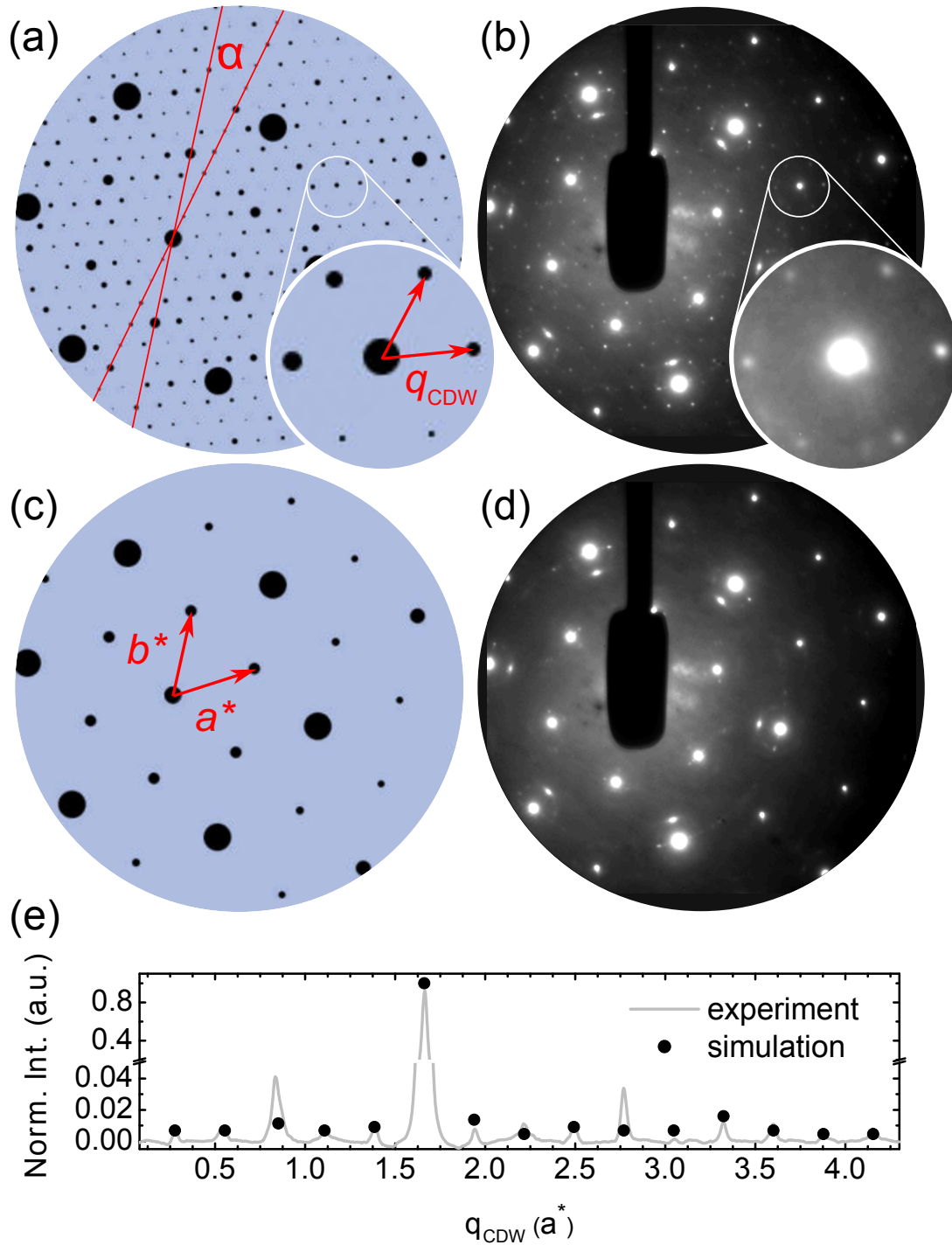


Figure 3.3: Energy-momentum space electron diffraction patterns for  $4H_b$ -TaSe<sub>2</sub> crystal along its  $b \perp a$  plane ([001] zone axis). Panels (a) and (b) refer to the low temperature CDW phase; panels (c) and (d) refer to the high temperature metallic phase. The commensurate CDW parameters for both the simulation and the experiment are  $q_{\text{CDW}} = 0.277a^*$ ; and  $\alpha = 13.9^\circ$ . The insets in (a) and (b) show the distribution of the CDW spots around the host lattice Bragg spots. A line profile is taken along the green line shown in (b). Panel (e) shows that the scaled simulated Bragg/CDW intensity ratio compares well with the experiment's. The scaling factor between the simulated and the experimental reflections,  $s = 8.7$ .

envisaged to contribute to the observable diffraction patterns. For the high temperature metallic phase, the intensity distribution of the Bragg peaks primarily arises from the electron density distribution in the undistorted scattering domains of these layers.

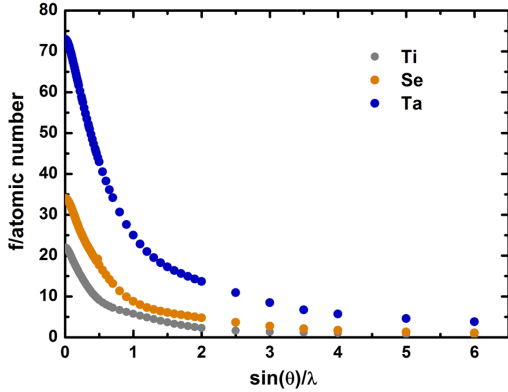


Figure 3.4: The atomic scattering powers of the constituent atoms in TMD crystals. Data taken from [21].

From the atomic form factor point of view, the scattering capacities of the tantalum atoms are more than twice those of selenium atoms (see Figure 3.4). Thus, the observable Bragg intensities could approximately arise from the tantalum atoms' scattering domains. To ascertain this approximation, we carried out series of simulation to determine the origin of the intensity distribution of experimentally observable Bragg intensities. We found that the simulated diffraction pattern deviate from experimental diffraction pattern, when only tantalum atoms' coordinates were used in the simulation. The simulation shows that the relaxation of the selenium atoms in both layers plays an important role in accurately modelling the experimentally observable re-

fections. Therefore, the overall scattering factor is envisaged to be contributed by atomic perturbations from each layer through elastic coupling, as was argued by Ludecke *et al.* [35] and also evidenced by scanning tunnelling microscopy (STM) measurements reported in Ref. [38].

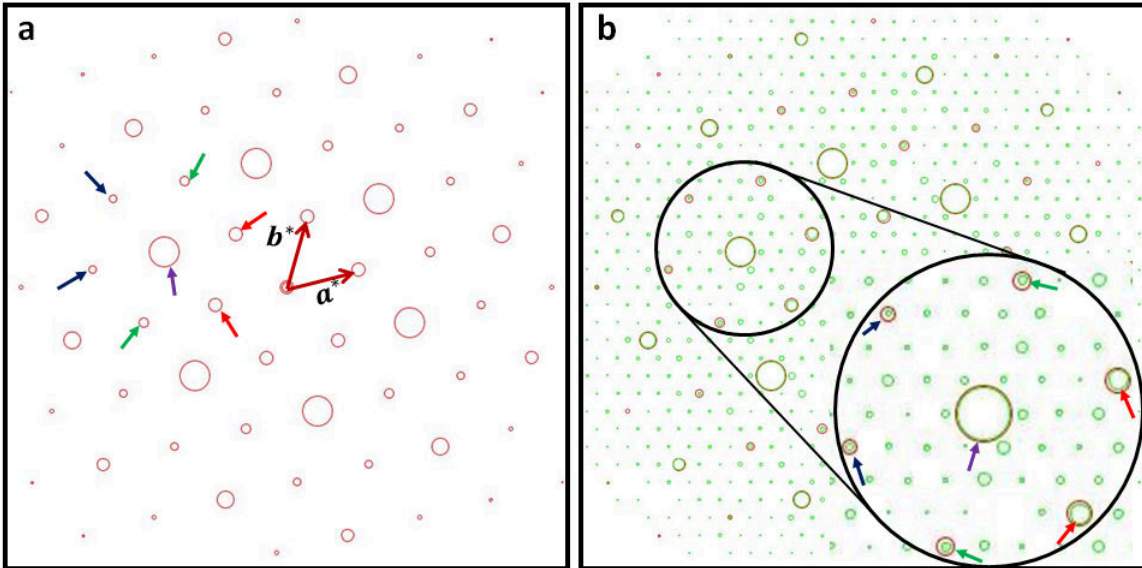


Figure 3.5: The intensity distribution of the host lattice Bragg reflections and the charge density wave signatures in  $4H_b$ -TaSe<sub>2</sub> crystals revisited. Shown in panel (a) is the metallic phase diffraction pattern, indicating three diffraction orders (marked by green, red and blue arrows), from which the charge density wave intensity distribution arises. The Bragg reflection indicated by purple arrow is the  $(-2\ 1\ 0)$  peak, on which a charge distribution due to Mott localisation is envisaged. The surrounding six Bragg reflections' intensities are appreciably reduced in the charge density wave phase, shown in the inset of panel (b) with corresponding arrows. In panel (b), the high metallic phase reflections (open red circles) are overlapped with the CDW phase (open green circles). The drop in intensities of the six surrounding reflections are clearly seen in the enlarged inset in panel (b) (see text).

It is instructive to interpret the intensity distribution of the Bragg reflections obtained for both the metallic and the charge density wave phases through scattering by *intertwined domains*, which are unique features of TMD crystals. In essence the tantalum layers are intertwined with the selenium layers such that the longitudinal displacement of the in-plane tantalum atoms results in the transversal disorderliness of the selenium atoms. Across the scattering domains of the crystal, the distribution of electron density is based on the band overlaps between tantalum and selenium atoms and this determines the strength of each observable Bragg reflection.

In the 13 atoms hexagram picture ("Stars of David"), there are three distinct tantalum atoms: the tantalum atoms at the center of each hexagram, one from the nearest neighbour six-member ring and one from the next nearest neighbour six-member ring (see Figure 3.6). Fazekas *et al.* [39] reckoned that there is a localisation of charge distribution on the central tantalum atom, which accepts charges from the outermost tantalum atoms through the inner tantalum atoms. This antecedent proposition perfectly fits the Bragg reflections' intensity distribution obtained. Whereas the intensities' amplitudes of the six Bragg reflections (marked by red and blue arrows in Figure 3.5 (a)) surrounding the  $(-2\ 1\ 0)$  peak are significantly reduced as the crystal undergoes phase transition, there is no drastic change in the intensity amplitude of the  $(-2\ 1\ 0)$  peak. The signature of the host lattice Bragg reflections is such that three different diffraction orders form hexagonal reflections around a coordinating Bragg reflection of different order, as indicated by the red, green and blue arrows in Figure 3.5 (a).

Relative to the coordinating central Bragg reflection, the hexagonal Bragg reflections are of lower unequal intensities (see Figure 3.5 (a)). During phase transition, the charge distribution associated with the scattering domains of these central Bragg reflections are *localised*, unlike the surrounding six reflections whose charges are depleted (see Figure 3.5 (b)). This indicates that (1) there is a coexistence of localised and depleted electronic density of states; (2) the pull of electronic charge is towards the center of the hexagram as clearly proposed in the literature [5, 34, 35, 38, 39, 40]; (3) the unequal amplitudes of the surrounding six reflections appear to arise from different transversal relaxation's amplitudes of the selenium atoms, whose sheets "buckle" or "warp" around the modulated scattering domains of the tantalum atoms' sheets. This then would lead to the different electronic density of states of twelve CDW intensities' amplitudes, which are expected to surround each of the host lattice Bragg reflections.

Recapping the inference "3" in the preceding paragraph, the charge density wave intensity distribution is argued to arise from the "collapse" of the surrounding six reflections of the metallic phase electron diffraction patterns. The reason behind the unequal CDW peaks then unfolds: the "six reflections" generating the CDW signatures are also of unequal intensities in the metallic phase (compare panels (a) and (b) in Figure 3.5: the Bragg reflections with colour arrows in panels (a) and (b)). These unequal CDW intensities are both evident in the experiment and the simulation, as shown in Figure 3.6. Furthermore, obtaining unequal CDW intensities means that the atomic (selenium and tantalum) positions do not have the same modulation amplitude. In other words, each tantalum atom of the inner and the outer rings of the 13 hexagram picture experiences different modulation, or the buckling of the Se atoms' sheets mediates different potential field screenings around the superlattice clusters. From the *t*-plot analysis (to determine Ta-Ta atoms distance) on different isostructures ( $4H_b$ -TaSe<sub>2</sub>,  $1T$ -TaSe<sub>2</sub> and  $1T$ -TaS<sub>2</sub>) reported in Ref. [35], the average modulation amplitudes estimated for the inner and outer ring Ta atoms were  $\sim 0.2\ \text{\AA}$  and  $\sim 0.1\ \text{\AA}$ , respectively.

Hinged on the existence of twinning and layer interaction in  $4H_b$ -TaSe<sub>2</sub> single crystals [35, 43, 44], two domains of satellite reflections comprising six CDW signatures each are identified as shown in Figure 3.6. The first and second domains are held in position by Coulomb mode repulsion. Given that the spatial distribution of CDW signatures at room temperature are commensurate with the host lattice reflections, the CDW orders are contained in each of the

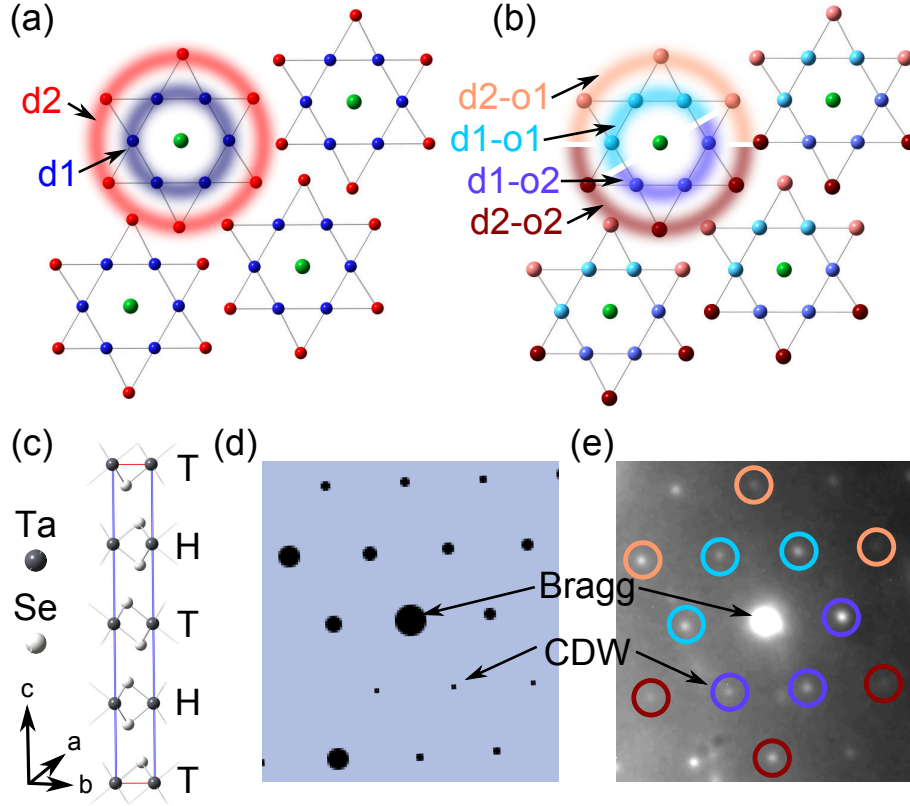


Figure 3.6: Real and reciprocal space representations of the superlattice clusters in  $4H_b$ -TaSe<sub>2</sub> single crystals. Panels (a) and (b) show the octahedral projections (only Ta atoms) of the crystal along the [001] zone axis ( $b \angle a$  plane), where the different colour codes indicate 3 and 5 independent crystallographic Ta atoms. The two satellite domains are represented in real space by d1 and d2; and their respective orders by d1-o1, d1-o2 and d2-o1, d2-o2, as shown in (a) and (b). Panels (d) and (e) represent a supercluster unit of the simulated and the experimental commensurate phase electron diffraction pattern, respectively. Each superlattice cluster contains two satellite domains with 6 CDW signatures apiece. See text for discussion.

six CDW reflections of the identified satellite domains. Based on the different Friedel's signs and the well established different CDW zoning in the literature [36, 43, 44, 45], the 12 CDW signatures in each superlattice cluster could be categorised into two zones: 1:6:6 and 1:3:3:3:3. The former (1:6:6) involves a coordinating Bragg reflection and six CDW signatures apiece of the first and second satellite domains. Anchored on the interlayer interaction, the latter (1:3:3:3:3) comprises a Bragg reflection and 3 CDW signatures apiece of the satellite domains' orders (first and second). The real space representations of these two zones are shown in Figure 3.6 (a & b). The corresponding simulated and experimental reciprocal space representations are shown in Figure 3.6 (c & d).

As a sequel to the experimental electron diffraction analysis carried out on  $4H_b$ -TaSe<sub>2</sub> single crystals and reported in two PhD theses [7, 10] of former students in our research group, the author herewith demonstrates simultaneous dynamics and suppression of the identified CDW domains. The previous analysis only included the photo-induced commensurate-incommensurate (C-IC) evolution of the first satellite domain's six CDW signatures. The analysis here includes the simultaneous evolution of both satellite domains.

Using variable optical excitation densities, the experimental data of three independent scans are analysed and plotted as shown in Figure 3.7. The analysis of the two domains was done using a LabView program written by Kerstin Haupt, as reported in Ref. [10], with a slight

modification to suit the selection of Bragg, CDW and background masks. The independent selections of the CDW signatures, together with the Bragg signals, of the two satellite domains are shown in Appendix A. The commonly employed fitting model for spatial-temporal evolution of CDW transitions in TMDs is based on coherent and incoherent relaxations [7]:

$$\frac{\Delta I}{I_0}(t) = B_1(1 - e^{-t/\tau_{\text{coh}}}) + B_2(1 - e^{-t/\tau_{\text{incoh}}}), \quad (3.1)$$

where the amplitudes  $B_1$  and  $B_2$  are both negative for CDW domain suppression, but have alternating signs for the evolution of Bragg peaks. Whereas the rise in the Bragg signal due to the breathing modes of the two domains and the concomitant satellite CDW domain suppression are due to coherent electron-electron (e-e) scattering (suppression of the electronic order and the subsequent release of the periodic lattice distortion), the further suppression of the CDW signatures and the drop in the Bragg signal are hinged on incoherent electron-phonon (e-p) coupling and reminiscent of Debye-Waller lattice fluctuation. The graphic representations of the fitting models are shown in Figure 3.9.

We first consider the temporal evolution of the identified satellite (CDW) domains. The two exponential functions given in Equation 3.1 are characterised by two time constants and convoluted with a 400 fs Gaussian pulse and a step function to account for the system response. The convoluted signal perfectly describes the temporal evolution of both the electronic (CDW) and the lattice (Bragg) orders (The Matlab codes are given in Appendix B). The first,  $\tau_{\text{coh}}$ , which characterises coherent e-e scattering, is estimated to be a quarter of a period of oscillations (breathing modes of the Ta-Ta atoms in the superlattice clusters). This estimation is founded on the time required for the constituent atoms to return to their unmodulated positions.

Nakashizu *et al.*, [46] reported two temperature-dependent Raman-active soft phonon modes ( $A_g = 60 \text{ cm}^{-1}$  and  $E_{2g} = 70 \text{ cm}^{-1}$ ) associated with band gap closure or formation in  $4H_b$ -TaS<sub>2</sub> single crystals. The corresponding quarters of the period of oscillations for the two soft phonon modes are  $\sim 140$  fs and  $\sim 120$  fs, respectively. This means that  $\tau_{\text{coh}}$  could take on any of these values. It would be interesting if each of the two identified CDW domains could separately be associated with these phonon modes. However, our experimental temporal resolution is  $\geq 400$  fs and as such the difference of  $\sim 20$  fs between the phonon modes could not be resolved. Therefore, we chose  $\tau_{\text{coh}} = 140$  fs (using 120 fs gives the same result).

For all the data fits and the associated optical excitation densities, we find the same time constant,  $\tau_{\text{incoh}} \approx 550$  fs for the incoherent relaxation of the lattice modes and the incoherent quenching of the CDW signatures for both domains. This estimated time constant points to a strong correlation between the electronic and lattice orders in the crystal, while undergoing structural transition.

The quenching of superlattice (CDW) periodicities is generally associated with CDW amplitude and phase modes [46, 47, 48]. Thus, the difference between the suppression of the two CDW domains are as a result of these two CDW collective modes. The phase mode is due to the sliding of the CDW during quenching, such that the CDW phase of one domain is shifted relative to the other. The amplitude mode is due to the different degrees of quenching. Due to the same time constant estimated for the two satellite domains, we propose that the evolution of the domains are perfectly in phase and as such the phase mode is absent. As shown in Figure 3.7, it is, however, clear that the quenching of the satellite domains is either complete or perturbative in nature. While the CDW suppressions associated with low optical excitation densities (fluence,  $F < 2.4 \text{ mJ/cm}^2$ ) are subject to recovery, those associated with high fluence ( $F \geq 2.6 \text{ mJ/cm}^2$ ) are fully suppressed. It is interesting to note that the Raman-active soft phonon modes reported for  $4H_b$ -TaS<sub>2</sub> single crystals are amplitude modes [46]. Moreover, the quenching of fluctuating CDWs in cuprates [47] is also attributed to CDW amplitude mode.

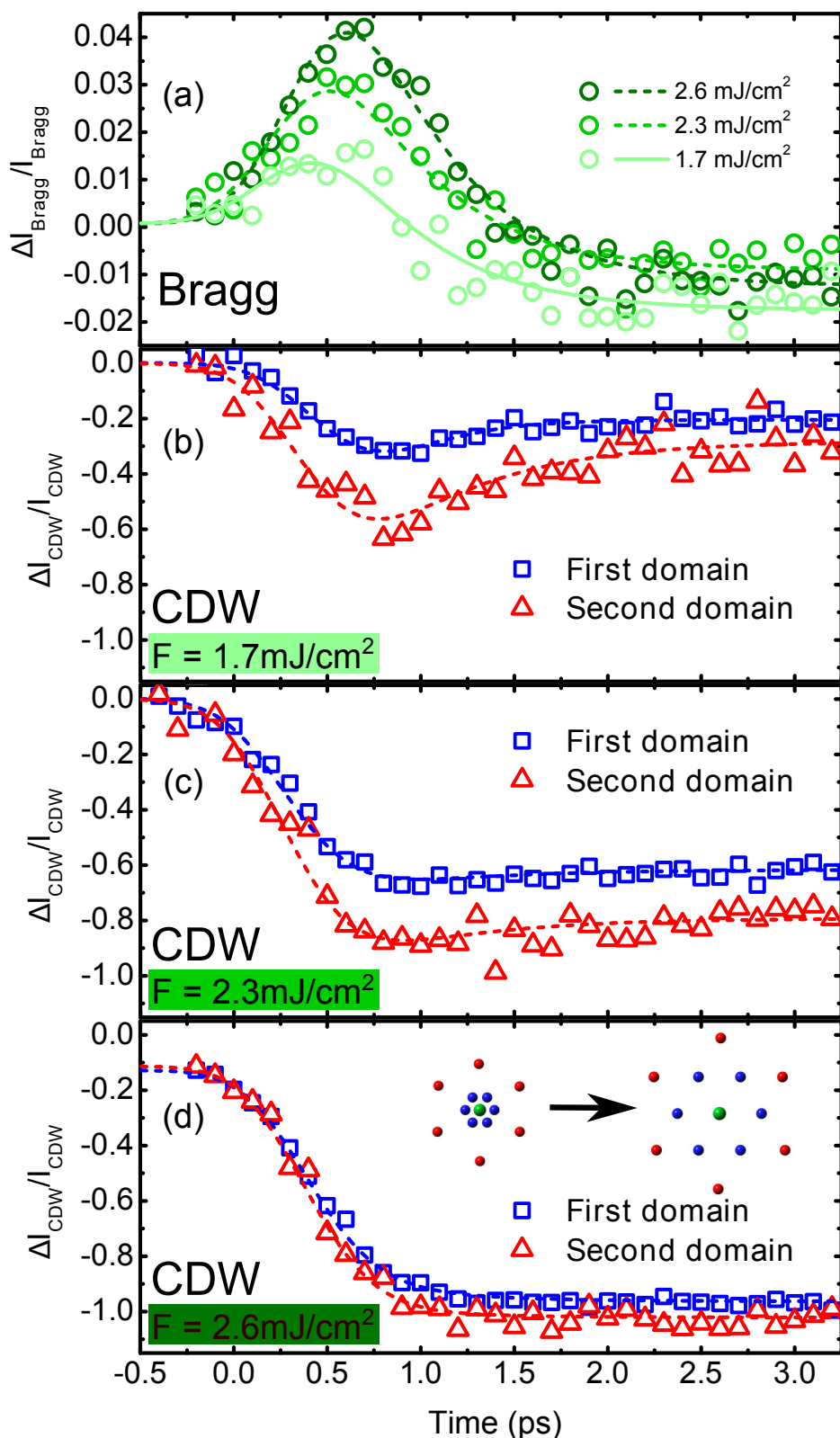


Figure 3.7: Temporal evolution of decoupled superlattice domains. Panel (a) shows the evolutions of the host lattice Bragg reflections for three different optical excitation densities. Panels (b-d) show the concomitant suppression of the satellite domains, each corresponding to the different optical excitation densities, and representing three independent experimental scans. The CDW decay of both satellite domains are simultaneous. The dash lines represent fits to the different experimental data sets. The inset in panel (d) indicates the relaxation of both the modulated electron density and periodic lattice distortion. This analysis represents CDW zone: 1:6:6. See text for discussion.

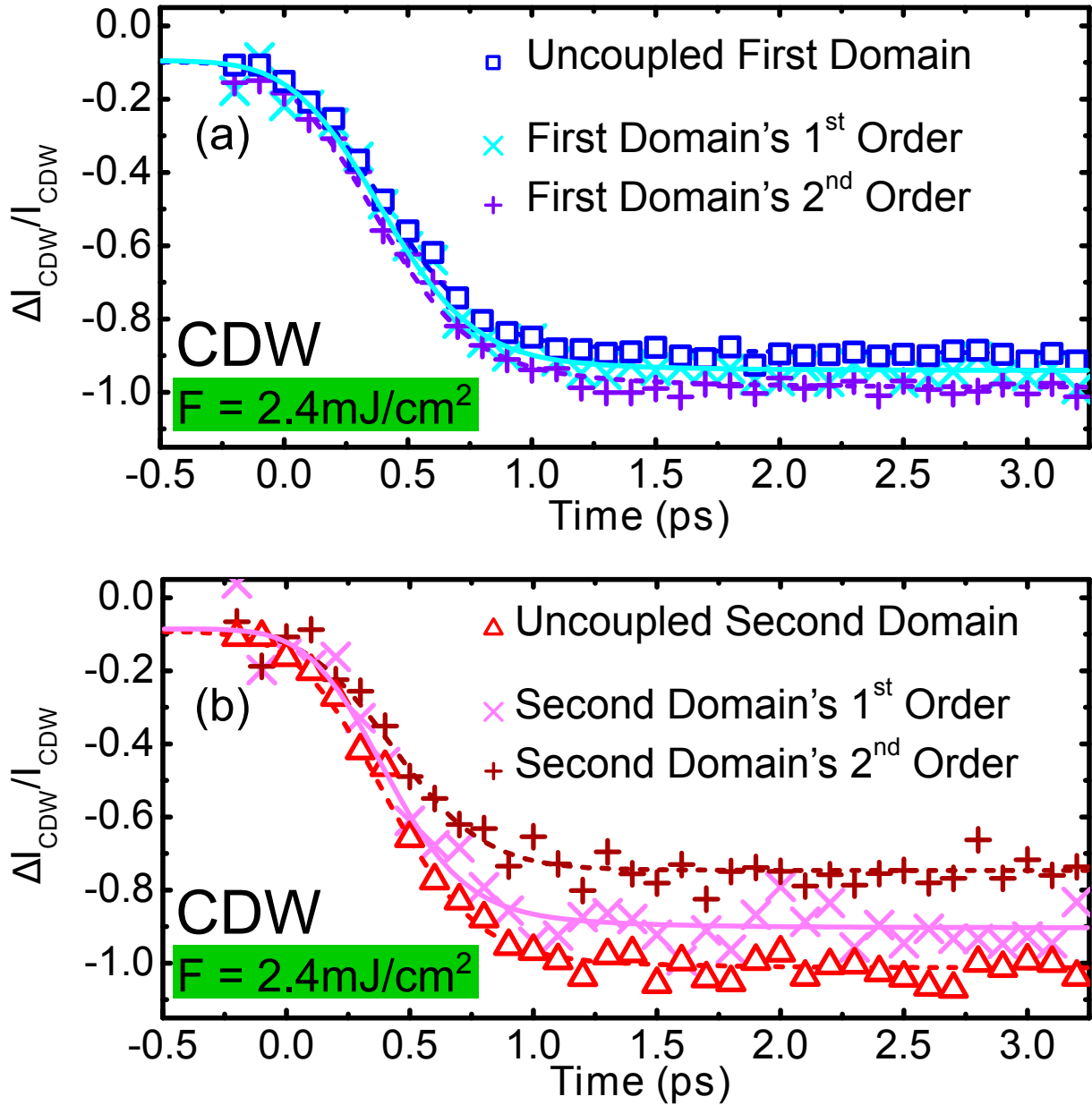


Figure 3.8: Temporal evolution of decoupled superlattice domains' orders in  $4H_b\text{-TaSe}_2$  single crystals (optical excitation density,  $F = 2.4 \text{ mJ/cm}^2$ ). Panels (a) and (b) show the overlap of the evolutions of CDW signatures in the first and second domains, respectively. The dominance of CDW amplitude mode over phase mode is evident in the quenching of the second domains' CDW signatures. This analysis represents CDW zone: 1:3:3:3:3. See texts for discussion.

The different degrees of CDW suppression are related to the different modulation of the inner and outer Ta atoms, so that one satellite domain is more suppressed relative to the other for an associated optical excitation density. Furthermore, the observed separation between the suppression of the satellite domains is found to be fluence-dependent. The difference between the CDW domains' amplitudes decreases as the fluence increases (See Figures 3.7). With  $F = 1.7 \text{ mJ/cm}^2$ , the first and second domains' CDW signatures are suppressed by 30 % and 60 %, respectively, before they start recovering. When  $F = 2.3 \text{ mJ/cm}^2$ , the domains are suppressed by 60 % and 80 %.

To investigate this further, we analysed the evolution of the satellite domains' orders (CDW zone: 1:3:3:3:3), as shown in Figure 3.8. The same time constants as stated above are also fitted for the different domains' orders. The quenching of the first domain's CDW orders are not so different from the overall quenching of the first domain's CDW signatures. However, the existence of amplitude mode is evident in the quenching of those of the second domain. Therefore, the variation of the degrees of quenching in one domain relative to the other readily points to the dominance of the amplitude mode over phase mode during structural transition in  $4H_b$ -TaSe<sub>2</sub> single crystals. It is envisaged that the different amplitude modes of the two satellite domains in the perturbative regime induce a fluctuating Fermi gap, which reduces or become stable with an increasing excitation density.

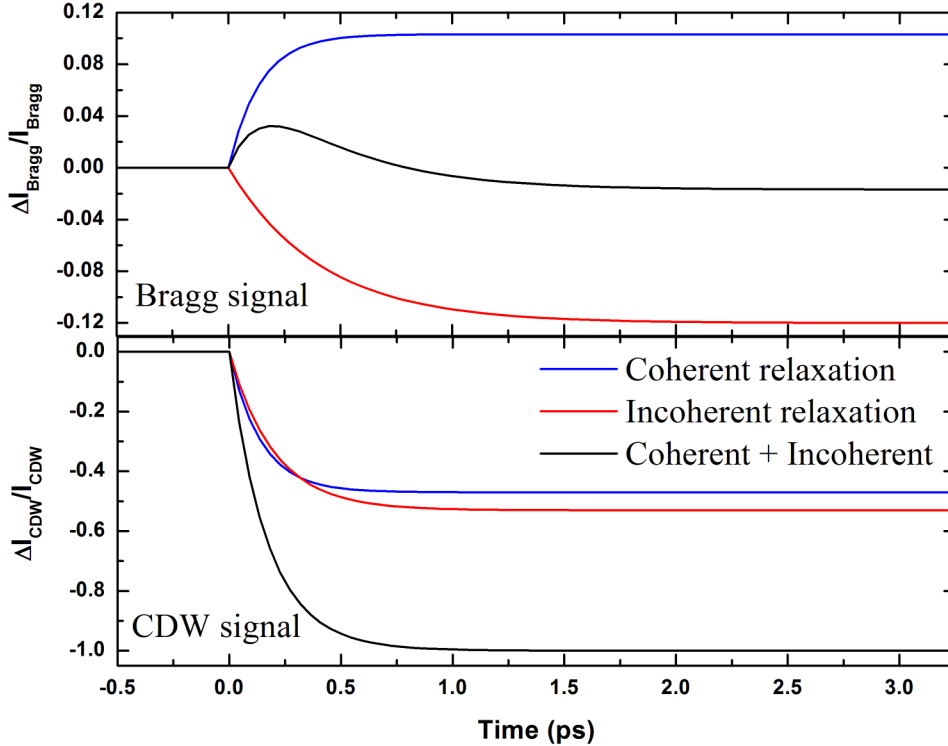


Figure 3.9: Fitting models for the temporal evolution of superlattice domains. The top panel represents the evolution of the Bragg signals, where the coherent and the incoherent relaxations account for rise and drop in the Bragg signals, respectively. The bottom panel represent the evolution of the CDW signals, where both the coherent and the incoherent relaxations account for the suppression of the CDW signals.

The full quenching of the commensurate CDW signatures in  $4H_b$ -TaSe<sub>2</sub> single crystals is expected to either switch the structure into its incommensurate CDW or metallic phase, with a characteristic finite or zero Fermi gap at the Fermi energy level [49]. The signatures of the incommensurate CDW phase could not be detected with our experimental spatial resolution.

As reported in Ref. [7, 12, 10], this could be as a result of weaker CDW signals associated with the incommensurate phase or that the optical excitation density drives the crystal directly into its metallic phase. The two assertions appear to hold true. It could be that a sudden surge of energy deposition ( $F \geq 2.6 \text{ mJ/cm}^2$ ) into the crystal completely destroys the intermediate incommensurate transition or the signals are too weak and therefore buried in the background. Judging from the X-ray structural refinement studies [35, 37] on the crystal, lower atomic modulation amplitudes were reported for the incommensurate CDW phase. This means that the incommensurate CDW intensities are inherently weaker compared to those of the commensurate CDW phase. Only the fully suppressed commensurate CDW signatures could give rise to the emergence of the incommensurate phase's signatures.

### 3.3 Commensurate charge density wave formation in $1T$ -TiSe<sub>2</sub> single crystals

As mentioned earlier,  $1T$ -TiSe<sub>2</sub> single crystal is at the early phase of characterisations, with the ultimate aim of using time-resolved electron diffraction to investigate the dynamics of its charge density wave signatures. Therefore, the simulated electron diffraction patterns and analysis presented here form a foundation for a better understanding and interpretation of the observable experimental electron diffraction patterns.

$1T$ -TiSe<sub>2</sub> is a quasi-two-dimensional transition metal dichalcogenide, which exhibits a second order phase transition at 202 K [5, 38].  $1T$ -TiSe<sub>2</sub> single crystal has a trigonal (or an hexagonal) lattice structure with unit cell parameters:  $a = b = 3.54 \text{ \AA}$ ;  $c = 6.008 \text{ \AA}$  and a space group:  $P\bar{3}m1$ , at room temperature [5, 54]. The crystal structure of  $1T$ -TiSe<sub>2</sub> is mono-layered, whereby each titanium atom is octahedrally coordinated by six selenium atoms, as shown in Figure 3.10. Unlike the  $4H_b$ -TaSe<sub>2</sub> that was described in the preceding section,  $1T$ -TiSe<sub>2</sub> crystal structure has two independent atoms comprising one titanium and one selenium atoms per unit cell. The configuration of the layered sheets also follows: Se-Ti-Se in a three-thick slab manner. At phase transition temperature (202 K) the unit cell is doubled, leading to a superstructure of dimension,  $2a \times 2a \times 2c$  [5, 38], as shown in Figure 3.10 (c).

The atomic sheets of the group IVb compounds (e.g TiSe<sub>2</sub>, ZrSe<sub>2</sub>, HfSe<sub>2</sub>) are held together by a weaker van der Waal's force of attraction, when compared to those obtainable in the group Vb transition metal dichalcogenide compounds (e.g  $4H_b$ -TaSe<sub>2</sub>,  $1T$ -TaSe<sub>2</sub>,  $1T$ -TaS<sub>2</sub>) [38, 54]. Conversely, the covalent bonds between the constituent atoms of the group IVb compounds usually mediate a stronger correlation between the  $p$ -band of the chalcogen atoms and the  $d$ -band of the transition metals, relative to those found in group Vb compounds. From the electronic point of view, the small indirect overlap between the Se valence  $s/p$  band and the Ti  $3d$  band along the high symmetry points ensures that  $1T$ -TiSe<sub>2</sub> single crystals are narrow band semiconductors, as investigated using STM [38] and photo-electron spectroscopy [5, 55]. In the angle resolved photoelectron spectroscopy measurements performed by Wiesenmayer *et al.* [55], it was proposed that the backfolding of the Se  $4p$  band, which lies below the Fermi energy level, and the decay of electron density population in the unoccupied states of Ti  $3d$  band drive the  $2a \times 2a \times 2c$  superlattice CDW formation at low temperature.

The origin of and/or the driving force behind charge density wave formation in  $1T$ -TiSe<sub>2</sub> crystal is rather controversial and has received several interpretations, stemming from different experimental measurements and theoretical calculations [5, 38, 52, 53]. Nevertheless, the CDW instability in this crystal was proposed to be driven by one of band-Jahn-Teller distortion and excitonic model (in which the hole carriers in the  $p$ -band of the selenium atoms pair with the electron carriers in the  $d$ -band of the titanium atoms) [5, 36, 54]. Di Salvo and co-workers [36] believed that electron-hole couplings (excitonic model) should be the driving factor leading to

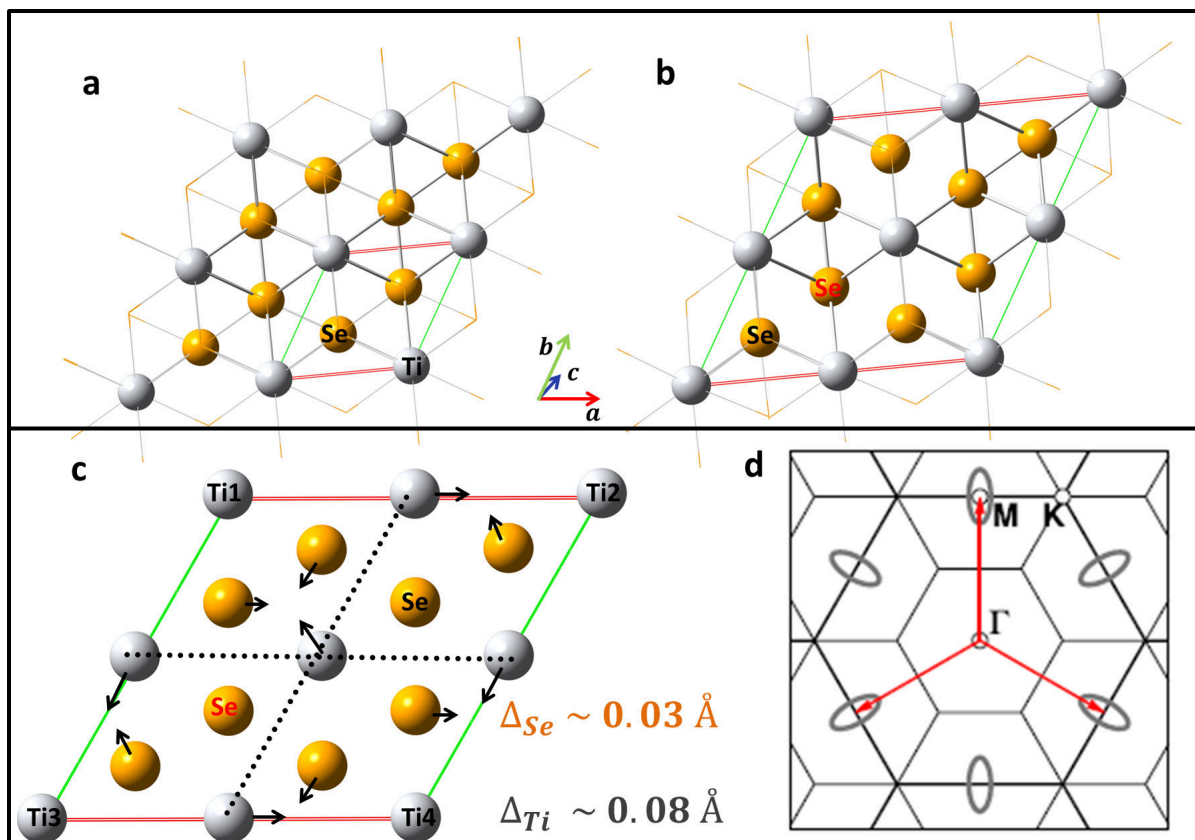


Figure 3.10: Crystal structures of  $1T$ - $\text{TiSe}_2$  showing (a) the unit cell at room temperature, (b) the doubling of the unit cell at phase transition temperature (202 K), (c) the modulation of the constituent atoms to form the superstructure lattice at and below phase transition and (d) the Brillouin zone's schematics [5] together with the high symmetry points and charge density wave vectors (red arrows) along the  $b \perp a$  plane ([001] zone axis). In (a) only the titanium and the selenium atoms highlighted are needed for the room temperature diffraction pattern simulation. In (b) an upper selenium atom (in red) and a lower selenium atom (in black) are highlighted; one of each serves as reference unmodulated atoms during phase transition as shown in (c). Altogether, seventeen (17) atoms comprising unmodulated four (4) titanium and two (2) selenium atoms are shown in (c) to form the superstructure (with dimension  $2a \times 2a \times 2c$ ). Shown on the figure are the modulation amplitudes for selenium and titanium atoms at 77 K, as determined by neutron diffraction structural refinement [36].

the formation of commensurate CDW in  $1T$ - $\text{TiSe}_2$ . This proposition is founded on the mode of atomic clustering (see Figure 3.10 (c)) and the shortening of the covalent bonds between the titanium and the selenium atoms. More recently Porer *et al.* [56] found that a coupling between a persisting periodic lattice distortion and excitonic correlations, among other charge density wave order parameters, provides a profound insight into the dynamics of charge density wave signatures in  $1T$ - $\text{TiSe}_2$  single crystals.

Based on the neutron diffraction structural refinements done and reported in Refs. [36, 52, 57], the high and the low temperature phases' electron diffraction patterns (EDP) are simulated for  $1T$ - $\text{TiSe}_2$  single crystals, as respectively shown in Figure 3.11 (a) and (b), together with the corresponding experimental EDP ((c) and (d)). The signatures of  $1T$ - $\text{TiSe}_2$  real space hexagonal structure are revealed through hexagonal intensity distribution of Bragg reflections in the reciprocal space. The intensity distribution obtained by using the lower symmetry ( $P3c1$ ) proposed for the low temperature phase [54], led to the rotation of the main Bragg peaks, which was not consistent with what was observed in the corresponding experimental EDP. Furthermore,

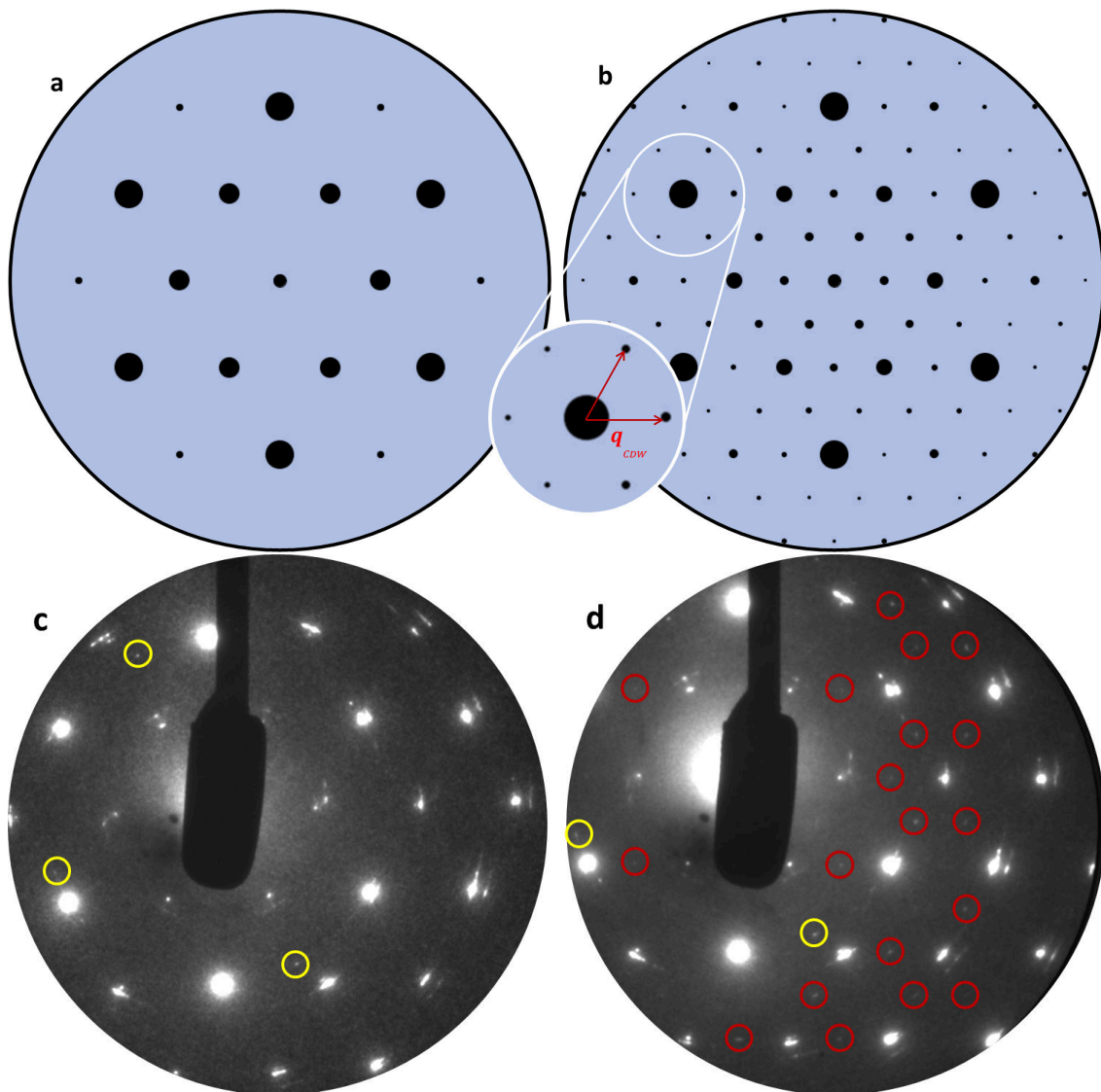


Figure 3.11: Electron diffraction patterns obtained for the metallic and the commensurate CDW phases in  $1T$ - $\text{TiSe}_2$  single crystals. The simulation shown in (a) and (b) (at  $T = 298$  K and  $T = 77$  K, respectively) were based on neutron diffraction structural refined atomic coordinates and the modulation amplitudes shown in Figure 3.10 (a) & (c). The symmetry of the high temperature phase shown in (a) and (c) was proposed to be lowered from  $P\bar{3}m1 \rightarrow P\bar{3}$ , as the crystal undergoes phase transition. Designated by the red rings, only some of the CDW signatures are observed at  $T = 85$  K in the experimental electron diffraction pattern as shown in (d). The CDW amplitudes are relatively weak compared to those obtained in the simulation, possibly due to cooling effect on the sample. Shown in the inset of (b) are six commensurate CDW signatures coordinated by a central host lattice Bragg reflection; with the vector  $\mathbf{q}_{\text{CDW}} = 0.5\mathbf{a}^*$ . The reflections designated by yellow circles in (c) and (d) are attributed to inelastic scattering, arising from interstitial or defect sites.

the simulated EDP obtained from using  $P\bar{3}c1$  symmetry was not consistent with the expected  $2 \times 2 \times 2$  commensurate CDW formation predicted by neutron diffraction structural analysis and the STM measurements [36, 38, 54]. After modulating the atomic positions, the Gaussian software [29] we used to manipulate atomic positions constrained the  $1T$ -TiSe<sub>2</sub> superstructure to  $P\bar{3}$  symmetry, which is classified as a subgroup of  $P\bar{3}m1$ . The simulated diffraction patterns obtained by using  $P\bar{3}$  symmetry was found consistent, both with commensurate CDW analysis and the observable experimental Bragg reflections' intensity distribution.

Different Bragg reflection amplitudes but same intensity distribution are observed in both the simulated and the experimental EDP. The difference in the amplitudes again is due to different intensity scaling in both simulation and experiment. Characteristically for TMD crystals, the strengths of the inner and the outer six Bragg reflections depend on how strong the orbital overlaps between the Se  $p$ -bands and the Ti  $d$ -bands are. In other words, the strength of the overlap of the  $p$ - $d$  bands (hybridised orbitals) of the constituent atoms determines the population of electronic density of states in  $1T$ -TiSe<sub>2</sub>, as is the case for other TMD crystals. The population of the density of states translate to the scattering capacities of the titanium and selenium domain sheets, which eventually influence the observable or obtainable Bragg reflections in the reciprocal space.

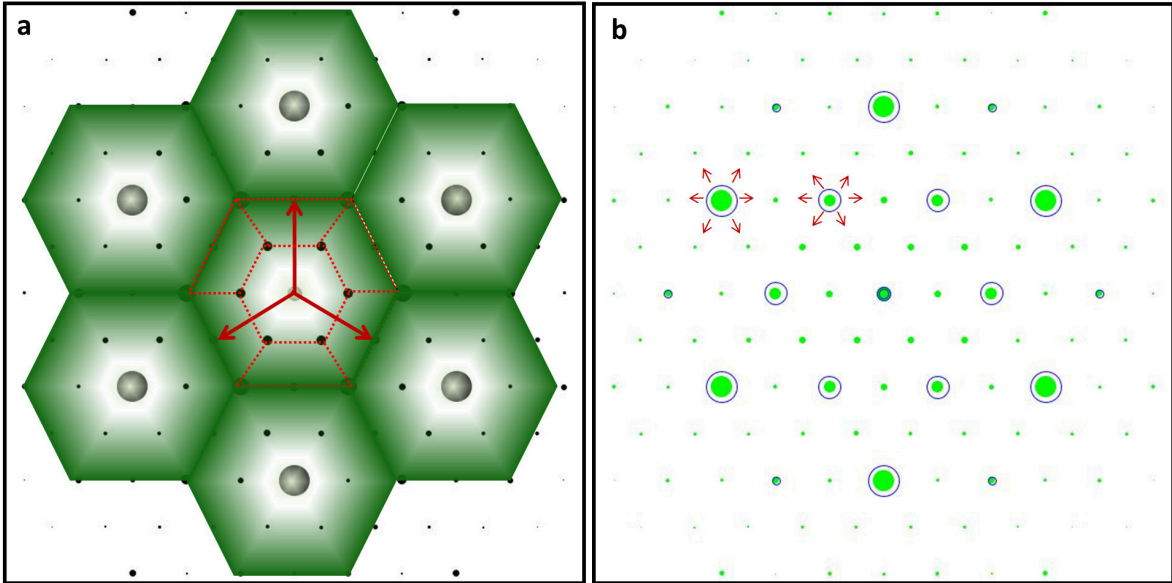


Figure 3.12: Electron diffraction simulation models for CDW transport and/or formation in  $1T$ -TiSe<sub>2</sub> single crystals. Plotted in (a) is the commensurate CDW phase (77 K) electron diffraction spots, together with the Brillouin zones (compare with Figure 3.10 (d)). The red arrows shows the CDW vector along the high symmetry points. In panel (b), the metallic phase (298 K) electron diffraction patterns are overlapped with the commensurate CDW phase's. This model shows that the population of the CDW density of states are mediated or driven by the reduction of the density of states of the host lattice Bragg reflections. Strong electron-hole couplings due to domain and/or band overlaps are envisaged (see text for more detail).

We find that the commensurate CDW transport around the first and second order reflections (from the innermost ring to outer rings) depends on either the intensity drop of all reflection orders or of alternating reflection orders, as shown in Figure 3.12 (b). The population of the density of states from which the CDW signatures arise is principally influenced by the interstitial defects and the extra titanium sites associated with  $1T$ -TiSe<sub>2</sub> single crystals [36, 54]. Therefore, the strengths of each experimentally observable Bragg and CDW signal are influenced by these

defect sites. As expected from a  $2 \times 2 \times 2$  superlattice, there is a CDW signature between every two host lattice Bragg reflections; so that six CDW signatures surround each Bragg reflection.

Recently, Ishioka *et al.* [54] found that CDW transport in  $1T$ -TiSe<sub>2</sub> arises from chiral (anticlockwise and clockwise) domains, at and below phase transition temperature, through STM measurements. In analogy to the intertwined domains found in other TMD crystals, these chiral domains each have three reflection signatures, whose intensities decrease clockwise and anticlockwise. Each of the three CDW reflections arising from the clockwise domain have a Friedel counterpart arising from the anticlockwise domain (CDW reflections with labels "1, 2, 3" have Friedel pairs in those with labels "4, 5, 6", as shown in Figure 3.13). The reduction in the electronic density population corresponding to each Bragg reflection could thus be conceived to mediate the transport of CDW signatures across the scattering domains of  $1T$ -TiSe<sub>2</sub> crystals. In other words, electrons are removed from the populated regions to the unpopulated regions. As shown in Figure 3.12 (a) and (b), the population of density of states for every CDW signature is contributed by two neighbouring host lattice Bragg reflections, which as a direct consequence points to the existence of strong orbital or band or domain overlaps. Moreover, since the structural transition is followed by semi-metal – semi-metal electronic transition, the CDW signatures thus formed could be adjudged to be driven by strong electron-hole couplings.

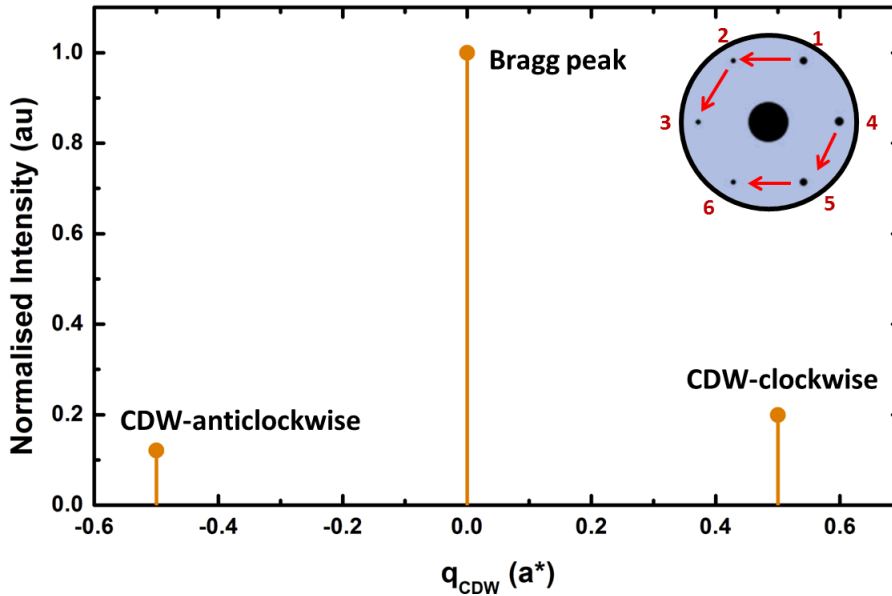


Figure 3.13: Plotted are the normalised calculated intensities of the host lattice Bragg reflection and the average signal strengths for CDW signatures in  $1T$ -TiSe<sub>2</sub> single crystals. The CDW signatures are categorised and averaged into clockwise and anticlockwise chiral domains (CDWs labelled 1 – 3 have Friedel pairs in those with labels 4 – 6). The CDW signatures decrease in both direction as shown in the inset. As compared to the host lattice Bragg peak, the average CDW signal strength for both domains are respectively 12.1% and 19.9%. The x-axis is plotted in the units of  $\mathbf{a}^*$  to show CDW vectors  $\mathbf{q}_{\text{CDW}} = 0.5\mathbf{a}^*$ .

Relative to the host lattice Bragg reflections, the strength of the CDW signals arising from each chiral domain in  $1T$ -TiSe<sub>2</sub> could also be estimated as we did for  $4H_b$ -TaSe<sub>2</sub> crystals in the preceding section. A line profile was taken across each Friedel pair (1&6, 2&5 and 3&4; see Figure 3.13), giving rise to three CDW signal strengths each of chiral domains. These are averaged and plotted alongside the host lattice Bragg reflection, which coordinates the six (labels 1 – 6 in Figure 3.13) CDW signatures. It is found that the average intensities for the

anticlockwise and clockwise domains are respectively 12.1% and 19.9% of the host lattice Bragg reflection. The initial experimental characterisation of  $1T$ -TiSe<sub>2</sub> crystals reveals that the optical excitation density required to totally suppress the CDW signatures is 1.3 mJ/cm<sup>2</sup> [59].

The average CDW signal strengths in  $1T$ -TiSe<sub>2</sub> are in the same order as those estimated for  $4H_b$ -TaSe<sub>2</sub> crystal, whose commensurate CDW phase exists at room temperature. The commensurate CDW phase temperature window (410–75 K) for  $4H_b$ -TaSe<sub>2</sub> afforded a lesser complication in ultrafast electron diffraction experimental set up, as against ( $\leq 202$  K) for  $1T$ -TiSe<sub>2</sub> due to the introduction of cooling processes when investigating metallic-to-CDW structural transition. First, the cooling effects introduce water condensation on  $1T$ -TiSe<sub>2</sub> crystal sample during experiment. This affects the overall quality of the obtainable diffraction patterns. The strength of the Bragg reflections and the resulting CDW peaks at low temperature are significantly influenced by the pronounced background in the images shown for experimental diffraction patterns. Moreover, the nature of electronic transition in  $1T$ -TiSe<sub>2</sub> single crystals, the relatively weak van der Waals force holding together the layers of the crystals and the crystal contraction during cooling, might well affect the observation of the six CDW signatures surrounding each of the host lattice Bragg reflections, as was observed in  $4H_b$ -TaSe<sub>2</sub> CDW phase (compare Figure 3.3 (d) and Figure 3.11 (d))<sup>1</sup>.

### 3.4 Closing inferences

Structural transitions in two classes ( $4H_b$ -TaSe<sub>2</sub> and  $1T$ -TiSe<sub>2</sub>) of transition metal dichalcogenide (TMD) single crystals have been studied by the means of electron diffraction simulations for the first time. The commensurate CDW phase in  $4H_b$ -TaSe<sub>2</sub> single crystals was simulated using atomic coordinates refined at room temperature. The CDW parameters were estimated as:  $\mathbf{q}_{\text{CDW}} = 0.277\mathbf{a}^*$  and  $\mathbf{q}_{\text{CDW}} \angle \mathbf{a}^* = 13.9^\circ$ . The characteristic charge depletion and charge localisation associated with structural transition in  $4H_b$ -TaSe<sub>2</sub> point to strong electron-phonon couplings due to Mott localisation charge distribution, which was proposed in literature to be the driving factor behind CDW formation. Anchored on the analysis of electron diffraction patterns obtained through simulation, two satellite domains containing two reflection orders each were identified in the commensurate CDW phase of  $4H_b$ -TaSe<sub>2</sub>. This was then used to analyse structural evolution of the decoupled satellite domains, according to two zones: 1:6:6 and 1:3:3:3:3. The temporal evolutions of the identified satellite domains were fitted to the same time constants:  $\tau_{\text{coh}} = 140$  fs and  $\tau_{\text{incoh}} = 550$  fs. These time constants are reminiscent of strong electron-lattice correlations in condensed matter systems. The degree of suppression of the two satellite domains increases with an increasing optical excitation density. Relating to the observed separation between the CDW domains' amplitudes, it was shown that CDW amplitude modes dominate over the corresponding phase modes.

The charge density wave phase of  $1T$ -TiSe<sub>2</sub> single crystals required sample cooling down below 202 K (phase transition temperature). The cooling effects introduced new challenges<sup>2</sup> such as water condensation on the crystal sample. Together with other intrinsic properties of  $1T$ -TiSe<sub>2</sub> single crystals (e.g. the weak van der Waal's attractive force holding the crystal layers together), the condensation affected the number and the quality of CDW signals experimentally observed<sup>3</sup>. The analysis revealed that the CDW transport was mediated by the "collapse" or reduction in intensity of the host lattice Bragg reflections. Each CDW density of state was

<sup>1</sup>The details of the initial characterisations, sample preparation, experimental measurement and analysis are reported by Aminat Suleiman in her Masters' thesis [59].

<sup>2</sup>The initial solution to these challenges was pumping (or blowing) off the water condensation by the means of a 775 nm laser pump. This improved the signal-to-noise ratio but we could still not resolve all the obtainable CDW signatures, as in the simulation.

<sup>3</sup>The grand solution proposed is a rather robust new vacuum chamber, with  $\sim 10^{-9}$  mbar and better sample

populated by electron transport from two neighbouring host lattice Bragg spots, such that six CDW signatures surround every Bragg reflection. Apriori to electronic transition (semi-metal – semi-metal), electronic band calculations, ARPES measurements and the more recent terahertz measurements [5, 54, 55, 58, 56], in addition to the simulation analysis done here, we propose that the CDW phase in  $1T$ -TiSe<sub>2</sub> single crystals is driven by a combination of strong band overlaps and electron-hole couplings (excitonic correlations).

We shall now report on Cu-DCNQI salts in the remaining chapters of this dissertation. Since the investigation of structural dynamics in Cu-DCNQI salts is a major part of this study, and for the fact that they are relatively complex organic crystals, we shall first of all consider the general perspectives on organic molecular crystals in relation to phase transition. Electron diffraction analysis on Cu-DCNQI salts will then be presented in Chapter 5.

---

loading systems. This should prevent water condensation and other complications. Bart Smit and Andrea Rohwer, who were Master students and colleagues, have carefully outlined the details of the improvements proposed, ranging from sample preparations, sample mounts, to the design and running of the new vacuum chamber in their theses [13, 85].

## Chapter 4

# General perspectives on the radical anion organic salts of Cu-DCNQI

### 4.1 Introduction to organic molecular crystals

Organic molecular crystals form one aspect of the exotic materials that have attracted the interest of many researchers in Condensed Matter Physics, with increasing volume of research outputs in the last two decades. Organic crystals have phenomenal characteristics stemming from wide varieties of atomic and/or molecular substitutions. More fascinating are the organic crystals whose structures contain  $\pi$ -conjugated compounds. Whereas the delocalisation of  $\pi$ -electrons in these crystals affords a rich flow of free conduction electrons, the different substitution possibilities, in addition, usually lead to increased anisotropic electric conductivities. Furthermore, the presence or inclusion of transition metals, usually characterised by strongly correlated  $d$ -electrons, produces intriguing structural dynamics in organic molecular crystals. Ranging from molecular electronics to light harvesting applications, organic crystals could be used as insulators, semiconductors, metallic conductors and superconductors (with anisotropic electric conductivities in the order of  $10^{-14} - 10^8 (\Omega \text{ cm})^{-1}$ ), especially in the low temperature range [60].

The degrees of electric conductivity in organic crystals are often mapped with the rate of charge transfer, arising from either weak or strong donor-acceptor crystal conformations [11, 60]:

$$\psi_o = a\psi_{DA} + b\psi_{D^{+\delta}A^{-\delta}} \quad \text{and} \quad [D] + [A] \rightarrow [D]^{+\delta} + [A]^{-\delta}, \quad (4.1)$$

where  $\psi_o$  is the charge-transfer ground state wave function,  $D$  and  $A$  respectively represent donor and acceptor,  $b \gg a$  connotes a strong charge transfer and  $0 \leq \delta \leq 1$  is the ratio of charge transfer. Usually, the donor has a low ionisation energy ( $I_G$ ) and the acceptor has a high electron affinity ( $A_G$ ) so that the Madelung energy (i.e., the energy of the charge transfer bonding),  $E_M > |I_G - A_G|$  [60].

The metallic character (or conductivity) of organic crystals depends on the mode of stacking of the donor and acceptor along a unique axis of the crystal structure. As shown in Figure 4.1, an organic crystal with mixed stacking of the donor and the acceptor moieties could either be an insulator or a semiconductor while the ones with separate stacking possess a partial electron transfer, which affords them to be either a semiconductor or a metal. Approximately, if the attractive Coulombic interaction is greater than the intermolecular forces between the stacks, then the mixed stacking state is favoured and vice-versa [60].

With the discovery and synthesis of the first stable radical-ion organic molecular crystal TTF-TCNQ (tetrathio-fulvalene-tetracyano-quinodimethane) in the early 1970s [60, 61], where TTF acts as a donor and TCNQ as an acceptor, the interest in organic conductors has received a great attention from chemists and physicists alike. TTF is especially a good donor of electrons,

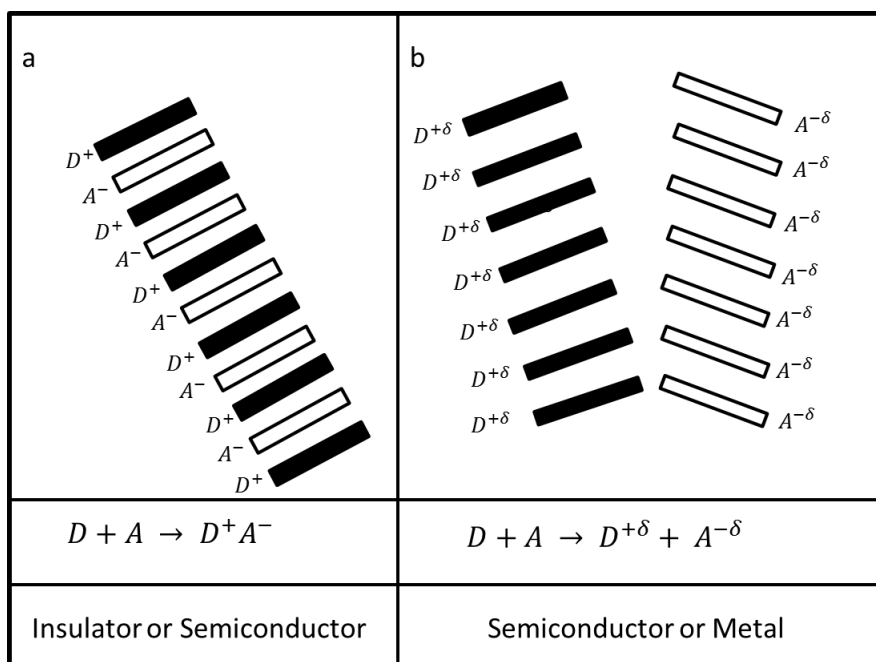


Figure 4.1: Schematic diagram [60] of donor-acceptor (a) mixed stacking and (b) separate stacking modes. Organic crystals could take on any of these stacking modes depending on the balance of intermolecular forces within the stacks. As shown in (a) and (b), the angles between the donor (D) and acceptor (A) could be zero in the mixed stacking mode; the donors and acceptors of the separate stacking mode are often inclined at a certain angle to each other – this inherently influences the rate of charge transfer in organic crystals [60].

which has been combined with different acceptors such as in  $(\text{EDO-TTF})_2\text{PF}_6$  [6, 60, 62] and TTF-TCNQ [61]. For example, the rate of charge transfer in TTF-TCNQ crystal was found to be  $\delta = 0.59$  (leading to mixed valence states) and its electric conductivity rising from two to four orders of magnitude when cooled from room temperature to about 66 K [60]. A smaller charge transfer rate (with  $\delta = 0.5$ ) was found in the radical-cation crystal salts of  $(\text{Fa})_2\text{PF}_6$  (Di-fluoranthene-hexafluorophosphate) [60].

The morphology of most of these organic crystals is often in 1-D, so that a first order phase transition due to Peierls instability is inherent, and their structural evolution when cooling or heating can thus be followed by a time-resolved femtosecond electron diffraction. Such mapping of molecular motion with femtosecond electron diffraction has been done for  $(\text{EDO-TTF})_2\text{PF}_6$  recently by Gao *et al.* [6]. In a similar fashion, the structural dynamics in TTF-TCNQ has also been characterised by time-resolved X-ray diffraction [63]. The successes [7, 9, 10, 12] of the investigation of time-resolved structural dynamics in two members of transition metal dichalcogenides, one of which was reported in Chapter 3 create a viable platform to investigate more complex crystals in our research group.

The main organic crystals studied in this work are the radical anion crystal salts of  $\text{Cu}[2, 5\text{R}_1, \text{R}_2 - \text{DCNQI}]_2$  (e.g.  $\text{Cu}[2, 5\text{DMe} - \text{DCNQI}]_2$ : Copper, 2,5-dimethyl-dicyano-quiononediimine), which have higher degrees of electric conductivity and charge transfer compared to other organic crystals. We can in no way exhaust all the interesting properties that had been investigated in these crystals; therefore, some highlights of interest relating to the purpose of this study are given here. The rest of this chapter shall thus be on the general perspectives of DCNQI salts, highlighting the crystal structures, energy band diagram in relation to electron density distributions, electric conductivity and a case for reduced dimensionality leading to phase transition accompanied with charge wave formation in  $\text{Cu}[2, 5\text{R}_1, \text{R}_2 - \text{DCNQI}]_2$ .

## 4.2 Organic molecular crystals of dicyanoquinonediimine (DCNQI) salts

**Crystal structure:** Organic molecular crystals of dicyanoquinonediimine (DCNQI) salts are radical anion salts, where DCNQI is the acceptor molecule and a metal is the donor (i.e.,  $M^{+\delta} DCNQI^{-\delta}$ ). For example, the copper salts are usually synthesised by the electrolysis of acetonitrile solution of 2,5-DMe-DCNQI and copper (II) bromide, which results in the formation of long black needles of  $Cu[2,5-DMe-DCNQI]_2$  at the cathode of the electrolytic cell [14]<sup>1</sup>. These crystals are famous for their high anisotropic electric conductivity, with up to eight orders of magnitude depending on the radicals and the metal used [14, 60]. The crystal structure of DCNQI salts, as shown in Figure 4.2 has many substitution possibilities, with different charge transfer rates and morphologies. The metal atoms are surrounded and tetragonally coordinated by four DCNQI molecules, with a slight distortion arising from the angle formed by the cyano groups (N-C-N) and the metal atom (see Figure 4.6). The crystal conforms to a body-centered tetragonal unit cell with  $a = b = 21.6062 \text{ \AA}$ ,  $c = 3.8811 \text{ \AA}$  and has a space group  $I4_1/a : 2$  (number:88) [60, 64].

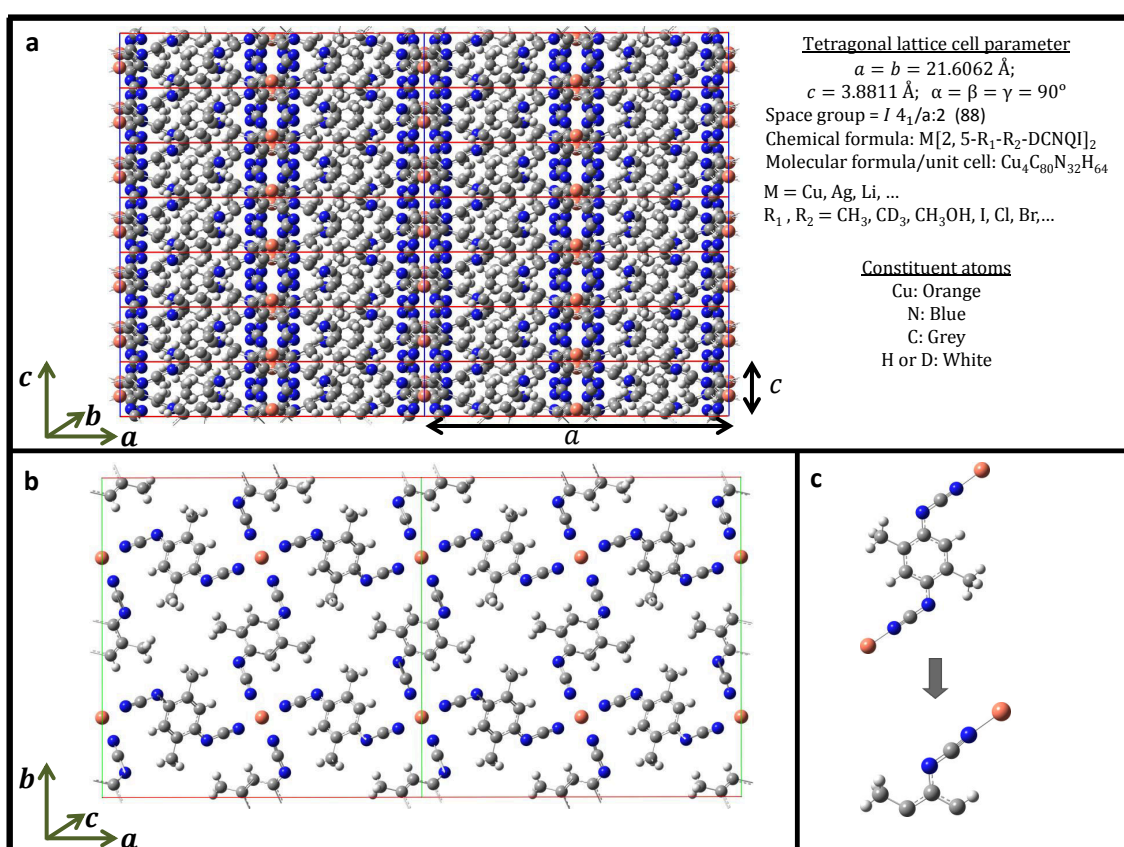


Figure 4.2: Crystal structure of Copper, 2,5-dimethyl-dicyano-quinone-diimine (DCNQI salt) projected along (a) [010] [ $c|a$  plane] and (b) [001] [ $a|b$  plane] Laue zones. The tetragonal unit cell dimension is  $a \times b \times c$ , with  $c$ -axis being the direction of stacking (or crystal growth) as shown in (a). The dimension ( $2a \times b \times c$ ) of the crystal structure is shown in both (a) and (b) to indicate the boundary copper atoms' positions, shared between adjacent unit cells. The asymmetry unit of the crystal structure is shown in (c) and reduced by symmetry operation to 12 possible minimum atoms, which are used in simulation.

<sup>1</sup>A full procedure of the synthesis and growing of DCNQI crystals could be found in [14] and [11].

A separate stacking mode of the DCNQI molecules (acceptor) and the metal atom (donor) is along the  $c$ -axis, which is the unique axis of the crystal structure. This stacking mode and the angle formed by the cyano groups are inherently responsible for an increase or a decrease in the electric conductivity of DCNQI salts [60, 64, 76]. Due to the balance between the intermolecular and Coulombic forces in the crystal system, each of the metal atoms and the nearly planar DCNQI molecules are usually shared by the adjacent unit cells along  $a$ - and  $c$ -axes (see Figure 4.2), so that four copper atoms are present in a 180-atom unit cell. The number of atoms in a unit cell could be  $\leq 180$ , depending on the radicals used to replace the hydrogen atoms at positions 2 and 5 of each of the DCNQI molecules. The different radicals that could be used are shown in Figure 4.2.

**Electronic band structure:** All organic salts of DCNQI are isomorphic (with a space group  $I4_1/a$ ) and exhibit metallic characters at room temperature [60, 64, 68]. The distribution of electron density in the highest occupied molecular orbitals (HOMO) of the DCNQI molecules forms the valence band, while the corresponding lowest unoccupied molecular orbitals (LUMO) forms the conduction band. The energy levels of the  $s$ -bands of the metal atoms (e.g. lithium (Li), silver (Ag) and copper (Cu)), commonly used as donors, are usually higher than the Fermi level and the LUMO band of the DCNQI, so that electron transfer is energetically favourable [66, 67, 68, 69]. Peculiar to all DCNQI salts is the transfer of one  $s$ -electron from the conduction band of the metal atom to the LUMO of DCNQI molecules.

The electronic band structures of DCNQI salts are generally reported to be dependent on the metal-type and the radicals (at the 2,5 positions of the DCNQI molecules) used [71, 72]. Both lithium and silver are monovalent 1-D metal (satisfying Peierls instability) and their electronic structures are not influenced by the choice of radicals. The degree of charge transfer in lithium and silver salts is  $\delta = 0.5$ , such that the conduction band of DCNQI is quarter-filled. In both metals one  $s$ -electron is transferred to and shared by two DCNQI molecules so that the Fermi wave-vector of the charge transfer in the  $k$ -space is thus  $2k_F$  or  $4k_F$  (with  $k_F = \frac{\pi}{4c}$ ). Both a  $2k_F$  spin (occurring at 83 K) and a  $4k_F$  (occurring at 100 K) Peierls instability have been found in these monovalent salts, where the formation of charge density wave leads to a phase transition from a metallic to a Mott-type insulating state (for silver salts) and a paramagnetic insulator in lithium salts [68]. In both salts, a four-fold periodicity or a tetramerisation of the unit cells is invoked when they undergo phase transition.

The electronic structures of copper salts are, however, influenced by the choice of radicals and the degree of electron transfer, pointing to a multidimensional conductor character and a 3D Fermi surface. As shown in Figure 4.4, there are more degenerate energy states when bromine was used as a radical, in comparison to the salt with a methyl radical. It is known that the degeneracy of energy states favours formation of a band gap, leading to a reduction in the dimensionality of the crystal system. It is therefore envisaged that the degree of degeneracies in Cu-DCNQI salts is influenced by the choice of radicals.

In addition to the transfer of one  $s$ -electron, a fraction of  $d$ -electron from the  $3d$  band of copper atoms could also be transferred, so that a mixed valency<sup>2</sup> was found in copper salts, with contributions from  $3d$  and  $4s$  electrons. The charge transfer rate from the conduction band of a copper atom to the LUMO bands of the DCNQI molecules was found to be  $\delta = 0.67$  ( $\frac{1}{3}d + 1s$  electrons =  $+\frac{4}{3}$  for two DCNQI molecules) [60, 69]. This mixed valence found in all copper salts enhances their density of states and gives rise to stronger electron-electron and electron-lattice correlations, better than in other DCNQI salts [76]. The wave vector of the charge density wave in the  $k$ -space for copper salts is  $3k_F$  (with  $k_F = \frac{\pi}{3c}$ ), and this leads to trimerisation (tripling) of the unit cell or a 3-fold periodicity below phase transition temperature.

<sup>2</sup>XPS was used to determine the mixed valency in copper salts [76].

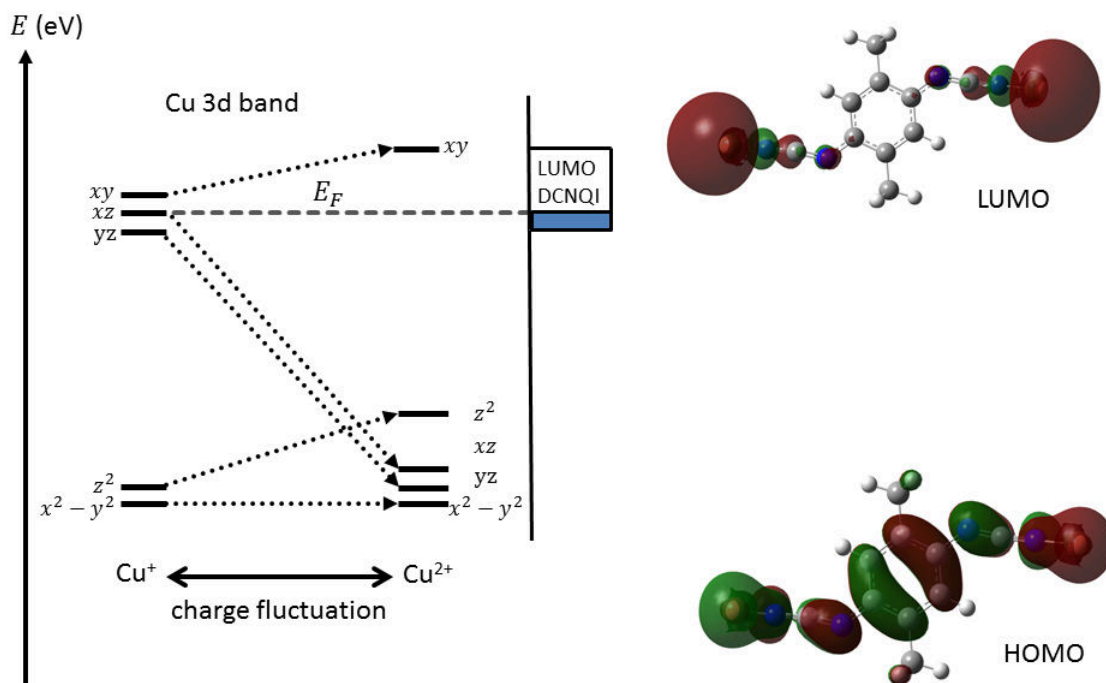


Figure 4.3: Schematics of the energy band splitting of copper 3d band, which necessitates a partial electron transfer from the copper atoms to the LUMO band of DCNQI molecules. The  $d-p$  orbitals of the copper atoms and the cyano groups are hybridised with  $\pi$ -orbital of the DCNQI at the HOMO level, but are disconnected and localised at the LUMO level and consistent with literature [64, 69, 71, 72]. The  $3d_{xy}$  band is raised during phase transition due to charge fluctuation between  $Cu^+$  and  $Cu^{2+}$ . At phase transition, a charge ordering state of the form,  $Cu^+Cu^+Cu^{2+}$  is induced, so that there is a 30% ( $Cu^+ : Cu^{2+} = 2 : 1$ )  $d$ -electron transfer from the copper sites. The total possible charge transfer can then be envisaged to be  $\frac{1}{3}d + 1s$  electrons =  $+\frac{4}{3}$  for two DCNQI molecules.

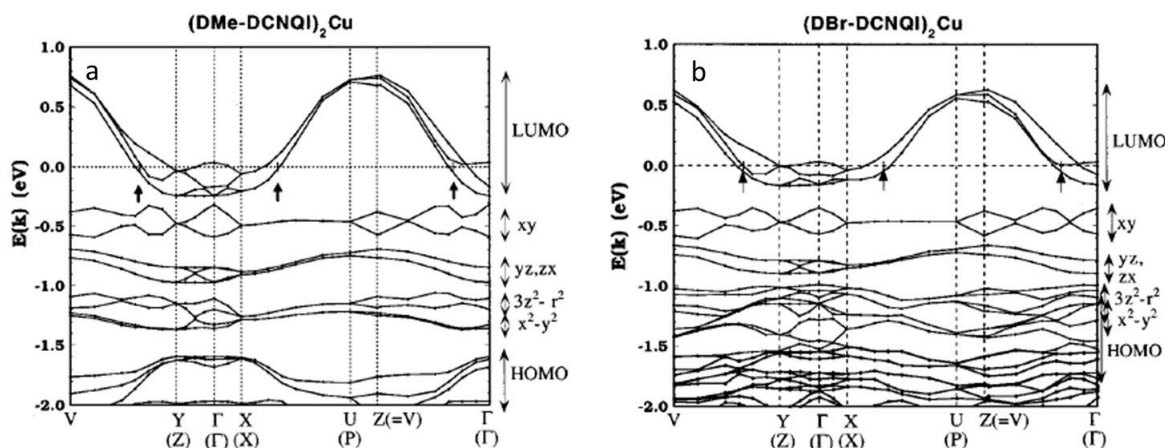


Figure 4.4: Plotted are the calculated electronic band structures [71] of (a)  $Cu[DMe-DCNQI]_2$  and (b)  $Cu[DBr-DCNQI]_2$  salts, along the high symmetry points. The arrows in both figures designate the positions of energy degeneracy (crossing the Fermi surface), which leads to the formation of band gap and a 3-fold periodicity of the charge density wave phase. The  $3d_{xy}$ ,  $3d_{xz}$  and  $3d_{yz}$  sub-bands have similar energy levels in both salts. Higher energy degeneracy found in  $Cu[DBr-DCNQI]_2$ , as compared to that of  $Cu[DMe-DCNQI]_2$ , favours phase transition with an accompanied charge density wave. The calculations were based on the room temperature structures obtained from X-ray structural refinements done by Sinzger *et al.* [64].

Furthermore, owing to the three dimensional nature of copper atoms, copper salts with methyl or lower electron radicals are metallic down to 3.5 K [65, 76], unlike in silver and lithium salts. Interestingly, the electric conductivity of the copper metal atom (about  $5 \times 10^8 \Omega^{-1}\text{cm}^{-1}$ ) is similar to that of  $\text{Cu}[2,5\text{-DMe-DCNQI}]_2$ , which continuously increases with a decreasing temperature ( $800 \Omega^{-1}\text{cm}^{-1}$  at 295 K to  $6 \times 10^6 \Omega^{-1}\text{cm}^{-1}$  at 3.5 K, see Figure 4.8) [14, 60].

One may then wonder if the copper atoms are the carriers of the free conduction electrons along the stacking axis of the crystal structure. This is not to be because (1) the average Cu-Cu distance (3.88 Å) along the *c*-axis of DCNQI salts is fairly greater than in Cu metal (2.56 Å) [14]; (2) the *d-p-π* hybridization of the copper atoms and the DCNQI molecules, which is evident in the metallic state (see Figures 2.4 and 4.3), is disconnected in the insulating phase and the erstwhile itinerant *d*-electrons are localised on the copper ion sites [69] and (3) the *photoconductive current* measurement recently done on selectively deuterated DCNQI salts (see Figure 4.5) by Karutz *et al.* [70] suggested that the carriers of the free electrons (conducting electrons) along the stacking axis are the delocalised  $\pi$ -electrons of the DCNQI molecules. This view was also supported in other references [14, 60, 69, 71]. The copper atoms were therefore suggested to be a *conductivity bridge* between adjacent unit cells along the stacks [14].

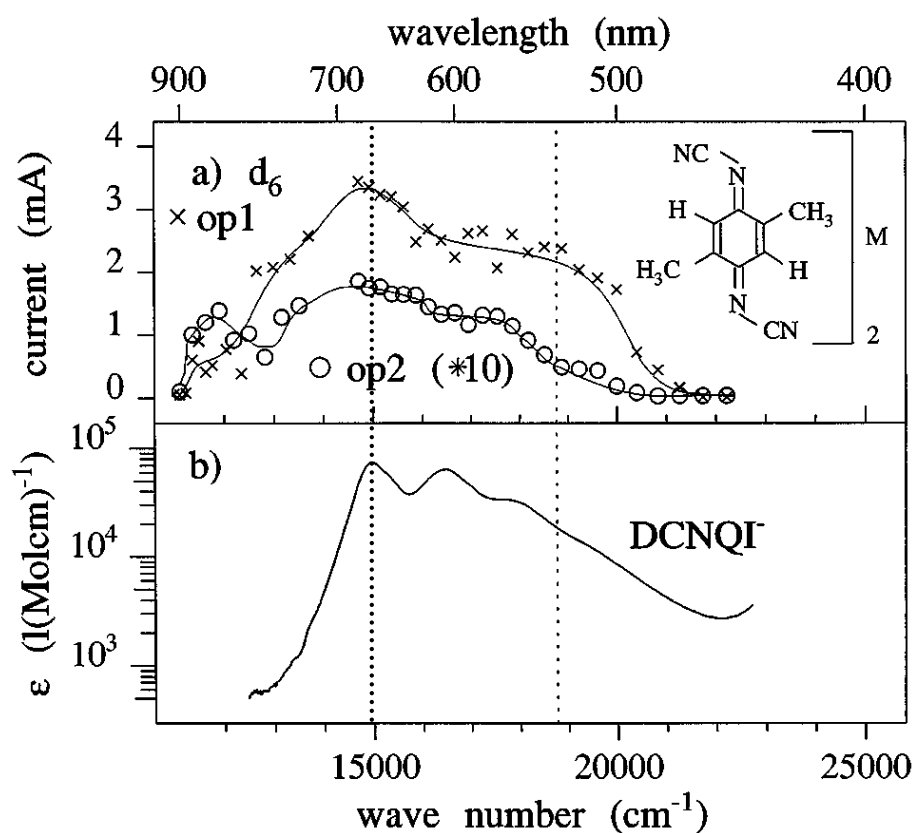


Figure 4.5: Plotted [70] in (a) is the transient photoconductive current measurement, showing the energy absorption range of a partially deuterated  $\text{Cu}[2,5\text{CD}_3\text{-DCNQI}]_2$  salt. The secondary band (maximum peak) of the absorption spectrum of the current measurement compares well to that of DCNQI molecule anion shown in (b), which ultimately suggests that DCNQI  $\pi$ -orbitals are the free conduction electrons' carriers. The vertical dotted lines around  $15000\text{cm}^{-1}$  and  $19000\text{cm}^{-1}$  respectively serve as a guide between peaks and laser output of the experiment. The measurement was done through two operating points op1 and op2. Figure taken from Ref. [70].

### 4.3 Phase transitions and charge density wave formation in $\text{Cu}[2,5\text{R}_1,\text{R}_2\text{-DCNQI}]_2$ salts

Organic molecular crystals of DCNQI salts are quasi metallic above phase transition temperature. The non-copper (Li & Ag) salts are highly one-dimensional and thus undergo phase transition that is closely related to Peierls instability. Copper salts are three-dimensional due to the three-dimensional morphology of copper atoms, and therefore do not naturally undergo phase transition. Since the geometry and the nesting of 3D Fermi surface highly favours 3D solids to remain metallic, even at very low temperature, no charge density wave formation is expected. Given that a ligand-induced distortion imposed on the planarity of a crystal system often favours Peierls instability leading to phase transitions; it is then surprising that the steric effect that the methyl groups in  $\text{Cu}[2,5\text{DMe-DCNQI}]_2$  imposed on the tetragonal coordination could not induce the Jahn-Teller distortion<sup>3</sup> [78] necessary for phase transition in  $\text{Cu}[2,5\text{DMe-DCNQI}]_2$  crystals [64]. Thus, for a 3D crystal to undergo phase transition, say from metal to insulator, a geometrical distortion that facilitates a reduction in the crystal's dimensionality and the lowering of the whole crystal system's energy is required.

Reduced dimensionality has often been famed to be one of the reasons behind phase transition and charge density wave formation in crystal lattices [5, 12]. The quality of Fermi surface nesting is highest in 1D materials so that phase transition is easily induced, as compared to 2D and 3D solids [7]. Taking Peierls distortion as a theory that well describes phase transitions and that serves as the origin of charge density wave formation in quasi 1D metals, it is justifiable that one ventures to know what theory governs electron dynamics and/or charge density wave formation in higher dimensional solids. The quest to find a theoretical extension of Peierls instability for higher dimensional solids is ongoing [5].

Phase transitions accompanied with charge density wave formation in inorganic crystals of transitional metal dichalcogenides are well established in literature, all of which are quasi two-dimensional solids [5, 7, 10, 12]. The geometry of the 2D Fermi surface and a strong electron-phonon coupling in these materials, as well as lowering of crystal symmetry when undergoing phase transitions have been favoured to be the major factors that support charge density wave formation.

Recently, Lee *et al.* [73] found that a band gap opening in graphene is indeed due to the manifestation of two-dimensional Peierls instability, which was attributed to Kekule distortion. Their main discovery was that the band gap formation in graphene was as a result of *chiral symmetry breaking*. They further maintained that there was no such band gap when graphene was confined to 1D. This may emphasise that charge density wave naturally<sup>4</sup> forms in 2D solids undergoing phase transition, without converting them to 1D.

An interplay between the steric effects produced by different radical substitutions and the Jahn-Teller distortion on the tetragonal coordination (see Figure 4.6), however, induces a dramatic phase transition accompanied with charge density wave formation [64, 71, 74, 75, 76]. First observation of this phase transition involves different degrees of deuteration, that is replacing the hydrogen atoms by deuterium, and halogenation of the DCNQI crystals [64, 74, 76].

For the purpose of studying the effects of the choice of radical substitution on the planarity of the DCNQI ligands, as well as the electrostatic potential distribution, we carried out DFT calculations on the room temperature asymmetry structure of DCNQI molecules attached to copper atoms, as shown in Figure 4.7. The distribution of electron clouds projected on the

<sup>3</sup>Jahn-Teller effect (or distortion) is associated with the geometrical distortion, which arises from the electron configuration and transfer between the donor ion and the acceptor orbitals.

<sup>4</sup>The reader should note that not all solids undergoing phase transition are accompanied by charge density wave formation.

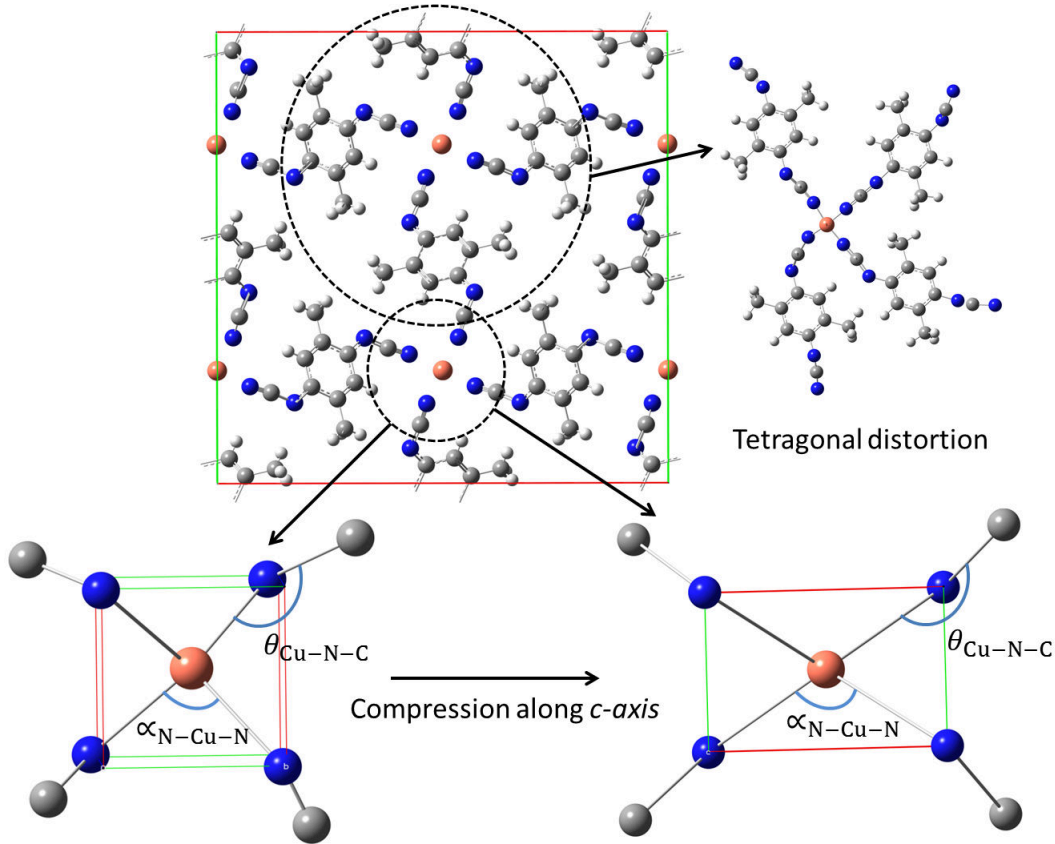


Figure 4.6: Schematics to illustrate the cooperative Jahn-Teller distortion and the dependence of coordinating angles on the tetragonal compression induced by cooling the crystals below phase transition temperature. The coordinating angle ranges as  $124.5^\circ \leq \alpha_{\text{N-Cu-N}} \leq 126.3^\circ$  and  $124.8^\circ \leq \alpha_{\text{N-Cu-N}} \leq 128.5^\circ$  (from 295 K to 20 K) in  $h_8$  ( $\text{Cu}[2, 5\text{DMe-DCNQI}]_2$ ) and  $d_6$  ( $\text{Cu}[2, 5\text{DCD}_3\text{-DCNQI}]_2$ ), respectively. The large deviation found in  $d_6$ , compared to the deviation found in  $h_8$ , was suggested to have led to a reduced dimensionality and hence phase transition. By the same token, the deviations (a decrease) in angle  $\theta_{\text{Cu-N-C}}$  were found to be  $-1.60^\circ$  and  $-1.30^\circ$  in  $h_8$  and  $d_6$  structures, respectively [60, 64].

Table 4.1: Effects of selected radicals on the planarity of the DCNQI ligands, the coordinating angle  $\alpha$  and the transition temperatures in DCNQI salts. Data on deuterated methyl ( $\text{DCD}_3$ ) were taken from Ref. [64]; where  $\Delta = \Delta_{20\text{ K}} - \Delta_{298\text{ K}}$ . All other data were taken from Ref. [65]; where  $\Delta = \Delta_{100\text{ K}} - \Delta_{298\text{ K}}$ . Phase transition occurs when the threshold value  $\alpha \approx 126.4^\circ$  at low temperature is exceeded [64].

R	$\Delta_{\text{N-C-N}}(^{\circ})$	$\Delta_{\text{C-N-C}}(^{\circ})$	$\alpha_{298\text{ K}}(^{\circ})$	$\Delta\alpha(^{\circ})$	$\Delta\theta_{\text{Cu-N-C}}(^{\circ})$	$\Delta c$ ( $\text{\AA}$ )	$\Delta a$ ( $\text{\AA}$ )	$T_{\text{M-I}}$ (K)
DMe	0.40	0.30	124.50	1.50	-1.60	0.070	-0.018	M
$\text{DCD}_3$	-	-	124.80	3.70	-1.30	0.098	-0.074	73
MeBr	0.70	0.20	125.30	2.90	-0.40	0.076	-0.026	156
MeCl	0.10	0.10	126.20	2.90	-0.30	0.078	-0.081	210
BrCl	0.70	0.00	126.10	3.00	-0.40	0.062	-0.114	210

electrostatic field contours across the asymmetry unit of DCNQI crystals reveals higher electron

density isovalues around the bromide radical, compared to the methyl radical (see Figure 4.7). Together with the literature data [64, 65] shown in Table 4.1, the results we obtained show that the radicals with higher cloud of electrons (MeBr, MeCl & BrCl) impose relatively the same amount of deformation to the crystal systems, especially in terms of the angles  $\alpha_{\text{N-Cu-N}}$  and  $\theta_{\text{C-N-Cu}}$ . The deformation is more intensive in the deuterated structure (with DCD<sub>3</sub> radical), having the highest deviation both in terms of angle  $\alpha_{\text{N-Cu-N}}$  and lattice parameter  $c$ , as shown in Table 4.1. The deviations recorded for angles  $\angle\text{N-C-N}$  and  $\angle\text{C-N-C}$  of the cyano groups contributed to the overall non-planarity of the DCNQI molecules, and these presumably govern the deviations observed in angles  $\alpha_{\text{N-Cu-N}}$  and  $\theta_{\text{C-N-Cu}}$ .

The structures with electron-rich radicals (MeBr, MeCl & BrCl) already possess high coordinating angles  $\alpha_{\text{N-Cu-N}}$  at ambient (or room) temperature, very close to the threshold value ( $\alpha \approx 126.4^\circ$ ) [64], and thus only need a slight deformation (less energy, less temperature decrease) to undergo phase transition. This inherently accounts for their high transition temperatures in comparison to the deuterated structure. From the electronic point of view the deuterated structure possesses electron donating radicals, which lengthen the overall delocalised crystal's electronic system. Thus, it could be inferred that the deformation leading to phase transition in the deuterated sample was mainly mediated by electron mass enhancement, as was proposed by Kobayashi *et al.* [76]. In contrast, the depletion of the density of states of the crystals' electronic system by the radicals having high electron affinities (such as BrCl and MeBr) would be seen to mediate phase transition and at higher transition temperatures.

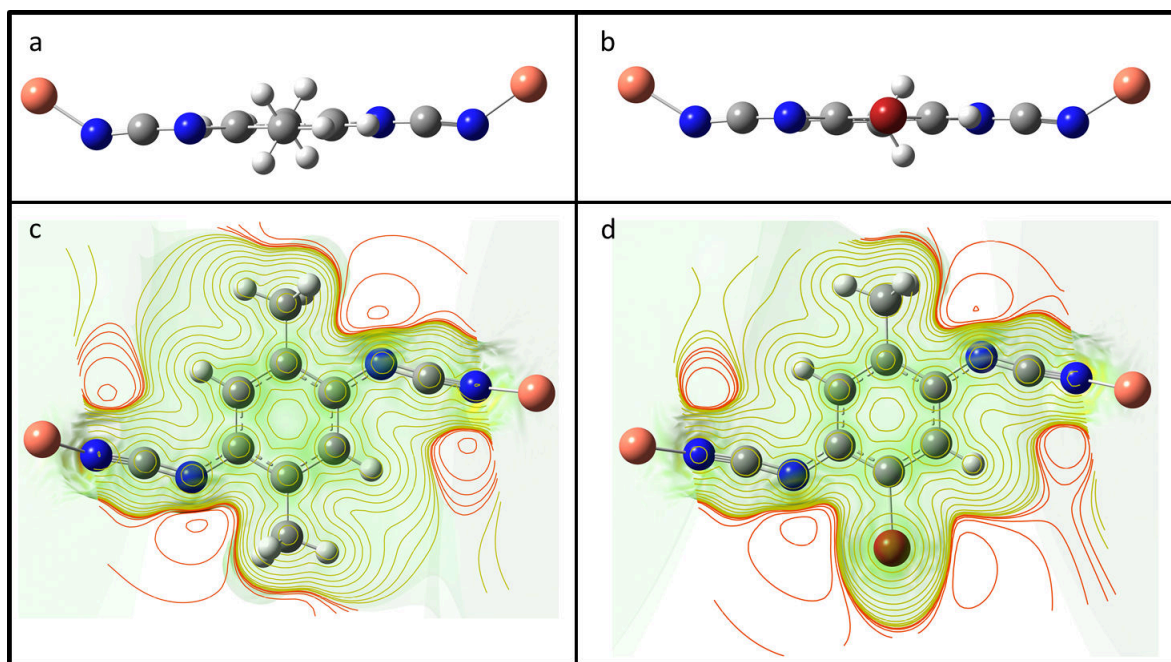


Figure 4.7: Calculated optimized structures [(a) & (b)] and mapped electrostatic potential [(c) & (d)] of the asymmetry units of  $d_6\text{-Cu}[\text{DMe-DCNQI}]_2$  and  $\text{Cu}[\text{MeBr-DCNQI}]_2$  salts, respectively. The planarity of both units are greatly influenced by the choice of the radicals, with MeBr radical posing a higher geometrical distortion on the cyano groups shown in (a) and (b). The cloud of electrons surrounding the bromine atoms is more intense than in methyl position, designated by different shading of the potential plots of maximum isovalue of  $4 \times 10^{-3} \text{ e}/\text{\AA}^3$ . The calculations are done using density functional (DFT) (B3LYP functional + CEP-31G basis set) and through Gaussian software [29].

A delicate balance between the use of radicals with high-electron cloud and low-electron cloud, however, seems to be a decisive factor in crystals undergoing phase transition with ac-

companied charge density waves. To corroborate this assertion, it was reported in [72] that the salts with iodide and methyl-iodide radicals do not undergo phase transition unless a pressure of 15 kbar is exerted. More surprising is the fact that a 2-fold rather than a 3-fold periodicity was found in  $\text{Cu}[2,5\text{DI-DCNQI}]_2$  under pressure, in contrast to other copper salts [72]. It should be noted that  $\text{Cu}[2,5\text{DMe-DCNQI}]_2$  also undergoes phase transition under much less pressure (150 bar) [64, 72, 74].

Four groups are identified in the Cu-DCNQI systems: Group 1 are metallic down to  $\sim 4$  K and comprises  $\text{Cu}[\text{DMe-DCNQI}]_2$  and  $\text{Cu}[\text{DMeO-DCNQI}]_2$ . Group 2 undergoes metal-insulator phase transitions and comprises  $\text{Cu}[\text{d}_N\text{-Me-DCNQI}]_2$  systems (d and N stand for dueteration and the number of hydrogen atoms replaced by deuterium, respectively). Group 3 undergoes metal-insulator transitions and comprises  $\text{Cu}[\text{mixed-radicals-DCNQI}]_2$  systems (here, the radicals used could simply be halogen atoms such as iodine (I), chlorine (Cl), bromine (Br), etc., or a mixture of halogen atoms and methyl radical as seen in  $\text{Cu}[\text{DI-DCNQI}]_2$ ,  $\text{Cu}[\text{MeCl-DCNQI}]_2$  and  $\text{Cu}[\text{MeBr-DCNQI}]_2$ ). Group 4 undergoes metal-insulator-metal phase transition and comprises the mixture of two groups forming an alloy, as seen in the mixture of a purely undeuterated  $\text{Cu}[2,5\text{DMe-DCNQI}]_2$  and a partially deuterated  $\text{Cu}[2,5\text{CD}_3\text{-DCNQI}]_2$  crystals [64, 70, 74].

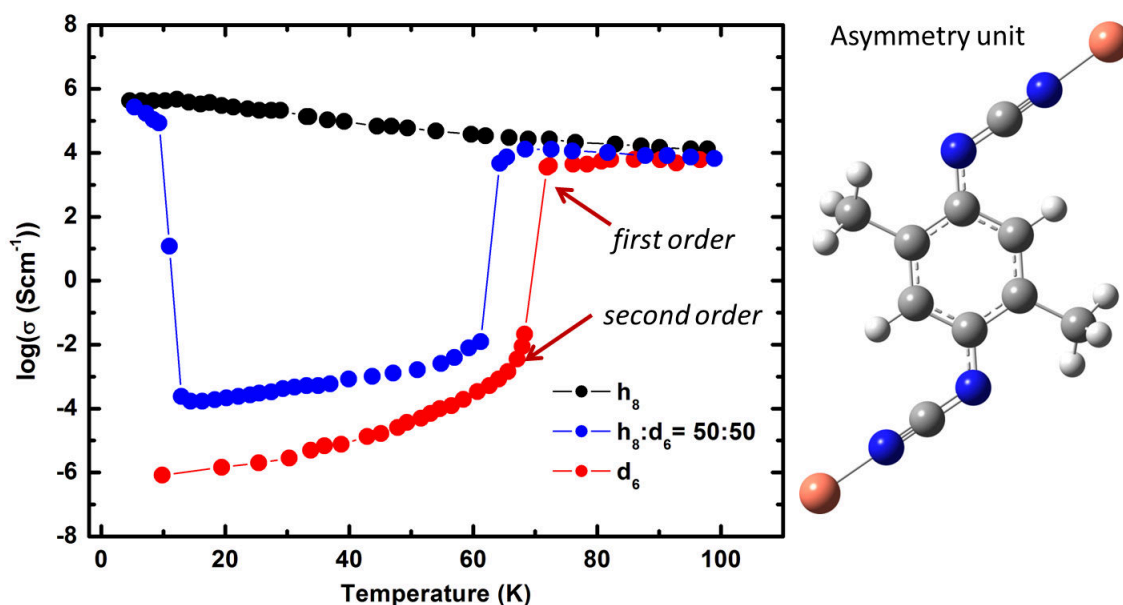


Figure 4.8: Plotted (data points extracted from Ref [77]) are the electric conductivities  $\sigma$  (log scale) versus temperature showing metal-insulator phase transitions in undeuterated ( $h_8$ ) and deuterated ( $d_6$ ) Cu-DCNQI crystals. As shown, each asymmetry unit of  $\text{Cu}[2,5\text{DMe-DCNQI}]_2$  crystals contains 8 hydrogen atoms that can be substituted for deuterium (hydrogen with mass number= 2). In the non-substituted  $h_8$  case the crystal remains metallic down to a very low temperature. At around 73 K  $d_6$  undergoes a combination of first and second order metal-insulator phase transitions – a character that is also evident in the alloy containing the equal mixture of  $h_8$  and  $d_6$  around 63 K. The alloy, however, gains an insulator-metal re-entrance at around 12 K.

The order or nature of phase transition occurring in Cu-DCNQI crystals could be inferred from the temperature dependent conductivity measurements performed by Hünig *et al.* [77]. A phenomenal sudden drop of up to 8 orders of magnitude within few kelvins in the electric conductivity of the groups exhibiting phase transition was generally reported [60, 77, 76]. A careful examination of the temperature dependent conductivity measurement shown in Figure 4.8 clearly reveals a mixture of first and second order phase transitions. Whereas the initial

sudden drop exhibits a first order phase transition character, the *continual* decrease of the electric conductivity suggests a "knee" transition, which is of second order character.

The phase transition temperatures for some of the different systems are given in Ref. [64]. Higher phase transition temperatures (in the range 156 – 230 K) are observed in group 3 systems (mixed-radicals) with higher electron density distribution across DCNQI sites, as compared to the group 2 systems (deuterated radicals) (in the range 58 – 82 K) [76, 64, 77].

Conclusively, three inferences could be made from the effects of radical substitutions: (1) Electron-mass enhancement and/or steric effects introduced by the radicals results in the increase of the coordinating angle  $\alpha$  (see Figure 4.6), thereby decreasing the phase transition temperature. (2) The free conduction electrons in the LUMO bands of DCNQI molecules may be *depleted* by the electron-withdrawing radicals (group 3 systems or simply halogen atoms). This depletion could then lead to high geometrical distortion, so that a phase transition is induced at higher temperatures, compared to electron-donating radicals (group 1 systems). (3) The probability of charge transfer from the donor to the acceptor is more enhanced when radicals with high electron affinities are used. By inference, we could then say that a low Madelung energy is required to induce phase transition, which by extension occurs at higher phase transition temperature.

We shall now examine the structural transitions in these crystals through simulation and analysis of electron diffraction patterns of both the room and low temperature phases. Judging from both the simulation and experimental perspectives, the formation and/or transport of charge density waves in the DCNQI salts will be analysed in the next chapter.

## Chapter 5

# Structural transition studies of Cu-DCNQI salts via diffraction analysis

### 5.1 Introduction

Approaching the investigation of structural evolution in organic molecular crystals through femtosecond electron diffraction (FED) experiment is somewhat subtle and challenging, thanks to the weak scattering centres, high thermal lability, poor heat conduction and the preferred stacking arrangements found in their crystal structures [6, 60]. To gain necessary insights required to unravel the structural dynamics in relation to electron-electron and/or electron-lattice correlations and phase transition accompanied with charge density wave formation in DCNQI crystals (Figure 5.1), we use electron diffraction simulation as a tool to study structural transitions via the analysis of obtainable ideal diffraction patterns under different conditions. There will always be a quantitative deviation when comparing experimental measurements with simulations. Therefore, we emphasise qualitative rather than quantitative treatments in the comparison and analysis of all diffraction patterns presented in this chapter. Kinematic scattering theory based on weak object phase approximation is employed for all the simulations, the foundation of which was treated in Chapter 2.

Charge density wave signatures in Cu-DCNQI are simulated and characterised for the first time in this study. A thorough and systematic analysis of structural transitions in the crystal is provided, together with different identified phases during cooling processes. Independently, X-ray diffraction measurements we did in collaboration with Chemistry Department, Stellenbosch University, which also revealed CDW signatures in  $\text{Cu}(\text{MeBr-DCNQI})_2$  at 90 K, are analysed and discussed. Finally, the reader is introduced to an evidence of CDW signatures in  $\text{Cu}(\text{MeBr-DCNQI})_2$  at 63 K, obtained for the first time via electron diffraction experiments in our laboratory. The chapter closes with an initial characterisation of the low temperature phase experimental electron diffraction patterns. The electron energy and the sample thickness used throughout this chapter are 30 kV and 30 nm, respectively.

### 5.2 Analysis of room temperature electron diffraction patterns in undeuterated and deuterated Cu-DCNQI salts

The room temperature crystal structures' electron diffraction patterns (EDP) presented here are simulated using the published X-ray structural refinement data [64, 65]. The unit cells of DCNQI salts are reduced by symmetry to 12 atoms, and the structurally refined atomic coordinates are written into crystallographic information files used for simulation. Since the crystal's growth

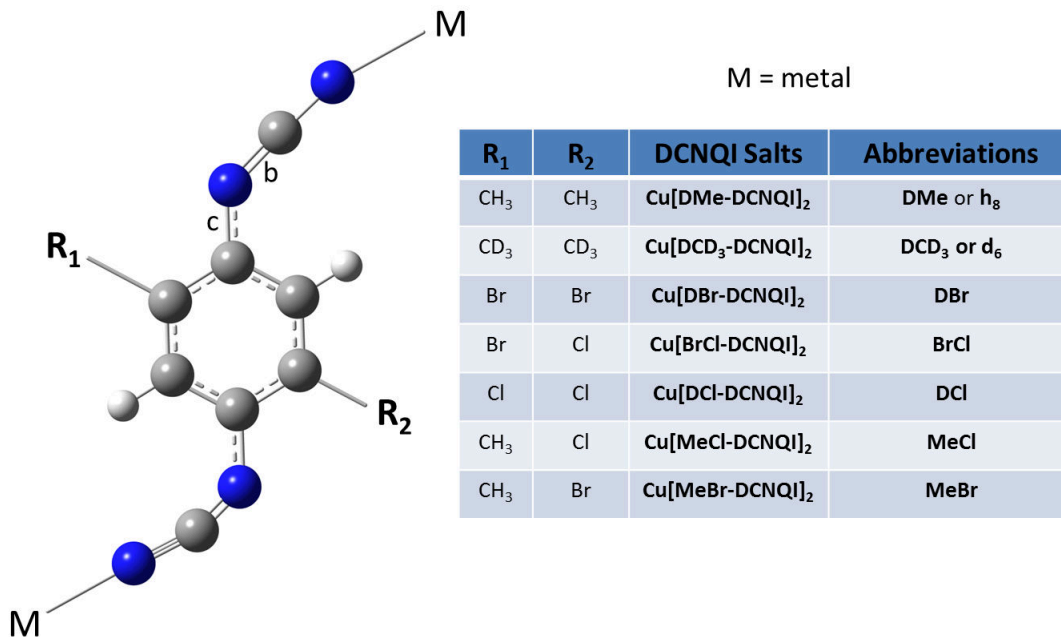


Figure 5.1: Molecular structure of DCNQI salts. Different radical substitutions discussed in this chapter are shown in the table. The cyano groups (N-C-N) comprise the bonding  $b$  and the antibonding  $c$ , whose lengths determine the rate of charge transfer in DCNQI salts (see Section 5.4 for details). All the salts investigated have copper metal (M) as the cation. Key: nitrogen - blue; carbon - grey and hydrogen - white.

Table 5.1: Lattice parameters used in the simulation. Data labelled  $s$  were taken from Ref. [64]: room temperature = 298 K; low temperature = 20 K. Data labelled  $k$  were taken from Ref. [65]: room temperature = 298 K; low temperature = 100 K. Diffraction patterns were also obtained for DCD<sub>3</sub> at 156 K using lattice parameters:  $a = b = 21.63$  Å,  $c = 3.799$  Å [64]; and MeBr at 163 K:  $a = b = 21.606$  Å,  $c = 3.809$  Å [65].

Salts	Room temperature			Low temperature		
	a (Å)	b (Å)	c (Å)	a (Å)	b (Å)	c (Å)
<sup>k</sup> DMe	21.548	21.548	3.871	21.566	21.566	3.801
<sup>s</sup> DCD <sub>3</sub>	21.619	21.619	3.874	21.693	21.693	3.776
<sup>k</sup> DCl	21.55	21.55	3.816	NA	NA	NA
<sup>k</sup> DBr	21.558	21.558	3.896	NA	NA	NA
<sup>k</sup> MeBr	21.601	21.601	3.856	21.627	21.627	3.780
<sup>k</sup> MeCl	21.559	21.559	3.823	21.640	21.640	3.745
<sup>k</sup> BrCl	21.569	21.569	3.845	21.683	21.683	3.783

and charge density wave formation are along  $c$ -axis, the crystal samples are usually prepared in such a way that  $c|a$  plane is perpendicular to the electron beam direction. The family of Bragg planes along this direction conforms to  $[010]$  Laue zone, thereby producing a periodic array of  $\{h\ 0\ l\}$  reflections. This makes the experimentally accessible EDP to only constitute sets of

$\{h\ 0\ l\}$  reflections, where the signatures of the electron density distribution are along the rows (see Figure 5.2 (a) & (b)). For the purpose of visualising and comparing the signature of the tetragonal coordination as it pertains to the structural arrangement of the donor (metal atom) and the acceptor molecules, the simulation of EDP along the  $[001]$  Laue zone axis ( $b|a$  plane), resulting into  $\{h\ k\ 0\}$  reflections, are also presented.

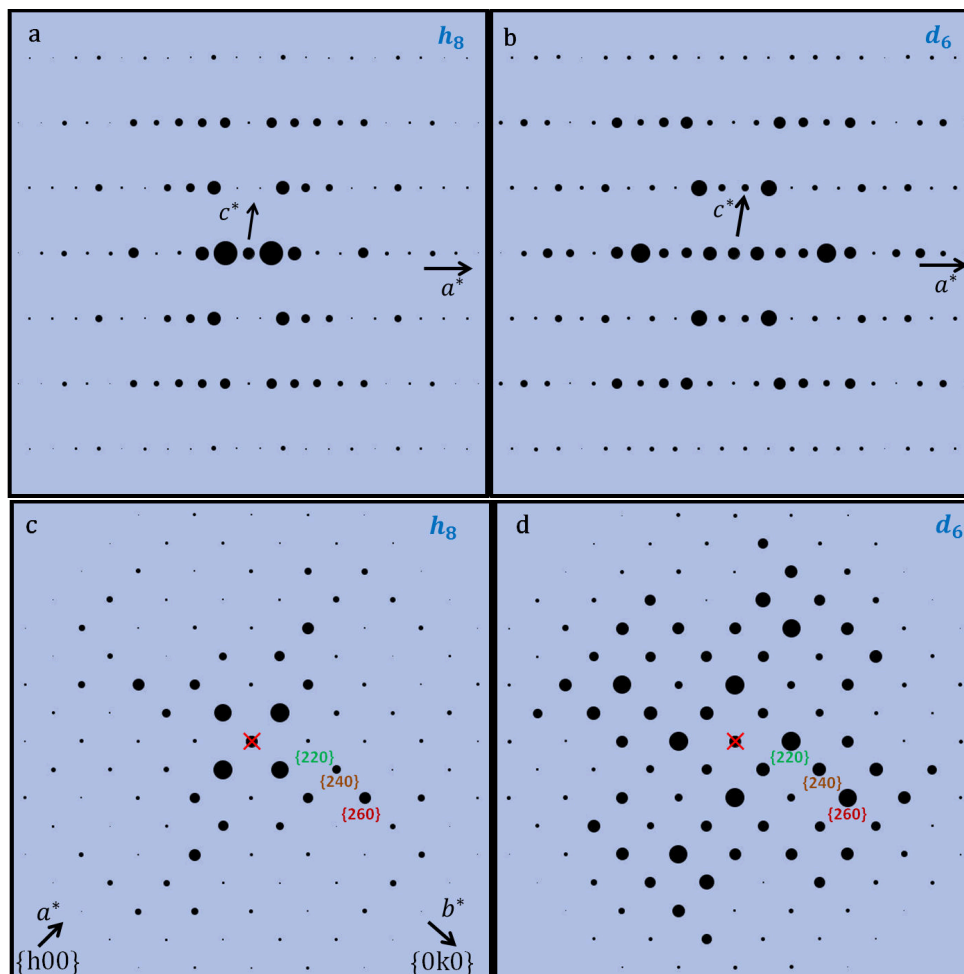


Figure 5.2: Simulated electron diffraction patterns for the room temperature structures of  $h_8$  and  $d_6$ . The crystals are projected along  $[010]$  zone axis in (a) & (b) and along  $[001]$  in (c) & (d). In both projections, the signature of a 4-fold symmetry, body-centered tetragonal crystal is evident. The increase in Bragg intensities in  $d_6$ , in contrast to those obtained in  $h_8$  suggests that the scattering domains of the DCNQI sites are enhanced, as expected (See for example the families of Bragg planes indexed in (c) and (d)). In other words, the redistribution of electron densities across the scattering domains in  $d_6$  structure, caused by the secondary isotope effect, allows for intense Bragg peaks observed and the distinct change in the intensity distribution profile.

Due to the weak scattering centres associated with DCNQI salts, the reflections from the Bragg planes are relatively weak. Thus, the simulated EDP obtained from two derivatives of  $\text{Cu}[2,5\text{-R}_1, \text{R}_2\text{-DCNQI}]_2$ , namely  $\text{Cu}[2,5\text{DCD}_3\text{-DCNQI}]_2$  (hereafter referred to as  $d_6$ ) and  $\text{Cu}[2,5\text{DMe-DCNQI}]_2$  (hereafter referred to as  $h_8$ ), are first compared and contrasted to investigate the secondary deuteration effect on the obtainable intensity distribution profiles. The importance of this comparison stems from the nature of the electronic structures of each of these derivatives: (1) Both are metallic and belong to the same symmetry group at room temperature.

This means that the intensity distribution profiles obtainable from both structures should be similar. (2) The deuterated ( $d_6$ ) structure undergoes a metal-insulator phase transition and as such should reveal intra-structural changes with regards to an influence on the intensity distribution profile and the reduction of diffracted intensities at low temperatures. The undeuterated  $h_8$  structure is metallic down to a very low temperature and should approximately maintain the same intensity distribution profile during cooling processes. (3) Experimentally, the delicate balance between the electron energy that drives the scattering and the fragility of crystal samples ( $\sim 30$  nm) require a trade-off, such that a relative rather than a maximum diffracted intensity obtainable from a particular scatterer is often achieved. (4) Given that there is a difference in the orientation of the scattering domains in these structures, their scattering capacities at room temperature should give us an insight into what to expect at low temperature, or during cooling.

In both structures the same space group and intensity scale are employed. Therefore, the obtainable electron diffraction patterns can be compared qualitatively and quantitatively. In the reciprocal space of both structures, the periodicity ratio  $c^*/a^* \approx 5.57$ , which perfectly corresponds to the ratio of their lattice constants in the real space. Since both structures are quasi-metallic at room temperature, and only differ in hydrogen mass, one would expect to obtain fairly the same electron diffraction patterns (Hydrogen atoms generally do not contribute to the scattering capacities of crystals). As shown in Figure 5.2, it is surprising to observe not only an appreciable increase in intensity amplitudes but also a change in the intensity distribution profile in  $d_6$ , relative to  $h_8$ . Judging from the fact that the intensity distribution profile of any diffraction pattern arises from the scattering of a crystal's periodic electron density distribution (or electrostatic potential), a redistribution of electrons, due to secondary deuteration effect, across the whole crystal is envisaged.

The observable stronger reflections in  $d_6$ , relative to  $h_8$ , crystal structure are presumably due to strong correlation of  $\sigma$ - and  $\pi$ -orbital overlaps, respectively between the deuterium atoms and carbon atoms of the radicals, and carbon-carbon atoms within the DCNQI molecules. The family of the obtainable strong reflections could also be presumed to inherently arise from the geometrical distortion of the Fermi surface and the redistribution of the delocalised  $\pi$ -electrons. Comparing the scattering powers of the constituent atoms or between the donor and the acceptor (Figure 5.3), it is evident that copper atoms have the highest scattering power. Hence, the copper atoms would have the highest contributions to diffraction intensities observed.

It is also envisaged that the  $d$ - $p$ - $\pi$  hybridisation in  $d_6$  is stronger than in  $h_8$ , so that the redistribution of the total electron density across the whole crystal favours more intense scattering from the DCNQI sites. Furthermore, the orientation of the nearly planar DCNQI molecules, influenced by the increased steric effect on the cyano moieties, to the beam direction in both crystal groups is envisaged to play a role in reinforcing the DCNQI scatterers. The author, therefore, posits that the weak scattering centres hitherto present at DCNQI sites are enhanced by the imposition of the secondary deuteration on the crystal structure.

Notably, the showing of family of high intense Bragg peaks that are particularly evident in the electron diffraction patterns obtained from  $d_6$  along its [001] direction (see Figure 5.2 (c)

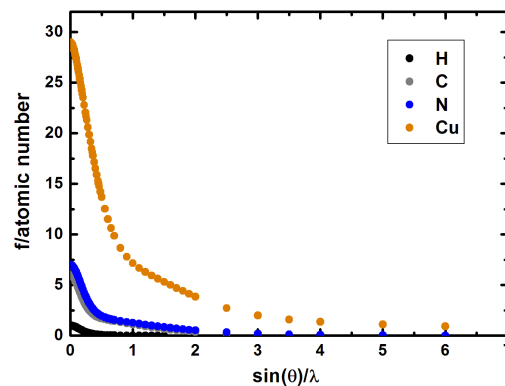


Figure 5.3: The atomic scattering powers of the constituent atoms in DCNQI crystals. Data taken from [21].

& (d)), in contrast to  $h_8$ , point to a greater degree of electron-electron and/or electron-lattice correlations, which ultimately drive the crystal to undergo phase transition. Moreover, a careful examination of the stacked unit cells along the  $c$ -axis shows that most of the Bragg planes appearing in the reciprocal space cut through the DCNQi sites, which either receive a rich or a poor contribution from the copper atoms. Again, the contributions from the copper atoms could be seen to enhance the alignment of perfectly or slightly-off-planar DCNQi scattering domains to the direction of the beam, depending on the geometrical distortion that each of the DCNQi sites experiences. We could then imagine that the scattering domains, which constitute the regions of high and low electron densities differ in DCNQi samples with different radicals. This is even more so when comparing one Bragg plane in one crystal sample to the other.

For a clearer assessment of the quality and quantity differences between the strengths of the Bragg reflections obtained from  $d_6$  and  $h_8$  structures, we integrated along the  $\{h0l\}$  planes, as shown in Figure 5.4. The Bragg intensities are displayed as the area of the circles representing different Bragg planes, such that

$$\{I(hkl)\}_{\text{sim}} = \pi r^2 = \frac{1}{4}\pi D^2, \quad (5.1)$$

where  $r$  and  $D$ , respectively, are radius and diameter of the reflection circles. We immediately see that the intensity is proportional to the square of each circle's diameter (or amplitude square). The results obtained from these integrations are shown in Figure 5.5. The intensities of the Bragg reflections are plotted against the scattering angles  $2\theta$ , which are calculated using the lattice parameters of  $h_8$  and  $d_6$  structures and the Bragg relation given in Equation 2.4. Here, we applied Friedel's relation to reduce the number of Bragg planes considered in the integration. Quantitatively, the difference between the amplitudes of  $h_8$  and  $d_6$  intensity distributions along the  $\{h01\}$  and  $\{h02\}$  reflections are also plotted. This is calculated using the relation

$$\Delta I = \left[ \frac{I_{h_8} - I_{d_6}}{I_{h_8}} \right]_{\{h0l\}}. \quad (5.2)$$

The resulting percentage change in intensity  $\Delta I$  is then normalised to the brightest Bragg reflection (this is the (301) peak) in both structures. For a similar sample thickness (30–50 nm), the overall quality of the obtainable Bragg reflections in  $d_6$ , in contrast to  $h_8$  could thus be inferred from the plots shown in Figure 5.5. However, as the sample thickness increases the crystals' potential fields become less smooth, such that there is a decrease in the number of Bragg reflections observed and also a general decrease in the Bragg intensities of all the existing reflections (See Equations 2.10 - 2.12).

Based on the symmetry considerations of the tetragonal body-centered crystals, forbidden reflections between every two Bragg spots shown in Figure 5.2(a & b) are absent, so that the indexing of the Bragg reflections obey the relation

$$h + k + l = 2n \quad \text{and} \quad u.h + v.k + w.l = 0. \quad (5.3)$$

In particular, the detailed conditions that limit possible reflections for the space group ( $I4_1/a$ ) to which Cu-DCNQi salts belong are:

$$\{hkl\} : h + k + l = 2n, \quad \{hk0\} : h = 2n \quad \text{and} \quad \{00l\} : l = 4n, \quad (5.4)$$

as determined by the space group software [80] used in our analysis.

Electron diffraction experiments are carried out on the  $d_6$  structure, which undergoes a metal-insulator phase transition at 73 K, as shown in Figure 4.8. Fresh samples of  $d_6$  crystals were obtained from our collaborators [11, 60] and prepared into ultra-thin samples (30–50 nm), using

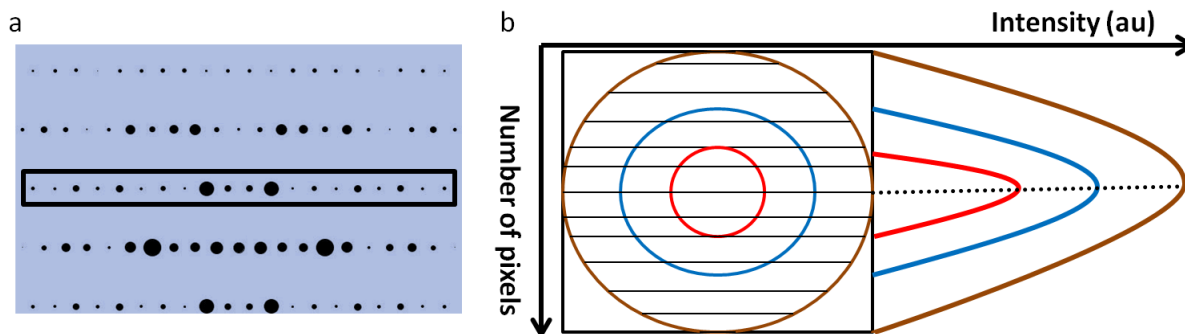


Figure 5.4: (a) Integrating over Bragg reflections along the  $c$ -axis ([010] direction). The ( $h01$ ) Bragg reflections inside the designated box are divided into two equal parts by Friedel's relation. This operation was performed for all the integrated intensities presented in this chapter. In (b) the expected integrated profile shape and amplitude for different sizes of the circular discs representing Bragg reflections are shown.

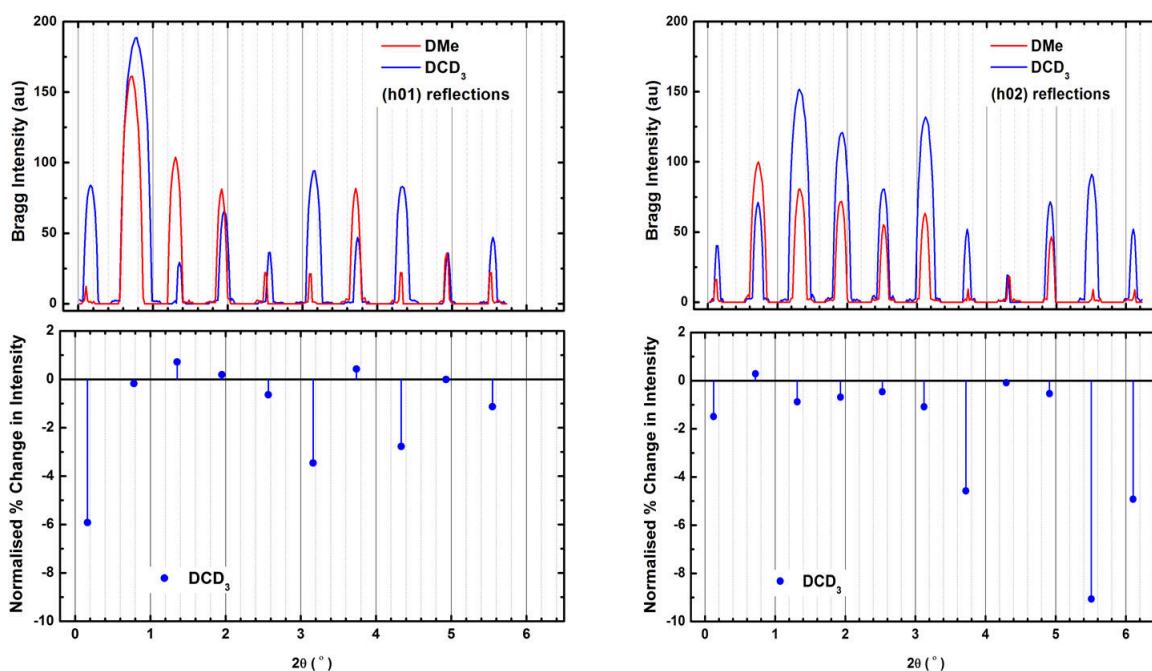


Figure 5.5: Integrated profiles of intensity distribution for the first and second order Bragg reflections along the  $c$ -axis ([010] direction) of the  $d_6$  ( $Cu[DCD_3-DCNQI]_2$ ) and  $h_8$  ( $Cu[DMe-DCNQI]_2$ ) structures. It is evident that most of the Bragg reflections in  $d_6$  structure are stronger in intensities as compared to those obtained in  $h_8$ . The intensity profiles for these structures are not exactly on top of one another due to the slight differences in their lattice parameters.

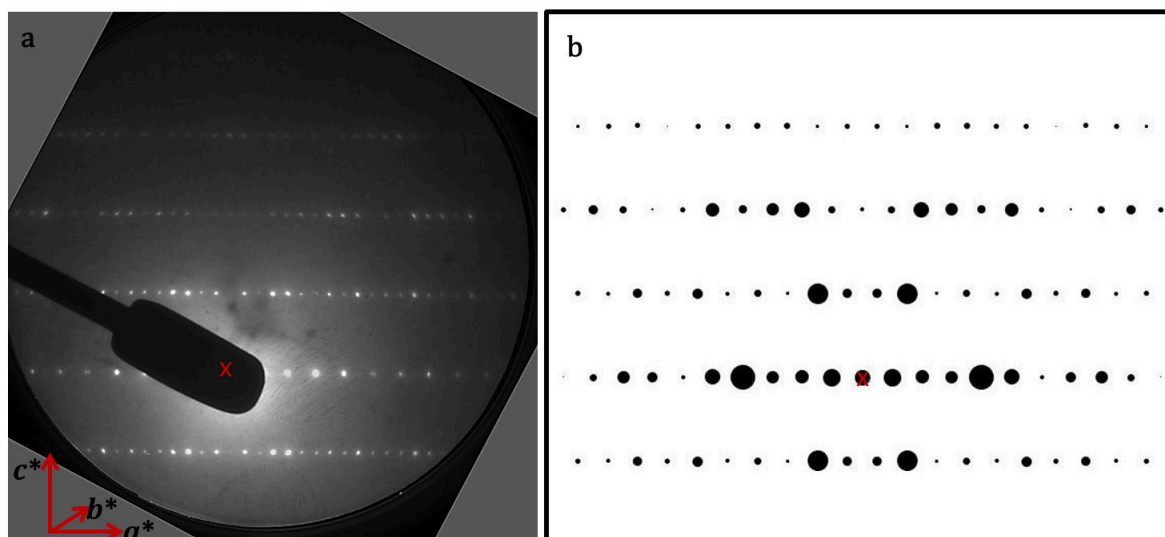


Figure 5.6: Comparison of electron diffraction patterns obtained (a) from experiment and (b) simulation of  $\text{Cu}[\text{DCD}_3\text{-DCNQI}]_2$  ( $d_6$ ) structure along its  $c$ -axis ( $[010]$  direction). The Bragg reflections show the periodicities along the  $c^*$  [ $a^*$  reciprocal plane]. The periodicity along the central order reflections  $\{h\ 0\ 0\}$  of the experimental pattern matches that of simulation. In the higher order reflections, it is evident that there are more Bragg spots in the experiment, in contrast to simulation. The extra spots are rendered as forbidden reflections (see text for detailed explanation).

an ultramicrotome machine available at the Central Analytical Facilities (CAF) at Stellenbosch University <sup>1</sup>. A typical room temperature experimental diffraction pattern obtained is shown in Figure 5.6 (a). A careful comparison between the simulated and the experimental electron diffraction patterns shown in Figure 5.6 (a) and (b) reveals that the number of Bragg reflections along the rows in the experimental EDP is twice that obtained in the simulation. This clearly contradicts the symmetry requirements and thus, the extra spots are rendered as forbidden reflections. A close look at what causes the appearance of forbidden reflections in electron diffraction was thus needed. The probable reasons behind this anomaly were highlighted in Chapter 2, of which two major candidates stood out: imperfect experimental beam parameter and sample thickness (which may or may not cause multiple scattering).

The coherence property of the Ewald sphere is possibly relaxed in the case of imperfection of the experimental electron beam, such that the scatterings by the constituent atoms favour the appearance of the forbidden spots. Undoubtedly, the creation of these forbidden spots may also arise from strain-induced lattice distortion. This assertion being probable, it would mean that there exist large optical phonons, which mediate constructive interferences at the forbidden positions as the electron beams are scattered into multiple angles. Mulyavko *et al.* [30] asserted that crystal deformation induced by strain imposed on crystals during sample preparation led to the creation of forbidden reflections and in the process caused a "weak change" in the crystal symmetry. More so, the forbidden reflections experimentally found in germanium (Ge) and zinc oxide (ZnO) crystals were said to have violated their lattice symmetries [81].

The intensity distribution of the Bragg reflections observed in the experimental EDP reveals a line of symmetry, which is contrary to what is obtained in the simulation as shown in Figure 5.7 (a & b). Two lines of thought came to mind:

<sup>1</sup>The details of the initial experimental measurements and characterisation, including sample preparation, has been carefully outlined by Andrea Rohwer in her Masters thesis, available online on SUNScholar of Stellenbosch University.

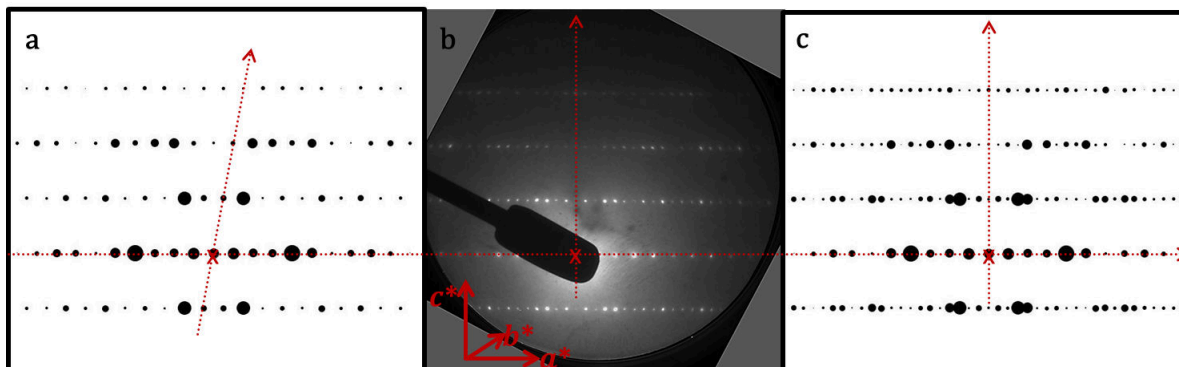


Figure 5.7: Analysis of symmetry lines along the stacking direction of  $\text{Cu}[\text{DCD}_3\text{-DCNQI}]_2$  ( $d_6$ ) structure's diffraction patterns. Shown in panel (a) is the simulated zeroth order Laue zone (ZOLZ) reflections (main diffraction pattern). In (b) the corresponding experimental diffraction pattern is shown. The lines of symmetry dividing the simulated Bragg reflections into two halves (using Friedel's relation) evidently is contrary to what obtains in the experiment as shown in panels (a) and (b). The solution to this discrepancy is the inclusion of first order Laue zone (FOLZ) reflections as shown in panel (c), and explained in the text.

(1) That the extra spots observed in the experimental diffraction pattern render the real space lattice to be a  $P$ -type (primitive, with no forbidden reflections) rather than an  $I$ -type (body-centered, with forbidden reflections). This possibility is eliminated because (a) the central order  $\{h\ 0\ 0\}$  reflections conform to a body-centered lattice; therefore, the appearance of the extra spots in the higher order reflections ( $\{h\ 0\ l\}$ ; with  $l \neq 0$ ) should be due to a different interaction. (b) The intensity distribution of the Bragg reflections obtained by imposing a closely related  $P$ -type space group ( $P4/n$ ) on the refined crystal structure deviates from those observed in the experiment. We chose  $P4/n$  space group because it was found in some DCNQI salts (with cations K,  $\text{NH}_4$ , Rb & Tl) [77].

(2) That the extra spots arise from higher order Laue zone (HOLZ) reflections, with the most probable being the first order Laue zone (FOLZ) reflections such that

$$h + k + l = 2n \quad \text{and} \quad u.h + v.k + w.l = 1. \quad (5.5)$$

That the summation of the Miller indices ( $h, k, l$ ) remains an even number suggests that the body-centered lattice restriction is still retained. Furthermore, this means that the Bragg reflections obtainable along the  $[010]$  Laue zone axis will generally have both  $\{h\ 0\ l\}$  and  $\{h\ 1\ l\}$  reflections. This possibility was then explored by including the reflections from FOLZ in the simulation. To validate the inclusion of FOLZ reflections, we investigated their positions along the three major Laue axes:  $[010]$ ,  $[100]$  and  $[001]$  in the simulation. We found that there is no appearance of FOLZ reflections along the  $[001]$  axis, suggesting that they are outside the zeroth order Laue zone (ZOLZ) reflections (main reflections along this zone), as generally reported in the literature [18, 82]. In both  $[010]$  and  $[100]$  axes, the simulation revealed that the FOLZ reflections are interposed between the ZOLZ reflections, such that there is a FOLZ reflection at every forbidden positions and interestingly none between the central order reflections. This fits what was observed in the experimental EDP and therefore, we concluded that the forbidden reflections truly belong to FOLZ. The simulated EDP containing both ZOLZ and FOLZ reflections along the  $[010]$  axis is shown in Figure 5.7 (c). The identification of selected peaks for the experimental EDP obtained from the  $d_6$  structure, using the Miller indices notation, is shown in Figure 5.8.

The integrated intensity distribution profile along the  $\{h\ 0\ l\}$  reflections obtained from the

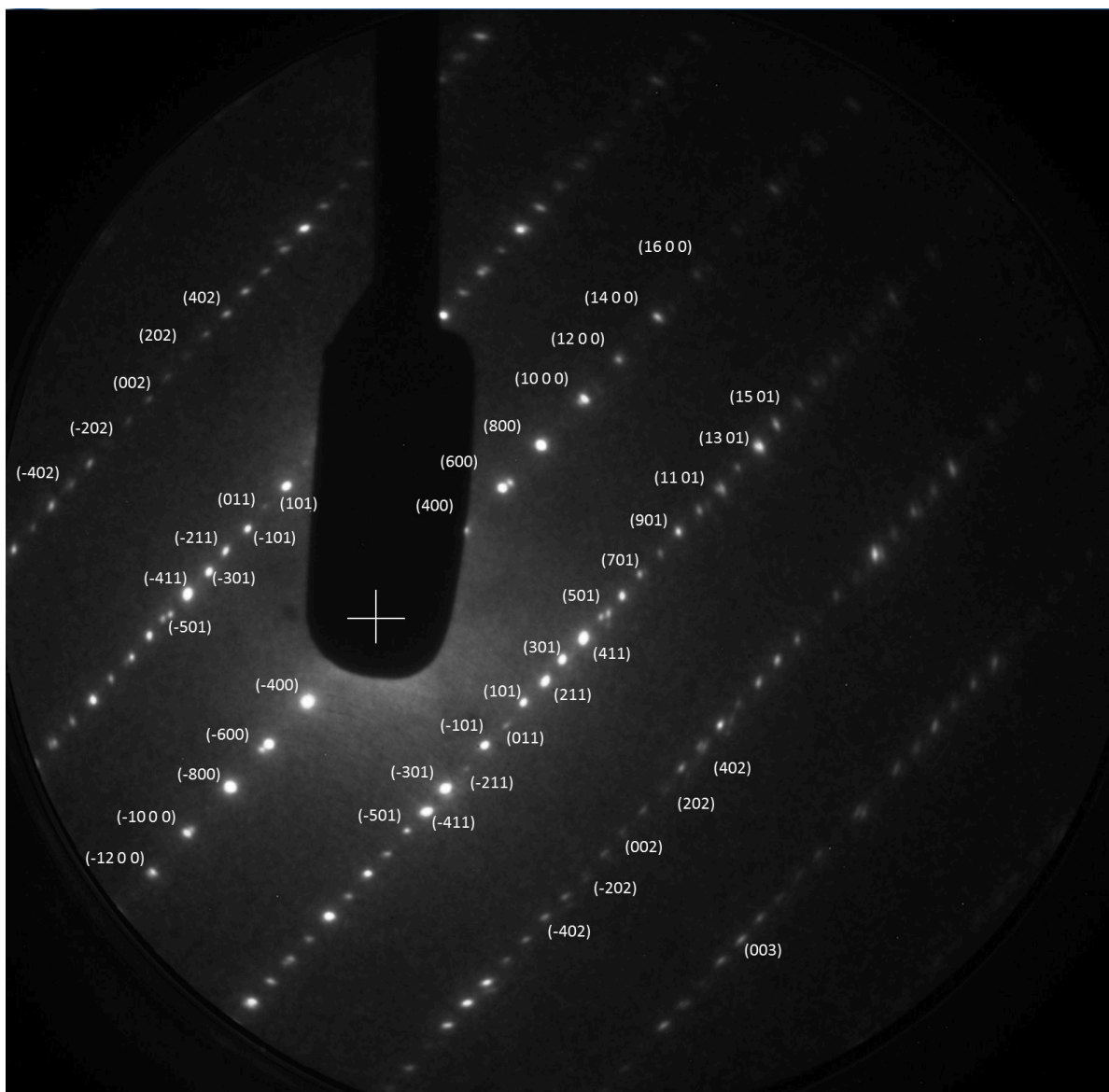


Figure 5.8: Identification of peaks using the Miller indices notation. The experimental diffraction pattern shown is obtained from the  $d_6$  structure at room temperature. The peaks marked with  $\{h\ 0\ l\}$  (e.g.  $(3\ 0\ 1)$ ) indices are the allowed reflections while those marked with  $\{h\ 1\ l\}$  (e.g.  $(2\ 1\ 1)$ ) are the forbidden reflections. All the reflections with  $k = 1$  are forbidden and relatively weak as compared to the allowed reflections.

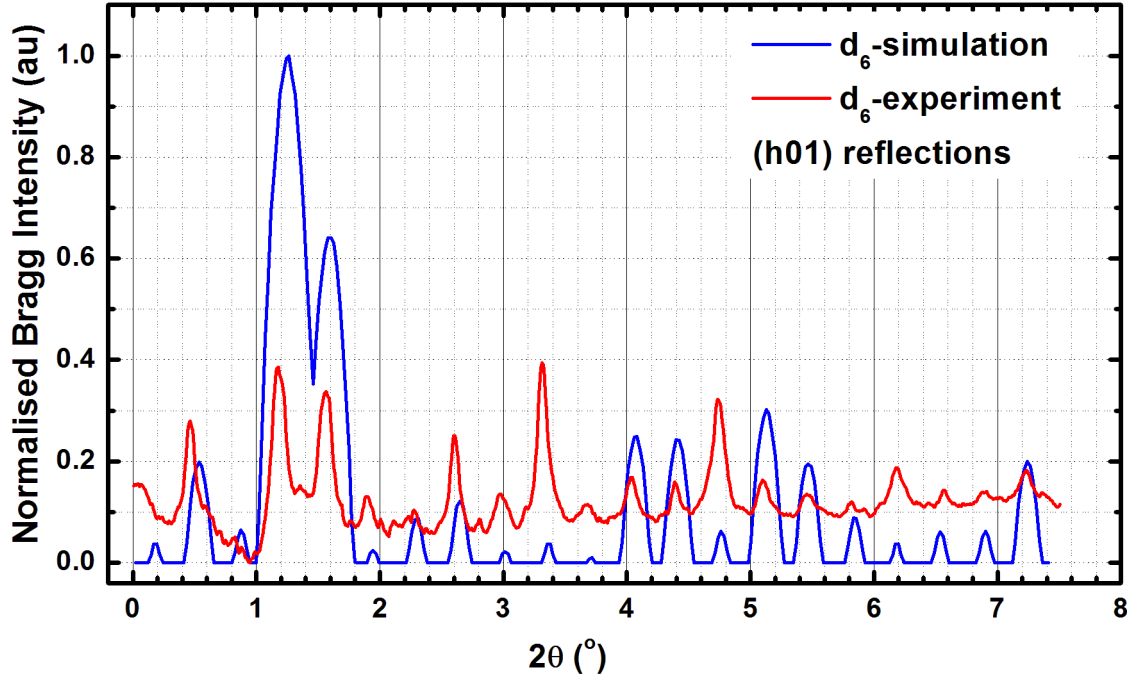


Figure 5.9: Integrated intensity distribution profiles of the calculated and the observed  $\{h\ 0\ l\}$  and  $\{h\ 1\ l\}$  Bragg reflections. Both ZOLZ and FOLZ reflections are included in the simulation to compensate for the forbidden reflections observed in the experimental diffraction pattern. Qualitatively, the intensity amplitudes' distribution of the simulation match with the experiment's. The quantitative difference between the experiment and the simulation can only be approximately inferred. See the text for a detailed discussion.

experiment, overlapped with the corresponding simulated reflections, is plotted in Figure 5.9. The plotted profiles reveal both the quantitative and qualitative aspects of the Bragg reflections observed, in comparison to the calculated. Qualitatively, the distribution of amplitudes of experimental Bragg intensities to an appreciable approximation match those obtained from the simulation. Quantitatively, it is shown that the amplitudes of the Bragg reflections observed in the experiment are generally lower than those obtained from the simulation. The explanation for this is simply that we can only observe *relative* intensity amplitudes in the experimental pattern due to the allowed electron per pulse and the fragility of the sample. The simulated patterns give the *absolute* intensity. Thus, it suffices that we scale both the observed and calculated intensities in order to compare them. The experimental Bragg intensity profiles are approximated by a Gaussian profile, such that

$$\{I(hkl)\}_{\text{expt.}} \approx \int_{-\infty}^{+\infty} A e^{-y^2} dy = A\sqrt{\pi}, \quad (5.6)$$

where  $A$  is the amplitude of the experimental Bragg intensity. Thus,  $A$  is related to  $D$  in Equation 5.1 as:

$$A = \frac{1}{4} D^2 \sqrt{\pi}.$$

Here, we draw the reader's attention to the fact that we left out some constants in the intensity scaling for both the simulation and the experiment. Remember that the simulation is based on kinematic theory, which in itself is an approximation of the dynamical theory. Kinematic scattering theory does treat (absolutely) the qualitative aspect of Bragg intensities but is somewhat deficient in the quantitative treatment. Also, the true shape of a diffracted intensity profile is the

Voigt profile, which is a convolution of both the Gaussian and Lorentzian profiles in addition to background oscillations. Voigt profiles are generally obtained from complex error functions, and often are not easily resolved. Therefore, experimental diffracted intensities are usually approximated as having a Gaussian shape. Note also that an appreciable amount of electron energy is lost to the background as a result of inelastic scattering. The background is subtracted from the experimental data to fine-tune its intensity distribution profile. Due to these deficiencies highlighted in both what the experiment and simulation have to offer, the author posits that a comparative study on electron diffraction patterns obtained should be treated qualitatively rather than quantitatively.

### 5.3 Why do Cu-DCNQI salts with halogen or mixed radicals have *high* transition temperatures?

It appears that the subtle redistribution of electron density (leading to change in intensity distribution) is generally responsible for Cu-DCNQI salts undergoing phase transition. Instinctively, even though all Cu-DCNQI salts have an isomorphic space group, we expect to see a deviation in the population of electron-rich scattering domains, contrasted by the different possibilities of radical substitutions. In other words, we want to explore the data presented in Table 4.1 using electron diffraction simulation. We therefore painstakingly perform electron diffraction simulations on some selected room temperature X-ray structurally refined Cu-DCNQI salts that contain mixed and pure halogen radicals. The atomic coordinates data were taken from Ref. [65].

The simulated diffraction patterns for the room temperature structures of  $\text{Cu}[2,5\text{DCl-DCNQI}]_2$ ,  $\text{Cu}[2,5\text{DBr-DCNQI}]_2$ ,  $\text{Cu}[2,5\text{MeBr-DCNQI}]_2$ ,  $\text{Cu}[2,5\text{MeCl-DCNQI}]_2$ ,  $\text{Cu}[2,5\text{BrCl-DCNQI}]_2$  (DCl: di-chloro; MeBr: methyl-bromo; DBr: di-bromo; MeCl: methyl-chloro and BrCl: bromo-chloro radicals) along the [010] direction are shown in Figure 5.10. It is immediately evident that there is no drastic change and/or amplitude reduction in the intensity distribution of the Bragg reflections obtained from these structures, in comparison to  $\text{Cu}[2,5\text{DMe-DCNQI}]_2$  salt. Indeed, one may not be able to identify what diffraction patterns belong to which structure if not labelled.

However, through a closer look it was found that there is a subtle (or slight) redistribution of electron density across the scattering domains in these structures. The integrated intensity profiles and the percentage change are shown in Figure 5.11. (These are also obtained by the same procedure explained in Section 5.2). Comparing the scattering powers of the different radicals in relation to the amplitudes of Bragg intensities obtainable from these structures does not give an observable trend. What is generally evident is that some Bragg peaks are stronger in one structure compared to the other. From the perspective of electron density population across the scattering domains, one may wonder, and validly so, why  $h_8$  structure that is of similar intensity distribution as in the halogenated structures does not undergo phase transition when subjected to a similar external factor.

One plausible line of argument could be in relation to the influence that these radicals have on the planarity of the DCNQI scattering centres and the coordinating angles of the DCNQI ligands, as presented in Table 4.1. All the mixed radicals have similar coordinating angles and so the orientation of the DCNQI scattering centres to the direction of the electron beam should be similar. Better still, halogen radicals are known to have electron-poor scattering centres, regardless of their electron mass [76]. This is why most of the Cu-DCNQI salts with mixed radicals presented *relatively stronger* Bragg reflections than those with the pure halogen radicals.

Electron affinities of these radicals could as well play a role in interpreting the electron diffraction patterns obtained from these structures. The radical with the highest electron affinity

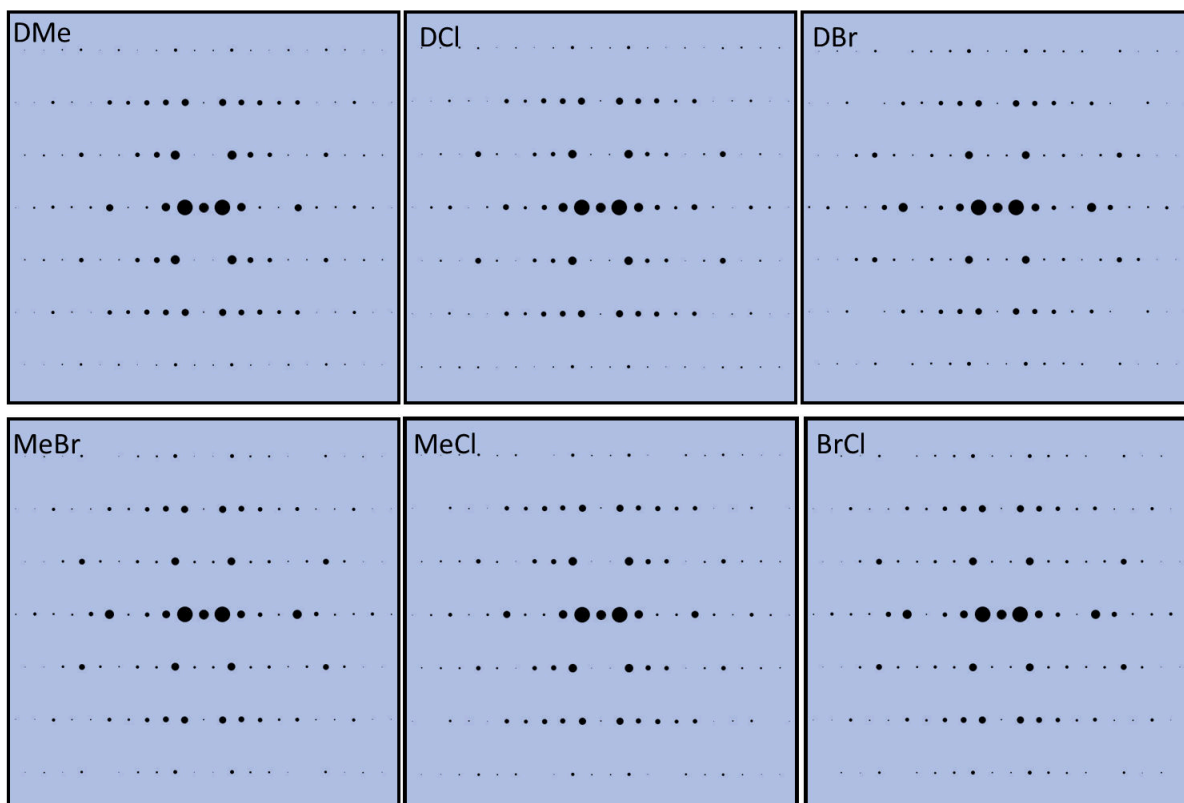


Figure 5.10: Comparison between the electron diffraction patterns obtained from the different radical substitutions along the  $[010]$  zone. All Bragg intensities are on the same scale. All patterns are obtained from the X-ray refined atomic coordinates at room temperature (298 K). No drastic change is observed in the intensity distribution profiles of these structures in contrast to  $h_8$  (structure with DMe radical), except for some subtle intensity changes of some Bragg reflections in one structure compared to another. The energy used is 30 kV and the thickness of the samples is 30 nm.

is chlorine (Cl) and it is not surprising that the highest phase transition temperatures were found in the structures containing chlorine atoms (MeCl at 210 K; BrCl at 210 K and DCl at 230 K [64, 65]). One could imagine that the electron density distribution across the DCNQI scattering centres are pulled towards the domains of the halogen radicals and as such present overall weak scattering amplitudes, in comparison to those observed in  $h_8$  structure. Conversely, it is clear that the intensity distribution profiles obtainable from the halogenated structures along the  $[010]$  zone axis ( $a|c$  plane) deviate from that of the deuterated structure ( $d_6$ ) that was introduced earlier. Certainly, the simulated diffraction patterns obtained along  $[001]$  ( $a|b$  plane) zone axes of the structures with mixed radicals, contrasted with that obtained from  $d_6$  structure, clearly reveal a different population of electron density as shown in Figure 5.12. Using the structure with dimethyl (DMe) as a reference (since it is metallic down to low temperature), it could, therefore, reasonably be concluded that the introduction of deuterium leads to enhancement of density of states (being translated to the observable strong families of Bragg reflections) and by extension improves the scattering capacities of DCNQI domains, in contrast to the halogenated structures.

Probing further, we decided to simulate the electron diffraction patterns obtainable from the intermediate structure of the deuterated crystal ( $d_6$ ) and compared this with those of the halogenated structure. The data found in literature for this analysis favour  $\text{Cu}[2,5\text{MeBr-DCNQI}]_2$  (at 163 K; the phase transition temperature is at 156 K) and  $\text{Cu}[2,5\text{DCD}_3\text{-DCNQI}]_2$  ( $d_6$  at

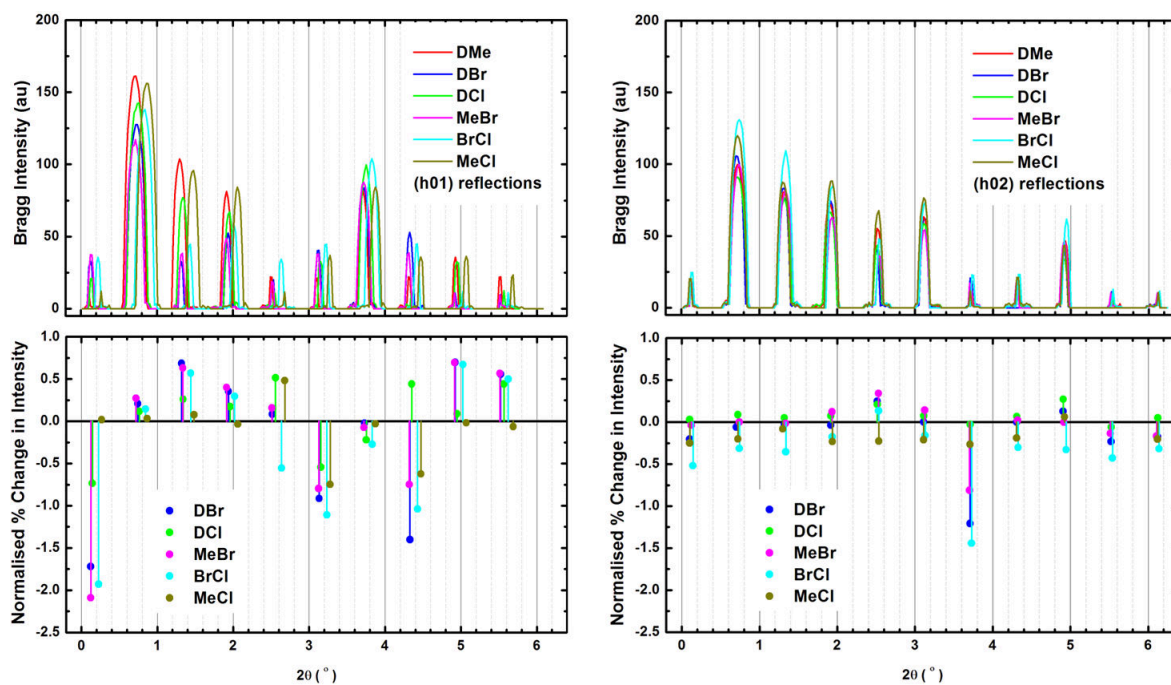


Figure 5.11: The integrated Bragg intensities of the  $\{h\ 0\ 1\}$  and  $\{h\ 0\ 2\}$  reflections obtained from halogenated structures are compared with that containing only methyl radicals (DMe or  $h_8$ ). Again, this is a qualitative, rather than quantitative comparison. Reflecting on the overall intensity amplitudes, there is only a slight rearrangement in the population of the electron density distribution in the halogenated structures, in contrast to  $h_8$ . The shifts in the peaks are due to the different lattice periodicities, and hence their scattering angles.

156 K; the phase transition is at 73 K). The idea is to study the structural evolution, if any, as these structures undergo cooling.

As shown in Figure 5.13, the evolution of the deuterated ( $d_6$ ) structure into a typical reciprocal space intensity distribution profile (electron density distribution in the real space) found in halogenated structure is unmistakable. The family of intense Bragg peaks that was erstwhile evident along the  $[001]$  axis at the room temperature apparently is now reduced, possibly due to the combination of Jahn-Teller distortion and the intensive deformation experienced by the scattering domains. Since there is no drastic intensity distribution change in the simulated patterns obtained from  $\text{Cu}[2,5\text{MeBr-DCNQi}]_2$  at both intermediate and room temperature (163 K and 298 K respectively), a *sharp drop* first order metal-insulator phase transition is favoured. In terms of electron density population, the *structural switching* of the  $d_6$  structure into a typical halogenated structure provides an interesting insight: experimental diffraction patterns on the  $d_6$  structure are expected to undergo the same process during cooling before phase transition can occur. This points to the existence of at least three states in  $d_6$  structure. It remains to be seen if one state could be optically switched into another.

Then comes the existence of orientation disorder that arises as a result of structural imbalance across the DCNQi scattering domains: a proven difficulty in ascertaining the asymmetry unit of the Cu-DCNQi salts with  $R_1 \neq R_2$  (e.g BrCl and MeCl) in X-ray structural refinement [65, 66]. Moret *et al.* [66] reported that the orientation and/or substitution disorder found in silver salts with MeBr and MeCl radicals led to the observation of diffuse scattering peaks, which inadvertently made the quality of the observable Bragg reflections become worse at low temperature. A significant decay in the intensity of the Bragg reflections at low temperature is therefore envisaged for structures with mixed radicals. Generally, a solid system will always tend

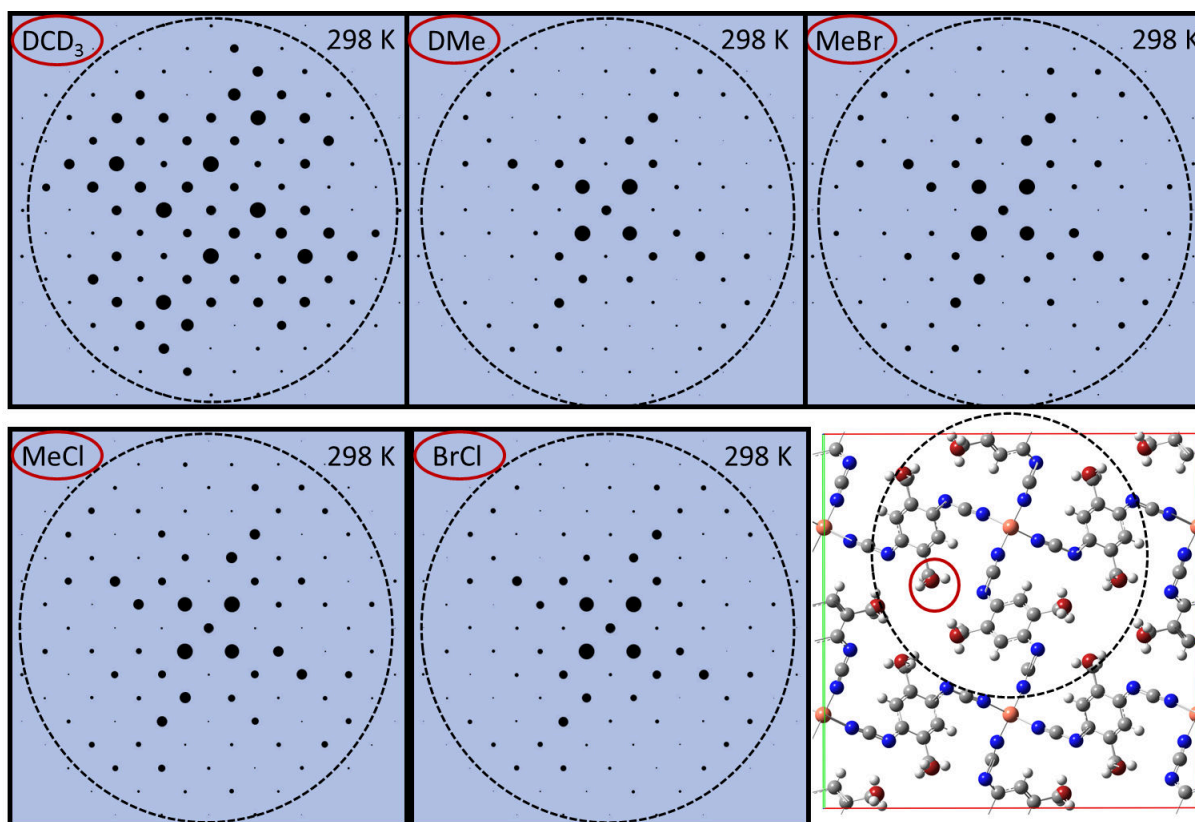


Figure 5.12: Comparison between the Bragg reflections obtainable from structures with mixed radicals (MeCl, MeBr & BrCl), deuterated structure ( $d_6$ ) and the undeuterated structure ( $h_8$ ) along the [001] direction. The red circle on the Cu-DCNQI unit cell corresponds to the position of the superposed radicals, which relates to the orientation disorder discussed in the text. The black dotted rings enclose periodic families of Bragg reflections, whose intensities' strengths depend on the electron mass enhancement and the orientation of the tetrahedrally coordinated DCNQI centres across unit cells of Cu-DCNQI salts. The Bragg reflections shown here suggest that the  $d_6$  structure offers highest enhanced density of states in these structures.

to orientate its atomic constituents along the equilibrium positions that favour lowest energy at a particular temperature. As such, the atomic refinement data could favour one of the radicals; but the "maximum likelihood" of the two competing radicals will eventually win out. The superposition or one of the competing radicals ( $R_1$  and  $R_2$ ) could be refined to be part of the asymmetry unit of the crystal, which is used in simulation (see Figure 5.12).

Whereas the structures with pure halogen radicals show no such disorder at room temperature, the refinements of their atomic coordinates at low temperature could not be resolved due to weak and/or smeared reflections obtained from the oscillation photographs [65, 76]. A valid reason for the less difficulty encountered in refining the structural data containing mixed radicals should then be as a result of the superposition of the amplitudes of the radicals' structure factors. Furthermore, the author debates that the initial magnitude of disorder experienced by a Cu-DCNQI salt with mixed radicals necessitates the relatively high coordinating angle ( $\alpha_{N-Cu-N}$ ), above the threshold value required for Cu-DCNQI salts undergoing phase transition (See Table 4.1). To close this section we list the possible factors responsible for high phase transition temperatures in Cu-DCNQI salts with halogen radicals:

1. *High electron affinities*, which mediate strong electron delocalisations across the DCNQI scattering domains.

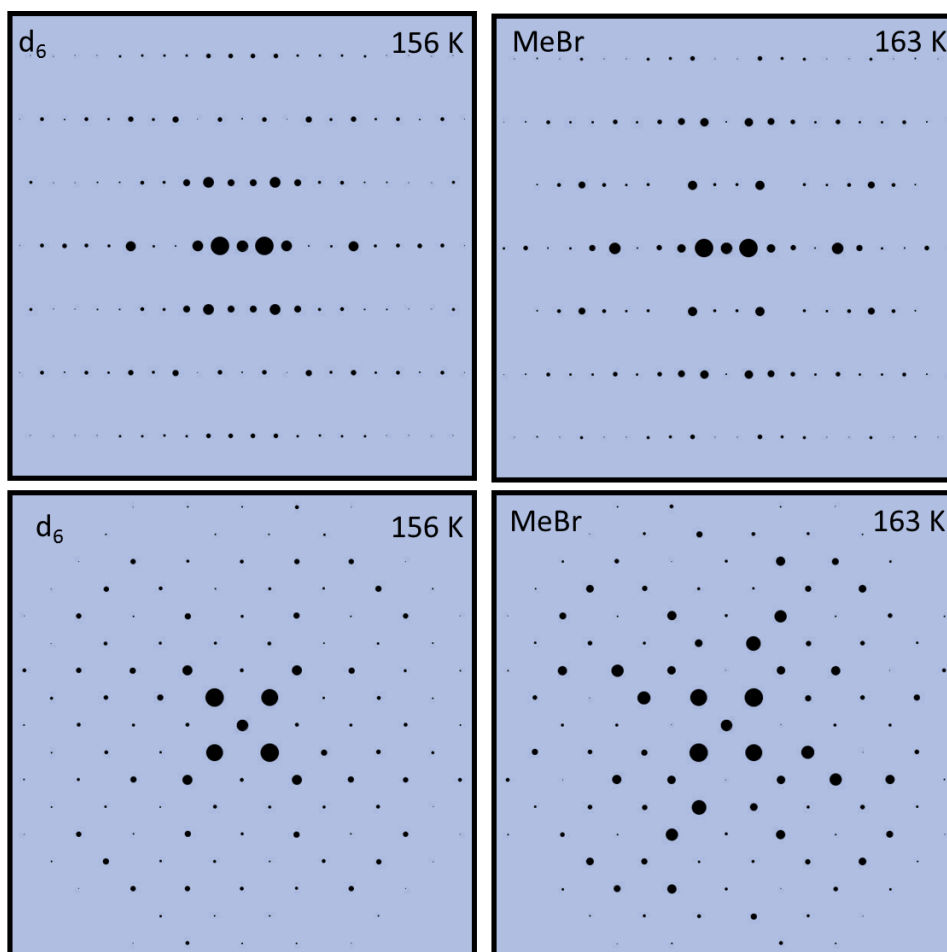


Figure 5.13: The simulated diffraction patterns obtained for the purpose of investigating structural evolution in the intermediate structures of  $\text{Cu}[2,5\text{MeBr-DCNQI}]_2$  and  $\text{Cu}[2,5\text{DCD}_3\text{-DCNQI}]_2$  ( $d_6$ ). The X-ray data used was taken from References [64, 65]. The erstwhile family of intense Bragg peaks present in the room temperature simulated diffraction patterns for  $d_6$  structure (Figure 5.2 (a & c)) are evidently transformed to the typical distribution in halogenated structures due to Jahn-Teller distortion and the intensive deformation experienced by the DCNQI scattering centres. Top and bottom panels refer to [010] and [001] zone axes, respectively.

2. *Orientation disorder in salts with mixed radicals*, which gives rise to a Peierls-related structural imbalance.
3. *Very high coordinating angles*, which are already observed at room temperature.

## 5.4 Structural lability, molecular motion and fluctuating Bragg reflections in Cu-DCNQI salts

For a start, it is always desirable to have qualitative diffraction images both at room and low temperatures for proper analysis. Diffraction patterns obtainable from all solids undergo intensity fluctuations arising from Debye-Waller-related atomic or molecular vibrations, while varying temperature. Organic crystals have high thermal lability [6, 87], which makes them prone to degradation during cooling or warming. Some diffraction images obtained (such as shown in Figure 5.14) from our experimental set-up reveal the effect of this structural lability in the deuterated structure. In addition to the difficulty in getting suitable thin samples for electron

diffraction experiments, a good sample might well be destroyed if care is not taken during sample cooling or warming. Therefore, an insight into the possible causes of structural lability in selected DCNQI salts, as well as the expected change in Bragg intensities, is important. This in turn projects a suitable consideration of the sample thickness, electron number per pulse and the electron energy to be used in electron diffraction experiments. We take a look at these in the following paragraphs.

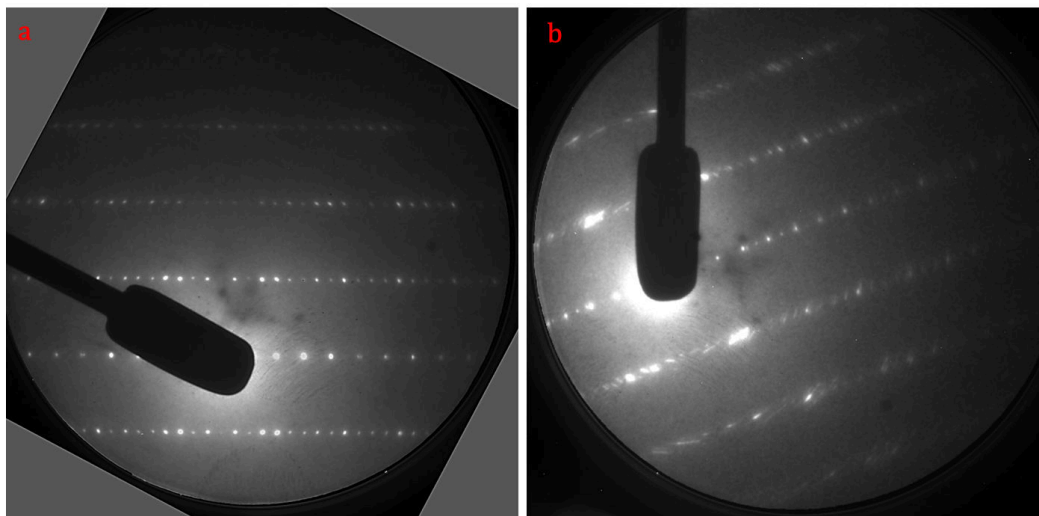


Figure 5.14: Experimental diffraction patterns obtained from  $d_6$  structure at (a) room temperature and (b) 65 K. Distortion of Bragg reflections is evident in panel (b). This may be caused by different factors, as discussed in this section.

Starting from the experimental point of view, the quality of the bulk crystal produced during crystal growth determines the obtainable diffraction image quality. Given that the crystal grown is suitable, the sample preparation, ranging from cutting to thin slices to mounting those that are homogeneous on an aperture, could subject the sample to a strain-induced negative pressure. The effect of this negative pressure might well not be significant on the room temperature diffraction patterns, but become more visible as the crystal undergoes cooling processes. The linear thermal expansion coefficient for the Cu-DCNQI crystal is reported to be  $\alpha_{\text{DCNQI}} = 110 \times 10^{-6} \text{ K}^{-1}$  [11], as against that of copper (copper mesh was used in the experiment), taken to be  $\alpha_{\text{Cu}} = 16.2 \times 10^{-6} \text{ K}^{-1}$  [88] at room temperature (See Figure 5.15). The difference in their expansion coefficients is presumed to induce structural lability, arising from strain imposed by the copper mesh on the sample, before and during cooling. In particular, condensation of water vapour on the sample during cooling processes, as observed in our measurements, significantly reduces the quality of diffraction images shown in Figure 5.14(b) <sup>2</sup>.

A first look at the X-ray refined data for all Cu-DCNQI salts reveals that the positions (atomic coordinates) of the copper atoms are fixed at both room and low temperatures [64, 65, 76]. All other atomic coordinates (at low temperature) are shifted (or modulated) from their equilibrium positions (at room temperature) according to the distortion that each atom and/or molecule experiences. This suggests that the copper atoms act as anchors to the distortion experienced (or vibrations sensed) by the DCNQI molecules and its ligands as the crystal undergoes cooling.

<sup>2</sup>The condensation of water on the sample and on the sample holder in our experimental set-up is attributed to the operating vacuum chamber pressure ( $10^{-6}$  mbar), which is considered to be insufficient for a sample cooling down to (20 K). A lower pressure ( $\sim 10^{-9}$  mbar) vacuum chamber is suggested and designed, and is now up and running. A Masters thesis written by Bart Smit, contains the details of the new chamber [13].

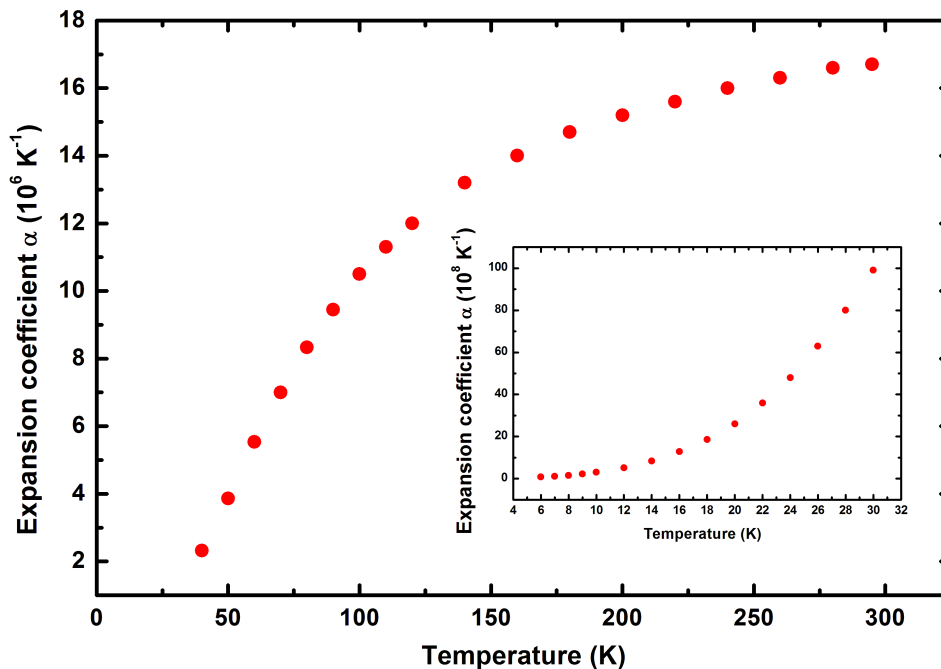


Figure 5.15: Experimental measurements (data taken from Ref. [88]) of the linear thermal expansion coefficient of copper from room temperature down to 6 K. A jump in the expansion coefficient to the tune of two orders of magnitude is observed below 30 K, as shown in the inset graph. The expansion coefficient continuously decreases until it reaches zero at 6 K.

The author envisages that during the cooling processes, the geometrical (Jahn-Teller) distortion experienced by these DCNQI moieties should induce different conformations in the electron density distribution across the scattering domains of the crystal structures containing different radicals. Thus, the amplitudes of the intensity distribution profiles obtainable from salts with different radical substitutions should vary before, and possibly after, phase transitions.

Miyazaki *et al.* [71, 72] have shown (see Figure 4.4) that the metallic states of DCNQI salts reveal a qualitative orbital degeneracy, arising from the  $p$ - $\pi$  hybridisation of the DCNQI molecular orbitals and the  $d$ -orbital of the copper atoms. H. A. Jahn and E. Teller [78] in their very old paper of 1937, asserted that a simultaneous occurrence of orbital degeneracy and stability of polyatomic molecules is not possible<sup>3</sup>. Instinctively, the deformation and/or modulation of the crystal lattice during cooling distorts the equilibrium positions of the crystal's atomic coordinates, and hence the stability of the whole system. Whereas the crystal system is unstable during cooling, the orbital degeneracy in the DCNQI crystal is sustained up to its phase transition temperature, where the crystal locks into a stable insulating state. The sustainability of the orbital degeneracy in the metallic state means that the scattering domains may only experience fluctuations in relation to the quality of the electron density of states. A fluctuation in the density of states, translating to the different Bragg planes, means a drop or an increase in the intensity as a result of temperature change.

Caviezel *et al.* [86] attributed the characteristic intensity fluctuations of the domain peaks in manganites to Jahn-Teller modes. Adopting and rearranging the relation they used in calculating

<sup>3</sup>Jahn-Teller distortions (or structural instabilities) are usually associated with non-linear polyatomic molecules (especially those containing  $d$ -electrons); the theories they formulated are based on orbital and spin degeneracies. These distortions are generally due to the overlap of metallic  $d$ -orbitals and the molecular orbital of a polyatomic molecule [78, 79].

changes in diffracted intensities, we obtain [86]

$$\frac{I^{hkl} - I_o^{hkl}}{I_o^{hkl}} = \frac{\Delta I^{hkl}}{I_o^{hkl}} = \frac{|\sum_{i=1}^N f_i e^{j\mathbf{G}\cdot(\mathbf{r}_i^{RT} + \eta\Delta\mathbf{r}_i)}|^2 - |\sum_{i=1}^N f_i e^{j\mathbf{G}\cdot\mathbf{r}_i^{RT}}|^2}{|\sum_{i=1}^N f_i e^{j\mathbf{G}\cdot\mathbf{r}_i^{RT}}|^2}, \quad (5.7)$$

where  $\eta$  is a distortion factor,  $I^{hkl}$  and  $I_o^{hkl}$  are the intensities at low temperature (LT = 20 K for  $d_6$  and 100 K for DMe-DCNQI, MeBr-DCNQI and BrCl-DCNQI salts) and room temperature (RT = 298 K) respectively,  $N$  is the number of atoms in the asymmetry units,  $\mathbf{r}_i^{RT}$  are the atomic coordinates of the room temperature structures and  $\Delta\mathbf{r}_i = \mathbf{r}_i^{LT} - \mathbf{r}_i^{RT}$ . We designate the distortion parameter  $\eta$  as a factor for temperature change, which translates to Debye-Waller fluctuations and lattice deformation in the crystals. A step of ten percent is taken from the room temperature ( $\eta = 0$ ; metallic state) to the low temperature structure ( $\eta = 1$ ; insulating state). No direct proportionality is found among these quantities; as we cannot ascertain the actual temperature decrease for a specific percentage of lattice deformation. The crystals are not refined for step-wise temperature range.

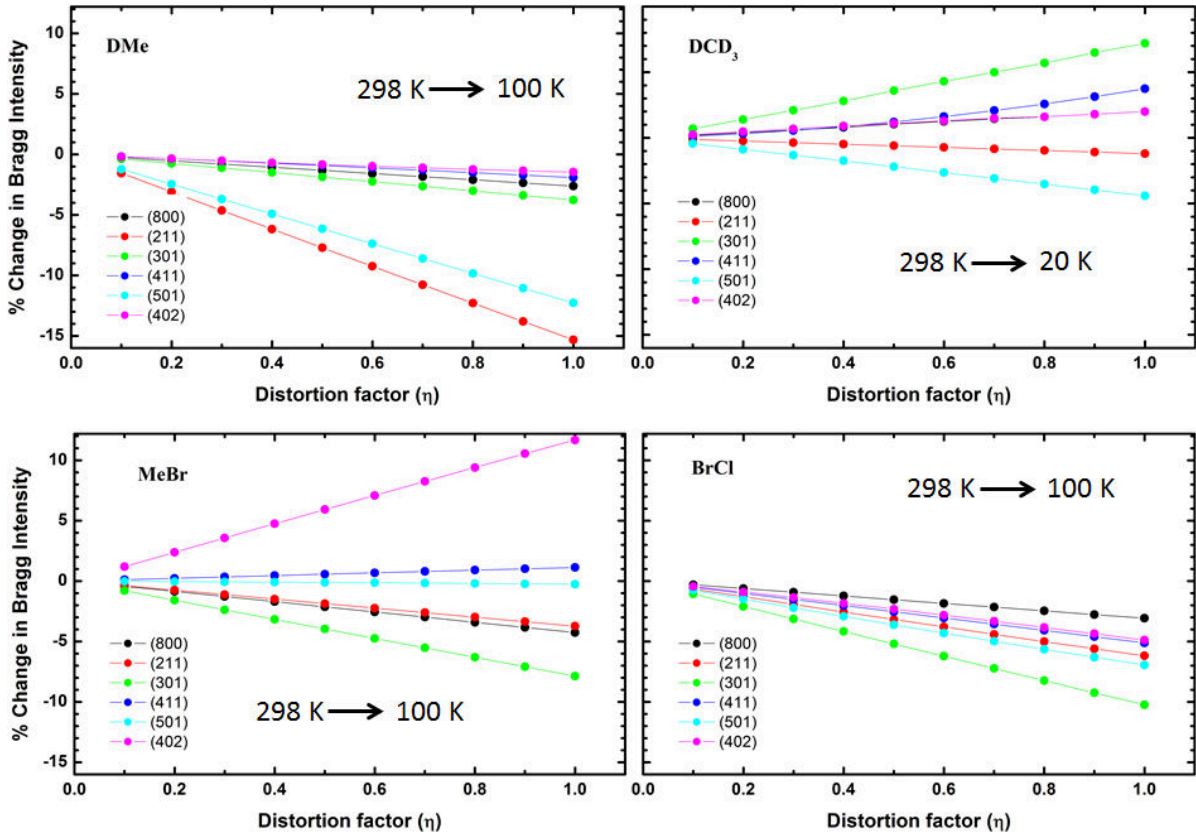


Figure 5.16: Expected Bragg intensity fluctuations in selected DCNQI salts during metal-insulator transitions. Different radical substitutions produce different Debye-Waller effects and lattice deformations as related to the reduction or increase in the intensities of the peaks selected. A maximum of 15% reduction and 12% increase of the Bragg intensities obtainable at room temperature are estimated for the selected salts.

The intensity changes for some randomly selected Bragg reflections from the diffraction patterns obtained for four different DCNQI salts are plotted in Figure 5.16. The different intensities' drop or increase in the Bragg peaks from one salt to the other emphasises the expected different populations of the electron density. The selected salts show intensity increase (of up

to 12%) and decrease (of up to 15%). From these plots intensity fluctuations expected from experimental diffraction patterns, when cooling or warming these salts, could be inferred. This inference will especially be important when a set of Bragg reflections is to be temporally resolved under a varied external factor such as temperature.

We have established in the previous sections that the stability of the in-plane and/or out-of-plane DCNQi scattering domains and their alignment to the direction of the electron beams determine the quality of obtainable Bragg reflections. Now, the vibrational motion, lattice deformation and charge transfer rates along the stacking axes of DCNQi salts have been suggested to be interdependent [64, 76, 83, 84]. Specifically, the dependence of the energy band splitting on the magnitude of lattice vibrations in relation to temperature, has been attributed to the vibronic coupling between the copper atoms and the DCNQi molecules [64].

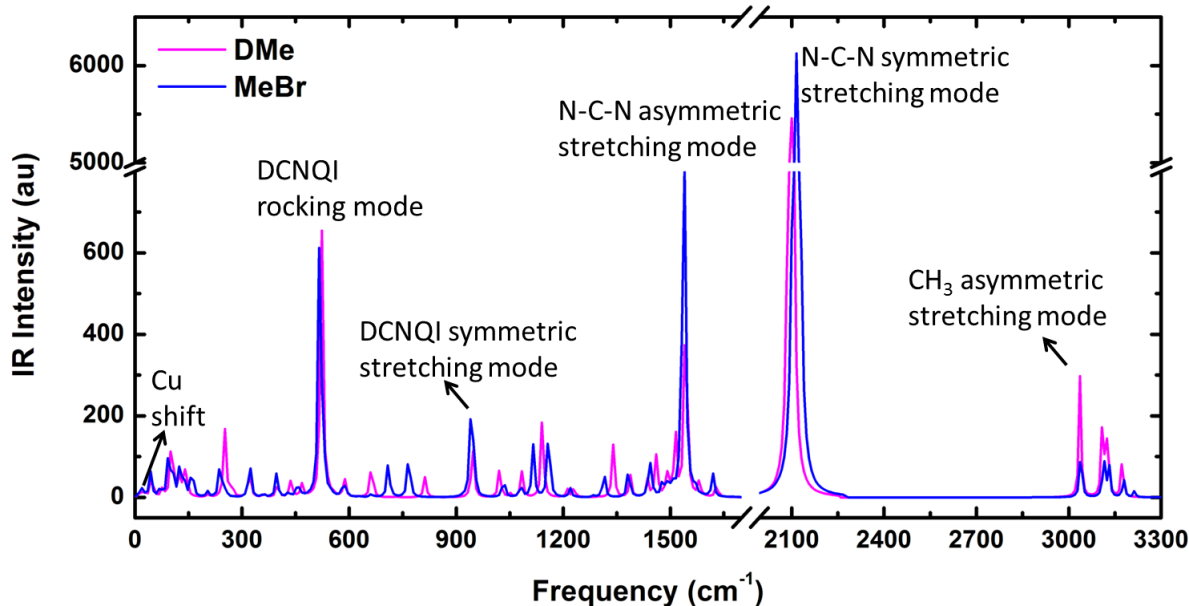


Figure 5.17: Infra-red active normal vibrational modes calculations in the room temperature asymmetry units of  $\text{Cu}(\text{MeBr-DCNQi})_2$  and  $\text{Cu}(\text{DMe-DCNQi})_2$  salts. In both salts Jahn-Teller (geometrical) distortions are most significant in N-C-N symmetric stretching modes (Note the breaks along both  $x$  and  $y$  axes. The infra-red intensity of N-C-N stretching modes are one order of magnitude higher compared to other modes). We propose that this high infra-red active frequency found in N-C-N stretching modes mediate large deviations in the coordinating angle ( $\alpha$ ), as shown in Table 4.1. Comparatively, it is possible that the higher infra-red frequency calculated for N-C-N mode in DCNQi salt with MeBr radical, in contrast to DMe radical, could be responsible for an enhanced energy band splitting and by extension high transition temperature in the halogenated DCNQi salts. Calculation was done using DFT (with B3LYP/CEP31-G accuracy) available in Gaussian software package [29]. See text for detailed explanation.

To investigate the nature or typical modes of vibrations in DCNQi salts, we have performed infra-red active frequency calculations on the asymmetry units of two DCNQi salts:  $\text{Cu}(\text{MeBr-DCNQi})_2$  and  $\text{Cu}(\text{DMe-DCNQi})_2$ . (We remind the reader that DMe and  $\text{DCD}_3$  radicals only differ in the hydrogen mass. The vibration modes are thus slightly different due to the influence of the C-D and C-H bond lengths on the overall vibrations.) As shown in Figure 5.17, the very first mode around  $3 \text{ cm}^{-1}$  is assigned to copper atoms, meaning that they sense the lowest vibration. This could be responsible for the fixed position refined for copper atoms in copper salts at both room and low temperatures. The signature of the frequency distribution at the other end of vibrational modes ( $3300 \text{ cm}^{-1}$ ) belong to the *radical* ( $\text{CH}_3$  radical and hydrogen atom)

motions, where it is evident that  $\text{CH}_3$  in DMe or  $\text{DCD}_3$  sense more vibration than in MeBr. This is due to the difference in the mass of the bromine atom and that of  $\text{CH}_3$ . Different vibrational modes are observed for the DCNQi motion (basically the six-member ring of carbon atoms) as shown. Most intense vibrations that are an order of magnitude higher than other vibrational modes, are found for the cyano group (N-C-N) symmetric and asymmetric modes, which in turn are proposed to mediate large deviation in the coordinating angle that is responsible for phase transition in these salts. The infra-red active frequency calculated for the N-C-N stretching modes in the DCNQi salt containing MeBr radical is higher as compared to the salt with DMe radical, and this points to an enhanced energy band splitting which in turn favours a general high transition temperature found in the halogenated Cu-DCNQi salts. The author therefore proposes that the improvement to the electronic mass in the halogenated structures results in different degrees of vibronic couplings between the copper atoms and the DCNQi molecules and its ligands. It is interesting to note that the N-C-N asymmetric vibration around  $1550 \text{ cm}^{-1}$ , as obtained in our calculation, has been experimentally measured and reported in Ref. [76].

It is reported in Refs. [83, 84] that the vibrational modes in both the neutral DCNQi molecules and DCNQi salts, especially the N-C-N symmetric stretching mode (see Figure 5.17), are responsible for the rate of charge transfer from the metal (copper atoms; donor) to the DCNQi acceptor molecules (or responsible for the determination of the localised charge on copper atoms at room temperature). Kato *et al.* [65] particularly reported that the transition of the DCNQi neutral molecules into the corresponding DCNQi anions reflects on the shortening of the bonding  $b$  (N-C bond length) and the lengthening of the antibonding  $c$  (C-N bond length) (see Figure 5.1), respectively. In other words, the bond lengths are transformed from  $b > c$  to  $b < c$ . Strange enough this transformation is only found in copper salts; other salts have  $b > c$  [65]. Hence it was suggested that this transformation supports the notion of mixed valency ( $\delta = +1.3$ ) in copper salts and the sustainability of crystallographic equivalent positions occupied by copper atoms from room temperature up to phase transition temperature. The rate of charge transfer in DCNQi salts with different cations (e.g. Cu, Ba, Li) is estimated via XPS measurements [65, 76]. At phase transition temperature, Cu-DCNQi structures lock into a charge ordering state with the formal charges at the copper sites following a three-fold periodicity:  $\text{Cu}^{2+}\text{Cu}^+\text{Cu}^+ \dots$ . This leads to the discussion of the next section.

## 5.5 Electron diffraction simulation and analysis of charge ordering and CDW formation in Cu-DCNQi salts

The charge fluctuation at the copper sites in the metallic state means that all copper atoms in Cu-DCNQi salts are crystallographically equivalent at room temperature, where each copper atom has an average charge of  $\delta = +1.3$ . This means that the two cyano moieties per one DCNQi molecule, which assume a trans-configuration, are connected to similar charge-donating copper ions. Thus, the charge distribution at room temperature will then follow as:  $\text{Cu}^{\frac{4}{3}+} \text{DCNQi}^{\frac{2}{3}-} \text{DCNQi}^{\frac{2}{3}-}$ . During cooling the coordinating tetrahedron in the metallic phase of DCNQi salts is subjected to an intensive deformation, such that a radical-imposed  $D_{2d}$  (Jahn-Teller) distortion leads to the lowering of the  $3d_{xz}$  and  $3d_{yz}$  bands well below the Fermi level and the raising of the  $3d_{xy}$  band above the Fermi level (see Figure 4.3). This disconnects the  $d$  band of the copper atoms from the DCNQi  $p\pi$  band, and in the process induces the metallic multi-Fermi surface to give way to the formation of a band gap. This process is evidenced by the appearance of charge ordering at the copper sites and charge density wave formation on the DCNQi columns along the crystallographic  $c$ -axis. It is expected that the Mott-Peierls-related frustration among the DCNQi scattering domains should induce lowering of the DCNQi crystal lattice symmetry with the formation of insulating domains at and below phase transition temperature. The paragraphs

that follow examine the considerations for charge ordering and charge density waves formation in selected DCNQi salts, as well as the analysis of their appearances in the diffraction patterns obtained.

The analysis of the possible structural arrangements of the copper atoms and the DCNQi molecules at low temperature is not straightforward and has received a lot of considerations from different authors over the years (all references given on DCNQi salts point to these considerations in one way or the other). Of these considerations, one that is critical to electron diffraction simulation and analysis is the crystal symmetry: Is there a break in the symmetry or not?

On the one hand, one may quickly conclude that there is no symmetry breaking, judging from the fact that the same space group was assigned to all average structural refinements obtained from X-ray diffraction data found in the literature [64, 65, 76], both at room and low temperatures. The average structures of the X-ray diffraction data on DCNQi salts reveal that the copper atoms' coordinates are not displaced, even at low temperature, as we discussed in the previous section. On the other hand the equally important charge ordering at the copper sites, which is unanimously agreed on by all authors, and evidenced by different types of measurements (NMR and XPS [76]), means that the DCNQi anions are not equivalently connected to copper cations of the same charge. Thus, introducing the charge orderings on the copper sites leads to a different structural arrangement and hence, a possibility that the crystal's symmetry is broken at low temperature.

The insightful analysis done by Kobayashi *et al.* [76] on the three-fold arrangement in DCNQi crystal structure may well be a decisive propeller in the understanding of the low temperature structural arrangement. Granted that the charge ordering at the copper sites follows the trend  $\text{Cu}^{2+} \text{Cu}^+ \text{Cu}^+$ , the *spiral* frustration along the DCNQi stacking columns requires the DCNQi molecules to be connected to either charge-rich  $\text{Cu}^{2+}$  sites or charge-poor  $\text{Cu}^+$  sites. A modified proposed schematics of the structural arrangement is shown in Figure 5.18. Two modes of spiral frustrations, designated by the large blue arrows in Figure 5.18, are identified among the DCNQi scattering domains: clockwise (DCNQi sites V and P) and anticlockwise (DCNQi sites T and U) tilting of the DCNQi molecules (resulting into out-of-unit-cell-plane modes on the DCNQi centres).

Examining the average structures of DCNQi salts, it was found that each DCNQi molecule, as well as each copper atom, is shared between two adjacent unit cells stacked along the crystallographic *c*-axis. Kobayashi *et al.* [76] argued that if we take the copper atom attached to one end of the DCNQi scattering centre (e.g "T" in Figure 5.18) to be  $\text{Cu}^{2+}$  ion, then the other end must be  $\text{Cu}^+$  ion as shown in the bottom panel of Figure 5.18. This means that the copper ions of the same charge (i.e.,  $\text{Cu}^{2+} \dots \text{Cu}^{2+}$ ,  $\text{Cu}^+ \dots \text{Cu}^+$ ) are connected to each other by two DCNQi molecules constituted by a clockwise and an anticlockwise centres (e.g "P" and "U" or "T" and "V" as shown in Figure 5.18). This is in line with the requirement of the 3-fold arrangements of the charge ordering on the copper sites<sup>4</sup>. Based on the analysis we did, labels are assigned to the copper ions along the stacking axis as shown in Figure 5.18.

During phase transition, charge disproportionation is imminent at the DCNQi centres. Assuming that each DCNQi molecule is connected to the same charged copper ions at both ends, then the charge distribution in Cu-DCNQi salts at low temperature would have followed:  $\text{Cu}^{2+} \text{Cu}^+ \text{Cu}^+ \dots \text{DCNQi}^- \text{DCNQi}^{0.5-} \text{DCNQi}^{0.5-}$ . However, to properly assign charge distribution to the DCNQi centres, we have to incorporate the stacking arrangements of both the clockwise and anticlockwise centres. Since each DCNQi molecule could be split into two asymmetry units (i.e., the atomic coordinates usually refined for an average structure, which could be up to 12 atoms depending on the radical used), we can technically *isolate* each asymmetry unit connected

<sup>4</sup>As was analysed in Ref. [76], we also found this charge-alternating arrangement along the row of each unit cell to be consistent with the charge-ordering requirement for the simulation presented here.

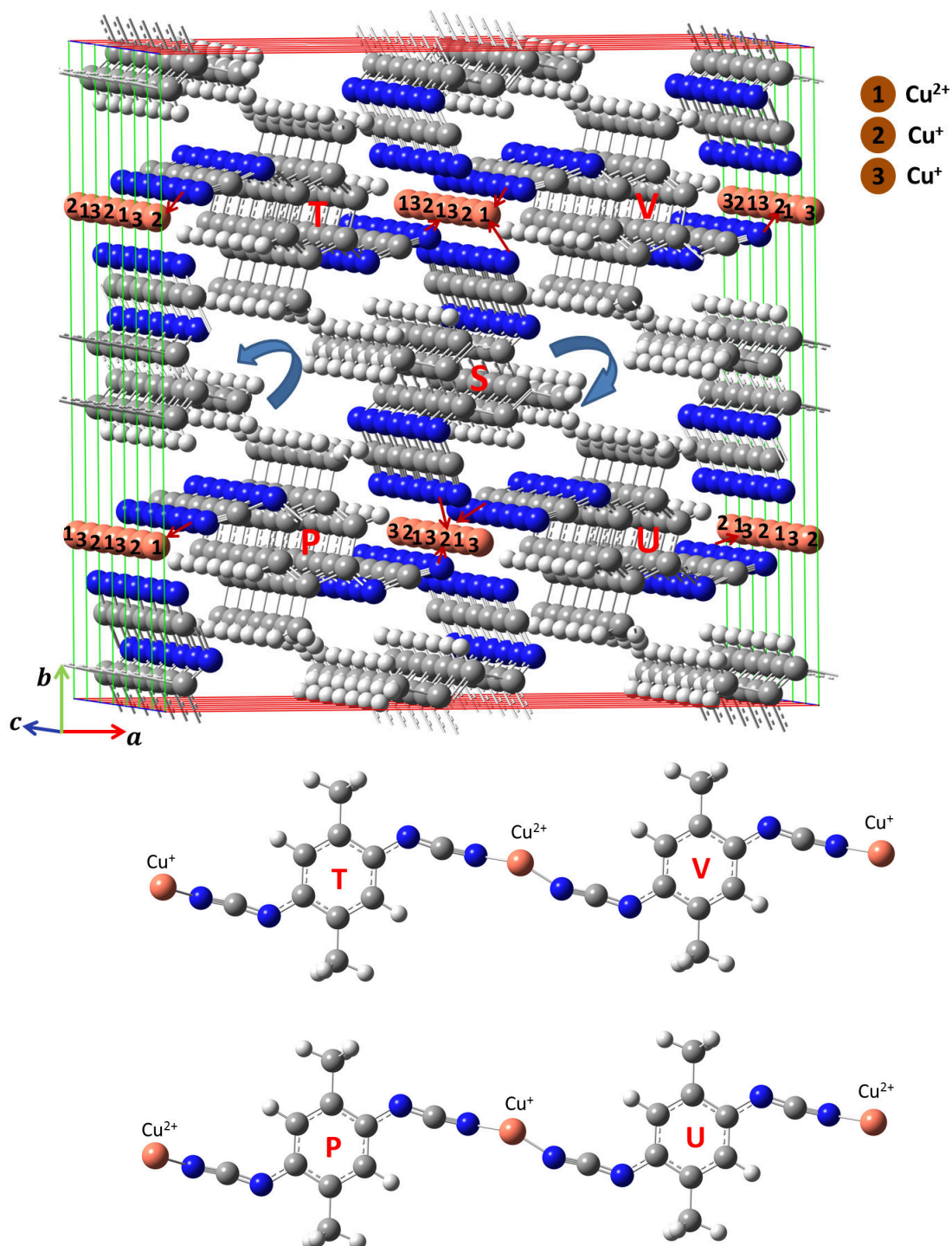


Figure 5.18: Proposed structural arrangement and charge ordering in the low temperature structure similar to the analysis done by Kobayashi *et al.* [76]. Two spiral modes (anticlockwise and clockwise) are identified among the DCNQI scattering domains/centres: Positions P and V are clockwise while positions T and U are anticlockwise. Going through the clockwise spiral at position P through S to the anticlockwise spiral at position T and back to P, the charge ordering trend  $\text{Cu}^{2+}$   $\text{Cu}^+$   $\text{Cu}^+$  along the crystallographic  $c$ -axis requires that the copper atoms be labelled as shown in the top panel. The bottom panel throws more light on this arrangement: two copper atoms of a similar charge and number (1 or 2 or 3, shown in the top panel) are connected by two DCNQI molecules. The alternating nature of the charge ordering along  $a$ -axis is also depicted in the bottom panel.

to either  $\text{Cu}^{2+}$  or  $\text{Cu}^+$ . Then, we have two charge-rich DCNQi domains with  $\delta \leq -0.75$  and one charge-poor DCNQi domain with  $\delta \leq -0.5$ , per each spiral (clockwise and anticlockwise). We have in total four crystallographically independent charge-rich DCNQi anions and two crystallographically independent charge-poor DCNQi anions so that the average charge distribution on each DCNQi anion maps into the range,  $-0.75 \leq \delta \leq -0.5$  (See Figure 5.19). Note that the average charge on the DCNQi anions at room temperature,  $\delta = -0.67$ , falls into this range.

According to the  $I4_1/a$  space group genealogy, the DCNQi crystal structures below phase transition temperature could attain one of the possible subgroups:  $P\bar{4}$  and  $P4_1$ . Kobayashi *et al.* [76] reckoned that the subgroup  $P4_1$  was not consistent with the different charge ordering arrangement in both the anticlockwise and clockwise DCNQi domains, hence  $P\bar{4}$  was chosen. Though Sawa *et al.* [89, 90] argued that  $P\bar{4}$  symmetry cannot sufficiently describe some properties of the low temperature DCNQi structures, but rather proposed  $P\bar{1}$  (a triclinic crystal, where  $a \neq b \neq c$ ), the argument is not well founded as their analysis could not ascertain the positions of charge-ordered copper ions at low temperature. More so, the lattice parameters assigned to all average structures refined by X-ray diffraction analysis points to the preservation of the room temperature tetragonal structure ( $a = b \neq c$ ), to which Cu-DCNQi crystals belong. Therefore, the lattice parameters and the atomic coordinates of the average structures refined in [64, 65], in addition to the positions of the charge-ordering copper ions [76] were used in the simulation presented here.

The projection of the structure with  $P\bar{4}$  symmetry, together with the positions of seven independent copper ions refined in Ref. [76] is shown in Figure 5.20. The extinction rule (conditions limiting possible Bragg reflections) for the  $P\bar{4}$  symmetry is given by [76]:

$$h + k + l = 2n + 1 \quad \text{and} \quad h + k + l = 2n, \quad (5.8)$$

where the *even sum* ( $2n$ ) satisfies a body-centered lattice and it corresponds to strong Bragg reflections; the *odd sum* ( $2n + 1$ ) breaks the lattice symmetry (from  $I4_1/a \rightarrow P\bar{4}$ ) and it corresponds to weak reflections present in the obtainable diffraction patterns below phase transition temperature.

It is well established in the literature that the Cu-DCNQi crystals lock into 3-fold periodicity below phase transition temperature, as schematically shown in Figure 5.21. Different DCNQi salts experience different periodic lattice distortions (designated by  $\Delta c$ ), as given in Table 4.1. The coupling between the periodic lattice distortion and electron density modulation in DCNQi salts manifests in form of super-lattice reflections along the DCNQi columns. This is evidenced by the appearance of two extra rows of Bragg reflections in between the diffraction orders observable at room temperature, as shown in Figure 5.22. These extra rows of Bragg reflections constitute what is known as charge density waves.

Interestingly, during the simulation and analysis, which mainly involves preparing different CIF files, we found that there is an interdependence between the charge-ordered copper ions' positions and the charge density wave signatures at the DCNQi centres. Modulation of the DCNQi crystal lattice positions without including the copper ions' positions gives no CDW signatures. Rather, the formation of CDW is driven by both the anti-phase<sup>5</sup> modulation of the DCNQi centres and the systematic longitudinal shift of the copper ions. This is consistent with what had been reported by different authors over the years: Charge orderings at the copper sites are coupled with the charge density waves along the DCNQi columns [64, 65, 74, 75, 76, 91].

Based on the available X-ray diffraction refined structural data [64, 65, 76], we simulated obtainable diffraction patterns of two derivatives of Cu-DCNQi salts:  $\text{Cu}[\text{DCD}_3\text{-DCNQi}]_2$  (deuterated salt) and  $\text{Cu}[\text{MeBr-DCNQi}]_2$  (halogenated salt). The copper ions' positions are refined

<sup>5</sup>The modulation of the electron density is in anti-phase fashion because of the existence of the clockwise and anticlockwise DCNQi scattering centres.

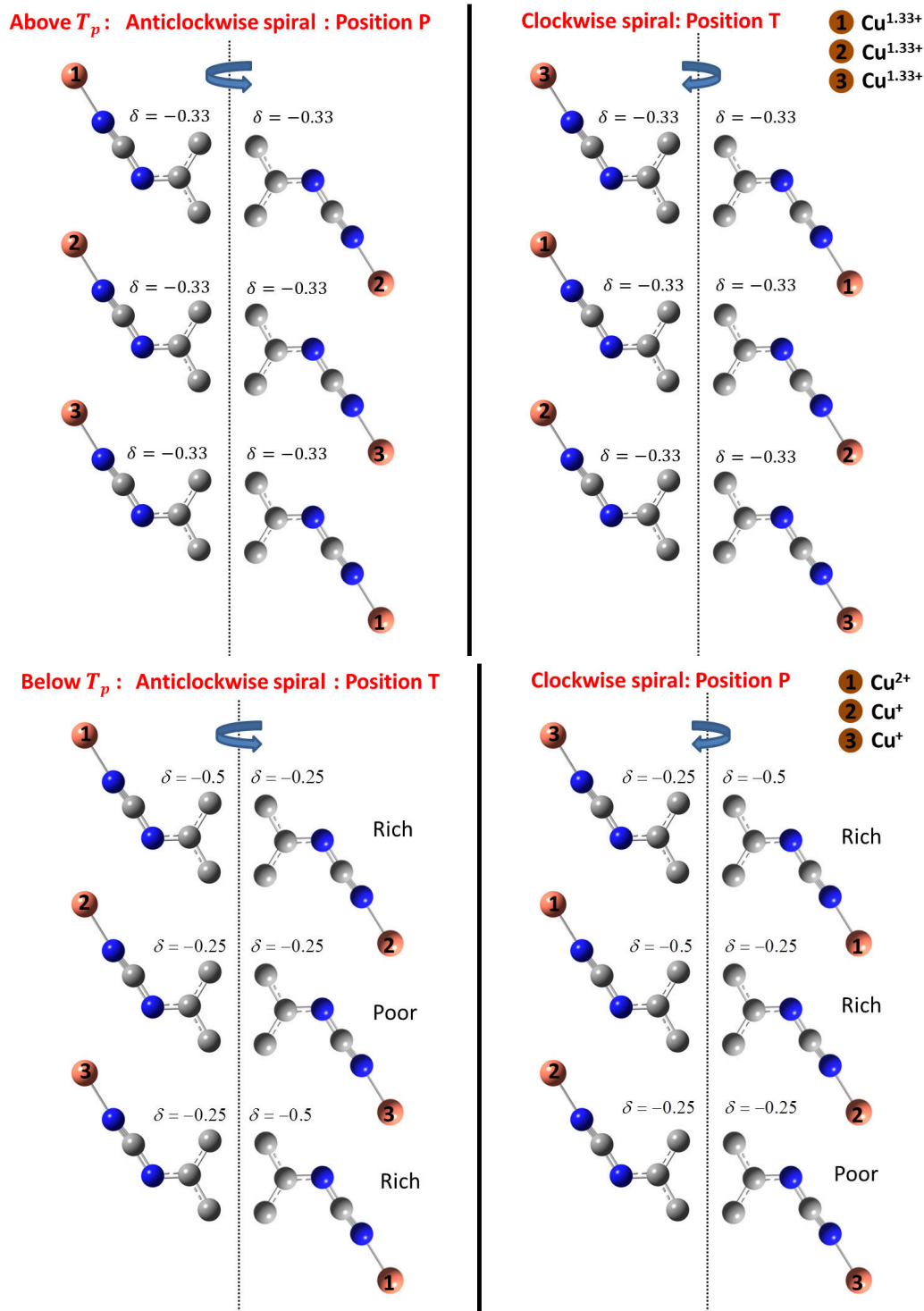


Figure 5.19: Schematics to show the charge distributions along the anticlockwise and clockwise asymmetry units of DCNQi domains. Above phase transition temperature  $T_p$ , each DCNQi asymmetry unit accepts equal charge ( $-0.33$ ). Frustration among DCNQi domains and the charge ordering at the copper sites lead to charge disproportionation as shown in the bottom panel. There is a total of four crystallographically independent charge-rich DCNQi centres and two independent centres for charge-poor DCNQIs. This charge distribution arrangement is derived from the low temperature structure described in Figure 5.18. The maximum charges that could be accepted by each asymmetry centre of the DCNQi crystals are shown. Note that the range for the charge distribution is given by  $-0.75 \leq \delta \leq -0.5$ , into which  $\delta = -0.67$  of the three-fold periodicity falls.

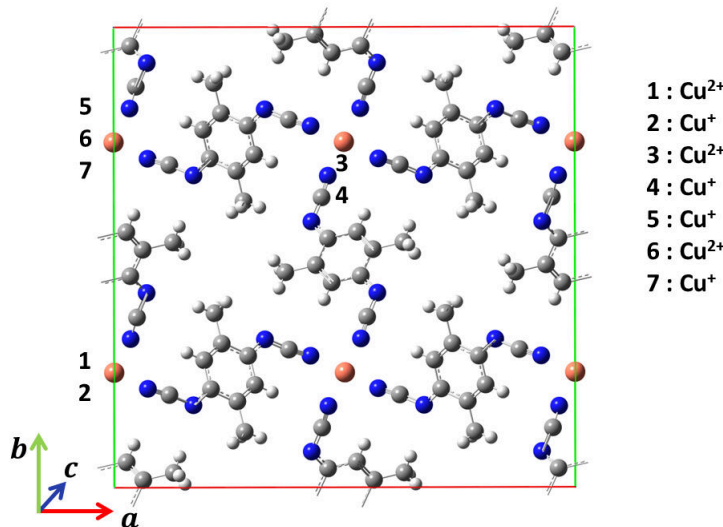


Figure 5.20: Projection of the proposed Cu-DCNQUI crystal structure with subgroup,  $P\bar{4}$ , along the  $c$ -axis. The positions for the seven (7) crystallographically independent copper ions refined by Kobayashi *et al.* [76] are shown. This is consistent with what was described in Figure 5.18. Together with these seven independent copper ions, six (6) DCNQUI (three at "clockwise centres" and three at "anticlockwise centres") form asymmetry unit of the superstructure ( $a \times b \times 3c$ ) below phase transition temperature.

at 115 K [76], where they presumably only experience slight longitudinal shifts, based on the Coulombic repulsion between the copper ions. The  $\text{Cu}^{2+} \dots \text{Cu}^+$  distance is between  $3.77 - 3.93 \text{ \AA}$ , while that of  $\text{Cu}^+ \dots \text{Cu}^+$  distance is between  $3.56 - 3.74 \text{ \AA}$  as reported by Ref. [76]. The average Cu-DCNQUI structures refined by X-ray diffraction analysis pointed out that the positions of these copper ions at low temperature supersede the possible longitudinal and/or transverse displacements. It is therefore justifiable to use these copper ions's positions together with the corresponding low temperature DCNQUI structural data in the simulation. The low temperature data refined by Sinzger *et al.* [64] for the deuterated structure was at 20 K, which is justifiable for phase transition at 73 K. The halogenated structure, which undergoes phase transition at 156 K, was refined at 100 K by Kato *et al.* [65]. The effective modulation of electron density from the metallic to the insulating phases of these structures are incorporated by displacing the unit cells by both the corresponding unit cell's contraction along the  $c$ -axis and expansion along  $a$  and  $b$  axes. The diffraction patterns obtained along  $[010]$  zone axis are shown in Figure 5.22.

A drastic change in the intensity distribution profile along the  $\{h\ 0\ l\}$  Bragg reflections (along  $c$ -axis) is evident. One fundamental reason for this drastic change is the broken lattice symmetry, which leads to the redistribution of electron density across the scattering domains of Cu-DCNQUI structures below phase transition temperature. Moreover, the structural change and/or evolution in DCNQUI salts is accompanied by electronic transition, which is manifested by the gradual development of commensurate charge density waves on the DCNQUI columns. Furthermore, the appearance of the 3-fold superlattice reflections reveals a characteristic coupling between CDW signatures and charge orderings (CO) at low temperature. The energy required to totally suppress these charge density wave orders is interrelated with the CDW-CO coupling strength, which will ultimately determine the optical excitation density, the temperature window and the characteristic time constants obtainable through ultrafast electron diffraction experiments.

Notably, the CDW reflections are comparatively weak. Whereas there are sharp drops in the Bragg intensities observable at low temperature, energy-momentum conservation of the observable Bragg intensities would mean that a particular Bragg peak, say  $(3\ 0\ 1)$  peak, splits into 3 distinct reflections:  $(3\ 0\ 1)$  (Bragg),  $(3\ 0\ 1/3)$  (CDW1) and  $(3\ 0\ 2/3)$  (CDW2); all adding

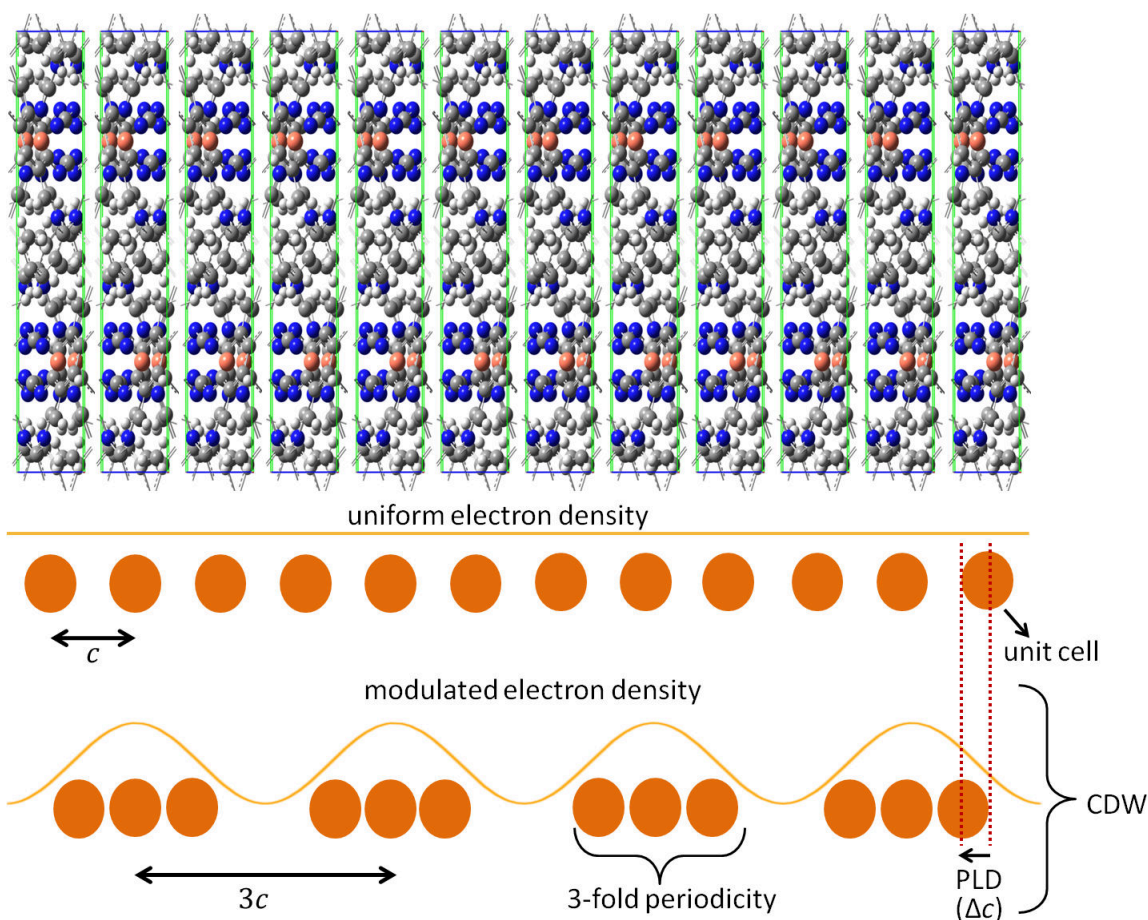


Figure 5.21: Schematics to illustrate the 3-fold modulation of the DCNQI crystal lattice. The electron density is uniform in the unmodulated lattice of the room temperature DCNQI structures, and defined by the dimension  $a \times b \times c$ . The electron density is periodically modulated by distorting the lattice by  $\Delta c$  along the  $c$ -axis. Two unit cells are moved towards a central reference unit cell. This results into a 3-fold periodicity – a signature of the low temperature structure, where there is a coupling between charge ordering on the copper atoms and charge density waves on the DCNQI columns. The resulting superstructure dimension below phase transition temperature is  $a \times b \times 3c$ .

up to the room temperature intensity amplitude (See Figure 5.8 for peaks identification). The superlattice reflections shown in Figure 5.22 reveal a characteristic trimerisation of the room temperature unit cells, giving rise to charge wave vector  $\mathbf{q}_{\text{CDW}} = \frac{1}{3}\mathbf{c}^*$ .

Characterising the strengths of the CDW peaks in the halogenated and deuterated structures, the author integrated over the 3-fold reflection orders as designated by the boxes shown in Figure 5.22. It was found that all CDW peaks' intensities were on the average between 20 – 30 % of the calculated low temperature Bragg intensities, as shown in Figure 5.23. All the  $\{0\ 0\ l\}$  CDW peaks (or reflections) are evidently strong, sometimes suppressing the main Bragg reflections. For example, the normalised integrated intensities in  $d_6$  structure along the  $\{h\ 0\ 1\}$  reflections reveal that the  $\{0\ 0\ 1/3\}$  reflection has the strongest intensity, in contrast to that of halogenated structure where it is 70% of the  $\{0\ 0\ 1\}$  peak. Furthermore, it is evident that the CDW spots are comparatively of the same strength for all reflections' orders (i.e.,  $\{h\ 0\ l\}$  reflections along  $c$ -axis).

We showed in the previous section that the Bragg intensities fluctuate as the crystal undergoes cooling, such that an initial drop and/or increase in intensity arises from the redistribution of the overall crystal's electron density. Thus, a direct comparison between the average Bragg

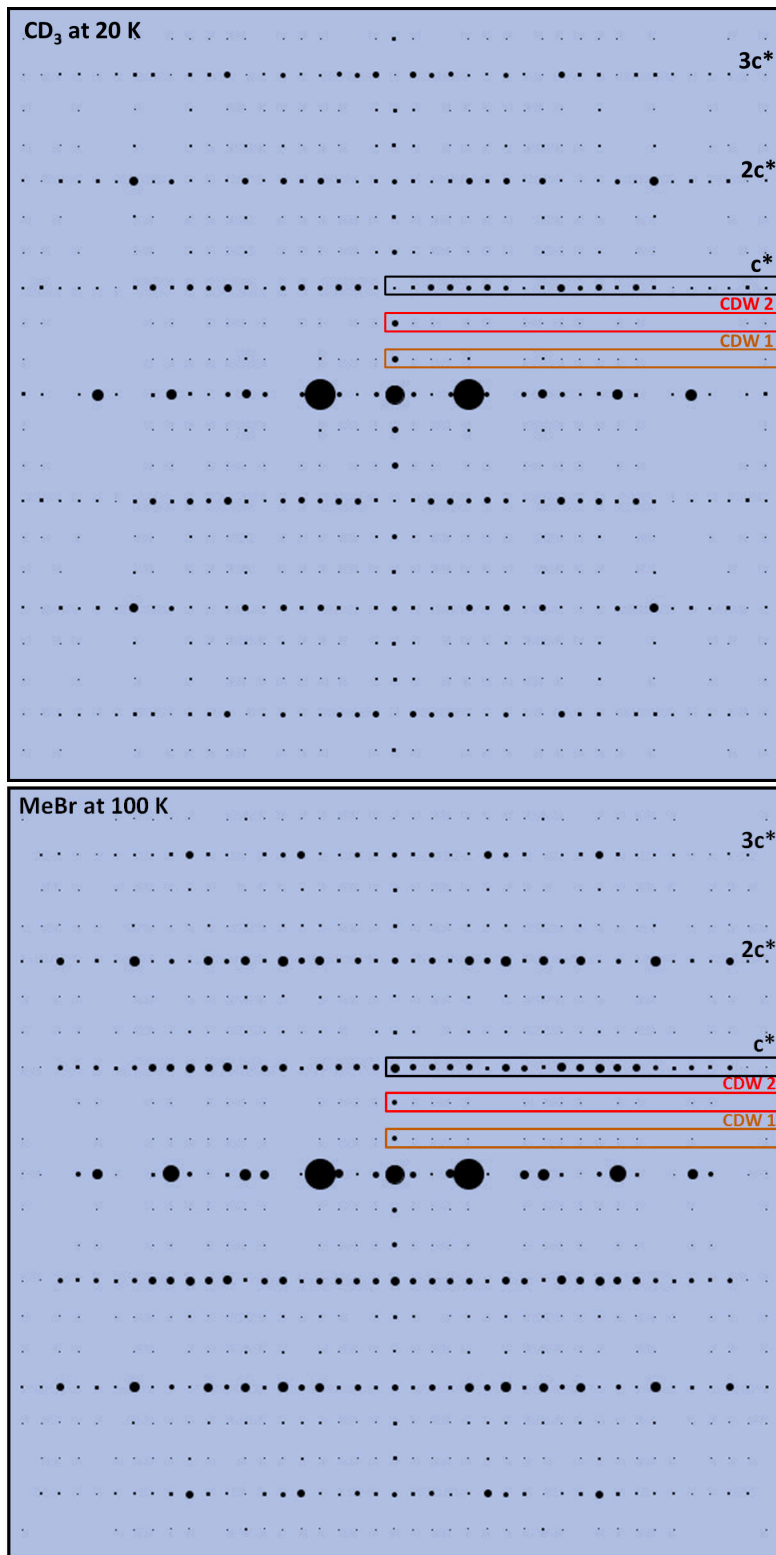


Figure 5.22: Commensurate charge density wave formation in the insulating phases of the dueterated ( $d_6$  at 20 K) and halogenated (MeBr at 100 K) structures. The structures evolve into a three-fold periodicity, labelled as CDW1, CDW2 and  $c^*$ . The charge density wave spots are comparatively weak. We integrated over the reflections enclosed by the colour boxes, and the resulting graphs are shown in Figure 5.23 (Box  $c^* \equiv \{h 0 1\}$ , CDW1  $\equiv \{h 0 1/3\}$  and CDW2  $\equiv \{h 0 2/3\}$  reflections). A combination of strong electron-phonon and electron-electron couplings between charge orderings at the copper sites and the gradual charge density wave formation on the DCNQI columns are envisaged. See text for detail.

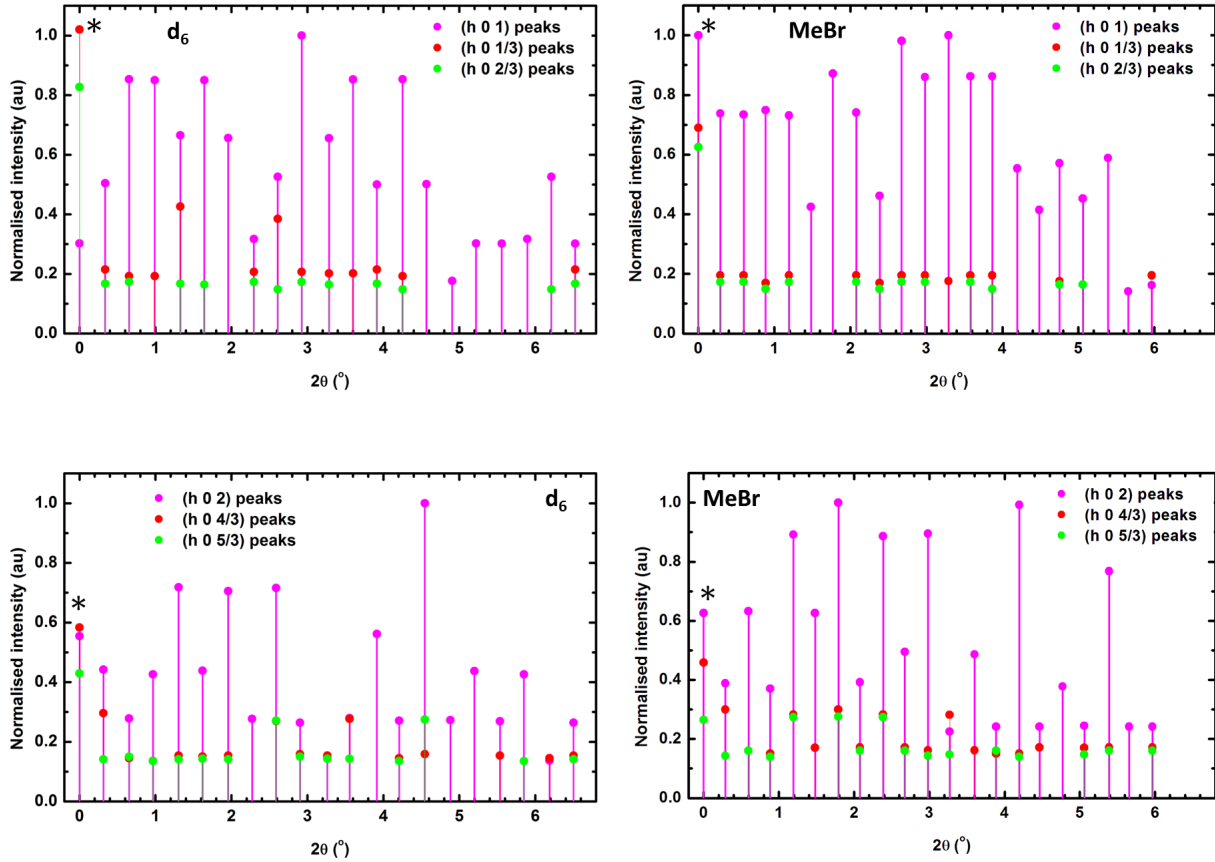


Figure 5.23: Normalised Bragg reflections' integrated intensities of the insulating phases of the deuterated and halogenated structures along the first and second order reflections (Top panel:  $\mathbf{c}^* \equiv \{h 0 1\}$ , CDW1  $\equiv \{h 0 1/3\}$  and CDW2  $\equiv \{h 0 2/3\}$  reflections; Bottom panel:  $2\mathbf{c}^* \equiv \{h 0 2\}$ , CDW1  $\equiv \{h 0 4/3\}$  and CDW2  $\equiv \{h 0 5/3\}$  reflections). The charge density wave spots are of equal strengths and on the average between 20–30 % of the host lattice Bragg reflections. It is interesting to note that the CDW spots along the  $\{0 0 l\}$  reflections (marked with \* on the figures) are quite strong. See text for detailed discussion.

intensity at room temperature and those obtained below phase transition temperature reveals that the CDW peak is on the average 7% of the Bragg intensities. However, the change in the crystal symmetry redefines the electron-poor and electron-rich Bragg planes. The DCNQi salts lock into a new symmetry, ( $P\bar{4}$ ), at and below phase transition temperature, where unlike in the room temperature structures, there are no systematic absences (forbidden reflections). It is therefore tricky to compare the intensities of the room and the low temperature structures, as the Bragg planes are defined differently in crystal lattices of different symmetries.

Each of the Cu-DCNQi structures with the deuterated and the halogenated radicals evolves such that new reflections appear along the  $\mathbf{a}^*$ -axis. Due to the change in the crystal symmetry from one lattice type to another ( $I \rightarrow P$ ), it appears as if electrons are removed and transported from the scattering domains describing the room temperature host lattice Bragg reflections to the erstwhile *forbidden* scattering domains, marked with zero electron density. From the electronic conservation point of view, the population of electron density of states of these forbidden domains ultimately leads to the depletion of the density of states of the host lattice Bragg reflections. This depletion leads to the reduction in the amplitudes of the observable Bragg reflections below phase transition temperatures.

The transport of commensurate CDW signatures in Cu-DCNQi structures is envisaged to arise from the *collapse* of the host lattice Bragg reflections along the  $\mathbf{c}^*$ -axis. A quite phenomenal

and collective electron density transport could then be associated with Cu-DCNQI structures at low temperature: (a) The emergence of two CDW reflection rows in between every two host lattice reflection orders relates to the longitudinal modulation of electron density of states along the  $c^*$ -axis; and (b) the appearance of Bragg reflections at the erstwhile forbidden domains (above phase transition temperature) relates to the transversal redistribution of electron density of states along the  $a^*$ -axis.

The progressive structural evolutions in the deuterated and the halogenated structures are revealed by electron diffraction simulations along the  $[010]$  ( $c|a$  plane) and the  $[001]$  ( $b|a$  plane) zone axes, as shown in Figures 5.24 and 5.25. Both zone axes' diffraction patterns revealed progressive changes in the Bragg reflections' intensity distribution profile in both structures.

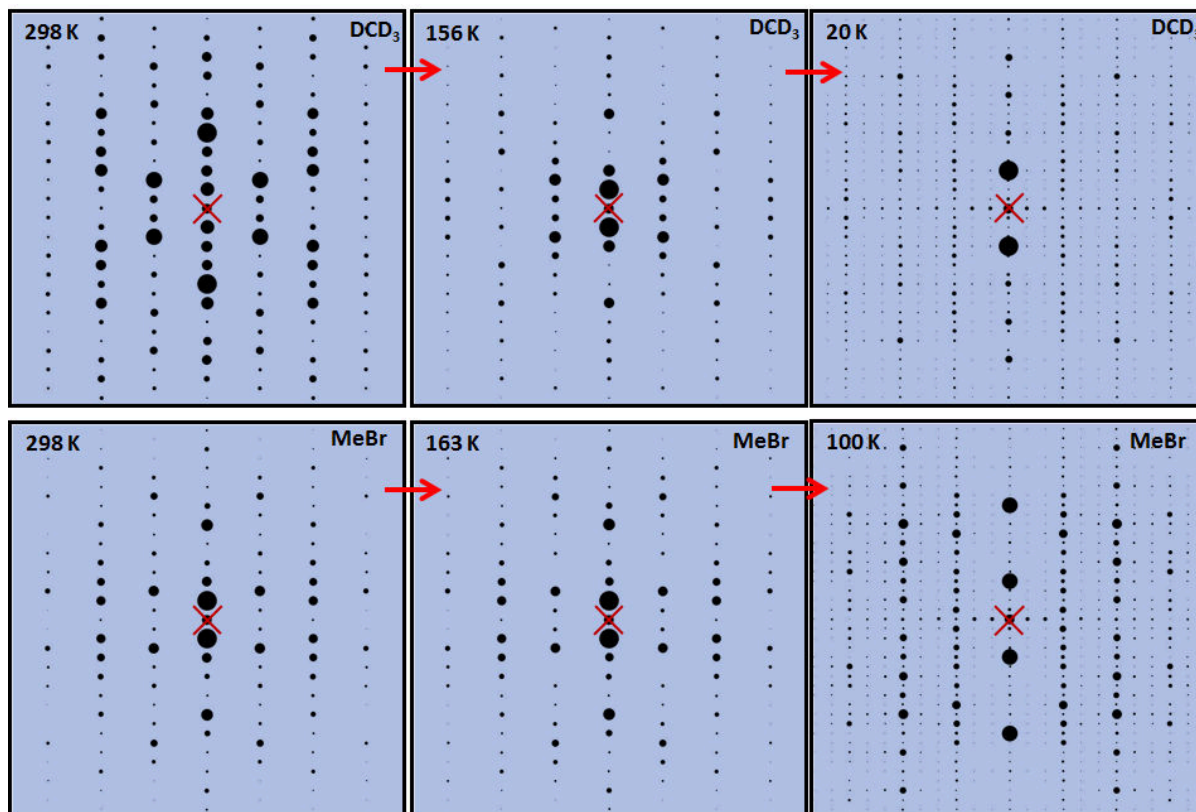


Figure 5.24: Structural evolution in the deuterated ( $CD_3$ ) and the halogenated ( $MeBr$ ) Cu-DCNQI structures along the  $c - a$  plane ( $[010]$  zone axis). At room temperature (298 K; left panel), it is evident that the scattering domains in these structures have different electron density population. This difference is adjudged to be due to different enhanced density of states, which are influenced by electron donating ( $CD_3$ ) and electron withdrawing ( $MeBr$ ) radicals. At the intermediate temperatures (middle panel), electron density populations in both structures are similar. This is envisaged to be due to the higher intensive lattice deformation experienced by the dueterated Cu-DCNQI, in contrast to the halogenated Cu-DCNQI structure. Both structures lock into a commensurate charge wave phase below their phase transition temperatures (right panel).

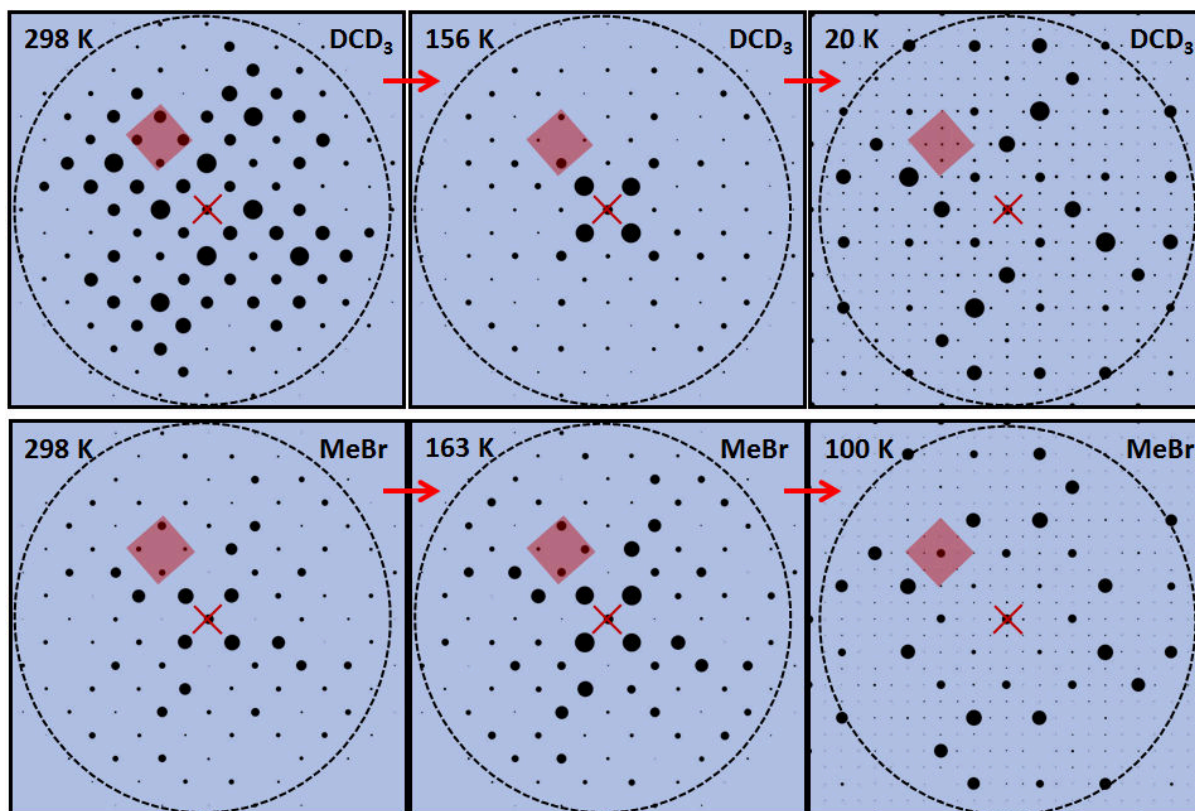


Figure 5.25: Structural evolution in the deuterated ( $\text{CD}_3$ ) and the halogenated ( $\text{MeBr}$ ) Cu-DCNQi structures along the  $b|a$  plane ( $[001]$  zone axis). The progressive nature of the structural evolution (from  $I \rightarrow P$  type lattice) in both structures is emphasised and more instructive along this zone axis. The enhanced density of states in the deuterated Cu-DCNQi structure manifests as enhanced scattering domains leading to strong families of Bragg reflections, in contrast to the halogenated Cu-DCNQi structure, whose Bragg reflections are influenced by the associated high electron affinity and poor scattering domains. The highlighted regions show a progressive different electron density population, as the structures undergo phase transitions, and point to a reduced Brillouin zone below the respective transition temperatures.

Interpreting the progressive structural evolution in Cu-DCNQi structures, we make the following remarks:

1. Relative to the electron diffraction patterns obtained at room temperature, different intensity distributions of the host lattices' Bragg reflections observed at low temperature are attributed to intensive lattice deformation, electron-lattice couplings and change in Bravais lattice type ( $I \rightarrow P$ ).
2. The fluctuation of the Bragg reflections during phase transition leads to the reduction and/or increase in the Bragg reflections at low temperatures. For experimental consideration, weaker reflections at phase transition will collectively give rise to high signal-to-noise ratio, which may affect an accurate characterisation of the CDW signatures.
3. The collective freezing of electron density on DCNQi domains along  $c$ -axis mediates strong electron-electron and/or electron phonon couplings at low temperature.
4. Enhancement of density of states in the deuterated Cu-DCNQi structure translates to strong families of Bragg reflections at room temperature. At intermediate temperature

(156 K), the intensity distribution of these strong reflections in the deuterated Cu-DCNQi structure changes to those found in the halogenated Cu-DCNQi structure. Both structures lock into a similar commensurate charge density wave phase below their respective phase transition temperatures.

5. In the halogenated Cu-DCNQi structures, the high electron affinity and the associated weak scattering centres of the halogens mediate a rather weakly enhanced density of states, such that the overall observable Bragg reflections are much weaker compared to those obtained from the deuterated Cu-DCNQi structure at room temperature. A case for electron donating and electron withdrawing radicals, respectively in the deuterated and the halogenated Cu-DCNQi structures account for the difference in their enhanced density of states.
6. The formation of charge density waves arises from an antiphase modulation of electron density along the DCNQi columns and a simultaneous charge orderings at the copper atoms' sites.

An overview of experimental considerations on structural transitions in Cu-DCNQi structures, via diffraction analysis, is discussed in the next section.

## 5.6 Evidence of CDW formation in Cu(MeBr-DCNQi)<sub>2</sub> through X-ray and electron diffraction experiments

### 5.6.1 X-ray diffraction experiment on Cu-DCNQi structures

We carried out an independent X-ray diffraction analysis on Cu(MeBr-DCNQi)<sub>2</sub> and Cu(DCD<sub>3</sub>-DCNQi)<sub>2</sub> (*d*<sub>6</sub>) salts, which are expected to undergo CDW phase transitions at 156 K and 73 K, respectively. We performed this experiment at the Chemistry Department of Stellenbosch University. An APEX DUO single crystal diffractometer with a cooling system (nitrogen gas, minimum temperature = 70 K) was used, such that a crystal sample can realistically be cooled down to 90 K. The crystal sample is rotated by 360° in ~ 1° steps during data collection. This ensures that all zone axes are taken into consideration when analysing the structure of a particular crystal sample. For both samples, three reflection data sets at 298 K, 130 K and 90 K were collected. The samples used in electron and X-ray diffraction experiments are shown in Figure 5.26.

The crystal structure of each sample was solved (or refined) by harvesting the possible *hkl* reflections from the raw data collected at different temperatures. At room temperature, the lattice parameters obtained from each structure agree with and confirm those reported in the literature [64, 65]. Moreover, the coordinates of the atoms of the refined structures were also used to simulate electron diffraction patterns. No phase transition was found in *d*<sub>6</sub>, as expected, but there was a change in the intensity distribution at 130 K, in accordance to what was predicted by the simulation analysis done in Section 5.3. The room temperature data obtained for *d*<sub>6</sub> also confirms the intensity distribution of the simulation and the experimental diffraction patterns shown in Section 5.2. We therefore will focus on Cu(MeBr-DCNQi)<sub>2</sub> in the remaining part of this section.

The observation and/or evidence of CDW formation in Cu-DCNQi salts through experimental diffraction techniques is primarily hampered by a low signal-to-noise ratio. The reported evidence of CDW signatures in the literature [76] is at best noisy and weak and could not be properly characterised or compared to the CDW simulation presented in Section 5.5. We indeed find this to be inherent to Cu-DCNQi salts, as there was a high competition between the signal and the background in the X-ray analysis we carried out at 90 K. After harvesting all the

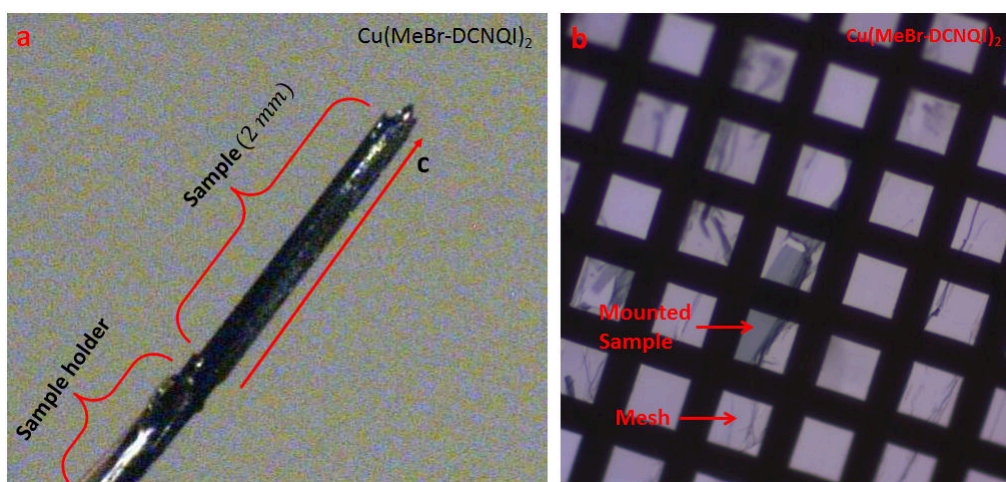


Figure 5.26: Cu-DCNQI samples used in electron and X-ray diffraction experiments. Panel (a) shows a long black needle of  $\text{Cu}(\text{MeBr-DCNQI})_2$  crystal sample for the independent X-ray analysis presented here. Panel (b) shows a thin mounted sample ( $\sim 30$  nm), customarily used for electron diffraction experiments in our laboratory. Whereas thick samples are usable in X-ray diffraction experiments, only thin samples ( $< 100$  nm) are usable in electron diffraction experiments.

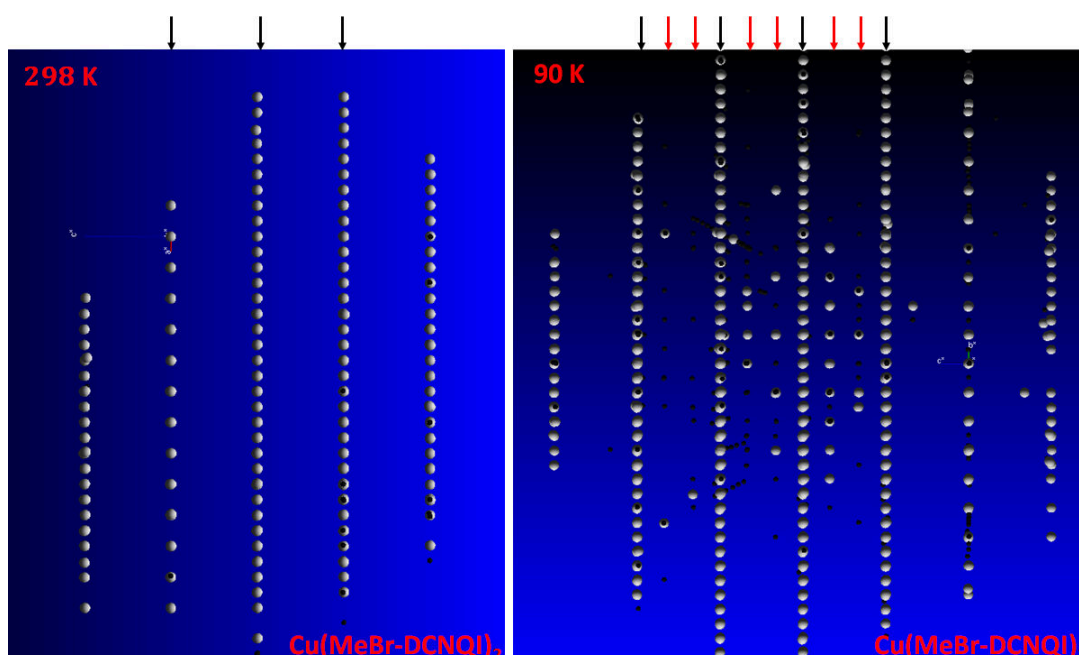


Figure 5.27: Reciprocal lattice representation of  $\text{Cu}(\text{MeBr-DCNQI})_2$  crystal obtained from the raw X-ray diffraction data. The left panel (298 K) shows the lattice positions representing columns of Bragg reflections along  $c^*$ , with tetragonal  $I$  lattice type. In the right panel (90 K), the reflection rows have a tetragonal  $P$  lattice type. The evidence of trimerisation of the crystal's unit cells is revealed by the additional two columns (indicated by red arrows) of reflections in between the main reflection orders (indicated by black arrows). See text for discussion.

possible reflections (at 90 K), the lattice parameters estimated immediately reveal  $a \times b \times 3c$  superstructure dimension. During structural refinement, two competing Bravais lattice types came up: tetragonal  $I$  and  $P$  Bravais lattice types, with  $P$  clearly dominating. We then approached the refinement processes in two steps in order to investigate the possible differences between the structures corresponding to each. Nearly the same lattice parameters were obtained for both lattice types ( $P$ :  $a = b = 21.72 \text{ \AA}$ ,  $c = 11.38 \text{ \AA}$ ;  $I$ :  $a = b = 21.70 \text{ \AA}$ ,  $c = 11.38 \text{ \AA}$ ). Thus, the superstructure dimensions obtained for both lattice types favour trimerisation of the unit cells at phase transition. However, as discussed in the preceding section, the appearance of weak reflections at the erstwhile forbidden domains along  $\mathbf{a}^*$  supports crystal symmetry breaking. Therefore, we believed that the true space group of the low temperature structure has a  $P$  lattice type. With the  $P$  lattice type, the N-Cu-N coordinating angle,  $\alpha$ , necessary for phase transition evolves as:  $125.4^\circ(298 \text{ K}) \rightarrow 128.3^\circ(130 \text{ K}) \rightarrow 128.6^\circ(90 \text{ K})$ , which exactly matches the previously reported values in the literature [65].

Shown in Figure 5.27 (a) and (b) are the reciprocal lattice representations of  $\text{Cu}(\text{MeBr-DCNQI})_2$  crystal obtained after harvesting and processing the raw X-ray diffraction data. The array of grey circles shows lattice positions which are analogous to the locations of reflections along  $\mathbf{c}^*$ . At room temperature, the expected rows of Bragg reflections along  $\mathbf{c}^*$ , with  $I4_1/a$  space group, are clearly represented in Figure 5.27 (a). Based on the space group genealogy analysis in the preceding section,  $P\bar{4}$  space group was chosen at low temperature. The additional two rows of reflections, represented by periodic grey and black circles in Figure 5.27 (b), are unambiguously an evidence of CDW signatures. The Bragg reflection and the CDW rows are indicated by black and red arrows respectively. The non-periodic black circles are scattered background, which evidently compete with CDW signatures. The number of grey and black circles along each row shows that the CDW reflections are weaker compared to the host lattice Bragg reflections.

### 5.6.2 Electron diffraction experiment on Cu-DCNQI in our laboratory

A landmark breakthrough was achieved with the new home-built ultra-high vacuum chamber (operating at  $\sim 10^{-9}$  mbar pressure) in our ultrafast laboratory. The new ultrafast electron diffraction (UED) experimental set-up is more robust and boasts a better coherence length, signal stability, sample loading, among others. The details of the characterisation of the new UED experimental set-up can be found in Bart Smit's Masters' thesis [13]. Having faced with different hurdles for a couple of years, my colleagues recorded the first observation of CDW signatures in  $\text{Cu}(\text{MeBr-DCNQI})_2$  single crystal through the new UED set-up. The observation of CDW signatures through electron diffraction experiment, and a corroborative evidence from a simultaneous X-ray diffraction experiment independently carried out, put to rest the suspicion that the structural transition in Cu-DCNQI salts might not be accompanied with electronic transition, manifested by CDW satellite reflections. Here, we will present an initial characterisation of the low and room temperature electron diffraction patterns obtained.

Shown in Figure 5.28 (a & b) are the  $\text{Cu}(\text{MeBr-DCNQI})_2$  electron diffraction patterns obtained at room (298 K) and low (63 K) temperatures with the new UED set-up. Comparing the diffraction patterns obtained at both temperatures, an evidence of trimerisation of the structure's unit cells is clearly seen (indicated by the red arrows in Figure 5.28 (b)). The Bragg reflections obtainable at both temperatures are relatively strong and well above the background, unlike in the old UED set-up where water condensation affects the quality of the Bragg reflections at low temperature. Examining the zeroth order reflection rows ( $h00$ ), indicated by black arrow) of both high and low temperatures, the appearance of weak reflections at the forbidden domains (indicated by yellow arrows) points to a change in lattice type. The appearance of these weak reflections reinforces the proposition that there is a break in crystal symmetry at phase transition, as we have discussed in Section 5.5. The diffraction pattern shown in Figure 5.28 (b)

has been scaled in order to enhance a better view of the charge density wave signatures, which are evidently weaker compared to the host lattice Bragg reflections.

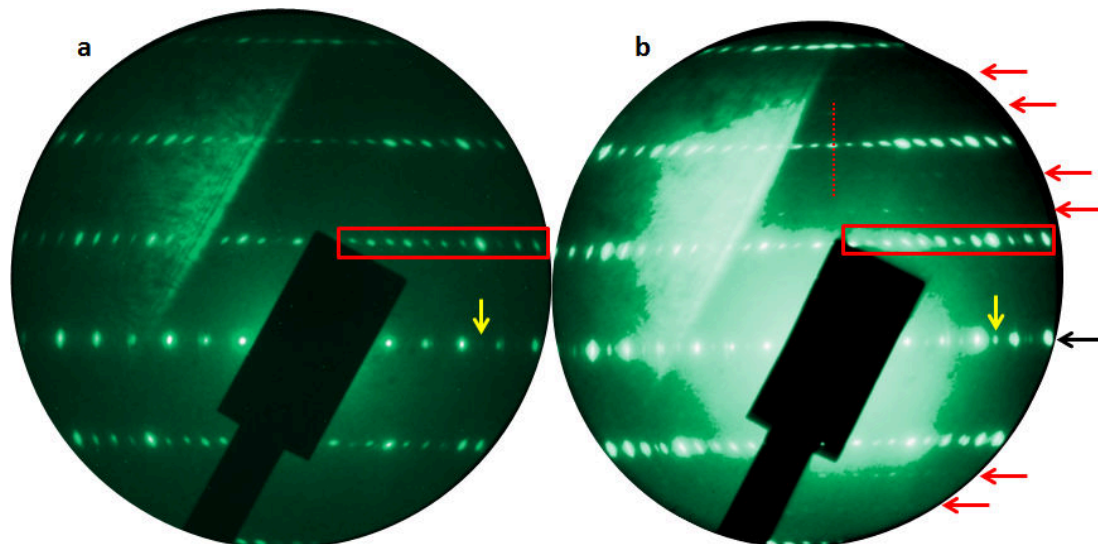


Figure 5.28: First evidence of structural transition in  $\text{Cu}(\text{MeBr-DCNQI})_2$  single crystal with the evidence of charge density wave formation, obtained through the new home-built ultrafast electron diffraction experimental set-up. Panels (a) and (b) show the diffraction patterns obtained at room (298 K) and low (63 K) temperatures. The Bragg reflections obtained at both temperatures are strong and well above the background. The CDW rows are indicated by the red arrows. The diffraction pattern shown in panel (b) has been so scaled in order to enhance a better view of the CDW signatures. A careful examination and comparison of the zeroth order diffraction rows (indicated by black arrow) of both panels shows that weak reflections appear at the erstwhile forbidden domains. The integration over the red boxes and dash lines are shown in Figures 5.29 and 5.30, respectively.

To investigate the possible Bragg reflections' fluctuation during phase transition, we integrated along the first order reflection rows as indicated by red boxes in Figure 5.28 (a) and (b). This integration is an allusion to the structural lability and Debye-Waller fluctuations generally associated with solids undergoing temperature-dependent phase transition, as has been extensively discussed in Section 5.4. The selected reflections' scattering angles are calculated following the same procedure presented in Section 5.2. We then overlap the integrated reflections of both the room and low temperatures, as plotted in Figure 5.29. The intensity signals obtained from both temperatures are scaled and normalised independently to the brightest signals for better comparison. From the plot it is clearly seen that the intensity distribution of these Bragg reflections are different, judging from the neutral, increase or decrease in signal strengths indicated by red arrows. This different intensity distribution points to electron-phonon coupling and a redistribution of electron density across the scattering domains of the crystal.

The CDW signatures in our electron diffraction patterns are characterised as shown in Figure 5.30. Here, to demonstrate the competition between the CDW signals and background oscillations, we have carefully selected the region indicated by red dash line shown in Figure 5.28 (b). This is to compare the strength of the CDW signals to the Bragg signals and to show the competition between the CDW signals and the background. It is evident that the CDW signatures are weak and many CDW domains' signatures are buried in the background. We therefore plot the background oscillations together with the Bragg and CDW signals as shown in Figure 5.30. Based on this, only few CDW signatures could be clearly seen and thus characterised. It is also clear that the strengths of the background oscillations are different from one region of the

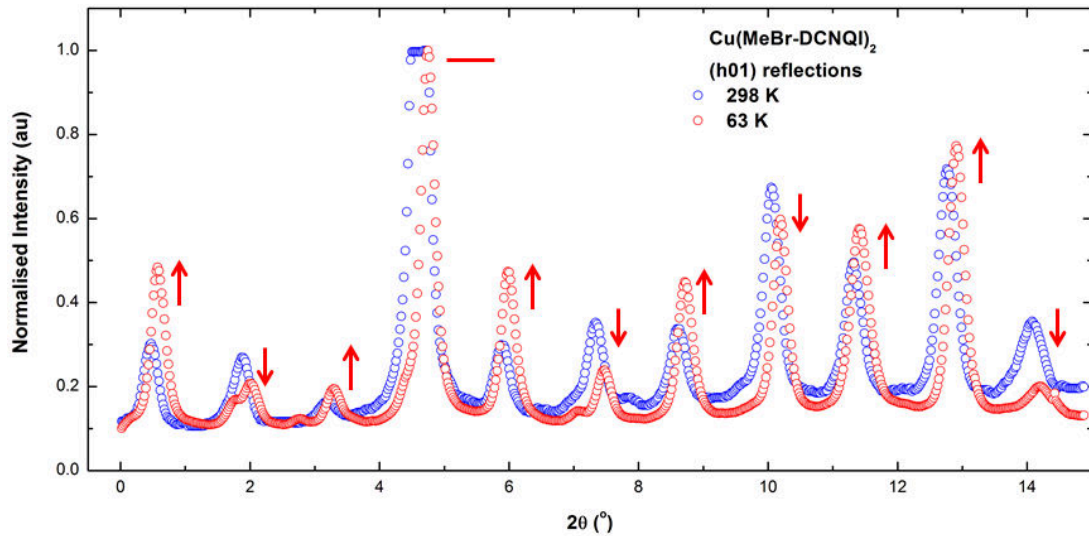


Figure 5.29: Bragg reflections' fluctuation as a pointer to structural lability and Debye-Waller effect associated with Cu-DCNQI structures. Shown is an overlap of the integrated Bragg reflections of the first order diffraction row indicated by red boxes in Figure 5.28 (a & b). The observable change in intensity distribution is attributed to a redistribution of electron density across the crystal's scattering domains and electron-phonon coupling during phase transition. The relative shift of the overlapped integrated signals along x-axis is due to the expansion of unit cell along **a**.

diffraction pattern to the other. Thus, the smoother the background in a region, the stronger are the CDW signatures in that region. With this in mind, it can be estimated from the figure that the average Bragg/CDW signal ratio is 5% taking the background into consideration.

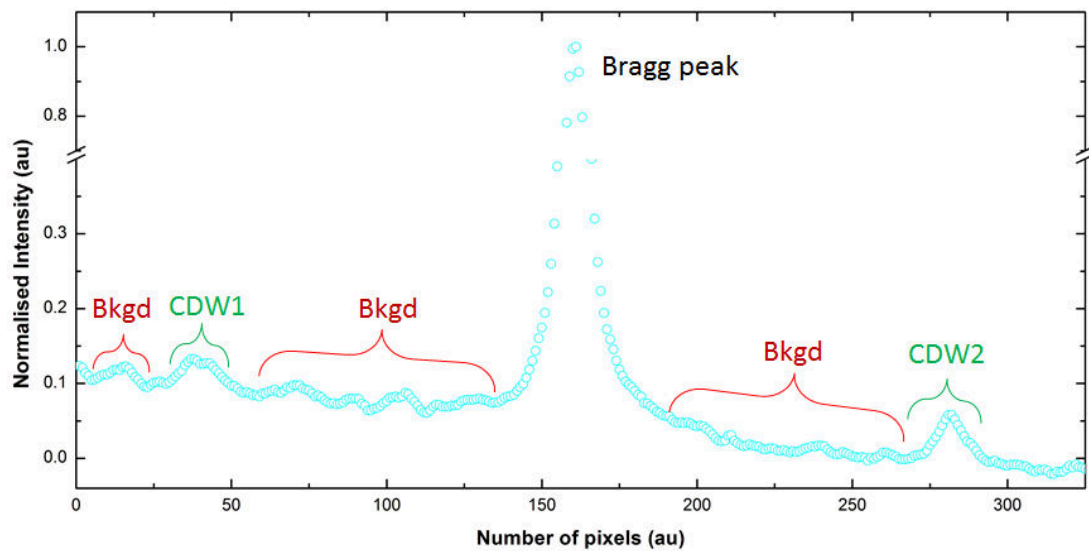


Figure 5.30: Characterisation of CDW signatures obtained in our electron diffraction patterns. The graph shows a line profile along the red dashed line in Figure 5.28. The CDW signatures around the region of smooth background are stronger than those associated with high background oscillations. The estimated Bragg/CDW signal ratio is 5%. Note the break along the vertical axis.

## 5.7 Closing inferences

We have provided a thorough insight into the structural evolution and an accompanied electronic transition in Cu-DCNQI structures through electron diffraction simulation, X-ray and electron diffraction experiments. A strong foundation is thus laid for a correct interpretation of the observable Bragg reflections and the overall structural dynamics in Cu-DCNQI structures. Static CDW signatures in Cu-DCNQI structures obtained through simulation, X-ray and electron diffraction are characterised for the first time. The experimental complications and challenges introduced and discussed in this chapter are resolved through a collaborative work (many students are involved in this project). Electron diffraction experiments on Cu-DCNQI samples are on-going. The results presented here will aid an easy interpretation of the observable commensurate charge density wave signatures and structural transitions in Cu-DCNQI salts. More so, the different phases of structural evolution in Cu-DCNQI salts and the CDW formation thus discussed open up plethora order parameters that could be investigated. Ultrafast time-resolved electron diffraction experimental measurements will provide insights into the details of electron-phonon couplings, the spatial-temporal evolution of optically-induced Cu-DCNQI structures from one phase to the other and the suppressing and/or recovery time constants for the charge density wave signatures.

## Chapter 6

# Summary and conclusion

A systematic study of metal-insulator structural transitions in Cu-DCNQI salts and two members of transition metal dichalcogenides, namely,  $4H_b$ -TaSe<sub>2</sub> and  $1T$ -TiSe<sub>2</sub>, has been done through electron diffraction analysis. A working relationship among X-ray crystallography, electron diffraction simulation and electron diffraction experiment was emphasised.

After introducing the relevant scattering theories that are needed for correct interpretation of electron diffraction patterns, examples of cubic lattices composed of tantalum atoms were used as toy models to provide a background insight into the formation and transport of charge density waves in crystalline solids. The concept of scattering by electron density and electrostatic potential was discussed in relation to sample thickness, quality of diffraction images and the scattering model to employ. Based on the ultrathin sample thickness (25 – 35 nm) customarily used in ultrafast electron diffraction (UED) experiments and the qualitative approach used in interpreting obtainable diffraction patterns, the kinematic scattering model was chosen over the dynamical scattering model.

The modulation of the atomic positions in the cubic lattices of tantalum atoms provided profound insights: (1) The direction of charge density wave depends on the direction of modulation. (2) The determination and the location of reference atoms or reference molecules or reference unit cells points to the existence of charge localisation and/or charge depletion in charge density wave compounds. These reference atoms or unit cells are undistorted or not displaced from their equilibrium positions during phase transitions. (3) Charge density wave phase often favours lower symmetries than those associated with high temperature or metallic phase. (4) The strength of charge density wave signatures depends on the modulation amplitude (i.e., how much the atoms or unit cells are displaced from their equilibrium positions). These insights were valuable for the interpretation of diffraction patterns obtained from the transition metal dichalcogenides and the Cu-DCNQI salts.

The simulated electron diffraction patterns obtained for the metallic and CDW phases in  $4H_b$ -TaSe<sub>2</sub> single crystals were first introduced, discussed and compared with the existing corresponding experimental electron diffraction patterns. A qualitative agreement was found between the high temperature (> 600 K) metallic phase and low temperature (< 410 K) commensurate CDW phase of both simulation and experiment. The analysis of the commensurate CDW signatures in  $4H_b$ -TaSe<sub>2</sub> crystals revealed two intertwined satellite domains (first and second), each consisting of six reflections of unequal amplitudes.

The two satellite domains were decoupled based on two decay mechanisms: 1:6:6 and 1:3:3:3:3. The former involved one coordinating Bragg reflection and six CDW signatures of the first and second domains. The latter, consisting of one coordinating Bragg reflection and three CDW signatures of the two domains' first and second orders, was based on interlayer interaction between the CDW-carrying  $T$  layer and the non-CDW-carrying  $H$  layer. These decay

mechanisms were used to analyse the obtained femtosecond electron diffraction experiment data on  $4H_b$ -TaSe<sub>2</sub> single crystals in our laboratory. The resulting extracted data were analysed in the context of coherent and incoherent relaxations of electronic and lattice orders.

The estimated time constants for the simultaneous temporal evolutions of the two satellite domains were  $\tau_{\text{coh}} = 140$  fs; and  $\tau_{\text{incoh}} = 550$  fs. These estimated time constants point to a strong electron-lattice correlation in  $4H_b$ -TaSe<sub>2</sub> single crystals. The quenching of the satellite reflections was attributed to collective CDW amplitude and phase modes. Associated with variable optical excitation densities, different degrees of suppression were found for the two satellite domains. Due to the same time constants estimated for the evolution of both domains, the phase mode is absent. However, different suppression amplitudes obtained for the two domains point to the existence of amplitude modes. The two domains were fully suppressed with optical excitation density,  $F = 2.6$  mJ/cm<sup>2</sup>.

The analysis of commensurate CDW phase in  $1T$ -TiSe<sub>2</sub> was next reported. The simulated metallic ( $T = 298$  K) and commensurate CDW ( $T = 77$  K) phases' diffraction patterns were consistent with those obtained from the experiment. From the electron diffraction analysis, it was argued that the corresponding density of state translated to each CDW reflection was contributed by the depletion of the density of states of two neighbouring host lattice Bragg reflections. The simulated average CDW signatures' strength was 16% of the host lattice Bragg reflections.

A detailed analysis on the simulated electron diffraction patterns for both the metallic and CDW phases of Cu-DCNQI salts was carried out, based on the X-ray structural refinement data found in the literature. In discussing the general perspectives on the phase transition and CDW formation in these radical anion organic salts, we emphasised that a case for reduced dimensionality in Cu-DCNQI structures is associated with Jahn-Teller distortion that is coupled with steric effects on the DCNQI ligands. Cu-DCNQI salt with methyl radicals is metallic down to a very low temperature because it did not fulfil the requirement for Peierls instability. The threshold coordinating angle  $\alpha_{\text{N-Cu-N}} = 126.4^\circ$  required for phase transition in Cu-DCNQI salts was fulfilled by introducing secondary isotopic effect (deuterating the methyl radicals) and by halogenation of the DCNQI ligands. The halogenated Cu-DCNQI crystal samples were found to have high coordinating angles that led to their high phase transition temperatures (156 – 230 K), while the deuterated counterparts have low phase transition temperatures (58 – 82 K) due to the low coordinating angles ( $\alpha_{\text{N-Cu-N}} \leq 124.8^\circ$ ).

The depletion or the enhancement of Cu-DCNQI scattering domains' density of states was discussed in the contexts of electron donating (deuterated) and electron withdrawing (halogenated) radicals, which are governed by low and high electron affinities, respectively. Thus, the enhanced density of states in the deuterated Cu-DCNQI salts was proposed to translate to the observable high intense families of Bragg reflections at room temperature, in contrast to the weak reflections obtained from the halogenated Cu-DCNQI structures. Attributed to different electron density of states' population in different Cu-DCNQI structures, slight variations were found in the intensity amplitudes obtained from salts with different halogenated radicals.

The structural transition and/or evolution in Cu-DCNQI salts was discussed in the context of fluctuations of host lattice Bragg reflections, and a progressive change in intensity distribution. Two examples representing the deuterated and the halogenated crystal samples were presented and discussed. It was estimated from the calculation of Jahn-Teller modes that the expected reduction in the intensity amplitudes in Cu-DCNQI varies between 3% – 15%, as the crystal samples undergo phase transitions. Structurally refined atomic coordinates at intermediate temperatures, above the phase transition, and obtained from literature, gave an insight into the nature of structural evolution in these organic crystals. The redistribution of electron density in deuterated ( $d_6$ ) Cu-DCNQI salt at 156 K led to its structural transformation. The

transformation was marked by reduced intensity amplitudes and the emergence of the same intensity distribution as found in the halogenated Cu-DCNQi structures at room temperature. The halogenated Cu(MeBr-DCNQi)<sub>2</sub> salt did not show any drastic change, both in intensity amplitudes and intensity distribution at the intermediate temperature (163 K).

The commensurate charge density wave phase in Cu-DCNQi structures was argued to be driven by charge disproportionation (spiral frustration) among the DCNQi scattering domains and the charge orderings at the copper (Cu) sites. The structural analysis carried out revealed the existence of four charge-rich and two charge-poor DCNQi centres ( $-0.75 \leq \delta \leq -0.5$ ). Two domains were identified with these DCNQi centres (anticlockwise and clockwise spirals), which ultimately revealed the charge distribution in Cu-DCNQi structures at low temperature: two copper ions of the same charge are connected by two DCNQi centres (one anticlockwise and one clockwise spirals). The average strength of CDW signatures was found to be between 20 – 30% of the host lattice Bragg reflections and the CDW vector, estimated as  $\mathbf{q}_{\text{CDW}} = 0.33\mathbf{c}^*$ , was consistent with the trimerisation of the real space unit cells.

Static commensurate CDW signatures in Cu(MeBr-DCNQi)<sub>2</sub> salt below phase transition temperature were observed for the first time through X-ray (at 90 K) and electron diffraction (at 63 K) experiments independently carried out in our laboratory and at X-ray Diffraction division of Chemistry Department, Stellenbosch University. Improvements to the femtosecond electron diffraction experimental set-up in our laboratory (new vacuum chamber with  $\sim 10^{-9}$  mbar operating pressure and a better electron probe's transverse coherence length among others) solved the experimental complications introduced by cooling processes. Initial characterisation of commensurate CDW signatures in Cu(MeBr-DCNQi)<sub>2</sub> salt revealed weak satellite reflections, most of which compete with background oscillations. These characteristic weak CDW signatures were observed in both electron and X-ray diffraction measurements we carried out. The strength of CDW signatures in Cu-DCNQi salts depends on many interwoven factors, among which the depth of unit cell modulation, structural lability and associated weak scattering domains stood out. The characterisation of the intensity distribution of the metallic and CDW phase host lattice reflections revealed a fairly stable signal during cooling processes. A full-fledged time-resolved structural dynamics investigation at cryogenic temperatures is under way. This will definitely give more detail into the nature of electron-phonon couplings, CDW recovery or suppressing time constants and the host lattice reflections' relaxation time.

**Recommendation and outlook:** It has been shown that electron diffraction analysis is a powerful technique that can be employed in unravelling structural dynamics in crystalline solids. The same technique used to analyse the structural evolution in  $4H_b$ -TaSe<sub>2</sub> crystals could be used to study correlated materials featuring intertwined superlattice domains. The analysis of structural evolution in Cu-DCNQi salts presented in this study provided a strong foundation for correct interpretation of CDW dynamics in radical anion organic molecular crystals. Furthermore, in relation to DCNQi salts, this dissertation opens up a plethora of order parameters that could be experimentally investigated, such as infra-red active frequency measurements, Jahn-Teller modes and/or Debye-Waller intensity fluctuation, intermediate and metal-insulator optical transitions. A systematic working relationship between X-ray crystallography, ultrafast electron diffraction experiments and electron diffraction simulation and analysis will provide a better insight and a correct interpretation when investigating structural evolution in a crystalline solid. It was shown that the spatial resolution of Bragg reflections obtainable from electron diffraction simulation is par excellence and could be used as a guide to scale the quality of the experimental diffraction patterns. A qualitative, rather than quantitative analysis should then provide better analyses and inferences. The author anticipates intriguing technological advancements in electronics, which will evolve as more insights are being provided by these structural analysis techniques.

# Appendices

## Appendix A

# Decoupled superlattice domain analysis in $4H_b$ -TaSe<sub>2</sub> single crystals

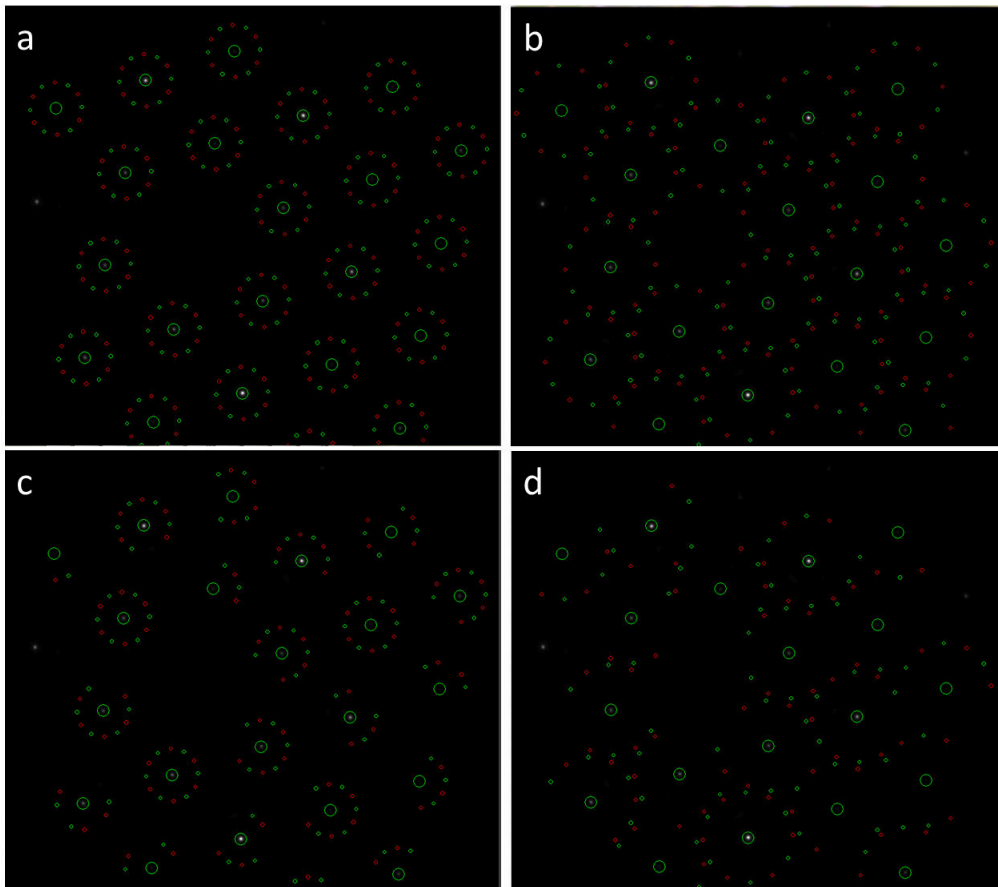


Figure A.1: Selection procedure for charge density wave (CDW) signatures and the host lattice Bragg reflections, during experimental electron diffraction analysis. Shown in (a) and (b) are the possible reflections for the first and second satellite domains, respectively. In panels (c) and (d), the corresponding usable reflections are shown; some reflections have been deselected due to strange artefacts surrounding them. Bragg and CDW reflections' masks are designated by small and big green circles, respectively. Background masks, represented by red circles, are selected correspondingly to the number of reflections usable. These are based on a decoupled superlattice domain analysis presented in Chapter 3.

## Appendix B

# Matlab codes

### Main fit parameters

```
close all;
clc;

%% import data form csv %%
data = importdata('2.3mJ_first_second_domain_matlab.csv');

time = data(:,1); % time
sig = data(:,2); % signal
%size(time)

%% bragg fit initial guess values %%
B_1 = 0.03;
tau_coh = 0.12; % ps
B_2 = -0.03;
tau_icoh = 0.55; % ps
time_shift = -0.27; % ps
int_shift = 0;

initial_fit_par = [A,tau_coh,B,tau_icoh,time_shift,int_shift];

%% plot data with initial guess fit%%
guess_fit = my_fit(initial_fit_par,time);
figure
plot(time,sig,'o',time,guess_fit)

%% fit data %%
options = optimset('MaxFunEvals',1e8,'TolFun',1e-8,'TolX',1e-8,'MaxIter',1e8);
lb=[-inf 0.12 -inf 0.5 -inf -0.0001];
ub=[inf 0.15 inf 0.6 inf 0.0001];
final_fit_par = lsqcurvefit(@my_fit,initial_fit_par,time,sig,lb,ub,options);

%% plot data with final fit%%
fit_time = linspace(-1,4,100);
```

```

final_fit = my_fit(final_fit_par,fit_time') ./2;
figure
plot(time,sig,'o',fit_time,final_fit,'*')

%% export fit transient as txt %%
dlmwrite('fit_Bragg.txt',[fit_time,final_fit],'delimiter','\t','newline','pc');
dlmwrite('fit_par_Bragg.txt',final_fit_par,'delimiter','\t','newline','pc');

```

### Fit function

```

function fit_function = my_fit(par,t)

a = par(1);
t_coh = par(2); % ps
b = par(3);
t_icoh = par(4); % ps
t_shift = par(5); % ps
i_shift = par(6);

SR = 0.6; %system response FWHM in ps

%% generate step function used to make all values before t0 = 0 %%
step_func = 0.5*(tanh(1000*(t+t_shift))+1);

%% two exponentials for fit %%
coh = a*(1-exp(-(t+t_shift)/t_coh));
icoh = b*(1-exp(-(t+t_shift)/t_icoh));

%% sum of exponentials, multiplied with step function %%
fit = step_func.*(coh+icoh) + i_shift;

%% fit function convoluted with temporal response of experiment %%
SR_gauss = exp(-4.*log(2)...
    .*((t-(max(t)+min(t))/2)./SR).^2); % gaussian with FWHM = SR
fit_function = my_conv(t,fit,SR_gauss)';

```

## Convolution function

```
function conv_function = my_conv(time,funct1,funct2)

% pad data left with first value and right with last value
L = length(time);
N_pad = round(L*0.4); % pad data set 40% each side

funct1_pad = [ones(1,N_pad).*funct1(1) funct1' ones(1,N_pad).*funct1(L)];
funct2_pad = [ones(1,N_pad).*funct2(1) funct2' ones(1,N_pad).*funct2(L)];

% figure
% plot(funct1_pad);
% figure
% plot(funct2);

con = conv(funct1_pad,funct2_pad,'same');
conv_function = con(N_pad+1:length(funct1_pad)-N_pad);
```

## Appendix C

# Procedure for electron diffraction simulation

Shown below is the interface for the software used to simulate all the electron diffraction patterns presented in this dissertation. The software was developed by Xingzhong Li [15].

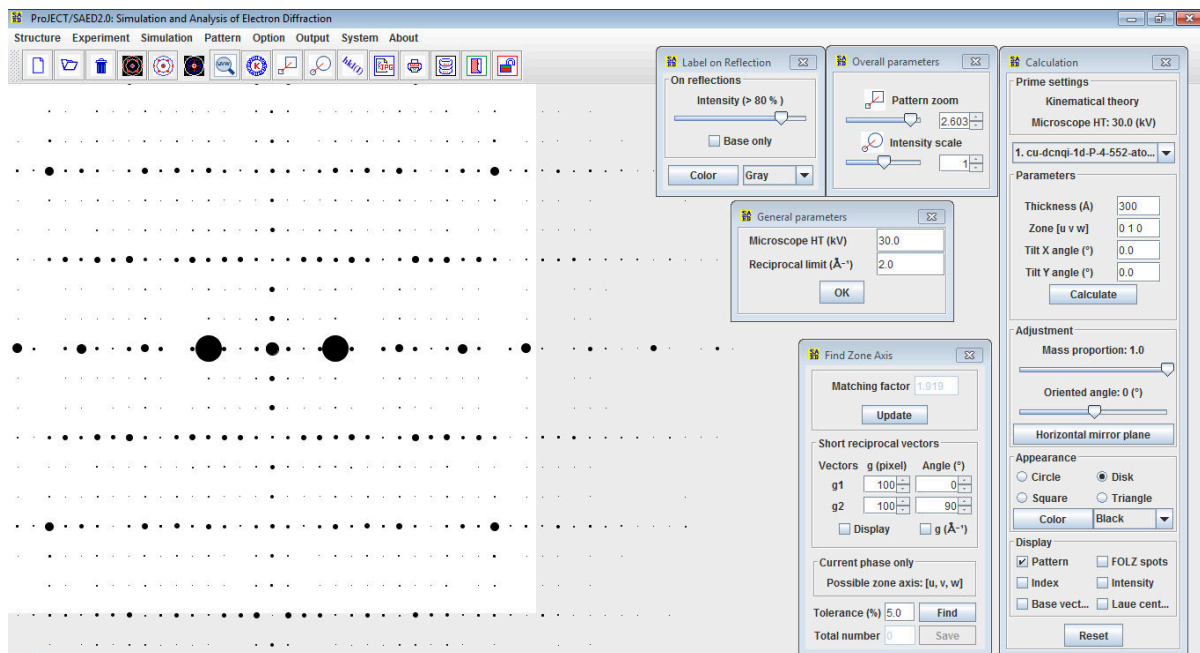


Figure C.1: User-end interface of the software package [15] for simulation and analysis of electron diffraction patterns. Most of the available functions in the software are displayed.

## Appendix D

# CIF codes used in electron diffraction simulation

$4H_b$ -TaSe<sub>2</sub> single crystals: CIF for metallic phase (> 600 K)

```
[titl] Ta-Se2 unit cell
[cell] P 3.455 3.455 25.15 90.0 90.0 120.0
[spgr] 194 P 63/mmc
[na tm] 18
Ta 73      0.0000  0.0000  0.0000  1.0
Ta 73      0.0000  0.0000  0.2500  1.0
Ta 73      0.0000  0.0000  0.5000  1.0
Ta 73      0.0000  0.0000  0.7500  1.0
Ta 73      0.0000  0.0000  1.0000  1.0
Ta 73      1.0000  0.0000  1.0000  1.0
Ta 73      1.0000  0.0000  0.7500  1.0
Ta 73      1.0000  0.0000  0.5000  1.0
Ta 73      1.0000  0.0000  0.2500  1.0
Ta 73      1.0000  0.0000  0.0000  1.0
Se 34      0.6667  0.3333  0.0657  1.0
Se 34      0.6667  0.3333  0.6840  1.0
Se 34      0.6667  0.3333  0.8157  1.0
Se 34      0.3333  0.6667  0.1843  1.0
Se 34      0.3333  0.6667  0.3157  1.0
Se 34      0.3333  0.6667  0.5657  1.0
Se 34      0.3333  0.6667  0.9343  1.0
Se 34      0.6667  0.3333  0.4343  1.0
[bi so] 0.0
[no te] Ref. 34
```

$4H_b$ -TaSe<sub>2</sub> single crystals: CIF for commensurate charge density wave phase (300 K)

```
[titl] Ta-Se2 superstructure cell
[cell] P 12.4572 12.4572 25.15 90.0 90.0 120.0
[spgr] 176 P 63/m
[natm] 18
Ta 73      0.0000   0.0000   0.00000 1.0
Ta 73      0.0695   0.2867   0.00003 1.0
Ta 73      0.1519   0.6347   0.00401 1.0
Ta 73      0.0000   0.0000   0.25000 1.0
Ta 73      0.00746  0.3068   0.25000 1.0
Ta 73      0.1570   0.6154   0.25000 1.0
Ta 73      0.3116   0.2321   0.25000 1.0
Ta 73      0.5366   0.1516   0.25000 1.0
Se 34      0.6667   0.3333   0.06147 1.0
Se 34      0.1241   0.1750   0.07060 1.0
Se 34      0.3540   0.1027   0.06905 1.0
Se 34      0.5929   0.0281   0.06198 1.0
Se 34      0.1979   0.4842   0.06254 1.0
Se 34      0.3333   0.6667   0.18350 1.0
Se 34      0.1803   0.0513   0.18460 1.0
Se 34      0.0257   0.4363   0.18380 1.0
Se 34      0.2569   0.3597   0.18366 1.0
Se 34      0.4875   0.2820   0.18408 1.0
[briso] 0.0
[notel] Ref. 34
```

**1T-TiSe<sub>2</sub> single crystals: CIF for metallic phase (300 K)**

```
[titl] Ti-Se2 unit cell
[cell] P 3.54 3.54 6.008 90.0 90.0 120.0
[spgr] 164 P -3 m 1
[na tm] 2
Ti 22 0.0000 0.0000 0.0000 1.000
Se 34 0.3333 0.6667 -0.2550 1.000
[bi so] 0.0
[no te] Ref. 35
```

**1T-TiSe<sub>2</sub> single crystals: CIF for commensurate charge density wave phase (77 K)**

```
[titl] Ti-Se2 superstructure cell (2.4 percent-Ti, 0.8 percent-Se)
[cell] P 7.08 7.08 12.016 90.0 90.0 120.0
[spgr] 143 P 3
[na tm] 17
Ti 22 0.0000 0.0000 0.0000 1.0
Ti 22 0.4880 0.0000 0.0000 1.0
Ti 22 1.0000 0.0000 0.0000 1.0
Ti 22 0.0000 0.4880 0.0000 1.0
Ti 22 0.5120 0.5120 0.0000 1.0
Ti 22 1.0000 0.4880 0.0000 1.0
Ti 22 0.0000 1.0000 0.0000 1.0
Ti 22 0.4880 1.0000 0.0000 1.0
Ti 22 1.0000 1.0000 0.0000 1.0
Se 34 0.1627 0.3334 0.1275 1.0
Se 34 0.3334 0.1627 0.3725 1.0
Se 34 0.8374 0.1707 0.3725 1.0
Se 34 0.6667 0.3334 0.1275 1.0
Se 34 0.3334 0.6667 0.3725 1.0
Se 34 0.1707 0.8374 0.1275 1.0
Se 34 0.6667 0.8294 0.1275 1.0
Se 34 0.8294 0.6667 0.3275 1.0
[bi so] 0.0
[no te] Ref. 35
```

**Cu[DCD<sub>3</sub>-DCNQI]<sub>2</sub> salts: CIF for metallic phase (300 K)**

```

[titl] Cu-DCNQI asymmetry unit (deuterated salt - d6)
[cell] I 21.6177 21.6177 3.8658 90.0 90.0 90.0
[spgr] 88 I 41/a:2
[na tm] 12
Cu1 29      0.0000      0.2500      -0.3750      1
N2  7       0.7141      0.42261     0.10416     1
N3  7       0.3561      0.32311     -0.13796    1
C4  6       0.4911      0.37031     -0.1767     1
C5  6       0.3611      0.45921     0.29817     1
C6  6       0.6261      0.51681     0.41887     1
C7  6       0.13121     0.53301     0.32657     1
D1  1       0.1421      0.5718      0.4307      1
D2  1       0.1354      0.5361      0.799       1
D3  1       0.1580      0.5012      0.412       1
C8  6       0.2701      0.55511     0.61256     1
D4  1       0.439       0.5921      0.6907      1
[bi so] 0.0
[no te] Ref. 62

```

**Cu[DMe-DCNQI]<sub>2</sub> salts: CIF for metallic phase (300 K)**

```

[titl] Cu-DCNQI asymmetry unit (undeuterated salt - h8)
[cell] I 21.548 21.548 3.871 90.0 90.0 90.0
[spgr] 88 I 41/a:2
[na tm] 12
Cu1 29  0.0000  0.2500  0.1250  1.0
N1  7  0.4269  0.2853 -0.3873  1.0
N2  7  0.3274  0.3217 -0.1461  1.0
C1  6  0.2902  0.2859  0.0477  1.0
C2  6  0.3051  0.2227  0.1376  1.0
C3  6  0.2664  0.1874  0.3289  1.0
C4  6  0.2819  0.1210  0.4195  1.0
C5  6  0.3796  0.2991 -0.2666  1.0
H1  1  0.3422  0.2072  0.0452  1.0
H2  1  0.3113  0.1033  0.2762  1.0
H3  1  0.2513  0.0923  0.3652  1.0
H4  1  0.2933  0.1163  0.6292  1.0
[bi so] 0.0
[no te] Ref. 63

```

**Cu[MeBr-DCNQI]<sub>2</sub> salts: CIF for metallic phase (298 K)**

```
[titl] Cu(MeBr-DCNQI)-RT-Xray-refined_Chem_Dept
[cell] I 21.6597 21.6597 3.8716 90.0 90.0 90.0
[spgr] 88 I 41/a:2
[natm] 13
Cu 29 0.000000 0.250000 0.125 1
Br 35 -0.141026 -0.038037 0.796125 1
N 7 -0.035419 0.176839 0.35966 1
C 6 -0.061386 -0.016865 0.912568 1
N 7 -0.070348 0.076999 0.594668 1
C 6 -0.048516 0.129552 0.476771 1
C 6 -0.026575 -0.055393 1.108929 1
H 1 -0.044000 -0.093377 1.183422 1
C 6 -0.035301 0.040909 0.792357 1
C 6 -0.128416 -0.030569 0.800430 1
H 1 -0.133928 -0.018713 0.558103 1
H 1 -0.157027 -0.006918 0.945149 1
H 1 -0.136832 -0.074773 0.826869 1
[diso] 0.0
[note] This work
```

**Cu[MeCl-DCNQI]<sub>2</sub> salts: CIF for metallic phase (300 K)**

```
[titl] Cu-MeCl-DCNQI-RT
[cell] I 21.559 21.559 3.823 90.0 90.0 90.0
[spgr] 88 I 41/a:2
[natm] 12
Cu1 29 0.0000 0.2500 0.1250 1
N1 7 0.4273 0.2863 -0.3925 1
N2 7 0.3273 0.3213 -0.1527 1
C1 6 0.2911 0.2855 0.0451 1
C2 6 0.3053 0.2228 0.1392 1
C3 6 0.2668 0.1881 0.3312 1
C4 6 0.3799 0.2997 -0.2718 1
C5 6 0.284 0.1159 0.4342 1
H1 1 0.3412 0.2042 0.0442 1
H2 1 0.3136 0.1026 0.3624 1
H3 1 0.2476 0.0895 0.4044 1
H4 1 0.3046 0.1156 0.5854 1
[diso] 0.0
[note] Ref. 63
```

**Cu[BrCl-DCNQI]<sub>2</sub> salts: CIF for metallic phase (300 K)**

```

[titl] Cu(BrCl-DCNQI)_2-RT
[cell] I 21.569 21.569 3.845 90.0 90.0 90.0
[spgr] 88 I 41/a:2
[na tm] 8
Cu1 29 0.0000 0.2500 0.1250 1.0
N1 7 0.4278 0.2870 -0.3936 1.0
N2 7 0.3267 0.3203 -0.1632 1.0
C1 6 0.2907 0.2849 0.0390 1.0
C2 6 0.3057 0.2233 0.1401 1.0
C3 6 0.2679 0.1900 0.3451 1.0
C4 6 0.3793 0.2989 -0.2793 1.0
Br1 35 0.2881 0.1110 0.4602 1.0
[bi so] 0.0
[no te] Ref. 63

```

**Cu[DBr-DCNQI]<sub>2</sub> salts: CIF for metallic phase (300 K)**

```

[titl] Cu(DBr-DCNQI)_2-RT
[cell] I 21.558 21.558 3.896 90.0 90.0 90.0
[spgr] 88 I 41/a:2
[na tm] 9
Cu1 29 0.0000 0.2500 0.1250 1.0
N1 7 0.4271 0.2860 -0.3923 1.0
N2 7 0.3266 0.3200 -0.1652 1.0
C1 6 0.2908 0.2856 0.0365 1.0
C2 6 0.3061 0.2235 0.1463 1.0
C3 6 0.2670 0.1899 0.3422 1.0
C4 6 0.3798 0.2988 -0.2744 1.0
Br1 35 0.2899 0.1092 0.4744 1.0
H1 1 0.3543 0.2064 0.0872 1.0
[bi so] 0.0
[no te] Ref. 63

```

**Cu[DCI-DCNQI]<sub>2</sub> salts: CIF for metallic phase (300 K)**

```
[titl] Cu(DCl-DCNQI)_2-RT
[cell] I 21.55 21.55 3.816 90.0 90.0 90.0
[spgr] 88 I 41/a:2
[naam] 9
Cu1 29 0.0000 0.2500 0.1250 1.0
N1 7 0.4271 0.2874 -0.3947 1.0
N2 7 0.3269 0.3211 -0.1634 1.0
C1 6 0.2911 0.2860 0.0399 1.0
C2 6 0.3061 0.2236 0.1386 1.0
C3 6 0.2671 0.1893 0.3361 1.0
C4 6 0.3796 0.2998 -0.2773 1.0
Cl1 17 0.2686 0.1138 0.4507 1.0
H1 1 0.3473 0.2093 0.0782 1.0
[diso] 0.0
[notu] Ref. 63
```

**Cu[DCD<sub>3</sub>-DCNQI]<sub>2</sub> salts: CIF for charge density wave phase (20 K)**

```
[titl] Deuterated Cu-DCNQI superstructure (modulated along c and a)
[cell] P 21.6192 21.6192 11.6232 90.0 90.0 90.0
[spgr] 81 P -4
[natm] 552
Cu 29 0.0000 0.2500 0.00000 1
N 7 0.0356 0.3232 0.2876 1
N 7 0.0714 0.4224 0.034666667 1
C 6 0.0492 0.3700 0.3282 1
C 6 0.0360 0.4593 0.0993 1
C 6 0.0626 0.5166 0.139933333 1
C 6 0.9731 0.4447 0.129 1
C 6 0.1285 0.5321 0.111466667 1
H 1 0.9558 0.4102 0.1047 1
H 1 0.1412 0.5262 0.038033333 1
H 1 0.1562 0.5042 0.131033333 1
H 1 0.1412 0.5662 0.138366667 1
Cu 29 0.5000 0.2500 0.000000 1
Cu 29 0.5000 0.7500 0.166666667 1
Cu 29 0.0000 0.7500 0.196666667 1
N 7 0.4268 0.2856 0.0376 1
N 7 0.4644 0.6768 0.120933333 1
N 7 0.0732 0.7144 0.204266667 1
N 7 0.9644 0.6768 0.045733333 1
N 7 0.5732 0.7144 0.295733333 1
N 7 0.5356 0.3232 0.2124 1
N 7 0.9268 0.2856 0.129066667 1
N 7 0.5356 0.8232 0.120933333 1
N 7 0.9268 0.7856 0.204266667 1
N 7 0.9644 0.1768 0.2876 1
N 7 0.5732 0.2144 0.0376 1
N 7 0.4644 0.1768 0.2124 1
N 7 0.0732 0.2144 0.129066667 1
N 7 0.0356 0.8232 0.045733333 1
N 7 0.4268 0.7856 0.295733333 1
N 7 0.3276 0.3214 0.118 1
N 7 0.4286 0.5776 0.201333333 1
N 7 0.1724 0.6786 0.284666667 1
N 7 0.9286 0.5776 0.298666667 1
N 7 0.6724 0.6786 0.215333333 1
N 7 0.5714 0.4224 0.132 1
N 7 0.8276 0.3214 0.048666667 1
N 7 0.5714 0.9224 0.201333333 1
N 7 0.8276 0.8214 0.284666667 1
N 7 0.9286 0.0776 0.034666667 1
N 7 0.6724 0.1786 0.118 1
N 7 0.4286 0.0776 0.132 1
```

N 7 0.1724 0.1786 0.048666667 1  
N 7 0.0714 0.9224 0.298666667 1  
N 7 0.3276 0.8214 0.215333333 1  
C 6 0.3800 0.2992 0.0782 1  
C 6 0.4508 0.630 0.161533333 1  
C 6 0.1200 0.7008 0.244866667 1  
C 6 0.9508 0.630 0.005133333 1  
C 6 0.6200 0.7008 0.255133333 1  
C 6 0.5492 0.370 0.1718 1  
C 6 0.8800 0.2992 0.088466667 1  
C 6 0.5492 0.870 0.161533333 1  
C 6 0.8800 0.7992 0.244866667 1  
C 6 0.9508 0.130 0.3282 1  
C 6 0.6200 0.2008 0.0782 1  
C 6 0.4508 0.130 0.1718 1  
C 6 0.1200 0.2008 0.088466667 1  
C 6 0.0492 0.870 0.005133333 1  
C 6 0.3800 0.7992 0.255133333 1  
C 6 0.2907 0.286 0.182633333 1  
C 6 0.4640 0.5407 0.265966667 1  
C 6 0.2093 0.714 0.015966667 1  
C 6 0.964 0.5407 0.234033333 1  
C 6 0.7093 0.714 0.1507 1  
C 6 0.536 0.4593 0.067366667 1  
C 6 0.7907 0.286 0.317366667 1  
C 6 0.536 0.9593 0.265966667 1  
C 6 0.7907 0.786 0.015966667 1  
C 6 0.964 0.0407 0.0993 1  
C 6 0.7093 0.214 0.182633333 1  
C 6 0.464 0.0407 0.067366667 1  
C 6 0.2093 0.214 0.317366667 1  
C 6 0.036 0.9593 0.234033333 1  
C 6 0.2907 0.786 0.1507 1  
C 6 0.2334 0.3126 0.223266667 1  
C 6 0.4374 0.4834 0.3066 1  
C 6 0.2666 0.6874 0.0566 1  
C 6 0.9374 0.4834 0.1934 1  
C 6 0.7666 0.6874 0.110066667 1  
C 6 0.5626 0.5166 0.026733333 1  
C 6 0.7334 0.3126 0.276733333 1  
C 6 0.5626 0.0166 0.3066 1  
C 6 0.7334 0.8126 0.0566 1  
C 6 0.9374 0.9834 0.139933333 1  
C 6 0.7666 0.1874 0.223266667 1  
C 6 0.4374 0.9834 0.026733333 1  
C 6 0.2666 0.1874 0.276733333 1  
C 6 0.0626 0.0166 0.1934 1  
C 6 0.2334 0.8126 0.110066667 1

C 6 0.3053 0.2231 0.212333333 1  
C 6 0.5269 0.5553 0.295666667 1  
C 6 0.1947 0.7769 0.045666667 1  
C 6 0.0269 0.5553 0.204333333 1  
C 6 0.6947 0.7769 0.121 1  
C 6 0.4731 0.4447 0.037666667 1  
C 6 0.8053 0.2231 0.287666667 1  
C 6 0.4731 0.9447 0.295666667 1  
C 6 0.8053 0.7231 0.045666667 1  
C 6 0.0269 0.0553 0.129 1  
C 6 0.6947 0.2769 0.212333333 1  
C 6 0.5269 0.0553 0.037666667 1  
C 6 0.1947 0.2769 0.287666667 1  
C 6 0.9731 0.9447 0.204333333 1  
C 6 0.3053 0.7231 0.121 1  
C 6 0.2179 0.3785 0.1948 1  
C 6 0.3715 0.4679 0.278133333 1  
C 6 0.2821 0.6215 0.028133333 1  
C 6 0.8715 0.4679 0.221866667 1  
C 6 0.7821 0.6215 0.138533333 1  
C 6 0.6285 0.5321 0.0552 1  
C 6 0.7179 0.3785 0.3052 1  
C 6 0.6285 0.0321 0.278133333 1  
C 6 0.7179 0.8785 0.028133333 1  
C 6 0.8715 0.9679 0.111466667 1  
C 6 0.7821 0.1215 0.1948 1  
C 6 0.3715 0.9679 0.0552 1  
C 6 0.2821 0.1215 0.3052 1  
C 6 0.1285 0.0321 0.221866667 1  
C 6 0.2179 0.8785 0.138533333 1  
H 1 0.3398 0.2058 0.188033333 1  
H 1 0.5442 0.5898 0.271366667 1  
H 1 0.1602 0.7942 0.021366667 1  
H 1 0.0442 0.5898 0.228633333 1  
H 1 0.6602 0.7942 0.1453 1  
H 1 0.4558 0.4102 0.061966667 1  
H 1 0.8398 0.2058 0.311966667 1  
H 1 0.4558 0.9102 0.271366667 1  
H 1 0.8398 0.7058 0.021366667 1  
H 1 0.0442 0.0898 0.1047 1  
H 1 0.6602 0.2942 0.188033333 1  
H 1 0.5442 0.0898 0.061966667 1  
H 1 0.1602 0.2942 0.311966667 1  
H 1 0.9558 0.9102 0.228633333 1  
H 1 0.3398 0.7058 0.1453 1  
H 1 0.2238 0.3912 0.121366667 1  
H 1 0.3588 0.4738 0.2047 1  
H 1 0.2762 0.6088 0.288033333 1

```
H 1 0.8588 0.4738 0.2953 1
H 1 0.7762 0.6088 0.211966667 1
H 1 0.6412 0.5262 0.128633333 1
H 1 0.7238 0.3912 0.0453 1
H 1 0.6412 0.0262 0.2047 1
H 1 0.7238 0.8912 0.288033333 1
H 1 0.8588 0.9738 0.038033333 1
H 1 0.7762 0.1088 0.121366667 1
H 1 0.3588 0.9738 0.128633333 1
H 1 0.2762 0.1088 0.0453 1
H 1 0.1412 0.0262 0.2953 1
H 1 0.2238 0.8912 0.211966667 1
H 1 0.2458 0.4062 0.214366667 1
H 1 0.3438 0.4958 0.2977 1
H 1 0.2542 0.5938 0.0477 1
H 1 0.8438 0.4958 0.2023 1
H 1 0.7542 0.5938 0.118966667 1
H 1 0.6562 0.5042 0.035633333 1
H 1 0.7458 0.4062 0.285633333 1
H 1 0.6562 0.0042 0.2977 1
H 1 0.7458 0.9062 0.0477 1
H 1 0.8438 0.9958 0.131033333 1
H 1 0.7542 0.0938 0.214366667 1
H 1 0.3438 0.9958 0.035633333 1
H 1 0.2542 0.0938 0.285633333 1
H 1 0.1562 0.0042 0.2023 1
H 1 0.2458 0.9062 0.118966667 1
H 1 0.1838 0.3912 0.2217 1
H 1 0.3588 0.4338 0.305033333 1
H 1 0.3162 0.6088 0.055033333 1
H 1 0.8588 0.4338 0.194966667 1
H 1 0.8162 0.6088 0.111633333 1
H 1 0.6412 0.5662 0.0283 1
H 1 0.6838 0.3912 0.2783 1
H 1 0.6412 0.0662 0.305033333 1
H 1 0.6838 0.8912 0.055033333 1
H 1 0.8588 0.9338 0.138366667 1
H 1 0.8162 0.1088 0.2217 1
H 1 0.3588 0.9338 0.0283 1
H 1 0.3162 0.1088 0.2783 1
H 1 0.1412 0.0662 0.194966667 1
H 1 0.1838 0.8912 0.111633333 1
Cu 29 0.0000 0.25 0.113333333 1
Cu 29 0.5000 0.75 0.051333333 1
Cu 29 0.0000 0.75 0.077666667 1
Cu 29 0.0000 0.75 0.300666667 1
Cu 29 0.0000 0.25 0.333333333 1
N 7 0.0356 0.3232 0.61247611 1
```

N 7 0.0714 0.4224 0.359542777 1  
C 6 0.0492 0.37 0.65307611 1  
C 6 0.0360 0.4593 0.42417611 1  
C 6 0.0626 0.5166 0.464809443 1  
C 6 0.9731 0.4447 0.45387611 1  
C 6 0.1285 0.5321 0.436342777 1  
H 1 0.9558 0.4102 0.42957611 1  
H 1 0.1412 0.5262 0.362909443 1  
H 1 0.1562 0.5042 0.455909443 1  
H 1 0.1412 0.5662 0.463242777 1  
Cu 29 0.5000 0.2500 0.333333333 1  
Cu 29 0.5000 0.7500 0.50000 1  
Cu 29 0.0000 0.7500 0.53000 1  
N 7 0.4268 0.2856 0.36247611 1  
N 7 0.4644 0.6768 0.445809443 1  
N 7 0.0732 0.7144 0.529142777 1  
N 7 0.9644 0.6768 0.370609443 1  
N 7 0.5732 0.7144 0.620609443 1  
N 7 0.5356 0.3232 0.53727611 1  
N 7 0.9268 0.2856 0.453942777 1  
N 7 0.5356 0.8232 0.445809443 1  
N 7 0.9268 0.7856 0.529142777 1  
N 7 0.9644 0.1768 0.61247611 1  
N 7 0.5732 0.2144 0.36247611 1  
N 7 0.4644 0.1768 0.53727611 1  
N 7 0.0732 0.2144 0.453942777 1  
N 7 0.0356 0.8232 0.370609443 1  
N 7 0.4268 0.7856 0.620609443 1  
N 7 0.3276 0.3214 0.44287611 1  
N 7 0.4286 0.5776 0.526209443 1  
N 7 0.1724 0.6786 0.609542777 1  
N 7 0.9286 0.5776 0.623542777 1  
N 7 0.6724 0.6786 0.540209443 1  
N 7 0.5714 0.4224 0.45687611 1  
N 7 0.8276 0.3214 0.373542777 1  
N 7 0.5714 0.9224 0.526209443 1  
N 7 0.8276 0.8214 0.609542777 1  
N 7 0.9286 0.0776 0.359542777 1  
N 7 0.6724 0.1786 0.44287611 1  
N 7 0.4286 0.0776 0.45687611 1  
N 7 0.1724 0.1786 0.373542777 1  
N 7 0.0714 0.9224 0.623542777 1  
N 7 0.3276 0.8214 0.540209443 1  
C 6 0.38 0.2992 0.40307611 1  
C 6 0.4508 0.63 0.486409443 1  
C 6 0.12 0.7008 0.569742777 1  
C 6 0.9508 0.63 0.330009443 1  
C 6 0.62 0.7008 0.580009443 1

C 6 0.5492 0.37 0.49667611 1  
C 6 0.88 0.2992 0.413342777 1  
C 6 0.5492 0.87 0.486409443 1  
C 6 0.88 0.7992 0.569742777 1  
C 6 0.9508 0.13 0.65307611 1  
C 6 0.62 0.2008 0.40307611 1  
C 6 0.4508 0.13 0.49667611 1  
C 6 0.12 0.2008 0.413342777 1  
C 6 0.0492 0.87 0.330009443 1  
C 6 0.38 0.7992 0.580009443 1  
C 6 0.2907 0.286 0.507509443 1  
C 6 0.464 0.5407 0.590842777 1  
C 6 0.2093 0.714 0.340842777 1  
C 6 0.964 0.5407 0.558909443 1  
C 6 0.7093 0.714 0.47557611 1  
C 6 0.536 0.4593 0.392242777 1  
C 6 0.7907 0.286 0.642242777 1  
C 6 0.536 0.9593 0.590842777 1  
C 6 0.7907 0.786 0.340842777 1  
C 6 0.964 0.0407 0.42417611 1  
C 6 0.7093 0.214 0.507509443 1  
C 6 0.464 0.0407 0.392242777 1  
C 6 0.2093 0.214 0.642242777 1  
C 6 0.036 0.9593 0.558909443 1  
C 6 0.2907 0.786 0.47557611 1  
C 6 0.2334 0.3126 0.548142777 1  
C 6 0.4374 0.4834 0.63147611 1  
C 6 0.2666 0.6874 0.38147611 1  
C 6 0.9374 0.4834 0.51827611 1  
C 6 0.7666 0.6874 0.434942777 1  
C 6 0.5626 0.5166 0.351609443 1  
C 6 0.7334 0.3126 0.601609443 1  
C 6 0.5626 0.0166 0.63147611 1  
C 6 0.7334 0.8126 0.38147611 1  
C 6 0.9374 0.9834 0.464809443 1  
C 6 0.7666 0.1874 0.548142777 1  
C 6 0.4374 0.9834 0.351609443 1  
C 6 0.2666 0.1874 0.601609443 1  
C 6 0.0626 0.0166 0.51827611 1  
C 6 0.2334 0.8126 0.434942777 1  
C 6 0.3053 0.2231 0.537209443 1  
C 6 0.5269 0.5553 0.620542777 1  
C 6 0.1947 0.7769 0.370542777 1  
C 6 0.0269 0.5553 0.529209443 1  
C 6 0.6947 0.7769 0.44587611 1  
C 6 0.4731 0.4447 0.362542777 1  
C 6 0.8053 0.2231 0.612542777 1  
C 6 0.4731 0.9447 0.620542777 1

C 6 0.8053 0.7231 0.370542777 1  
C 6 0.0269 0.0553 0.45387611 1  
C 6 0.6947 0.2769 0.537209443 1  
C 6 0.5269 0.0553 0.362542777 1  
C 6 0.1947 0.2769 0.612542777 1  
C 6 0.9731 0.9447 0.529209443 1  
C 6 0.3053 0.7231 0.44587611 1  
C 6 0.2179 0.3785 0.51967611 1  
C 6 0.3715 0.4679 0.603009443 1  
C 6 0.2821 0.6215 0.353009443 1  
C 6 0.8715 0.4679 0.546742777 1  
C 6 0.7821 0.6215 0.463409443 1  
C 6 0.6285 0.5321 0.38007611 1  
C 6 0.7179 0.3785 0.63007611 1  
C 6 0.6285 0.0321 0.603009443 1  
C 6 0.7179 0.8785 0.353009443 1  
C 6 0.8715 0.9679 0.436342777 1  
C 6 0.7821 0.1215 0.51967611 1  
C 6 0.3715 0.9679 0.38007611 1  
C 6 0.2821 0.1215 0.63007611 1  
C 6 0.1285 0.0321 0.546742777 1  
C 6 0.2179 0.8785 0.463409443 1  
H 1 0.3398 0.2058 0.512909443 1  
H 1 0.5442 0.5898 0.596242777 1  
H 1 0.1602 0.7942 0.346242777 1  
H 1 0.0442 0.5898 0.553509443 1  
H 1 0.6602 0.7942 0.47017611 1  
H 1 0.4558 0.4102 0.386842777 1  
H 1 0.8398 0.2058 0.636842777 1  
H 1 0.4558 0.9102 0.596242777 1  
H 1 0.8398 0.7058 0.346242777 1  
H 1 0.0442 0.0898 0.42957611 1  
H 1 0.6602 0.2942 0.512909443 1  
H 1 0.5442 0.0898 0.386842777 1  
H 1 0.1602 0.2942 0.636842777 1  
H 1 0.9558 0.9102 0.553509443 1  
H 1 0.3398 0.7058 0.47017611 1  
H 1 0.2238 0.3912 0.446242777 1  
H 1 0.3588 0.4738 0.52957611 1  
H 1 0.2762 0.6088 0.612909443 1  
H 1 0.8588 0.4738 0.62017611 1  
H 1 0.7762 0.6088 0.536842777 1  
H 1 0.6412 0.5262 0.453509443 1  
H 1 0.7238 0.3912 0.37017611 1  
H 1 0.6412 0.0262 0.52957611 1  
H 1 0.7238 0.8912 0.612909443 1  
H 1 0.8588 0.9738 0.362909443 1  
H 1 0.7762 0.1088 0.446242777 1

H 1 0.3588 0.9738 0.453509443 1  
H 1 0.2762 0.1088 0.37017611 1  
H 1 0.1412 0.0262 0.62017611 1  
H 1 0.2238 0.8912 0.536842777 1  
H 1 0.2458 0.4062 0.539242777 1  
H 1 0.3438 0.4958 0.62257611 1  
H 1 0.2542 0.5938 0.37257611 1  
H 1 0.8438 0.4958 0.52717611 1  
H 1 0.7542 0.5938 0.443842777 1  
H 1 0.6562 0.5042 0.360509443 1  
H 1 0.7458 0.4062 0.610509443 1  
H 1 0.6562 0.0042 0.62257611 1  
H 1 0.7458 0.9062 0.37257611 1  
H 1 0.8438 0.9958 0.455909443 1  
H 1 0.7542 0.0938 0.539242777 1  
H 1 0.3438 0.9958 0.360509443 1  
H 1 0.2542 0.0938 0.610509443 1  
H 1 0.1562 0.0042 0.52717611 1  
H 1 0.2458 0.9062 0.443842777 1  
H 1 0.1838 0.3912 0.54657611 1  
H 1 0.3588 0.4338 0.629909443 1  
H 1 0.3162 0.6088 0.379909443 1  
H 1 0.8588 0.4338 0.519842777 1  
H 1 0.8162 0.6088 0.436509443 1  
H 1 0.6412 0.5662 0.35317611 1  
H 1 0.6838 0.3912 0.60317611 1  
H 1 0.6412 0.0662 0.629909443 1  
H 1 0.6838 0.8912 0.379909443 1  
H 1 0.8588 0.9338 0.463242777 1  
H 1 0.8162 0.1088 0.54657611 1  
H 1 0.3588 0.9338 0.35317611 1  
H 1 0.3162 0.1088 0.60317611 1  
H 1 0.1412 0.0662 0.519842777 1  
H 1 0.1838 0.8912 0.436509443 1  
Cu 29 0.0000 0.2500 0.446666667 1  
Cu 29 0.5000 0.7500 0.384666667 1  
Cu 29 0.0000 0.7500 0.411 1  
Cu 29 0.0000 0.7500 0.634 1  
Cu 29 0.0000 0.2500 0.666666667 1  
N 7 0.0356 0.3232 0.945809443 1  
N 7 0.0714 0.4224 0.69287611 1  
C 6 0.0492 0.3700 0.986409443 1  
C 6 0.0360 0.4593 0.757509443 1  
C 6 0.0626 0.5166 0.798142777 1  
C 6 0.9731 0.4447 0.787209443 1  
C 6 0.1285 0.5321 0.76967611 1  
H 1 0.9558 0.4102 0.762909443 1  
H 1 0.1412 0.5262 0.696242777 1

H 1 0.1562 0.5042 0.789242777 1  
H 1 0.1412 0.5662 0.79657611 1  
Cu 29 0.5000 0.2500 0.666666667 1  
Cu 29 0.5000 0.7500 0.833333333 1  
Cu 29 0.0000 0.7500 0.863333333 1  
N 7 0.4268 0.2856 0.695809443 1  
N 7 0.4644 0.6768 0.779142777 1  
N 7 0.0732 0.7144 0.86247611 1  
N 7 0.9644 0.6768 0.703942777 1  
N 7 0.5732 0.7144 0.953942777 1  
N 7 0.5356 0.3232 0.870609443 1  
N 7 0.9268 0.2856 0.78727611 1  
N 7 0.5356 0.8232 0.779142777 1  
N 7 0.9268 0.7856 0.86247611 1  
N 7 0.9644 0.1768 0.945809443 1  
N 7 0.5732 0.2144 0.695809443 1  
N 7 0.4644 0.1768 0.870609443 1  
N 7 0.0732 0.2144 0.78727611 1  
N 7 0.0356 0.8232 0.703942777 1  
N 7 0.4268 0.7856 0.953942777 1  
N 7 0.3276 0.3214 0.776209443 1  
N 7 0.4286 0.5776 0.859542777 1  
N 7 0.1724 0.6786 0.94287611 1  
N 7 0.9286 0.5776 0.95687611 1  
N 7 0.6724 0.6786 0.873542777 1  
N 7 0.5714 0.4224 0.790209443 1  
N 7 0.8276 0.3214 0.70687611 1  
N 7 0.5714 0.9224 0.859542777 1  
N 7 0.8276 0.8214 0.94287611 1  
N 7 0.9286 0.0776 0.69287611 1  
N 7 0.6724 0.1786 0.776209443 1  
N 7 0.4286 0.0776 0.790209443 1  
N 7 0.1724 0.1786 0.70687611 1  
N 7 0.0714 0.9224 0.95687611 1  
N 7 0.3276 0.8214 0.873542777 1  
C 6 0.38 0.2992 0.736409443 1  
C 6 0.4508 0.63 0.819742777 1  
C 6 0.12 0.7008 0.90307611 1  
C 6 0.9508 0.63 0.663342777 1  
C 6 0.62 0.7008 0.913342777 1  
C 6 0.5492 0.37 0.830009443 1  
C 6 0.88 0.2992 0.74667611 1  
C 6 0.5492 0.87 0.819742777 1  
C 6 0.88 0.7992 0.90307611 1  
C 6 0.9508 0.13 0.986409443 1  
C 6 0.62 0.2008 0.736409443 1  
C 6 0.4508 0.13 0.830009443 1  
C 6 0.12 0.2008 0.74667611 1

C 6 0.0492 0.87 0.663342777 1  
C 6 0.38 0.7992 0.913342777 1  
C 6 0.2907 0.286 0.840842777 1  
C 6 0.464 0.5407 0.92417611 1  
C 6 0.2093 0.714 0.67417611 1  
C 6 0.964 0.5407 0.892242777 1  
C 6 0.7093 0.714 0.808909443 1  
C 6 0.536 0.4593 0.72557611 1  
C 6 0.7907 0.286 0.97557611 1  
C 6 0.536 0.9593 0.92417611 1  
C 6 0.7907 0.786 0.67417611 1  
C 6 0.964 0.0407 0.757509443 1  
C 6 0.7093 0.214 0.840842777 1  
C 6 0.464 0.0407 0.72557611 1  
C 6 0.2093 0.214 0.97557611 1  
C 6 0.036 0.9593 0.892242777 1  
C 6 0.2907 0.786 0.808909443 1  
C 6 0.2334 0.3126 0.88147611 1  
C 6 0.4374 0.4834 0.964809443 1  
C 6 0.2666 0.6874 0.714809443 1  
C 6 0.9374 0.4834 0.851609443 1  
C 6 0.7666 0.6874 0.76827611 1  
C 6 0.5626 0.5166 0.684942777 1  
C 6 0.7334 0.3126 0.934942777 1  
C 6 0.5626 0.0166 0.964809443 1  
C 6 0.7334 0.8126 0.714809443 1  
C 6 0.9374 0.9834 0.798142777 1  
C 6 0.7666 0.1874 0.88147611 1  
C 6 0.4374 0.9834 0.684942777 1  
C 6 0.2666 0.1874 0.934942777 1  
C 6 0.0626 0.0166 0.851609443 1  
C 6 0.2334 0.8126 0.76827611 1  
C 6 0.3053 0.2231 0.870542777 1  
C 6 0.5269 0.5553 0.95387611 1  
C 6 0.1947 0.7769 0.70387611 1  
C 6 0.0269 0.5553 0.862542777 1  
C 6 0.6947 0.7769 0.779209443 1  
C 6 0.4731 0.4447 0.69587611 1  
C 6 0.8053 0.2231 0.94587611 1  
C 6 0.4731 0.9447 0.95387611 1  
C 6 0.8053 0.7231 0.70387611 1  
C 6 0.0269 0.0553 0.787209443 1  
C 6 0.6947 0.2769 0.870542777 1  
C 6 0.5269 0.0553 0.69587611 1  
C 6 0.1947 0.2769 0.94587611 1  
C 6 0.9731 0.9447 0.862542777 1  
C 6 0.3053 0.7231 0.779209443 1  
C 6 0.2179 0.3785 0.853009443 1

C 6 0.3715 0.4679 0.936342777 1  
C 6 0.2821 0.6215 0.686342777 1  
C 6 0.8715 0.4679 0.88007611 1  
C 6 0.7821 0.6215 0.796742777 1  
C 6 0.6285 0.5321 0.713409443 1  
C 6 0.7179 0.3785 0.963409443 1  
C 6 0.6285 0.0321 0.936342777 1  
C 6 0.7179 0.8785 0.686342777 1  
C 6 0.8715 0.9679 0.76967611 1  
C 6 0.7821 0.1215 0.853009443 1  
C 6 0.3715 0.9679 0.713409443 1  
C 6 0.2821 0.1215 0.963409443 1  
C 6 0.1285 0.0321 0.88007611 1  
C 6 0.2179 0.8785 0.796742777 1  
H 1 0.3398 0.2058 0.846242777 1  
H 1 0.5442 0.5898 0.92957611 1  
H 1 0.1602 0.7942 0.67957611 1  
H 1 0.0442 0.5898 0.886842777 1  
H 1 0.6602 0.7942 0.803509443 1  
H 1 0.4558 0.4102 0.72017611 1  
H 1 0.8398 0.2058 0.97017611 1  
H 1 0.4558 0.9102 0.92957611 1  
H 1 0.8398 0.7058 0.67957611 1  
H 1 0.0442 0.0898 0.762909443 1  
H 1 0.6602 0.2942 0.846242777 1  
H 1 0.5442 0.0898 0.72017611 1  
H 1 0.1602 0.2942 0.97017611 1  
H 1 0.9558 0.9102 0.886842777 1  
H 1 0.3398 0.7058 0.803509443 1  
H 1 0.2238 0.3912 0.77957611 1  
H 1 0.3588 0.4738 0.862909443 1  
H 1 0.2762 0.6088 0.946242777 1  
H 1 0.8588 0.4738 0.953509443 1  
H 1 0.7762 0.6088 0.87017611 1  
H 1 0.6412 0.5262 0.786842777 1  
H 1 0.7238 0.3912 0.703509443 1  
H 1 0.6412 0.0262 0.862909443 1  
H 1 0.7238 0.8912 0.946242777 1  
H 1 0.8588 0.9738 0.696242777 1  
H 1 0.7762 0.1088 0.77957611 1  
H 1 0.3588 0.9738 0.786842777 1  
H 1 0.2762 0.1088 0.703509443 1  
H 1 0.1412 0.0262 0.953509443 1  
H 1 0.2238 0.8912 0.87017611 1  
H 1 0.2458 0.4062 0.87257611 1  
H 1 0.3438 0.4958 0.955909443 1  
H 1 0.2542 0.5938 0.705909443 1  
H 1 0.8438 0.4958 0.860509443 1

```
H 1 0.7542 0.5938 0.77717611 1
H 1 0.6562 0.5042 0.693842777 1
H 1 0.7458 0.4062 0.943842777 1
H 1 0.6562 0.0042 0.955909443 1
H 1 0.7458 0.9062 0.705909443 1
H 1 0.8438 0.9958 0.789242777 1
H 1 0.7542 0.0938 0.87257611 1
H 1 0.3438 0.9958 0.693842777 1
H 1 0.2542 0.0938 0.943842777 1
H 1 0.1562 0.0042 0.860509443 1
H 1 0.2458 0.9062 0.77717611 1
H 1 0.1838 0.3912 0.879909443 1
H 1 0.3588 0.4338 0.963242777 1
H 1 0.3162 0.6088 0.713242777 1
H 1 0.8588 0.4338 0.85317611 1
H 1 0.8162 0.6088 0.769842777 1
H 1 0.6412 0.5662 0.686509443 1
H 1 0.6838 0.3912 0.936509443 1
H 1 0.6412 0.0662 0.963242777 1
H 1 0.6838 0.8912 0.713242777 1
H 1 0.8588 0.9338 0.79657611 1
H 1 0.8162 0.1088 0.879909443 1
H 1 0.3588 0.9338 0.686509443 1
H 1 0.3162 0.1088 0.936509443 1
H 1 0.1412 0.0662 0.85317611 1
H 1 0.1838 0.8912 0.769842777 1
Cu 29 0.000 0.25 0.78000 1
Cu 29 0.5000 0.75 0.71800 1
Cu 29 0.000 0.75 0.744333333 1
Cu 29 0.0000 0.75 0.967333333 1
[briso] 0.0
[note] Refs. 62, 74 and this work
```

Cu[MeBr-DCNQI]<sub>2</sub> salts: CIF for charge density wave phase (90 K)

```
[titl] Cu-(MeBr-DCNQI) superstructure (modulated along c and a)
[cell] P 21.627 21.627 11.34 90.0 90.0 90.0
[spgr] 81 P -4
[natm] 600
Cu 29 0.00000000 0.25000000 0.00000000 1
Br 35 0.860176201 0.963165201 0.265375000 1
N 7 0.965783201 0.178041201 0.119886667 1
C 6 0.939816201 0.984337201 0.304189333 1
N 7 0.930854201 0.078201201 0.198222667 1
C 6 0.952686201 0.130754201 0.158923667 1
C 6 0.974627201 0.945809201 0.036309667 1
H 1 0.957202201 0.907825201 0.061140667 1
C 6 0.965901201 0.042111201 0.264119000 1
C 6 0.872786201 0.970633201 0.266810000 1
H 1 0.867274201 0.982489201 0.186034333 1
H 1 0.844175201 0.994284201 0.315049667 1
H 1 0.864370201 0.926429201 0.275623000 1
Cu 29 0.500000000 0.250000000 0.000000000 1
Cu 29 0.500000000 0.750000000 0.166666667 1
Cu 29 0.000000000 0.750000000 0.196666667 1
Br 35 0.789239201 0.110176201 0.015375000 1
Br 35 0.642228201 0.039239201 0.098708333 1
Br 35 0.713165201 0.892228201 0.182041667 1
Br 35 0.142228201 0.039239201 0.067958333 1
Br 35 0.213165201 0.892228201 0.317958333 1
Br 35 0.360176201 0.963165201 0.234625000 1
Br 35 0.289239201 0.110176201 0.151291667 1
Br 35 0.360176201 0.463165201 0.098708333 1
Br 35 0.289239201 0.610176201 0.182041667 1
Br 35 0.142228201 0.539239201 0.265375000 1
Br 35 0.213165201 0.392228201 0.015375000 1
Br 35 0.642228201 0.539239201 0.234625000 1
Br 35 0.713165201 0.392228201 0.151291667 1
Br 35 0.860176201 0.463165201 0.067958333 1
Br 35 0.789239201 0.610176201 0.317958333 1
N 7 0.574363201 0.215783201 0.203220000 1
N 7 0.536621201 0.824363201 0.286553333 1
N 7 0.928041201 0.786621201 0.036553333 1
N 7 0.036621201 0.824363201 0.213446667 1
N 7 0.428041201 0.786621201 0.130113333 1
N 7 0.465783201 0.178041201 0.046780000 1
N 7 0.074363201 0.215783201 0.296780000 1
N 7 0.465783201 0.678041201 0.286553333 1
N 7 0.074363201 0.715783201 0.036553333 1
N 7 0.036621201 0.324363201 0.119886667 1
N 7 0.428041201 0.286621201 0.203220000 1
```

N	7	0.536621201	0.324363201	0.046780000	1
N	7	0.928041201	0.286621201	0.296780000	1
N	7	0.965783201	0.678041201	0.213446667	1
N	7	0.574363201	0.715783201	0.130113333	1
C	6	0.768067201	0.189816201	0.054189333	1
C	6	0.562588201	0.018067201	0.137522667	1
C	6	0.734337201	0.812588201	0.220856000	1
C	6	0.062588201	0.018067201	0.029144000	1
C	6	0.234337201	0.812588201	0.279144000	1
C	6	0.439816201	0.984337201	0.195810667	1
C	6	0.268067201	0.189816201	0.112477333	1
C	6	0.439816201	0.484337201	0.137522667	1
C	6	0.268067201	0.689816201	0.220856000	1
C	6	0.062588201	0.518067201	0.304189333	1
C	6	0.234337201	0.312588201	0.054189333	1
C	6	0.562588201	0.518067201	0.195810667	1
C	6	0.734337201	0.312588201	0.112477333	1
C	6	0.939816201	0.484337201	0.029144000	1
C	6	0.768067201	0.689816201	0.279144000	1
N	7	0.674203201	0.180854201	0.281556000	1
N	7	0.571550201	0.924203201	0.031556000	1
N	7	0.828201201	0.821550201	0.114889333	1
N	7	0.071550201	0.924203201	0.135110667	1
N	7	0.328201201	0.821550201	0.051777333	1
N	7	0.430854201	0.078201201	0.301777333	1
N	7	0.174203201	0.180854201	0.218444000	1
N	7	0.430854201	0.578201201	0.031556000	1
N	7	0.174203201	0.680854201	0.114889333	1
N	7	0.071550201	0.424203201	0.198222667	1
N	7	0.328201201	0.321550201	0.281556000	1
N	7	0.571550201	0.424203201	0.301777333	1
N	7	0.828201201	0.321550201	0.218444000	1
N	7	0.930854201	0.578201201	0.135110667	1
N	7	0.674203201	0.680854201	0.051777333	1
C	6	0.621650201	0.202686201	0.242257000	1
C	6	0.549718201	0.871650201	0.325590333	1
C	6	0.880754201	0.799718201	0.075590333	1
C	6	0.049718201	0.871650201	0.174409667	1
C	6	0.380754201	0.799718201	0.091076333	1
C	6	0.452686201	0.130754201	0.007743000	1
C	6	0.121650201	0.202686201	0.257743000	1
C	6	0.452686201	0.630754201	0.325590333	1
C	6	0.121650201	0.702686201	0.075590333	1
C	6	0.049718201	0.371650201	0.158923667	1
C	6	0.380754201	0.299718201	0.242257000	1
C	6	0.549718201	0.371650201	0.007743000	1
C	6	0.880754201	0.299718201	0.257743000	1
C	6	0.952686201	0.630754201	0.174409667	1

C	6	0.621650201	0.702686201	0.091076333	1
C	6	0.806595201	0.224627201	0.119643000	1
C	6	0.527777201	0.056595201	0.202976333	1
C	6	0.695809201	0.777777201	0.286309667	1
C	6	0.027777201	0.056595201	0.297023667	1
C	6	0.195809201	0.777777201	0.213690333	1
C	6	0.474627201	0.945809201	0.130357000	1
C	6	0.306595201	0.224627201	0.047023667	1
C	6	0.474627201	0.445809201	0.202976333	1
C	6	0.306595201	0.724627201	0.286309667	1
C	6	0.027777201	0.556595201	0.036309667	1
C	6	0.195809201	0.277777201	0.119643000	1
C	6	0.527777201	0.556595201	0.130357000	1
C	6	0.695809201	0.277777201	0.047023667	1
C	6	0.974627201	0.445809201	0.297023667	1
C	6	0.806595201	0.724627201	0.213690333	1
H	1	0.844579201	0.207202201	0.144474000	1
H	1	0.545202201	0.094579201	0.227807333	1
H	1	0.657825201	0.795202201	0.311140667	1
H	1	0.045202201	0.094579201	0.272192667	1
H	1	0.157825201	0.795202201	0.188859333	1
H	1	0.457202201	0.907825201	0.105526000	1
H	1	0.344579201	0.207202201	0.022192667	1
H	1	0.457202201	0.407825201	0.227807333	1
H	1	0.344579201	0.707202201	0.311140667	1
H	1	0.045202201	0.594579201	0.061140667	1
H	1	0.157825201	0.295202201	0.144474000	1
H	1	0.545202201	0.594579201	0.105526000	1
H	1	0.657825201	0.295202201	0.022192667	1
H	1	0.957202201	0.407825201	0.272192667	1
H	1	0.844579201	0.707202201	0.188859333	1
C	6	0.710293201	0.215901201	0.014119000	1
C	6	0.536503201	0.960293201	0.097452333	1
C	6	0.792111201	0.786503201	0.180785667	1
C	6	0.036503201	0.960293201	0.069214333	1
C	6	0.292111201	0.786503201	0.319214333	1
C	6	0.465901201	0.042111201	0.235881000	1
C	6	0.210293201	0.215901201	0.152547667	1
C	6	0.465901201	0.542111201	0.097452333	1
C	6	0.210293201	0.715901201	0.180785667	1
C	6	0.036503201	0.460293201	0.264119000	1
C	6	0.292111201	0.286503201	0.014119000	1
C	6	0.536503201	0.460293201	0.235881000	1
C	6	0.792111201	0.286503201	0.152547667	1
C	6	0.965901201	0.542111201	0.069214333	1
C	6	0.710293201	0.715901201	0.319214333	1
C	6	0.781771201	0.122786201	0.016810000	1
C	6	0.629618201	0.031771201	0.100143333	1

C	6	0.720633201	0.879618201	0.183476667	1
C	6	0.129618201	0.031771201	0.066523333	1
C	6	0.220633201	0.879618201	0.316523333	1
C	6	0.372786201	0.970633201	0.233190000	1
C	6	0.281771201	0.122786201	0.149856667	1
C	6	0.372786201	0.470633201	0.100143333	1
C	6	0.281771201	0.622786201	0.183476667	1
C	6	0.129618201	0.531771201	0.266810000	1
C	6	0.220633201	0.379618201	0.016810000	1
C	6	0.629618201	0.531771201	0.233190000	1
C	6	0.720633201	0.379618201	0.149856667	1
C	6	0.872786201	0.470633201	0.066523333	1
C	6	0.781771201	0.622786201	0.316523333	1
H	1	0.769915201	0.117274201	0.269367667	1
H	1	0.635130201	0.019915201	0.019367667	1
H	1	0.732489201	0.885130201	0.102701000	1
H	1	0.135130201	0.019915201	0.147299000	1
H	1	0.232489201	0.885130201	0.063965667	1
H	1	0.367274201	0.982489201	0.313965667	1
H	1	0.269915201	0.117274201	0.230632333	1
H	1	0.367274201	0.482489201	0.019367667	1
H	1	0.269915201	0.617274201	0.102701000	1
H	1	0.135130201	0.519915201	0.186034333	1
H	1	0.232489201	0.385130201	0.269367667	1
H	1	0.635130201	0.519915201	0.313965667	1
H	1	0.732489201	0.385130201	0.230632333	1
H	1	0.867274201	0.482489201	0.147299000	1
H	1	0.769915201	0.617274201	0.063965667	1
H	1	0.758120201	0.094175201	0.065049667	1
H	1	0.658229201	0.008120201	0.148383000	1
H	1	0.744284201	0.908229201	0.231716333	1
H	1	0.158229201	0.008120201	0.018283667	1
H	1	0.244284201	0.908229201	0.268283667	1
H	1	0.344175201	0.994284201	0.184950333	1
H	1	0.258120201	0.094175201	0.101617000	1
H	1	0.344175201	0.494284201	0.148383000	1
H	1	0.258120201	0.594175201	0.231716333	1
H	1	0.158229201	0.508120201	0.315049667	1
H	1	0.244284201	0.408229201	0.065049667	1
H	1	0.658229201	0.508120201	0.184950333	1
H	1	0.744284201	0.408229201	0.101617000	1
H	1	0.844175201	0.494284201	0.018283667	1
H	1	0.758120201	0.594175201	0.268283667	1
H	1	0.825975201	0.114370201	0.025623000	1
H	1	0.638034201	0.075975201	0.108956333	1
H	1	0.676429201	0.888034201	0.192289667	1
H	1	0.138034201	0.075975201	0.057710333	1
H	1	0.176429201	0.888034201	0.307710333	1

H	1	0.364370201	0.926429201	0.224377000	1
H	1	0.325975201	0.114370201	0.141043667	1
H	1	0.364370201	0.426429201	0.108956333	1
H	1	0.325975201	0.614370201	0.192289667	1
H	1	0.138034201	0.575975201	0.275623000	1
H	1	0.176429201	0.388034201	0.025623000	1
H	1	0.638034201	0.575975201	0.224377000	1
H	1	0.676429201	0.388034201	0.141043667	1
H	1	0.864370201	0.426429201	0.057710333	1
H	1	0.825975201	0.614370201	0.307710333	1
Cu	29	0.000000000	0.500000000	0.113333300	1
Cu	29	0.500000000	0.750000000	0.051333300	1
Cu	29	0.000000000	0.750000000	0.077667000	1
Cu	29	0.000000000	0.750000000	0.300667000	1
Cu	29	0.000000000	0.250000000	0.333333333	1
Br	35	0.860176201	0.963165201	0.592006393	1
N	7	0.965783201	0.178041201	0.446518060	1
C	6	0.939816201	0.984337201	0.630820727	1
N	7	0.930854201	0.078201201	0.524854060	1
C	6	0.952686201	0.130754201	0.485555060	1
C	6	0.974627201	0.945809201	0.362941060	1
H	1	0.957202201	0.907825201	0.387772060	1
C	6	0.965901201	0.042111201	0.590750393	1
C	6	0.872786201	0.970633201	0.593441393	1
H	1	0.867274201	0.982489201	0.512665727	1
H	1	0.844175201	0.994284201	0.641681060	1
H	1	0.864370201	0.926429201	0.602254393	1
Cu	29	0.500000000	0.250000000	0.333333333	1
Cu	29	0.500000000	0.750000000	0.500000000	1
Cu	29	0.000000000	0.750000000	0.530000000	1
Br	35	0.789239201	0.110176201	0.342006393	1
Br	35	0.642228201	0.039239201	0.425339727	1
Br	35	0.713165201	0.892228201	0.508673060	1
Br	35	0.142228201	0.039239201	0.394589727	1
Br	35	0.213165201	0.892228201	0.644589727	1
Br	35	0.360176201	0.963165201	0.561256393	1
Br	35	0.289239201	0.110176201	0.477923060	1
Br	35	0.360176201	0.463165201	0.425339727	1
Br	35	0.289239201	0.610176201	0.508673060	1
Br	35	0.142228201	0.539239201	0.592006393	1
Br	35	0.213165201	0.392228201	0.342006393	1
Br	35	0.642228201	0.539239201	0.561256393	1
Br	35	0.713165201	0.392228201	0.477923060	1
Br	35	0.860176201	0.463165201	0.394589727	1
Br	35	0.789239201	0.610176201	0.644589727	1
N	7	0.574363201	0.215783201	0.529851393	1
N	7	0.536621201	0.824363201	0.613184727	1
N	7	0.928041201	0.786621201	0.363184727	1

N	7	0.036621201	0.824363201	0.540078060	1
N	7	0.428041201	0.786621201	0.456744727	1
N	7	0.465783201	0.178041201	0.373411393	1
N	7	0.074363201	0.215783201	0.623411393	1
N	7	0.465783201	0.678041201	0.613184727	1
N	7	0.074363201	0.715783201	0.363184727	1
N	7	0.036621201	0.324363201	0.446518060	1
N	7	0.428041201	0.286621201	0.529851393	1
N	7	0.536621201	0.324363201	0.373411393	1
N	7	0.928041201	0.286621201	0.623411393	1
N	7	0.965783201	0.678041201	0.540078060	1
N	7	0.574363201	0.715783201	0.456744727	1
C	6	0.768067201	0.189816201	0.380820727	1
C	6	0.562588201	0.018067201	0.464154060	1
C	6	0.734337201	0.812588201	0.547487393	1
C	6	0.062588201	0.018067201	0.355775393	1
C	6	0.234337201	0.812588201	0.605775393	1
C	6	0.439816201	0.984337201	0.522442060	1
C	6	0.268067201	0.189816201	0.439108727	1
C	6	0.439816201	0.484337201	0.464154060	1
C	6	0.268067201	0.689816201	0.547487393	1
C	6	0.062588201	0.518067201	0.630820727	1
C	6	0.234337201	0.312588201	0.380820727	1
C	6	0.562588201	0.518067201	0.522442060	1
C	6	0.734337201	0.312588201	0.439108727	1
C	6	0.939816201	0.484337201	0.355775393	1
C	6	0.768067201	0.689816201	0.605775393	1
N	7	0.674203201	0.180854201	0.608187393	1
N	7	0.571550201	0.924203201	0.358187393	1
N	7	0.828201201	0.821550201	0.441520727	1
N	7	0.071550201	0.924203201	0.461742060	1
N	7	0.328201201	0.821550201	0.378408727	1
N	7	0.430854201	0.078201201	0.628408727	1
N	7	0.174203201	0.180854201	0.545075393	1
N	7	0.430854201	0.578201201	0.358187393	1
N	7	0.174203201	0.680854201	0.441520727	1
N	7	0.071550201	0.424203201	0.524854060	1
N	7	0.328201201	0.321550201	0.608187393	1
N	7	0.571550201	0.424203201	0.628408727	1
N	7	0.828201201	0.321550201	0.545075393	1
N	7	0.930854201	0.578201201	0.461742060	1
N	7	0.674203201	0.680854201	0.378408727	1
C	6	0.621650201	0.202686201	0.568888393	1
C	6	0.549718201	0.871650201	0.652221727	1
C	6	0.880754201	0.799718201	0.402221727	1
C	6	0.049718201	0.871650201	0.501041060	1
C	6	0.380754201	0.799718201	0.417707727	1
C	6	0.452686201	0.130754201	0.334374393	1

C	6	0.121650201	0.202686201	0.584374393	1
C	6	0.452686201	0.630754201	0.652221727	1
C	6	0.121650201	0.702686201	0.402221727	1
C	6	0.049718201	0.371650201	0.485555060	1
C	6	0.380754201	0.299718201	0.568888393	1
C	6	0.549718201	0.371650201	0.334374393	1
C	6	0.880754201	0.299718201	0.584374393	1
C	6	0.952686201	0.630754201	0.501041060	1
C	6	0.621650201	0.702686201	0.417707727	1
C	6	0.806595201	0.224627201	0.446274393	1
C	6	0.527777201	0.056595201	0.529607727	1
C	6	0.695809201	0.777777201	0.612941060	1
C	6	0.027777201	0.056595201	0.623655060	1
C	6	0.195809201	0.777777201	0.540321727	1
C	6	0.474627201	0.945809201	0.456988393	1
C	6	0.306595201	0.224627201	0.373655060	1
C	6	0.474627201	0.445809201	0.529607727	1
C	6	0.306595201	0.724627201	0.612941060	1
C	6	0.027777201	0.556595201	0.362941060	1
C	6	0.195809201	0.277777201	0.446274393	1
C	6	0.527777201	0.556595201	0.456988393	1
C	6	0.695809201	0.277777201	0.373655060	1
C	6	0.974627201	0.445809201	0.623655060	1
C	6	0.806595201	0.724627201	0.540321727	1
H	1	0.844579201	0.207202201	0.471105393	1
H	1	0.545202201	0.094579201	0.554438727	1
H	1	0.657825201	0.795202201	0.637772060	1
H	1	0.045202201	0.094579201	0.598824060	1
H	1	0.157825201	0.795202201	0.515490727	1
H	1	0.457202201	0.907825201	0.432157393	1
H	1	0.344579201	0.207202201	0.348824060	1
H	1	0.457202201	0.407825201	0.554438727	1
H	1	0.344579201	0.707202201	0.637772060	1
H	1	0.045202201	0.594579201	0.387772060	1
H	1	0.157825201	0.295202201	0.471105393	1
H	1	0.545202201	0.594579201	0.432157393	1
H	1	0.657825201	0.295202201	0.348824060	1
H	1	0.957202201	0.407825201	0.598824060	1
H	1	0.844579201	0.707202201	0.515490727	1
C	6	0.710293201	0.215901201	0.340750393	1
C	6	0.536503201	0.960293201	0.424083727	1
C	6	0.792111201	0.786503201	0.507417060	1
C	6	0.036503201	0.960293201	0.395845727	1
C	6	0.292111201	0.786503201	0.645845727	1
C	6	0.465901201	0.042111201	0.562512393	1
C	6	0.210293201	0.215901201	0.479179060	1
C	6	0.465901201	0.542111201	0.424083727	1
C	6	0.210293201	0.715901201	0.507417060	1

C	6	0.036503201	0.460293201	0.590750393	1
C	6	0.292111201	0.286503201	0.340750393	1
C	6	0.536503201	0.460293201	0.562512393	1
C	6	0.792111201	0.286503201	0.479179060	1
C	6	0.965901201	0.542111201	0.395845727	1
C	6	0.710293201	0.715901201	0.645845727	1
C	6	0.781771201	0.122786201	0.343441393	1
C	6	0.629618201	0.031771201	0.426774727	1
C	6	0.720633201	0.879618201	0.510108060	1
C	6	0.129618201	0.031771201	0.393154727	1
C	6	0.220633201	0.879618201	0.643154727	1
C	6	0.372786201	0.970633201	0.559821393	1
C	6	0.281771201	0.122786201	0.476488060	1
C	6	0.372786201	0.470633201	0.426774727	1
C	6	0.281771201	0.622786201	0.510108060	1
C	6	0.129618201	0.531771201	0.593441393	1
C	6	0.220633201	0.379618201	0.343441393	1
C	6	0.629618201	0.531771201	0.559821393	1
C	6	0.720633201	0.379618201	0.476488060	1
C	6	0.872786201	0.470633201	0.393154727	1
C	6	0.781771201	0.622786201	0.643154727	1
H	1	0.769915201	0.117274201	0.595999060	1
H	1	0.635130201	0.019915201	0.345999060	1
H	1	0.732489201	0.885130201	0.429332393	1
H	1	0.135130201	0.019915201	0.473930393	1
H	1	0.232489201	0.885130201	0.390597060	1
H	1	0.367274201	0.982489201	0.640597060	1
H	1	0.269915201	0.117274201	0.557263727	1
H	1	0.367274201	0.482489201	0.345999060	1
H	1	0.269915201	0.617274201	0.429332393	1
H	1	0.135130201	0.519915201	0.512665727	1
H	1	0.232489201	0.385130201	0.595999060	1
H	1	0.635130201	0.519915201	0.640597060	1
H	1	0.732489201	0.385130201	0.557263727	1
H	1	0.867274201	0.482489201	0.473930393	1
H	1	0.769915201	0.617274201	0.390597060	1
H	1	0.758120201	0.094175201	0.391681060	1
H	1	0.658229201	0.008120201	0.475014393	1
H	1	0.744284201	0.908229201	0.558347727	1
H	1	0.158229201	0.008120201	0.344915060	1
H	1	0.244284201	0.908229201	0.594915060	1
H	1	0.344175201	0.994284201	0.511581727	1
H	1	0.258120201	0.094175201	0.428248393	1
H	1	0.344175201	0.494284201	0.475014393	1
H	1	0.258120201	0.594175201	0.558347727	1
H	1	0.158229201	0.508120201	0.641681060	1
H	1	0.244284201	0.408229201	0.391681060	1
H	1	0.658229201	0.508120201	0.511581727	1

H	1	0.744284201	0.408229201	0.428248393	1
H	1	0.844175201	0.494284201	0.344915060	1
H	1	0.758120201	0.594175201	0.594915060	1
H	1	0.825975201	0.114370201	0.352254393	1
H	1	0.638034201	0.075975201	0.435587727	1
H	1	0.676429201	0.888034201	0.518921060	1
H	1	0.138034201	0.075975201	0.384341727	1
H	1	0.176429201	0.888034201	0.634341727	1
H	1	0.364370201	0.926429201	0.551008393	1
H	1	0.325975201	0.114370201	0.467675060	1
H	1	0.364370201	0.426429201	0.435587727	1
H	1	0.325975201	0.614370201	0.51892106	1
H	1	0.138034201	0.575975201	0.602254393	1
H	1	0.176429201	0.388034201	0.352254393	1
H	1	0.638034201	0.575975201	0.551008393	1
H	1	0.676429201	0.388034201	0.46767506	1
H	1	0.864370201	0.426429201	0.384341727	1
H	1	0.825975201	0.614370201	0.634341727	1
Cu	29	0.0000000	0.5000000	0.446666667	1
Cu	29	0.500000	0.7500000	0.384666667	1
Cu	29	0.000000	0.7500000	0.41100000	1
Cu	29	0.000000	0.7500000	0.63400000	1
Cu	29	0.0000000	0.2500000	0.666666667	1
Br	35	0.860176201	0.963165201	0.918637787	1
N	7	0.965783201	0.178041201	0.773149453	1
C	6	0.939816201	0.984337201	0.95745212	1
N	7	0.930854201	0.078201201	0.851485453	1
C	6	0.952686201	0.130754201	0.812186453	1
C	6	0.974627201	0.945809201	0.689572453	1
H	1	0.957202201	0.907825201	0.714403453	1
C	6	0.965901201	0.042111201	0.917381787	1
C	6	0.872786201	0.970633201	0.920072787	1
H	1	0.867274201	0.982489201	0.83929712	1
H	1	0.844175201	0.994284201	0.968312453	1
H	1	0.864370201	0.926429201	0.928885787	1
Cu	29	0.5000000	0.2500000	0.666666667	1
Cu	29	0.500000	0.7500000	0.833333333	1
Cu	29	0.000000	0.7500000	0.863333333	1
Br	35	0.789239201	0.110176201	0.668637787	1
Br	35	0.642228201	0.039239201	0.75197112	1
Br	35	0.713165201	0.892228201	0.835304453	1
Br	35	0.142228201	0.039239201	0.72122112	1
Br	35	0.213165201	0.892228201	0.97122112	1
Br	35	0.360176201	0.963165201	0.887887787	1
Br	35	0.289239201	0.110176201	0.804554453	1
Br	35	0.360176201	0.463165201	0.75197112	1
Br	35	0.289239201	0.610176201	0.835304453	1
Br	35	0.142228201	0.539239201	0.918637787	1

Br 35 0.213165201 0.392228201 0.668637787 1  
Br 35 0.642228201 0.539239201 0.887887787 1  
Br 35 0.713165201 0.392228201 0.804554453 1  
Br 35 0.860176201 0.463165201 0.72122112 1  
Br 35 0.789239201 0.610176201 0.97122112 1  
N 7 0.574363201 0.215783201 0.856482787 1  
N 7 0.536621201 0.824363201 0.93981612 1  
N 7 0.928041201 0.786621201 0.68981612 1  
N 7 0.036621201 0.824363201 0.866709453 1  
N 7 0.428041201 0.786621201 0.78337612 1  
N 7 0.465783201 0.178041201 0.700042787 1  
N 7 0.074363201 0.215783201 0.950042787 1  
N 7 0.465783201 0.678041201 0.93981612 1  
N 7 0.074363201 0.715783201 0.68981612 1  
N 7 0.036621201 0.324363201 0.773149453 1  
N 7 0.428041201 0.286621201 0.856482787 1  
N 7 0.536621201 0.324363201 0.700042787 1  
N 7 0.928041201 0.286621201 0.950042787 1  
N 7 0.965783201 0.678041201 0.866709453 1  
N 7 0.574363201 0.715783201 0.78337612 1  
C 6 0.768067201 0.189816201 0.70745212 1  
C 6 0.562588201 0.018067201 0.790785453 1  
C 6 0.734337201 0.812588201 0.874118787 1  
C 6 0.062588201 0.018067201 0.682406787 1  
C 6 0.234337201 0.812588201 0.932406787 1  
C 6 0.439816201 0.984337201 0.849073453 1  
C 6 0.268067201 0.189816201 0.76574012 1  
C 6 0.439816201 0.484337201 0.790785453 1  
C 6 0.268067201 0.689816201 0.874118787 1  
C 6 0.062588201 0.518067201 0.95745212 1  
C 6 0.234337201 0.312588201 0.70745212 1  
C 6 0.562588201 0.518067201 0.849073453 1  
C 6 0.734337201 0.312588201 0.76574012 1  
C 6 0.939816201 0.484337201 0.682406787 1  
C 6 0.768067201 0.689816201 0.932406787 1  
N 7 0.674203201 0.180854201 0.934818787 1  
N 7 0.571550201 0.924203201 0.684818787 1  
N 7 0.828201201 0.821550201 0.76815212 1  
N 7 0.071550201 0.924203201 0.788373453 1  
N 7 0.328201201 0.821550201 0.70504012 1  
N 7 0.430854201 0.078201201 0.95504012 1  
N 7 0.174203201 0.180854201 0.871706787 1  
N 7 0.430854201 0.578201201 0.684818787 1  
N 7 0.174203201 0.680854201 0.76815212 1  
N 7 0.071550201 0.424203201 0.851485453 1  
N 7 0.328201201 0.321550201 0.934818787 1  
N 7 0.571550201 0.424203201 0.95504012 1  
N 7 0.828201201 0.321550201 0.871706787 1

N	7	0.930854201	0.578201201	0.788373453	1
N	7	0.674203201	0.680854201	0.70504012	1
C	6	0.621650201	0.202686201	0.895519787	1
C	6	0.549718201	0.871650201	0.97885312	1
C	6	0.880754201	0.799718201	0.72885312	1
C	6	0.049718201	0.871650201	0.827672453	1
C	6	0.380754201	0.799718201	0.74433912	1
C	6	0.452686201	0.130754201	0.661005787	1
C	6	0.121650201	0.202686201	0.911005787	1
C	6	0.452686201	0.630754201	0.97885312	1
C	6	0.121650201	0.702686201	0.72885312	1
C	6	0.049718201	0.371650201	0.812186453	1
C	6	0.380754201	0.299718201	0.895519787	1
C	6	0.549718201	0.371650201	0.661005787	1
C	6	0.880754201	0.299718201	0.911005787	1
C	6	0.952686201	0.630754201	0.827672453	1
C	6	0.621650201	0.702686201	0.74433912	1
C	6	0.806595201	0.224627201	0.772905787	1
C	6	0.527777201	0.056595201	0.85623912	1
C	6	0.695809201	0.777777201	0.939572453	1
C	6	0.027777201	0.056595201	0.950286453	1
C	6	0.195809201	0.777777201	0.86695312	1
C	6	0.474627201	0.945809201	0.783619787	1
C	6	0.306595201	0.224627201	0.700286453	1
C	6	0.474627201	0.445809201	0.85623912	1
C	6	0.306595201	0.724627201	0.939572453	1
C	6	0.027777201	0.556595201	0.689572453	1
C	6	0.195809201	0.277777201	0.772905787	1
C	6	0.527777201	0.556595201	0.783619787	1
C	6	0.695809201	0.277777201	0.700286453	1
C	6	0.974627201	0.445809201	0.950286453	1
C	6	0.806595201	0.724627201	0.86695312	1
H	1	0.844579201	0.207202201	0.797736787	1
H	1	0.545202201	0.094579201	0.88107012	1
H	1	0.657825201	0.795202201	0.964403453	1
H	1	0.045202201	0.094579201	0.925455453	1
H	1	0.157825201	0.795202201	0.84212212	1
H	1	0.457202201	0.907825201	0.758788787	1
H	1	0.344579201	0.207202201	0.675455453	1
H	1	0.457202201	0.407825201	0.88107012	1
H	1	0.344579201	0.707202201	0.964403453	1
H	1	0.045202201	0.594579201	0.714403453	1
H	1	0.157825201	0.295202201	0.797736787	1
H	1	0.545202201	0.594579201	0.758788787	1
H	1	0.657825201	0.295202201	0.675455453	1
H	1	0.957202201	0.407825201	0.925455453	1
H	1	0.844579201	0.707202201	0.84212212	1
C	6	0.710293201	0.215901201	0.667381787	1

C	6	0.536503201	0.960293201	0.75071512	1
C	6	0.792111201	0.786503201	0.834048453	1
C	6	0.036503201	0.960293201	0.72247712	1
C	6	0.292111201	0.786503201	0.97247712	1
C	6	0.465901201	0.042111201	0.889143787	1
C	6	0.210293201	0.215901201	0.805810453	1
C	6	0.465901201	0.542111201	0.75071512	1
C	6	0.210293201	0.715901201	0.834048453	1
C	6	0.036503201	0.460293201	0.917381787	1
C	6	0.292111201	0.286503201	0.667381787	1
C	6	0.536503201	0.460293201	0.889143787	1
C	6	0.792111201	0.286503201	0.805810453	1
C	6	0.965901201	0.542111201	0.72247712	1
C	6	0.710293201	0.715901201	0.97247712	1
C	6	0.781771201	0.122786201	0.670072787	1
C	6	0.629618201	0.031771201	0.75340612	1
C	6	0.720633201	0.879618201	0.836739453	1
C	6	0.129618201	0.031771201	0.71978612	1
C	6	0.220633201	0.879618201	0.96978612	1
C	6	0.372786201	0.970633201	0.886452787	1
C	6	0.281771201	0.122786201	0.803119453	1
C	6	0.372786201	0.470633201	0.75340612	1
C	6	0.281771201	0.622786201	0.836739453	1
C	6	0.129618201	0.531771201	0.920072787	1
C	6	0.220633201	0.379618201	0.670072787	1
C	6	0.629618201	0.531771201	0.886452787	1
C	6	0.720633201	0.379618201	0.803119453	1
C	6	0.872786201	0.470633201	0.71978612	1
C	6	0.781771201	0.622786201	0.96978612	1
H	1	0.769915201	0.117274201	0.922630453	1
H	1	0.635130201	0.019915201	0.672630453	1
H	1	0.732489201	0.885130201	0.755963787	1
H	1	0.135130201	0.019915201	0.800561787	1
H	1	0.232489201	0.885130201	0.717228453	1
H	1	0.367274201	0.982489201	0.967228453	1
H	1	0.269915201	0.117274201	0.88389512	1
H	1	0.367274201	0.482489201	0.672630453	1
H	1	0.269915201	0.617274201	0.755963787	1
H	1	0.135130201	0.519915201	0.83929712	1
H	1	0.232489201	0.385130201	0.922630453	1
H	1	0.635130201	0.519915201	0.967228453	1
H	1	0.732489201	0.385130201	0.88389512	1
H	1	0.867274201	0.482489201	0.800561787	1
H	1	0.769915201	0.617274201	0.717228453	1
H	1	0.758120201	0.094175201	0.718312453	1
H	1	0.658229201	0.008120201	0.801645787	1
H	1	0.744284201	0.908229201	0.88497912	1
H	1	0.158229201	0.008120201	0.671546453	1

```
H 1 0.244284201 0.908229201 0.921546453 1
H 1 0.344175201 0.994284201 0.83821312 1
H 1 0.258120201 0.094175201 0.754879787 1
H 1 0.344175201 0.494284201 0.801645787 1
H 1 0.258120201 0.594175201 0.88497912 1
H 1 0.158229201 0.508120201 0.968312453 1
H 1 0.244284201 0.408229201 0.718312453 1
H 1 0.658229201 0.508120201 0.83821312 1
H 1 0.744284201 0.408229201 0.754879787 1
H 1 0.844175201 0.494284201 0.671546453 1
H 1 0.758120201 0.594175201 0.921546453 1
H 1 0.825975201 0.114370201 0.678885787 1
H 1 0.638034201 0.075975201 0.76221912 1
H 1 0.676429201 0.888034201 0.845552453 1
H 1 0.138034201 0.075975201 0.71097312 1
H 1 0.176429201 0.888034201 0.96097312 1
H 1 0.364370201 0.926429201 0.877639787 1
H 1 0.325975201 0.114370201 0.794306453 1
H 1 0.364370201 0.426429201 0.76221912 1
H 1 0.325975201 0.614370201 0.845552453 1
H 1 0.138034201 0.575975201 0.928885787 1
H 1 0.176429201 0.388034201 0.678885787 1
H 1 0.638034201 0.575975201 0.877639787 1
H 1 0.676429201 0.388034201 0.794306453 1
H 1 0.864370201 0.426429201 0.71097312 1
H 1 0.825975201 0.614370201 0.96097312 1
Cu 29 0.000000 0.500000 0.780000 1
Cu 29 0.500000 0.750000 0.718000 1
Cu 29 0.000000 0.750000 0.744333333 1
Cu 29 0.000000 0.750000 0.967333333 1
[viso] 0.0
[note] Refs. 63, 74 and this work
```

# List of References

- [1] H. Ibach and H. Lüth. *Solid State Physics: An Introduction to Principles of Materials Science*. Springer-Verlag Berlin Heidelberg, 2003.
- [2] Charles Kittel. *Introduction to Solid State Physics*. John Wiley & Sons, Inc., 2005.
- [3] M. R. Ibarra and J. M. De Teresa. *Colossal magnetoresistance in manganese oxide perovskites*. *Journal of Magnetism and Magnetic Materials*, **177-181**, 846–849, 1998.
- [4] J. Bardeen, L. N. Cooper and J. R. Schrieffer. *Microscopic theory of superconductivity*. *Physical Review*, **106**, 162–164, 1957.
- [5] K. Rossnagel. *On the origin of charge-density waves in select layered transition metal dichalcogenides*. *Journal of Physics: Condensed Matter*, **23**, 2011.
- [6] M. Gao, C. Lu, H. Jean-Ruel, L. C. Liu, A. Marx, K. Onda, S. Koshihara, Y. Nakano, X. Shao, T. Hiramatsu, G. Saito, H. Yamochi, R. R. Cooney, G. Moriena, G. Sciaini and R. J. Dwayne Miller. *Mapping molecular motions leading to charge delocalization with ultrabright electrons*. *Nature: Macmillan Publishers Limited*, **496**, 343–346, 2013.
- [7] N. Erasmus. *Ultrafast Structural Dynamics in  $4H_b$ -TaSe<sub>2</sub> Observed by Femtosecond Electron Diffraction*. PhD Dissertation, University of Stellenbosch, 2013.
- [8] G. H. Kassier. *Ultrafast Electron Diffraction: Source Development, Diffractometer Design and Pulse Characterisation*. PhD Dissertation, University of Stellenbosch, 2010.
- [9] I. Boshoff. *Ultrafast Electron Diffraction on the Charge Density Wave Compound  $4H_b$ -TaSe<sub>2</sub>*. Masters Thesis, University of Stellenbosch, 2012.
- [10] K. A. Haupt. *Phase Transitions in Transition Metal Dichalcogenides Studied by Femtosecond Electron Diffraction*. PhD Dissertation, University of Stellenbosch, 2013.
- [11] F. Hüwe. *Growth and Characterisation of Radical Anion Salt Single Crystals*. Diploma Thesis, Julius-Maximilians-University of Würzburg, 2012.
- [12] N. Erasmus, M. Eichberger, K. Haupt, I. Boshoff, R. Birmurske, H. Berger, J. Demsar and H. Schwoerer. *Ultrafast dynamics of charge density waves in  $4H_b$ -TaSe<sub>2</sub> probed by femtosecond electron diffraction*. *Physical Review Letters*, **109**, 2012.
- [13] A. B. Smit. *A New Femtosecond Electron Diffractometer for Structural Dynamics Experiments at Cryogenic Temperatures*. Masters Thesis, University of Stellenbosch, 2014.
- [14] A. Aumüller, P. Erk, G. Klebe, S. Hünig, J. U. von Schütz and H. P. Werner. *A radical anion salt of 2,5-Dimethyl-N-N'-dicyanoquinonediimine with extremely high electrical conductivity*. *Angew. Chem. Int. Ed. Engl.*, **25**, 740–741, 1986.
- [15] X. Li. *Simulation and Analysis of Electron Diffraction* software package. This software is developed by Xingzhong Li, in collaboration with the University of Nebraska, USA. [www.unl.edu/ncmn-cfem/xzli/saed2/saed2.htm](http://www.unl.edu/ncmn-cfem/xzli/saed2/saed2.htm).

- [16] P. J. Grundy and G. A. Jones. *Electron Microscopy in the Study of Materials*. Edward Arnold Limited, 1976.
- [17] B. E. P. Beeston, R. W. Horne and R. Markham. *Electron Diffraction and Optical Diffraction Techniques*. Elsevier Science Limited, 1994.
- [18] X. Zou, S. Hovmöller and P. Oleynikov. *Electron Crystallography: Electron Microscopy and Electron Diffraction*. International Union of Crystallography, Oxford Science Publications, 2011.
- [19] L. Reimer and H. Kohl. *Transmission Electron Microscopy: Physics of Image Formation*. Springer, Fifth Edition, 2008.
- [20] P. Coppens. *The structure factor*. International Tables for Crystallography, **B**, Chapter 1.2, 10–24, 2006.
- [21] P. J. Brown, A. G. Fox, E. N. Maslen, M. A. O’Keefe and B. T. M. Willis. *Intensity of diffracted intensities*. International Tables for Crystallography, **C**, Chapter 6.1, 554–595, 2006.
- [22] A. G. Jackson. *Parity tables in convergent-beam diffraction*. *Ultramicroscopy*, **30**, 349–354, 1989.
- [23] J. A. Eades. *Laue zones: A clarification of nomenclature*. *Ultramicroscopy*, **32**, 183, 1990.
- [24] I. D. Brown. *CIF (Crystallographic Information File): A standard for crystallographic data interchange*. *Journal of Research of the National Institute of Standards and Technology*, **101**, 341–346, 1996.
- [25] S. R. Hall, F. H. Allen and I. D. Brown. *The crystallographic information file (CIF): A new standard archive file for crystallography*. *Acta Cryst.*, **A47**, 655–685, 1991.
- [26] I. D. Brown. *Space-group symmetry*. International Tables for Crystallography, **A**, 2002.
- [27] D. C. Bell, Y. Wu, C. J. Barrelet, S. Gradečak, J. Xiang, B. P. Timko and C. M. Lieber. *Imaging and analysis of nanowires*. *Microscopy Research and Technique*, **64**, 373–389, 2004.
- [28] J. Reyes-Gasga, D. Romeu and A. Gómez-Rodríguez. *Electron diffraction and HRTEM structure analysis of nanowires*. [www.intechopen.com](http://www.intechopen.com).
- [29] M. J. Frisch, G. W. Trucks, H. B. Schlegel, G. E. Scuseria, M. A. Robb, J. R. Cheeseman, G. Scalmani, V. Barone, B. Mennucci, G. A. Petersson, H. Nakatsuji, M. Caricato, X. Li, H. P. Hratchian, A. F. Izmaylov, J. Bloino, G. Zheng, J. L. Sonnenberg, M. Hada, M. Ehara, K. Toyota, R. Fukuda, J. Hasegawa, M. Ishida, T. Nakaajima, Y. Honda, O. Kitao, H. Nakai, T. Vreven, J. A. Montgomery, Jr., J. E. Peralta, F. Ogliaro, M. Bearpark, J. J. Heyd, E. Brothers, K. N. Kudin, V. N. Staroverov, R. Kobayashi, J. Normand, K. Raghavachari, A. Rendell, J. C. Burant, S. S. Iyengar, J. Tomasi, M. Cossi, N. Rega, J. M. Millam, M. Klene, J. E. Knox, J. B. Cross, V. Bakken, C. Adamo, J. Jaramillo, R. Gomperts, R. E. Stratmann, O. Yazyev, A. J. Austin, R. Cammi, C. Pomelli, J. W. Ochterski, R. L. Martin, K. Morokuma, V. G. Zakrzewski, G. A. Voth, P. Salvador, J. J. Dannenberg, S. Dapprich, A. D. Daniels, O. Farkas, J. B. Foresman, J. V. Ortiz, J. Cioslowski, and D. J. Fox. *Gaussian 09, Revision A.02*, Gaussian, Inc., Wallingford CT, 2009.
- [30] G. T. Mulyavko, E. N. Ovchinnikova, A. P. Oreshko, V. E. Dmitrienko and E. Kh. Mukhamedzhanov. *Effect of strain in crystal on the forbidden reflections in the resonant diffraction of synchrotron radiation*. *Crystallography Reports*, **57**, 18–23, 2012.
- [31] B. Yinon. Chemical elements. [www.chemicalelements.com](http://www.chemicalelements.com).
- [32] R. H. Friend and D. Jérôme. *Periodic lattice distortions and charge density waves in one- and two-dimensional metals*. *Journal of Physics C Solid State Physics*, **12**, 1441–1477, 1979.

- [33] S. Hellmann, T. Rohwer, M. Kalläne, K. Hanff, C. Sohrt, A. Stange, A. Carr, M. M. Murnane, H. C. Kapteyn, L. Kipp, M. Bauer and K. Rossnagel. *Time-domain classification of charge-density-wave insulators*. Nature Communications, 3:1069, DOI:10.1038/ncomms2078, [www.nature.com/naturecommunications](http://www.nature.com/naturecommunications), 2012.
- [34] M. Eichberger, H. Schäfer, M. Krumova, M. Beyer, J. Demsar, H. Berger, G. Moriena, G. Sciaini and R. J. Dwayne Miller. *Snapshots of cooperative atomic motions in the optical suppression of charge density waves*. Nature, **468**, 799–802, 2010.
- [35] J. Lüdecke, S. van Smaalen, A. Spijkerman, J. L. de Boer and G. A. Wiegers. *Commensurately modulated structure of  $4H_b$ - $TaSe_2$  determined by x-ray crystal-structure refinement*. Physical Review B, **59**, 6063–6071, 1999.
- [36] F. J. Di Salvo, D. E. Moncton and J. V. Waszczak. *Electronic properties and superlattice formation in the semimetal  $TiSe_2$* . Physical Review B, **14**, 4321–4328, 1976.
- [37] R. Moret and E. Tronc. *CDW induced atomic shifts in  $4H_bTaSe_2$* . Physica, **99B**, 56–58, 1980.
- [38] R. V. Coleman, Z. Dai, W. W. McNairy, C. G. Slough and C. Wang. *Surface Properties of Layered Structures Physics and Chemistry of Materials with Low-Dimensional Structures*. Springer, **16**, 27–95, 1992.
- [39] P. Fazekas and E. Tosatti. *Charge carrier localization in pure and doped  $1T-TaS_2$* . Physica, **99B**, 183–187, 1980.
- [40] F. J. Di Salvo, D. E. Moncton, J. A. Wilson and S. Mahajan. *Coexistence of two charge-density waves of different symmetry in  $4H_b-TaSe_2$* . Physical Review B, **14**, 1543–1546, 1976.
- [41] Y. Ge and A. Y. Liu. *First principles investigation of the charge-density-wave instability in  $1T-TaSe_2$* . Physical Review B, **82**, 155133-1–155133-7, 2010.
- [42] J. J. Kim and H. Olin. *Atomic- and electronic-structure study on the layers of  $4H_b-TaS_2$  prepared by a layer-by-layer etching technique*. Physical Review B, **52**, R14388–R14391, 1995.
- [43] G. K. Wertheim, F. J. DiSalvo and S. Chiang. *Charge-density waves and many-body effects in x-ray photoelectron spectroscopy of layer-structure chalcogenides*. Physical Review B, **13**, 5476–5483, 1976.
- [44] M. Eibschutz. *Sign and amplitude of commensurate charge-density wave in  $1T-TaSe_2$* . Physical Review B, **45**, 10914–10917, 1992.
- [45] A. Spijkerman, J. L. de Boer, A. Meetsma and G. A. Wiegers. *X-ray crystal-structure refinement of the nearly commensurate phase of  $1T-TaS_2$  in  $(3+2)$ -dimensional superspace*. Physical Review B, **56**, 13757–13767, 1997.
- [46] T. Nakashizu, T. Sekine, K. Uchinokura and E. Matsuura. *Raman study of charge density wave excitation in  $4H_b-TaS_2$* . Physical Review B, **29**, 3090–3097, 1984.
- [47] D. H. Torchinsky, F. Mahmood, A. T. Bollinger, I. Bobrevzvić and N. Gedik. *Fluctuating charge-density waves in cuprate superconductor*. Nature Materials, **12**, 387–391, 2013.
- [48] C. H. Sorht, A. Stange, M. Bauer and K. Rossnagel. *How fast can a Peierl-Mott insulator be melted?* Faraday Discuss, **171**, 243–257, 2014.
- [49] O. Olaoye, N. Erasmus, K. Haupt and H. Schwoerer. *Femtosecond dynamics of decoupled superlattice domains in  $4H_b-TaSe_2$  single crystals*. Journal of Physics B: Atomic, Molecular and Optical Physics, submitted, 2015.
- [50] S. C. Bayliss and W. Y. Liang. *Reflectivity, joint density of states and band structure of group IVb transition-metal dichalcogenides*. Journal of Physics C Solid State Physics, **18**, 3327–3335, 1985.

- [51] A. R. Beal, H. P. Hughes and W. Y. Liang. *The reflectivity spectra of some group VA transition-metal dichalcogenides*. Journal of Physics C Solid State Physics, **8**, 4236–4248, 1975.
- [52] K. C. Woo, F. C. Brown, W. L. McMillan, R. J. Miller, M. J. Schaffman and M. P. Sears. *Superlattice formation in titanium diselenide*. Physical Review B, **14**, 3242–3247, 1976.
- [53] E. Möhr-Vorobevea, S. L. Johnson, P. Beaud, U. Staub, R. De Souza, C. Milne, G. Ingold, J. Demsar, H. Schaefer and A. Titov. *Nonthermal melting of a charge density wave in  $TiSe_2$* . Physical Review Letter, **107**, 036403-1–036403-4, 2011.
- [54] J. Ishioka, Y. H. Liu, K. Shimatake, T. Kurosawa, K. Ichimura, Y. Toda, M. Oda and S. Tanda. *Chiral charge-density waves*. Physical Review Letter, **105**, 176401-1–176401-4, 2010.
- [55] M. Wiesenmayer, S. Hilgenfeldt, S. Mathias, F. Steeb, T. Rohwer and M. Bauer. *Spectroscopy and population decay of a van der Waals gap state in layered  $TiSe_2$* . Physical Review B, **82**, 035422-1–035422-10, 2010.
- [56] M. Porer, U. Leierseder, J.-M. Ménard, H. Dachraoui, L. Mouchliadis, I. E. Perakis, U. Heinzmann, J. Demsar, K. Rossnagel and R. Huber. *Non-thermal separation of electronic and structural orders in a persisting charge density wave*. Nature Materials, **13**, 857–861, 2014.
- [57] C. Riekel. *Structural refinement of  $TiSe_2$  by neutron diffraction*. Journal of Solid State Chemistry, **17**, 389–392, 1976.
- [58] T. E. Kidd, T. Miller, M. Y. Chou and T. C. Chiang. *Electron-hole coupling and charge density wave transition in  $TiSe_2$* . Physical Review Letter, **88**, 226402-1–226402-4, 2002.
- [59] A. O. Suleiman. *Structural Dynamics of 1T- $TiSe_2$  Using Femtosecond Electron Diffraction*. Masters Thesis, University of Stellenbosch, 2014.
- [60] M. Schworer and H. C. Wolf. *Organic Molecular Solids*. WILEY-VCH Verlag GmbH & Co. KGaA, Weinheim, 2007.
- [61] D. Jérôme. *The development of organic conductors: Organic superconductors*. Solid State Sciences, **10**, 1692–1700, 2008.
- [62] G. J. Linker, P. Th. van Duijnen, P. H. M. van Loosdrecht and R. Broer. *Off-planar geometry and structural instability of EDO-TTF explained by using the extended Debye polarizability model for bond angles*. The Journal of Physical Chemistry A, **116**, 7219–7227, 2012.
- [63] Christian Sager. *Zeitaufgelöste Untersuchung atomarer Ordnung in Tetrathiafulvalen-Tetracyanochinodimethane (TTF-TCNQ)-Einkristallen nach Anregung mit ultrakurzen Lichtpulsen*. PhD Dissertation, Universität Hamburg, 2010.
- [64] K. Sinzger, S. Hünig, M. Jopp, D. Bauer, W. Bietsch, J. U. von Schütz, H. C. Wolf, R. K. Kremer, T. Metzenthin, R. Bau, S. I. Khan, A. Lindbaum, C. L. Lengauer and E. Tillmanns. *The organic metal  $(Me_2 - DCNQI)_2Cu$ : Dramatic changes in solid-state properties and crystal structure due to secondary deuterium effects*. J. Am. Chem. Soc., **115**, 7696–7705, 1993.
- [65] R. Kato, H. Kobayashi and A. Kobayashi. *Crystal and electronic structures of conductive anion-radical salts,  $(2,5-R_1,R_2-DCNQI)_2Cu$  ( $DCNQI = N,N'$ -dicyanoquinonediimine;  $R_1, R_2 = CH_3, CH_3O, Cl, Br$ )*. J. Am. Chem. Soc., **111**, 5224–5232, 1989.
- [66] R. Moret, P. Erk, S. Hünig, J. U. von Schütz. *X-ray scattering evidence for dimerisation ( $4k_F$ ) and spin-Peierls distortion ( $2k_F$ ) in silver salts of dicyanoquinonediimine  $(2,5 MR-DCNQI)_2Ag$  ( $R=CH_3, Cl$  or  $Br, M = CH_3$ )*. J. Phys. France, **49**, 1925–1931, 1988.
- [67] K. Yamamoto, T. Yamamoto and K. Yakushi. *Bond and charge density waves in  $(DI-DCNQI)_2Ag$  ( $DI-DCNQI = 2,5$ -diiodo- $N,N'$ -dicyanoquinonediimine) studied by single-crystal infrared and Raman spectroscopy*. Physical Review B, **71**, 045118-1–045118-10, 2005.

- [68] K. Hiraki and K. Kanoda. *Comparative study on the magnetism and conductivity of (DI-DCNQI)<sub>2</sub>M*, ( $M = Li, Cu, Ag$ ). *Synthetic Metals*, **86**, 2103–2104, 1997.
- [69] M. Nakano, M. Kato and K. Yamada. *Metal-insulator transition in DCNQI-Cu*. *Physica B*, **186-188**, 1077–1079, 1993.
- [70] F. O. Karutz, J. U. von Schütz, H. Watchel and H. C. Wolf. *Optically reversed Peierls transition in crystals of Cu(dicyanoquinonediimine)<sub>2</sub>*. *Physical Review Letters*, **81**, 1077–1079, 1998.
- [71] T. Miyazaki and K. Terakura. *First-principles theoretical study of metallic states of DCNQI-(Cu,Ag,Li) systems*. *Physical Review B*, **54**, 10452–10464, 1996.
- [72] T. Miyazaki and K. Terakura. *(DI-DCNQI)<sub>2</sub>Cu as a unique member of the DCNQI-Cu family: A theoretical study of high-pressure phases*. *Physical Review B*, **56**, R447–R480, 1997.
- [73] S. H. Lee, H. J. Chung, J. Heo, H. Yang, J. Shin, U-In Chung and S. Seo. *Band gap opening by two-dimensional manifestation of Peierls instability in graphene*. *American Chemical Society*, **5**, 2964–2969, 2011.
- [74] A. Kobayashi, T. Mori, H. Inokuchi, R. Kato and H. Kobayashi. *The organic  $\pi$ -electron metal system with interaction through mixed-valence metal cation: Electronic and structural properties of highly conducting anion radical salts (2,5-R<sub>1</sub>-R<sub>2</sub>-DCNQI)<sub>2</sub>Cu*. *Synthetic Metals*, **27**, B275–B280, 1988.
- [75] A. Kobayashi, R. Kato, H. Kobayashi, T. Mori and H. Inokuchi. *The organic  $\pi$ -electron metal system with interaction through mixed-valence metal cation: Electronic and structural properties of radical salts of dicyano-quinonediimine, (DMe-DCNQI)<sub>2</sub>Cu and (MeCl-DCNQI)<sub>2</sub>Cu*. *Solid State Communications*, **64**, 45–51, 1987.
- [76] H. Kobayashi, A. Miyamoto, R. Kato, F. Sakai, A. Kobayashi, Y. Yamakita, Y. Furukawa, M. Tasumi and T. Watanabe. *Mixed-valency of Cu, electron-mass enhancement, and three-dimensional arrangement of magnetic sites in the organic conductors (R<sub>1</sub>,R<sub>2</sub>-N,N'-dicyano-quinonediimine)<sub>2</sub>Cu (where R<sub>1</sub>,R<sub>2</sub> = CH<sub>3</sub>, CH<sub>3</sub>O, Cl, Br)*. *Physical Review B*, **47**, 3500–3510, 1993.
- [77] S. Hünig, M. Kemmer, H. Meixner, K. Sinzger, H. Wenner, T. Bauer, E. Tillmanns, F. R. Lux, M. Hollstein, H. G. GroB, U. Langohr, H. P. Werner, J. U. von Schütz and H. C. Wolf. *2,5-Disubstituted N, N'-dicyanobenzoquinonediimines (DCNQIs): Charge-transfer complexes and radical-anion salts with ligand alloys: Syntheses, structures and conductivities*. *Eur. J. Inorg. Chem.*, 899–916, 1999.
- [78] H. A. Jahn and E. Teller. *Stability of polyatomic molecules in degenerate electronic states: I-Orbital degeneracy*. *Proc. R. Soc. Lond. A*, **161**, 220–235, 1937.
- [79] H. A. Jahn and E. Teller. *Stability of polyatomic molecules in degenerate electronic states: II-Spin degeneracy*. *Proc. R. Soc. Lond. A*, **164**, 117–131, 1938.
- [80] This space group explorer was designed and programmed by Maxim Larine and Slava Klimkovich, SoftHard technology, Ltd., Tvarozkova 8, 81103 Bratislava, Slovakia.
- [81] E. N. Ovchinnikova, V. E. Dmitrienko, K. Ishida, A. Kirfel, S. P. Collins, A. P. Oreshko, D. Cabaret, R. V. Vedrinskii, V. L. Kraizman, A. A. Novakovich, E. V. Krivitskii and B. P. Tolocchko. *Atomic displacement effects in near-edge resonant "forbidden" reflections*. *Nuclear Instruments and Methods in Physics Research A*, **543**, 111–126, 2005.
- [82] E. D. T. Kamga, W. Mader, C. M. Kede, L. M. Meva'a and A. Kirfel. *CBED phase and symmetry determination of a new member of homologous series Ga<sub>2</sub>O<sub>3</sub>(ZnO)<sub>10</sub>*. *International Journal of Engineering Research & Technology (IJERT)*, **2**, 1394–1400, 2013.
- [83] G. Lunardi and C. Pecile. *N,N'-dicyanoquinonediimines as a molecular constituent of organic conductors: Vibrational behaviour and electron-molecular vibration coupling*. *J. Chem. Phys.*, **95** (9), 6911–6923, 1991.

- [84] T. Yamamoto, H. Tajima, R. Kato, M. Uruichi and K. Yakushi. *Raman Spectra of  $(Me_2-DCNQI)_2Cu_xLi_{1-x}$  ( $0 \leq x \leq 1$ ): The evidence for charge separation at room temperature in a one-dimensional conductor having a quarter-filled band.* Journal of Physical Society of Japan, **71** (8), 1956–1964, 2002.
- [85] A. B. Rohwer. *Introducing Organic Molecular Crystals into Ultrafast Electron Diffraction.* Masters Thesis, University of Stellenbosch, 2014.
- [86] A. Caviezel, S. O. Mariager, S. L. Johnson, E. Möhr-Vorobeva, S. W. Huang, G. Ingold, U. Staub, C. J. Milne, S. W. Cheong and P. Beaud. *Identification of coherent lattice modulations coupled to charge and orbital order in a manganite.* Physical Review B, **87**, 205104-1–205104-6, 2013.
- [87] M. Pinterić, T. Vuletić, M. Lončarić, K. Petukhov, B. Gorshunov, J. U. von Schütz, S. Tomić and M. Dressel. *Mott-Peierls phase in deuterated copper-DCNQI systems: a comprehensive study of longitudinal and transverse conductivity and ageing effects.* J. Phys.: Condens. Matter, **15**, 7351–7364, 2003.
- [88] R. H. Carr, R. D. McCammon and G. K. White. *The thermal expansion of copper at low temperatures.* Proceedings of the Royal Society of London, Series A, Mathematical and Physical Sciences, **280**, 72–84, 1964.
- [89] H. Sawa, and T. Kakiuchi. *Study of the novel charge ordering state in molecular conductors using synchrotron radiation X-ray diffraction.* Molecular Electronic and Related Materials - Control and Probe with Light, 1–18, 2010.
- [90] H. Sawa, Y. Wakabayashi, R. Tazaki, T. Kakiuchi, K. Kanoda and R. Kato. *Role of frustration in quasi 1D conductor - Charge ordering and/or CDW in  $(R_1, R_2-DCNQI)_2M$  ( $M = Ag, Li, Cu$ ) system.* Journal of Low Temperature Physics, **142**, 355–360, 2006.
- [91] Y. Suzumura and T. Ogawa. *Metal-insulator transition in organic conductor DCNQI-Cu salt.* Synthetic Metals, **70**, 1083–1084, 1995.